Photoelectrochemical tandem cells with enzymes wired to hierarchically-structured electrodes for solar fuel synthesis

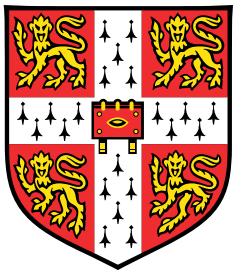

Katarzyna Paulina Sokół

Department of Chemistry
University of Cambridge

This dissertation is submitted for the degree of
Doctor of Philosophy

St John's College September 2018

This thesis is dedicated to my amazing parents, Elżbieta Paciej and Tomasz Sokół, whose love and endless faith in me led me through this life journey and made me become the person that I am today.

Declaration

I hereby declare that the contents of this dissertation entitled *'Photoelectrochemical tandem cells with enzymes wired to hierarchically-structured electrodes for solar fuel synthesis'* is the result of my own work which was carried out at the University of Cambridge between October 2014 and September 2018 and is not the outcome of work done in collaboration except as declared in the Acknowledgements and specified in the text. Several of the reported results have been published in peer-reviewed scientific journals which are referenced in the text and included in the List of publications. I further state that no substantial part of my dissertation has already been submitted, or, is being concurrently submitted for any degree, diploma or other qualification at the University of Cambridge or any other University or similar institution except as declared in the Acknowledgements and specified in the text. The thesis does not exceed 60,000 words in length.

Katarzyna Paulina Sokół
September 2018

Acknowledgements

First, I would like to thank my supervisor, Prof. Erwin Reisner, for giving me the opportunity to work in his group and for his guidance throughout my studies. I would like to thank my funding body, the EPSRC and the ERC, for funding my project. Thanks to the NanoDTC for their support and many interesting experiences.

Many thanks to Dr. Dirk Mersch and Dr. Jenny Zhang for providing guidance during the first year of my PhD studies. I would like to thank Dr. Dirk Mersch and Dr. William Robinson for all their contributions to this project, their help and patience. Dr. Julien Warnan and Dr. Janina Wilkomm are acknowledged for the dpp and RuP dye synthesis. Dr. Nikolay Kornienko is acknowledged for electrode characterisation by STEM and RRDE. Dr. Tarek Kandiel is acknowledged for ITO NPs characterisation by TEM. Thanks to the 'Enzyme' team for many intellectually-stimulating discussions. The departmental electrical workshop services are thanked for providing support. In particular, Mr. Wayne Bailey and Mr. Manuel Wentscher are acknowledged for building the customised LED lamp.

I would like to thank my collaborators at Ruhr-Universität Bochum: Dr Sascha Pöller, Ms Sabine Alsaoub and Dr. Adrian Ruff in the group of Prof. Wolfgang Schuhmann for their contributions to polymer synthesis and characterisation (NMR, UV-vis spectroscopy and DLS); Volker Hartmann and Dr. Marc Nowaczyk in the group of Prof. Matthias Rögner for providing isolated PSII; and Prof. Nicolas Plumeré for many fruitful discussions. Thanks to Dr Juan Fontecilla-Camps and Dr. Christine Cavazza at the Institut de Biologie Structurale for providing H_2ase. Ana R. Oliveira and Prof. Inês Pereira at the Instituto de Tecnologia Química e Biológica António Xavier are acknowledged for providing FDH.

Thanks to the staff, SBR Committee and my friends in St. John's College for your support and many memorable moments during my time in Cambridge. I would also like to thank my Varsity team and all the members of Cambridge University Kendo Club, for countless training sessions together that kept me sane during the past four years. Special thanks to my sempai, Vitor Zanni, Barry Rutter and Dr. Akihiro Mori, for all your teaching and support.

Huge thanks go to my friends and colleagues, Hatice Kasap, Demetra Achilleos, Will Robinson, Dirk Mersch, Nick Paul, Xin Fang and Virgil Andrei for many great memories, meetups and dinners together. These past four years would not have been the same without you. Thanks to everyone else in the Reisner group who has not been mentioned here by name. Thank you all for many amazing experiences, all your help and great company.

I would also like to specially thank Will Robinson for his endless support, patience and helping me to stay motivated during this last difficult year. Finally, I would like to thank my loving family for always encouraging me to pursue my goals and bringing me to this point.

Abstract

In photosynthesis, solar energy drives the conversion of CO_2 and H_2O into chemical energy carriers and building blocks, releasing O_2 as a by-product. Artificial photosynthesis attempts to mimic this process to produce a renewable and storable fuel, such as H_2. Semi-artificial photosynthesis combines the strengths of natural photosynthesis with synthetic chemistry and materials science to develop model systems that overcome Nature's limitations, such as low-yielding metabolic pathways and non-complementary light absorption by photosystem (PS) I and II. PSII, the first photosynthetic enzyme, is capable of photocatalytic water oxidation, a bottleneck reaction in artificial photosynthesis. The study of PSII in protein film photoelectrochemical (PF-PEC) platforms sheds light into its biological function and provides a blueprint for artificial water-splitting systems. However, the integration of biomolecules into electrodes is often limited by inefficient wiring at the biotic−abiotic interface.

In this thesis, a range of tuneable hierarchically-structured electrodes was developed, constituting a versatile platform to accommodate a variety of biotic guests for PF-PEC cells. A new benchmark PSII−electrode system was assembled, that combined the efficient wiring afforded by redox-active polymers with the high loading provided by hierarchically-structured inverse opal indium tin oxide (IO-ITO) electrodes. A fully-integrated host−guest system showed a substantially improved wiring of PSII to the IO-ITO electrode with an Os complex-based and a phenothiazine-based polymer. Subsequently, a bias-free tandem semi-artificial cell was assembled, that wired PSII to hydrogenase for overall solar-driven water splitting. This PEC cell integrated the red and blue light-absorber PSII with a green light-absorbing diketopyrrolopyrrole dye-sensitised TiO_2 photoanode enabling complementary panchromatic solar light absorption. Effective electronic communication at the enzyme−material interface was engineered using an Os complex-modified polymer on a hierarchically-structured IO-TiO_2. Finally, a semi-artificial tandem device was designed, which performed solar-driven CO_2 reduction to formate with formate dehydrogenase by coupling to the PSII−dye photoanode. The system achieved a metabolically-inaccessible pathway of light-driven CO_2 fixation to formate and demonstrated a precious metal-free model for solar-driven selective CO_2 to formate conversion using water as an electron donor.

These semi-artificial platforms demonstrate the translatability and versatility of coupling selective and efficient electrochemical reactions to create challenging models and proof-of-principle devices for solar fuel synthesis. They provide a design protocol for bias-free semi-artificial Z-schemes and an extended toolbox of biotic and abiotic components to re-engineer photosynthetic pathways. The assembly strategies presented here may form the basis of all-integrated electrode designs for a wide range of biological and synthetic catalysts.

List of Publications

The work carried out for this thesis have been included in the peer-reviewed journal articles:

1. Sokol, K.P.; Mersch, D.; Hartmann, V.; Zhang, J.Z.; Nowaczyk, M.M.; Rögner, M.; Ruff, A.; Schuhmann, W.; Plumeré, N.; Reisner, E., 'Rational wiring of photosystem II to hierarchical indium tin oxide electrodes using redox polymers', *Energy Environ. Sci.*, **2016**, 9, 3698−3709 (Front Cover Article)

2. Zhang, J.Z.; Sokol, K.P.; Paul, N.; Romero, E.; van Grondelle, R.; Reisner, E., 'Competing charge transfer pathways at the photosystem II−electrode interface', *Nat. Chem. Biol.*, **2016**, 12, 1046−1052

3. Zhang, J.Z.; Bombelli, P.; Sokol, K.P.; Fantuzzi, A.; Rutherford, A.W.; Howe, C.J.; Reisner, E., 'Photoelectrochemistry of photosystem II in vitro vs. in vivo', *J. Am. Chem. Soc.* **2018**, 140, 6−9

4. Nam, D.H.; Zhang, J.Z.; Andrei, V.; Kornienko, N.; Heidary, N.; Wagner, A.; Nakanishi, K.; Sokol, K.P.; Slater, B.; Zebger, I.; Hofmann, S.; Fontecilla-Camps, J.C.; Park, C.B.; Reisner, E., 'Solar water splitting with a hydrogenase integrated in photoelectrochemical tandem cells', *Angew. Chem. Int. Ed.* **2018**, 57, 10595−10599

5. Sokol, K.P.; Robinson, W.E.; Warnan, J.; Kornienko, N.; Nowaczyk, M.M.; Ruff, A.; Zhang, J.Z.; Reisner, E., 'Bias-free photoelectrochemical water splitting with photosystem II on a dye-sensitized photoanode wired to hydrogenase', *Nat. Energy*, **2018**, 3, 944–951

6. Sokol, K.P.; Robinson, W.E.; Oliveira, A.R.; Warnan, J.; Nowaczyk, M.M.; Ruff, A.; Pereira, I.A.C.; Reisner, E., 'Photoreduction of CO_2 with a formate dehydrogenase driven by photosystem II using a semi-artificial Z-scheme architecture', *J. Am. Chem. Soc.*, **2018**, 140, 16418–16422

7. Fang, X.; Sokol, K.P.; Kandiel, T.A.; Heidary, N.; Zhang, J.Z.; Reisner, E., 'Structure-activity relationships of hierarchical three-dimensional electrodes with photosystem II for semi-artificial photosynthesis', *Nano Lett.*, **2018**, DOI: 10.1021/acs.nanolett.8b04935

Contributions were also made to the following peer-reviewed journal articles:

1. Lee, C.-Y.; Reuillard, B.; Sokol, K.P.; Laftsoglou, T.; Lockwood, C.W.J.; Rowe, S.F.; Hwang, E.T.; Fontecilla-Camps, J.C.; Jeuken, L.J.C.; Butt, J.N.; Reisner, E., 'A decahaem cytochrome as electron conduit in protein-enzyme redox processes', *Chem. Commun.*, **2016**, 52, 7390−7393

2. Orchard, K.; Hojo, D.; Sokol, K.P; Chan, M; Asao, N.; Adschiri, T; Reisner, E.; Chem. Commun., 'Catechol−TiO_2 hybrids for photocatalytic H_2 production and photocathode assembly', *Chem. Commun.*, **2017**, 53, 12638−12641

3. Kornienko, N.; Zhang, J.Z.; Sokol, K.P.; Lamaison, S.; Fantuzzi, A.; van Grondelle, R.; Rutherford, A.; Reisner, E., 'Oxygenic photoreactivity in photosystem II studied by rotating ring disk electrochemistry', *J. Am. Chem. Soc.*, **2018**, 140, 17923−17931

Contents

List of Figures

List of Tables

Abbreviations

Roman Symbols

A	Area
D	Diffusion coefficient
E^0	Standard reduction potential
$E_{1/2}$	Formal midwave potential
E	Potential / Formal potential
F	Faraday constant
I	Current
J	Current density
n	Number of electrons
R	Ideal gas constant
T	Temperature
U	Voltage

Greek Symbols

η	Overpotential
Γ	Electroactive surface coverage
ν	Scan rate
ε	Molar extinction coefficient

Acronyms / Abbreviations

ADP Adenosine diphosphate

AM1.5G Air mass 1.5 global

ATP Adenosine triphosphate

bpy 2,2'-bipyridine

CB Conduction band

Chl *a* Chlorophyll *a*

CPE Controlled-potential electrolysis

CV Cyclic voltammetry

DCBQ 2,6-dichloro-1,4-benzoquinone

DET Direct electron transfer

dpp Diketopyrrolopyrrole

EDX Energy-dispersive X-ray spectroscopy

EQE External quantum efficiency

FDH Formate dehydrogenase

FTO Fluorine-doped tin oxide

H_2ase Hydrogenase

HER Hydrogen evolution reaction

ITO Tin-doped indium oxide

MES 2-(N-morpholino)ethanesulfonic acid

MET Mediated electron transfer

MV Methyl viologen

NADPH Reduced nicotinamide adenine dinucleotide phosphate

NADP Nicotinamide adenine dinucleotide phosphate

NP Nanoparticle

OEC Oxygen evolving complex in PSII

OER Oxygen evolution reaction

IO Inverse opal

P_{Os} Poly(1-vinylimidazole-*co*-allylamine)-[Os(bipy)$_2$Cl]Cl

P_{Phen} Phenothiazine-modified polymer

PEC Photoelectrochemistry

PF-PEC Protein-film photoelectrochemistry

PFE Protein-film electrochemistry

PSII Photosystem II

PSI Photosystem I

PS Polystyrene

PXRD Powder X-ray diffraction

Q_B Plastoquinone secondary electron acceptor in PSII

RuP [Ru(bpy)$_2$(4,4'-(PO$_3$H$_2$)$_2$bpy)](Br)$_2$

SEM Scanning electron microscopy

SHE Standard hydrogen electrode

STH Solar-to-hydrogen

TCO Transparent conductive oxide

TEM Transmission electron microscopy

TOF Turnover frequency

TON Turnover number

UV-vis Ultraviolet-visible

VB Valence band

Chapter 1

Introduction

1.1 Solar energy

The global energy crisis is one of the most important scientific and technological challenges facing society in the XXI century. [1, 2] In principle, the future energy demand could probably be met by fossil fuel resources, but the associated increase in anthropogenic CO_2 emission would result in a detrimental impact on the global ecosystem. Hence, moving towards sustainable development, circular economy and carbon-neutral energy sources is necessary. Among renewable energy resources, solar energy utilisation is viewed as an attractive and promising solution. The Sun provides us with an inexhaustible energy supply at the rate of 120,000 TW, about 10,000 times more than is currently consumed by the global population. [2] Thus, the development of economical and efficient solar energy capture, conversion and storage has been hotly pursued for many decades. Solar energy harvesting and conversion into electricity can be realised by photovoltaics, but the limitation of intermittency does not allow storage of the captured energy. Inspired by Nature, a promising approach is to store solar energy in the form of chemical fuels, such as hydrogen, in a process called artificial photosynthesis, which has a potential to provide clean, sustainable and secure energy supply. [3, 4]

1.2 Natural photosynthesis

An inspiration for artificial photosynthesis comes from Nature. In natural photosynthesis, sunlight provides the driving force to produce O_2 and carbohydrates from water and CO_2:

$$6\,CO_2 + 6\,H_2O + 48\,h\nu \rightarrow C_6H_{12}O_6 + 6\,O_2 \tag{1.1}$$

1.2.1 Light reactions

The light reactions proceed in the thylakoid membrane via a series of electron-transfer steps, known as the 'Z-scheme', to harness sufficient energy for water splitting (Fig. 1.1a). [5] The overall efficiency is determined by thermodynamics and kinetics of three key reaction processes: light-harvesting, charge generation and separation, and catalytic redox reactions. [3] A minimum of eight photons is required to move four electrons through each of the two photosynthetic enzymes: photosystem II (PSII) and photosystem I (PSI), located in the thylakoid membrane of plants, algae, and cyanobacteria, to evolve one molecule of O_2 and fix one molecule of CO_2. [6] To close the cycle and make one glucose molecule, fourty eight photons are needed overall.

PSII is the first enzyme in the Z-scheme, responsible for the catalysis of water oxidation (Fig. 1.1b). [7] The core of PSII consists of a dimer of two reaction centre subunit proteins D1 and D2, which bind the primary electron donor site (P680) and components of the electron transport system. Light is absorbed by the chlorophylls (Chl *a*) in PSII and funnelled into the P680 in the reaction centre complex where the charge separation occurs. In intact photoexcited PSII the charge is not distributed, but mostly localised on one chlorophyll P680 molecule (>70%). [8] Because of this, the $P680^+$ has a highly oxidising character capable of oxygen evolution catalysis. The photogenerated electrons are further transferred via pheophytin (Phe) to the electron acceptor plastoquinones A and B (Q_A/Q_B) on the stromal side of the enzyme. The Q_B is reduced to plastoquinol (Q_BH_2) and dissociates from the reaction centre to donate the electrons via the cytochrome b_6f complex (Cyt b_6f) and plastocyanin (PC) to the second light absorber, PSI. Holes generated at the P680 are transferred via a tyrosine (Tyr_Z) in the lumenal direction to the Mn_4Ca oxygen-evolving complex (OEC), where water is oxidised to O_2 and H^+ is liberated. [7, 9] Simultaneously, protons are pumped from the choloroplast stroma into the thylakoid lumen. The second excitation at the primary donor site (P700) in PSI generates a low potential electron transferred via a ferredoxin (FD) to ferredoxin-$NADP^+$ reductase (FNR) to reduce nicotinamide adenine dinucleotide phosphate ($NADP^+$) into NADPH, and ultimately drive CO_2 fixation into sugars. [9] The adenosine triphosphate (ATP) synthase complex uses the proton gradient generated by the electron transport chain to synthesise high-energy ATP by phosphorylation of adenosine diphosphate (ADP) with inorganic phosphate (P_i).

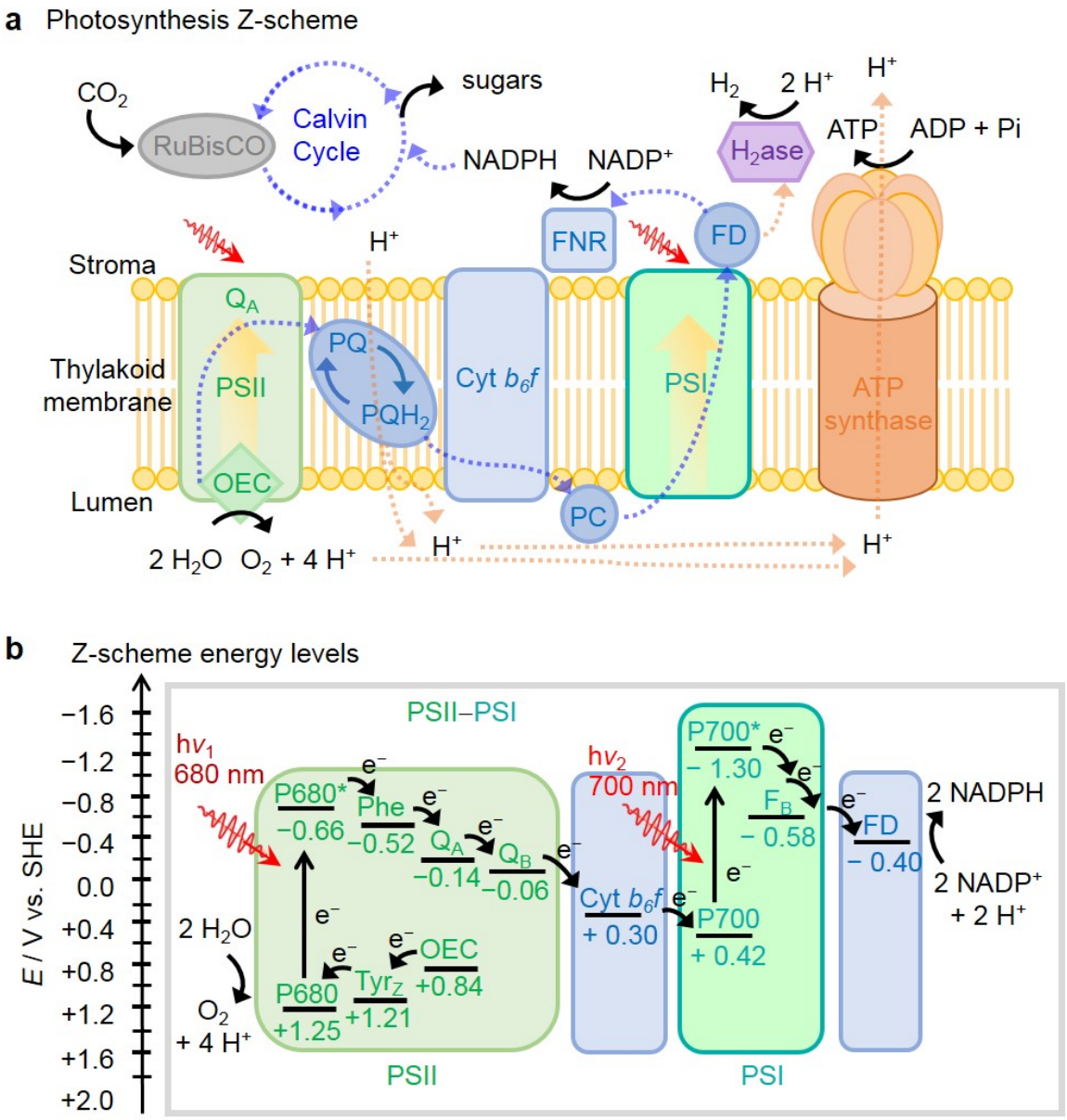

Figure 1.1 **Schematic of simplified Z-scheme in natural photosynthesis. a**, Light absorption, charge separation and redox reactions of Photosystem I (PSI) and Photosystem II (PSII). **b**, Energy level diagram. Abbreviations: E, applied potential; OEC, oxygen-evolving complex; Tyr_Z, tyrosine; P680, pigment/primary electron donor in PSII; Phe, pheophytin; Q_A/Q_B, plastoquinones A and B; Cyt b_6f, cytochrome b_6f; P700, pigment/primary donor in PSI; F_B, iron-sulfur cluster; FD, ferredoxin, $NADP^+$, nicotinamide adenine dinucleotide phosphate; FNR, ferrodoxin-$NADP^+$ reductase; PQ, plastoquinones; PC, plastocyanin; H_2ase, hydrogenase; RuBisCO, ribulose-1,5-bisphosphate carboxylase/oxygenase; ATP, adenosine triphosphate; ADP, adenosine diphosphate; P_i, inorganic phosphate. All potentials shown vs. standard hydrogen electrode (SHE) at pH = 6.5.

Although photosynthetic organisms can efficiently trap light energy at all wavelengths of visible solar radiation, the energy used for oxidising water and reducing CO_2 is only equivalent to the red region of the spectrum. Higher energy photons undergo internal conversion within the light-harvesting pigments to the energy of red photons (λ = 680 nm). [9] A typical product of carbon fixation is glucose with energy content (enthalpy of combustion, $\triangle H$) of -673 kcal mol^{-1}. [10] To make a glucose molecule, 48 red photons are required (Eq. 1.1), corresponding to 42 kcal mol^{-1} each, giving the estimated solar-to-biomass conversion efficiency of about 30%. [9] In fact, the overall conversion to glucose and large variety of other organic molecules, is much lower. Energy is lost through several routes. First, higher energy light, such as blue photons, is degraded to low energy red photons. Second, high light intensities result in photoinhibition due to electron flux limitation, reactive oxygen species generation and energy dissipation as heat. [11] Third, an enormous number of other reactions is driven to maintain the organisation, metabolism, reproduction and survival of the organism. Therefore, the estimated maximum efficiency of photosynthesis is about 4.5%, which is rarely reached. Normally, agricultural crops produce biomass at efficiencies <1%. [9]

However, the primary processes of photosynthesis (light-triggered charge separation), which are not directly involved in biomass production, occur with significantly higher efficiency of >95%. [12] For this reason, it may be possible to develop a highly efficient, artificial solar technology that utilises the principles of the front-end of natural photosynthesis. Our knowledge and understanding of the natural process can provide a blueprint for the design and assembly of artificial photosynthetic devices.

1.2.2 Dark reactions

Atmospheric CO_2 fixation occurs in the thylakoid stroma via the Calvin-Benson-Bassham (CBB) carbon cycle (Fig. 1.2), evolved for optimal synthesis of C_3 metabolites, precursors for all cellular constituents and most of the reduced carbon on Earth. [13, 14] The CBB cycle can be divided into three phases: CO_2 fixation, reduction reactions and ribulose 1,5-bisphosphate (RuBP) regeneration. The first major step of the CBB cycle is catalysed by the ribulose-1,5-bisphosphate carboxylase/oxygenase (RuBisCO) enzyme. CO_2 captured by the RuBisCO reacts with RuBP to generate an unstable C_6 intermediates that split into two 3-phosphoglycerates (3-PGA). Then, each of the 3-PGA molecules is phosphorylated by an ATP to form one 1,3-bisphosphoglycerate (1,3-BPG), further reduced by NADPH to glyceraldehyde 3-phosphate (G3P). One G3P exits the cycle as a final product to make glucose. Finally, the remaining G3P molecules regenerate RuBP in a series of ATP catalysed

reactions. Overall, three CO_2 molecules must be fixed before one G3P can be removed. Six cycle turns produce one glucose equivalent.

Even though the CBB cycle is the dominant mechanism for CO_2 photoassimilation on Earth, it contains several sources of inefficiency. [15] First, the decarboxylation of C_3 sugars leads to carbon loss, which decreases the maximum carbon yield of photosynthesis. [16] Second, RuBisCO, responsible for CO_2 fixation, has extremely low turnover rates (1-10 s^{-1}), creating a significant kinetic bottleneck in the cycle. RuBisCO also reacts with O_2 to produce 2-phosphoglycolate which must be recycled in energy-demanding CO_2 evolving photorespiration. [17, 18] Third, the CBB cycle involves significant ATP consumption, which leads to a lower biomass conversion efficiency. [19]

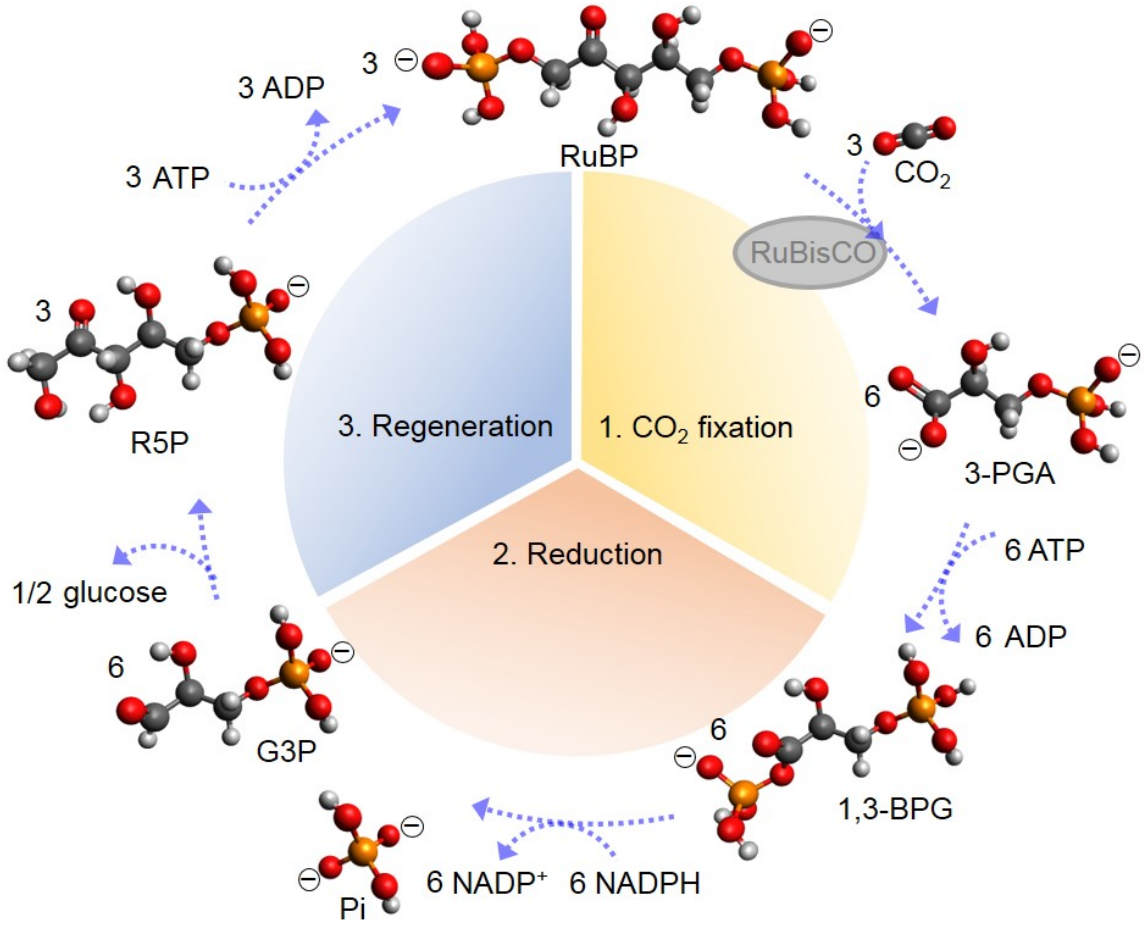

Figure 1.2 **Schematic of simplified Calvin-Benson-Bassham (CBB) carbon cycle.** Three phases are indicated: CO_2 fixation with RuBisCO enzyme, 3-phosphoglycerate (3-PGA) reduction and ribulose 1,5-bisphosphate (RuBP) regeneration. Abbreviations: 1,3-BPG, 1,3-bisphosphoglycerate; G3P, glyceraldehyde 3-phosphate; R5P, ribulose 5-phosphate. Atom labels: C (black), H (white), O (red), P (orange).

1.3 Artificial photosynthesis

In artificial photosynthesis, synthetic, often biomimetic, architectures are developed to gain better understanding of Nature's energy conversion process and to design and improve on the synthetic systems for solar fuel generation. [20–22] So far, two main artificial photosynthetic system types have been designed (Fig. 1.3a,b). [3] The first type is a colloidal particle system. The second type is a heterogeneous electrode system, a photoelectrochemical (PEC) cell, in which functional materials are integrated to form electrodes. [23] The focus of this work will be on the latter, benefiting from robustness, compartmentalisation of reactions and components, and separation of gaseous products evolved on different electrodes.

One of the most prominent model reactions in artificial photosynthesis is solar-driven water splitting into H_2 and O_2: [24]

$$\text{Anode (oxidation):} \quad 2\,H_2O \rightarrow O_2 + 4\,H^+ + 4\,e^- \qquad E^0_{anode} = +1.23\,V\ vs.\ SHE \tag{1.2}$$

$$\text{Cathode (reduction):} \quad 2\,H^+ + 2\,e^- \rightarrow H_2 \qquad E^0_{cathode} = 0.00\,V\ vs.\ SHE \tag{1.3}$$

$$\text{Cell (overall):} \quad 2\,H_2O \rightarrow 2\,H_2 + O_2 \qquad E^0_{cell} = -1.23\,V \tag{1.4}$$

Water electrolysis is thermodynamically unfavoured under standard conditions (25 °C, 1 atm, 1 M solutions, pH 0). The standard cell potential (E^0_{cell}) shows that 1.23 V of electrical energy and the standard Gibbs free energy ($\triangle G^0$) of 237 kJ mol^{-1} is required to split water:

$$\triangle G^0 = -nFE^0_{cell} = -nF(E^0_{cathode} - E^0_{anode}) \tag{1.5}$$

where n is the number of electrons exchanged between the cathodic and anodic sides of an electrochemical cell, F is the Faraday constant, $E^0_{cathode}$ and E^0_{anode} are the standard redox potentials of the cathodic and anodic half-cell reactions, respectively, referred to the standard hydrogen electrode (SHE). The standard potentials vary with pH according to the Nernst equation, reaching +0.84 V (anode) and −0.39 V (cathode) at pH 6.5 (a value used in the experiments in the subsequent Chapters):

$$E_{cell} = E^0_{cell} - \frac{RT}{nF} ln(\frac{[red]}{[ox]}) \tag{1.6}$$

where R is the ideal gas constant, T is the temperature, $[red]$ and $[ox]$ are the concentrations of reduced and oxidised species, respectively.

To drive an electrochemical cell reaction toward completion, a potential can be applied (E), providing a kinetic control. Typically, a greater applied potential is required (overpotential, η) to overcome factors, such as activation energy, ion diffusion and collision, wire resistance, surface blockage/bubble formation and entropy. [25]

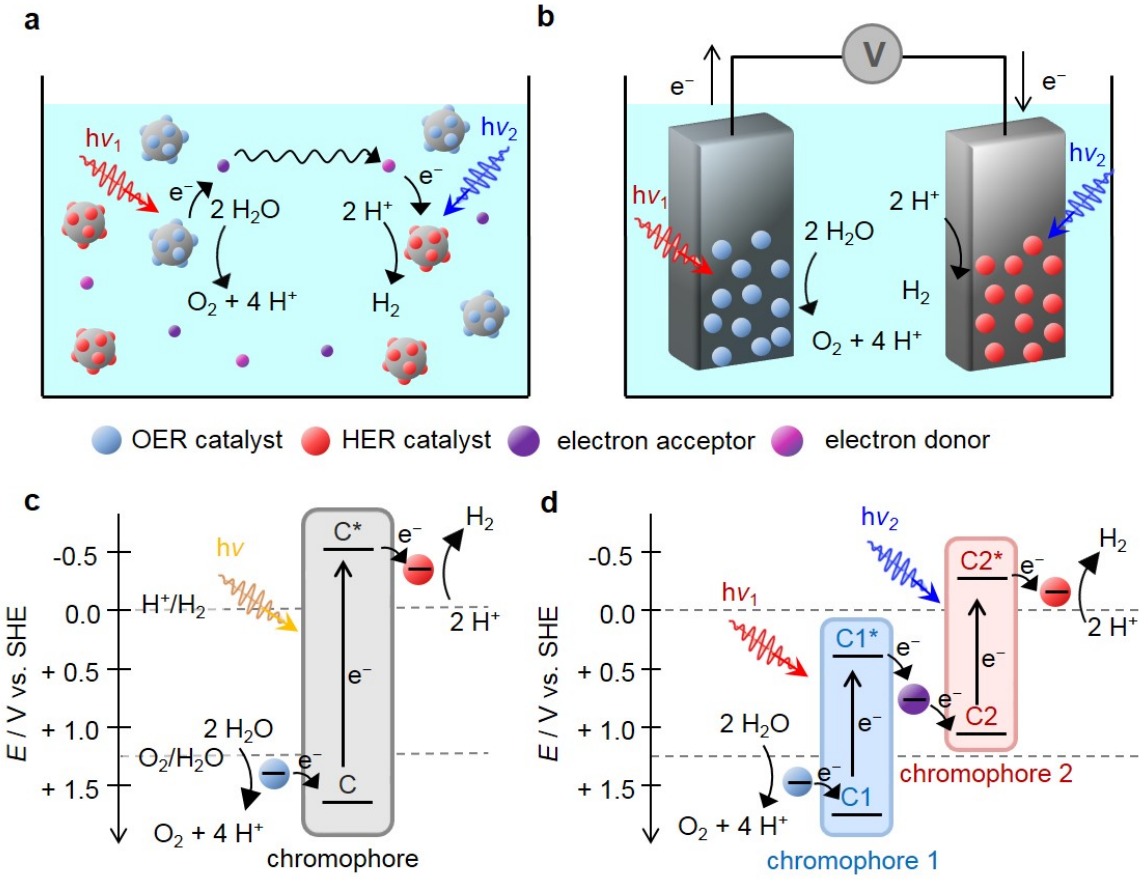

Figure 1.3 **Artificial photosynthesis modes.** Types of artificial systems, including **a**, semiconductor particle mixture with attached catalysts, and **b**, photoelectrochemical (PEC) cell containing a photoanode and photocathode with OER and HER catalysts attached, respectively. **c**, Artificial photosynthesis charge separation in a single-step excitation process and **d**, two-step excitation (Z-scheme mimicking) tandem process. Abbreviations: OER, oxygen evolution reaction; HER, hydrogen evolution reaction; C, chromophore of a single-step excitation; C1, the first chromophore of a two-step excitation; C2, the second chromophore of a two-step excitation; C*/C1*/C2*, excited states of C/C1/C2, respectively. E recorded vs. SHE at pH = 0.

PEC water splitting on semiconducting materials has been studied extensively since the 1970s, when Honda and Fujishima demonstrated water photolysis on a TiO_2 electrode. [23] When a semiconductor is irradiated with photons of energies higher than its band gap energy

(E_g), electron-hole pairs (excitons) are generated. These charge carriers can drive oxidation and reduction reactions provided charge injection into reactants is thermodynamically and kinetically favourable. Photocatalytic water splitting can be accomplished by either a one-step or two-step excitation process (Z-scheme analogue) (Fig. 1.3c,d). To achieve the former, the E_g must cover both, the oxidation and reduction potentials of water, which are +1.23 V and 0 V vs. SHE at pH 0, respectively (Fig. 1.3c). In the latter, two light-absorbing molecules (chromophores) or semiconductors are connected in series, usually in the presence of a reversible redox shuttle (Fig. 1.3d). Three main electrode configurations in PEC cells have been described so far (Fig. 1.4). [26] The first one is based on a metal cathode and an n-type (electron-doped) semiconductor photoanode, in which top of the valence band (VB) must be more positive than the oxygen evolution reaction (OER) potential. In the second one, a metal anode and a p-type (hole-doped) semiconductor photocathode are employed, where the conduction band (CB) edge is more negative than the hydrogen evolution reaction (HER) potential. Third configuration involves both, an n-type semiconductor photoanode and a p-type semiconductor photocathode arranged in a tandem PEC cell. Numerous synthetic OER catalysts, based on Mn, [27–29] Ru [30] and Co-Mn [31] have been designed to mimic the OEC in PSII. Similarly, Fe and Fe-Ru-based HER catalysts based on the [Fe-Fe] active site of H_2-evolving enzymes, such as hydrogenases, have been reported. [32, 33]

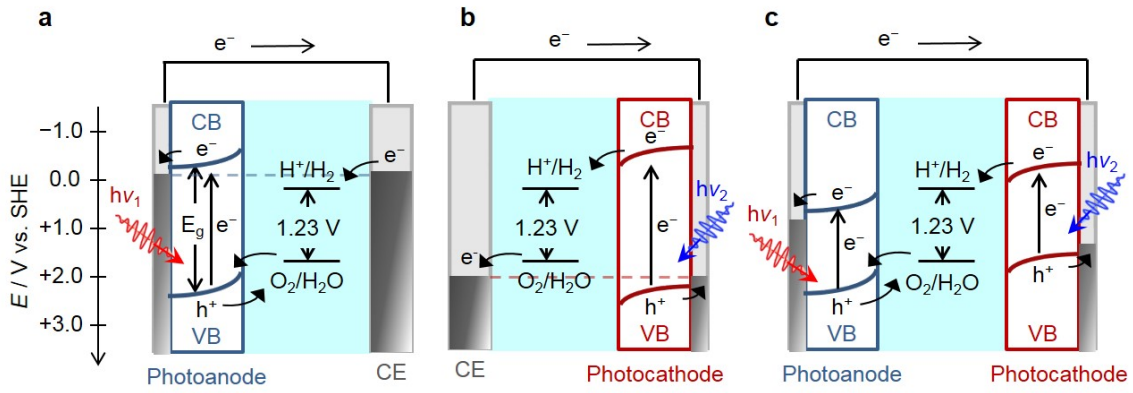

Figure 1.4 **Energy level diagrams of PEC water splitting.** PEC cell design employing a **a**, photoanode, **b**, photocathode and **c**, both photoelectrodes in a tandem configuration. E recorded vs. SHE at pH = 0.

1.4 Semi-artificial photosynthesis

Natural photosynthesis stores sunlight in chemical energy carriers, but it has not evolved for the efficient synthesis of fuels, such as H_2. Semi-artificial photosynthesis combines the

strengths of natural photosynthesis with synthetic chemistry and materials science to develop model systems that overcome Nature's limitations, such as low-yielding metabolic pathways and non-complementary light absorption.

This emerging field bridges the rapidly progressing fields of synthetic biology and artificial photosynthesis, offering a platform for developing and understanding solar fuel generation. [34–36] Synthetic biology has vastly opened up the way Nature can be manipulated to alter functionality and build artificial biological systems, forming a foundation of future biotechnology. For example, photobiological H_2 production is possible with the re-engineering of photosynthetic organisms, such as cyanobacteria and green algae. However, this field is still largely reliant on tools available in Nature, and its complex biological machineries and metabolic pathways limit engineering flexibility. [37] On the other hand, artificial photosynthesis utilises synthetic components and materials to convert and store solar energy, but is often constrained by inefficient catalysis and light harvesting that often incorporate costly metals and toxic elements. [4, 38] Semi-artificial photosynthesis aims to integrate the high efficiency and selectivity of enzymes with the controllability of synthetic materials to photocatalyse endergonic reactions in the absence of competing processes. [39] It also allows the construction of biologically-inaccessible pathways with a high level of control and flexibility. [36, 40] This field aims to develop model systems and platforms for solar fuel synthesis, in which key machineries from natural photosynthesis can be interfaced with synthetic pigments and electron carriers to drive a wide range of endergonic reactions, such as water splitting and CO_2 reduction, and bypass several competing metabolic steps, which is not achievable using synthetic biology or materials science alone.

1.5 Enzyme PEC cells

The catalytic activity of redox enzymes can be harnessed when adsorbed on electrodes by protein film electrochemistry (PFE) [41] and photoelectrochemistry (PF-PEC). [42–45] In PF-PEC, a protein containing a redox-active centre is immobilised on the electrode surface (Fig. 1.5) and a direct photoelectrochemical response can be measured with high sensitivity using a potentiostat, enabling the study of protein photoactivity, stability and electron transfer. [43] Addition of redox mediators allows further insight into the direct electron transfer (DET) and mediated electron transfer (MET) between the protein to the electrode surface. A key challenge in PF-PEC is to design biotic-abiotic interfaces that effectively wire together the biological and synthetic components to operate at their optimum.

1.5.1 Protein film photoelectrochemistry

In a typical PF-PEC setup a three-electrode configuration is used, including working, counter and reference electrodes (WE, CE, RE, respectively). A potential is applied between the WE and RE, and current is measured between the WE and CE. A three-electrode setup allows the behaviour of the WE (half-cell reaction) to be studied as a function of a well-defined potential. In the two-electrode setup, an anode is directly wired to a cathode. Both, potential and current are applied and measured between the two electrodes. This setup allows to assess the performance of the overall cell reaction.

There are two PF-PEC experiment types that were utilised in this work: voltammetry and chronoamperometry. In a voltammetry experiment, the electrode potential is swept linearly with time between two potentials, and current is monitored. Voltammetry can yield useful information, such as redox reaction potential, reversibility, stability, number of electrons transferred, interfacial electron transfer rate and electroactive film loading. The second mode is chronoamperometry, where the electrode is held at a set potential and (photo)current is monitored with time. It provides insight into the long-term enzyme stability under continuous operation.

1.5.2 Water splitting enzymes

H_2 was a vital energy source for organisms during the early stages of our planet, under reducing atmospheric conditions (i.e. in the absence of O_2). An enzyme, hydrogenase (H_2ase), catalysing proton reduction into H_2, was found to be responsible for H_2 production in photosynthetic organisms, such as unicellular green algae, under light illumination (Fig. 1.1a). [12] The activity of H_2ase has been supressed with the evolution of the Z-scheme, providing plenty of energy using sunlight and responsible for the O_2 production in our atmosphere on Earth. Thus, H_2-dependent processes lost their central role as a necessity for the survival of most photosynthetic cells. As a consequence, there was no strong evolutionary pressure for the design of oxygen-resistant H_2ases and the increasing O_2 content of the atmosphere produced by the water splitting process led to these enzymes being switched off. Today, H_2ases still exist in bacteria and microalgae (cyanobacteria and unicellular green algae) but their activity is typically maintained under anaerobic conditions. Their main function is either to provide an alternative electron source as a survival mechanism under sub-optimal conditions, or to capture electrons as a defence mechanism to prevent dangerous over-reduction of the electron transfer chain. [12] In green algae, the H_2-evolution H_2ase-based pathway could operate only under conditions of significantly reduced PSII activity. [11]

Inefficient catalysis of water splitting (particularly, kinetically slow O_2 evolution and formation of partially-oxidised side products) is a major limitation in synthetic systems, resulting in the requirement of large overpotentials and energy conversion losses. [3] Alternatively, H_2 can be produced from photosynthetic microalgae and cyanobacteria, via electron transfer from ferredoxin to a [FeFe]-H_2ase, reducing protons to H_2 (Fig. 1.1a). [46, 47] Efficiencies for photobiological H_2 production are low for several reasons. [11, 48] First, PSII and PSI overlap in light absorption and compete for a small fraction of the solar spectrum. Second, light saturation limits efficient electron flux up- and down-stream of PSII. Third, *in vivo* H_2 production relies on O_2-sensitive [FeFe]-H_2ases, preventing sustained water splitting. [49] Fourth, CO_2 fixation is preferred over proton reduction leading to low H_2 yields. Overcoming these limitations offers scope for enhancing H_2 production with biological components.

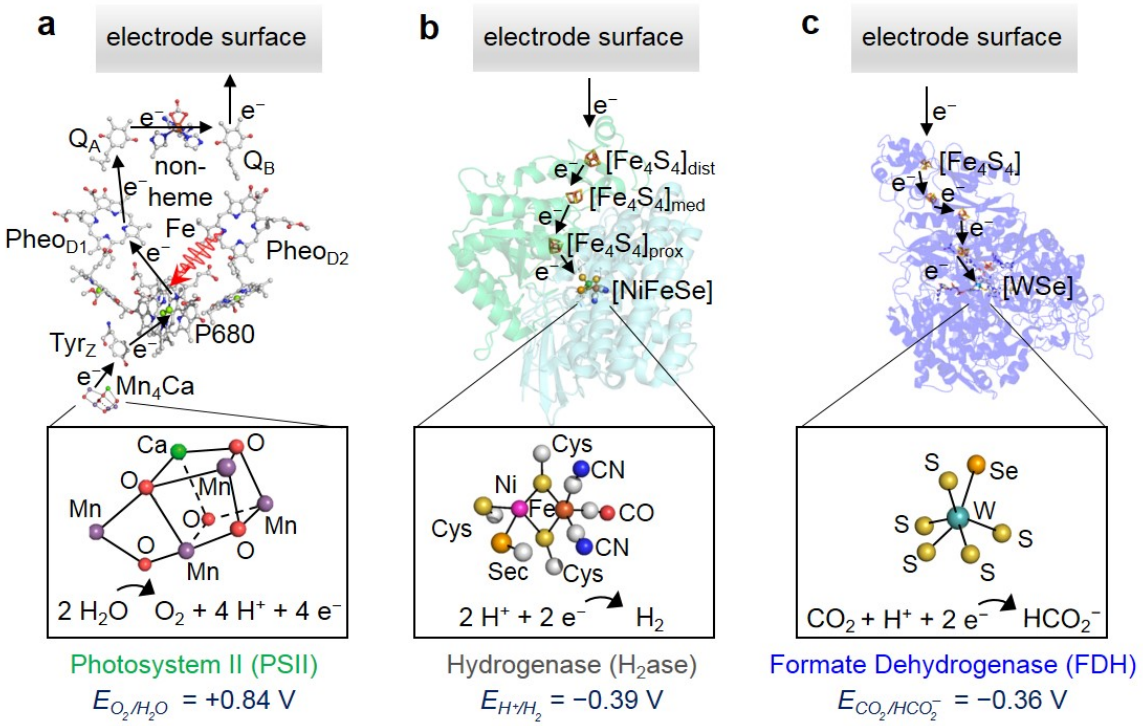

Figure 1.5 **Shematic of electrocatalysis of PSII, [NiFeSe]-H_2ase and W-FDH. a**, Four electrons are exchanged with the OEC via Q_A/Q_B co-factor driving water oxidation catalysis. **b**, Two electrons are exchanged with the [NiFeSe] active site via the $[Fe_4S_4]$ clusters driving H^+ reduction catalysis. **c**, Two electrons are exchanged with the [WSe] active site via the $[Fe_4S_4]$ clusters driving CO_2 reduction catalysis. *E* recorded vs. SHE at pH = 6.5.

PSII is the only enzyme in Nature able to photocatalyse water oxidation, a bottleneck reaction in artificial photosynthesis, at theoretical rates of up to 250 mol O_2 (mol PSII

monomer)$^{-1}$ s^{-1}. [50, 51] As such, there is considerable interest in the integration of PSII as a guest into electrode scaffolds, [52, 53] to improve our fundamental understanding of the protein function and also in PEC cells for proof-of-principle solar electricity/fuel generation. [35, 54–57] PSII remains photoactive when adsorbed on an electrode and if immobilised in the correct orientation, direct electron transfer from the Q_A/Q_B to the electrode can take place (Fig. 1.5a). [36, 58] However, a Q_B mimic, such as 2,6-dichloro-1,4-benzoquinone (DCBQ), is typically required as a diffusional mediator between the insufficiently wired PSII and the electrode to enhance photocurrent generation. [43] In the past, not only PSII, but also whole reaction centres, [59] thylakoid membranes [60–62] and full algae and cyanobacteria cells [63–66] have been interfaced with electrodes, but their bulk size and competing processes limit the photocurrent generation and overall efficiency.

The PSII-based photoanode can in principle be wired to a H_2ase-based cathode, [67, 68] utilising a selective and reversible biological electrocatalyst for H_2 production integrated in an electrode (Fig. 1.5b). [NiFe]-H_2ases are attractive candidates due to high H^+ reduction activity, O_2 tolerance under reductive conditions and marginal inhibition by H_2, offering advantageous properties for water splitting [69, 70] compared to O_2-sensitive [FeFe]-H_2ases available in algal H_2 production. [71, 72] The [NiFeSe]-H_2ase, a subclass of [NiFe]-H_2ase containing a terminal selenocysteine coordinated to Ni at the [NiFe]-active site and three $[Fe_4S_4]$-clusters, is more active for H_2 production than [NiFe]-H_2ases in low O_2 levels. [72–74] When [NiFeSe]-H_2ase is adsorbed on an electrode, the electrons can be transferred through $[Fe_4S_4]$ clusters to the [NiFeSe] reaction centre, where the H^+ is reduced.

1.5.3 CO_2 reduction enzymes

Addressing the CBB cycle inefficiencies in biological systems presents several challenges [16, 75–80] leading research towards *in vitro* CO_2 fixation pathways. [81] Artificial photosynthetic CO_2 fixation in currently infeasible due to a lack of catalysts with high activity (energetically-inefficient conditions required) and selectivity (multiple products generated), due to thermodynamic and kinetic stability of CO_2. [4] It has recently been proposed that carbon fixation pathways that reduce CO_2 directly are more efficient than carboxylation pathways, such as the CBB cycle. [19] One entry point of CO_2 into the direct reduction pathway is its conversion to formate. [82] Formate is a stable intermediate to methanol and methane, and has also been proposed as a viable fuel and H_2 carrier. [83] Under 25 °C, 1 atm, 1 M solutions, pH 7: [84]

$$CO_2 + 2\,H^+ + 2\,e^- \rightarrow HCO_2H \quad E^0_{cathode} = -0.61\,V\ vs.\ SHE \tag{1.7}$$

Formate dehydrogenases (FDHs) are enzymes capable of reversible interconversion of CO_2 and formate. [85] The most common, NAD-dependent FDHs have been employed as intermediates in methanol electrosynthesis [86–88] and in formate/O_2 enzymatic biofuel cells, mediated by methyl viologen (MV^{2+}), [89–91] re-generated NAD^+ [92–95] or redox polymer [96, 97]. NAD-FDHs catalyse the direct H^- transfer from formate to NAD^+, but the reverse reaction is constrained by sluggish electrooxidation of NADH and NAD^+ instability. [85] The metal-dependent FDHs, however, contain Mo or W co-factors to transfer the electrons from formate oxidation to an independent active site (Fig. 1.5c). [85, 98–104] These avoid using unstable, expensive and diffusive NADH/NAD^+ electron donor/acceptor pair, and show high CO_2 reduction electroactivity when adsorbed onto electrodes. [85] When adsorbed on an electrode, metal-dependent FDHs from *S. fumaroxidans* [85] and *E. coli* [101, 105] have been shown to catalyse the interconversion reaction with high efficiency via interfacial electron transfer. Electrons arrive at the CO_2-reducing [MoSe] or [WSe] active site via interfacial electron transfer to several [Fe_4S_4] clusters, which connect the FDH active site to the electrode surface. W-FDH are most associated with CO_2 reduction for their capacity to catalyse low-potential reactions, but were only reported in a few mediated [106, 107] and unmediated systems. [104]

1.6 PF-PEC electrode design

The effective electrode design for PF-PEC requires integration of components with the following three functionalities: light harvesting, exciton separation and redox catalysis. [3] The first two can be realised by the core electrode material: either a semiconductor absorbing in the visible region (λ = 400-750 nm, corresponding to E_g = 3.10-1.65 eV) or a dye-sensitised wide band gap semiconductor (E_g > 3.10 eV). The last function can be fulfilled by a biocatalyst incorporated on the electrode surface. The core electrode material can be regarded as a host for light absorber and catalyst guest species. In general, it should fulfil the following requirements: stability in aqueous media, economical fabrication method from cost-effective precursors, isotropic and efficient electron transport properties. To make a good host, additional aspects should be considered, such as affinity for guest species immobilisation, high effective surface area and loading capacity.

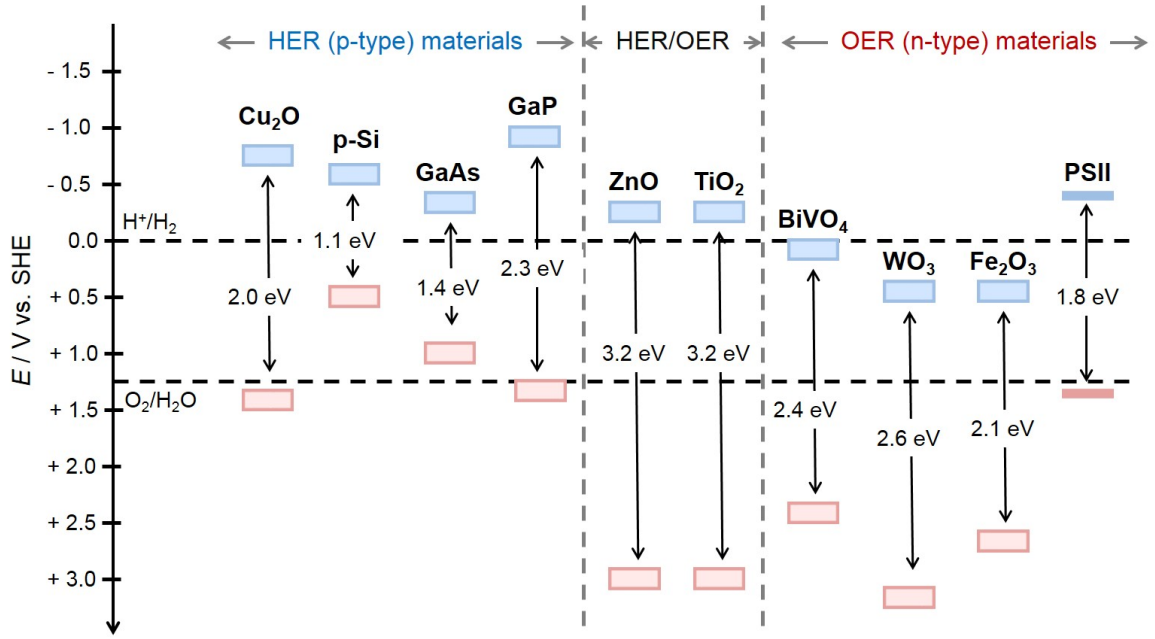

Figure 1.6 **Current state-of-the-art electrode materials for PEC water splitting.** Comparison with PSII acting as a light absorber. For semiconductors, the lower edge of the CB (blue) and upper edge of the VB (red) are shown (pH 0). For PSII, the P680 electronic state and P680* excited state are shown (pH 6.5).

1.6.1 Materials

The current state-of-the-art photoanode materials (Fig. 1.6) have been dominated by metal oxides due to their intrinsic stability under highly oxidative conditions required by the OER. [23] Few conventional examples with a visible light absorption include: α-Fe_2O_3, WO_3 and $BiVO_4$. [108] Among others, TiO_2 is an established photoelectrode candidate for water splitting, benefiting from low-cost, abundance, stability and ease of surface-modification. [109, 110] However, due to a wide band gap ($\sim$3.2 eV), TiO_2 does not absorb light in the visible region. Grätzel and co-workers developed a dye-sensitised solar cell (DSSC), in which a molecular dye was covalently bound to a nanoporous TiO_2 film, and upon visible light photoexcitation, electrons could be injected into the CB of TiO_2. [111, 112] The most effective DSSCs reported to date are based on the prototype Ru-polypyridine dye and I^-/I_3^- mediator in acetonitrile with overall conversion efficiencies of up to 11.4% [113, 114], Cu-complex redox electrolytes with 13.1% efficiency, [115] or otherwise based on a hybrid $CH_3NH_3PbI_3$ perovskite-sensitised TiO_2 with 14.1% efficiency. [116] Inspired by DSSCs, dye-sensitised TiO_2 photoelectrodes have been employed in PEC biofuel [117, 118] and water splitting cells [119] by interfacing dyes (e.g. $Ru(bpy)_3^{2+}$) with catalysts (e.g. IrO_2). [120–124] The

current state-of-the-art photocathode materials include p-type Cu_2O, NiO, black Si, p-type Si, GaAs and GaP. [108]

PSII performs all the functions required for PEC photoanode design: light harvesting, charge separation and water oxidation catalysis with extremely high efficiency. The enzyme can be integrated onto the electrode as a guest to yield a semi-artificial OER system. A key requirement for the electrode scaffold material is transparency. Therefore, functionalised transparent conductive oxides (TCOs) have been viewed as attractive candidates. Conventional TCOs include highly n-doped In_2O_3, ZnO and SnO_2. Tin-doped indium oxide, also known as indium tin oxide (ITO), is the most common conductive substrate material by far, outperforming other TCOs like fluorine-doped tin oxide (FTO), antimony-doped tin oxide (ATO) and aluminium-doped zinc oxide. ITO-based photoelectrodes have been utilised for PEC water splitting previously, [125] benefiting from the material transparency, hydrophilicity and ease of surface modification.

1.6.2 Structures

To improve O_2 and H_2 evolution efficiencies, recent PEC water splitting research has focused on developing highly structured materials. [126] Nanostructured electrodes benefit from high active surface area, easily tuneable electronic and optical properties. Depending whether materials exhibit structuring on one or more length scales, they can be divided into non-hierarchically-structured or hierarchically-structured, respectively (Fig. 1.7).

Non-hierarchical structures

Non-hierarchical structures are composed of one length scale building block, typically at the nanoscale dimension, such as: nanoparticles (NPs), nanowires (NWs), nanorods (NRs), nanotubes (NTs) or nanosheets (NSs) (Fig. 1.7a-c). Several recent low aspect-ratio morphologies included: nanostructured α-Fe_2O_3, WO_3, $BiVO_4$, mesoporous TiO_2 and dendrimeric Cu_2O. [108] Over the last decade, many high-aspect ratio structured Si and III-V semiconductors have been investigated, including: black Si NRs/NWs, p-type Si micropillars and crystalline Si NWs. [108] The direct band gap III-V semiconductors, GaAs and InP single-crystal epilayers have been utilised as photocathodes, and indirect band gap GaP NWs have been fabricated using etching techniques. [108] More recently, 3-D porous morphologies, such as TiO_2, SnO_2, ATO and ITO inverse opals (IOs) [127–130] were explored as prospective host materials (Fig. 1.7d).

Hierarchical structures

Hierarchical structures consist of smaller dimension building blocks that form a larger structure, integrating the advantages of both component length scales. [131] Inspired by biology, meso-micro, macro-micro and macro-meso hierarchical structuring can be introduced to assemble electrodes. Based on morphology, commonly reported hierarchically-structured materials include: sphere-like structures, tree/flower-like structures and 3-D mixed porous networks (Fig. 1.7e-h). [126]

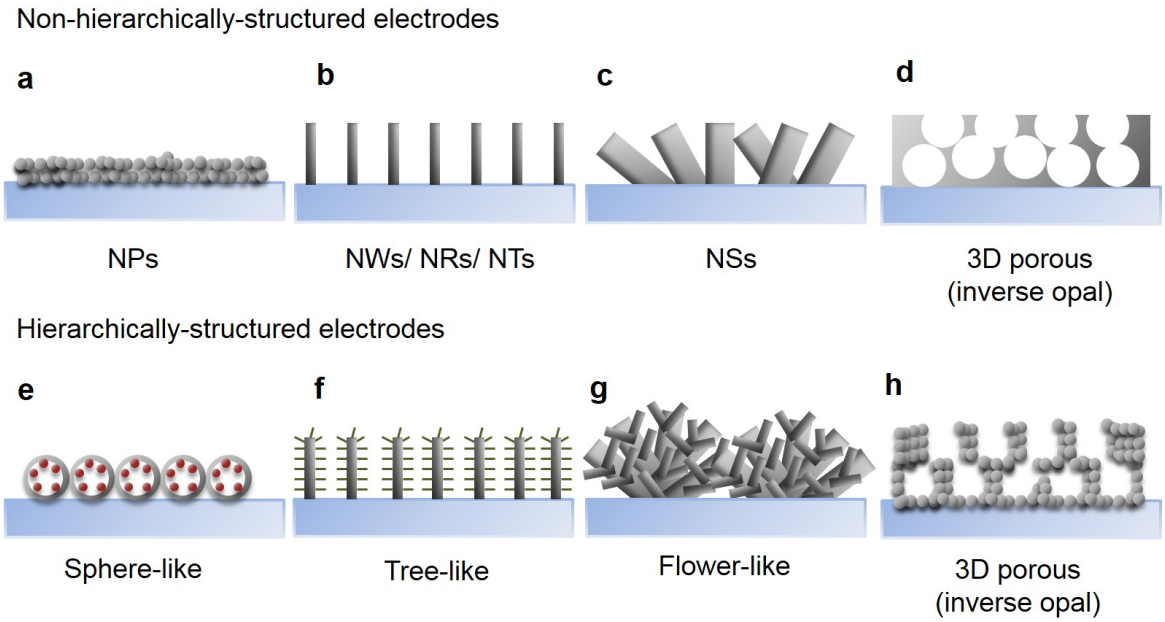

Figure 1.7 **Schematic representation of 3-D porous electrodes.** Non-hierarchically-structured electrodes composed of: **a**, mesoporous NPs films, **b**, NWs/NRs/NTs arrays, **c**, NSs assemblies and **d**, 3-D macroporous IOs, compared to hierarchically-structured electrode types: **e**, sphere-like yolk-shell films, **f**, tree-like branched NWs arrays, **g**, flower-like NSs assemblies and **h**, 3-D macro-mesoporous IOs.

Sphere-like hierarchical structures can be synthesised from nanosized building blocks (Fig. 1.7e). In this structure type, nanopores and nanochannels enhance fast electron and ion migration whereas spherical structure results in increased stability. Typical examples include: self-assembled highly-ordered V_2O_5 hollow sphere superstructures composed of NPs-based NRs, core-shell Fe_3O_4/WO_3 heterostructure composed of Fe_3O_4 spherical core with WO_3 NW branches, and NP-encapsulated hollow carbon spheres. [126, 127] Representative flower-like hierarchically-structured material (Fig. 1.7f) is nano-microstructured SnO_2 NS assembly built from SnO_2 NPs. [132] The third and most common architecture is a tree-like morphology (Fig. 1.7g). Typical examples include homostructures: ZnO and TiO_2 branched

NW-based structure, TiO_2 NT arrays coated with TiO_2 NPs, as well as heterostructures: Si NW arrays with ZnO or TiO_2 NW branches, AZO/TiO_2/CdS and CuO/ZnO branched NW architectures. [133] The last class, 3-D network hierarchical structures includes: TiO_2/RuO_2 nanocomposite of TiO_2 spheres coated with RuO_2 NPs, nanoporous carbon with $LiFePO_4$ NPs and self-assembled nano-microspheres of carbon NTs with CuO NPs. [134] An unique representative is a macro-mesoporous IO architecture (Fig. 1.7h), that can be composed of NPs. [135]

1.7 Enzyme immobilisation techniques

In comparison to the synthetic systems, semi-artificial PEC water splitting cells exploit the integration of enzymes, proteins and biological cells as guests *in vitro*. Utilisation of hierarchically-structured 3-D porous electrodes (Fig. 1.7h) in PF-PEC could address the current design issues: large protein size with limited stability on the electrode surface, poor photostability, photoelectrochemical response limited by enzyme loading and immobilisation in an effective orientation on the electrode (close enough proximity of the relevant co-factor donor/acceptor resulting in an electron transfer). To overcome these limitations, improved enzyme immobilisation strategies have been investigated, including: binding through self-assembled monolayers (SAMs), incorporation into the nanopores of structured electrodes and embedding into a redox polymer matrix (Fig. 1.8). [43]

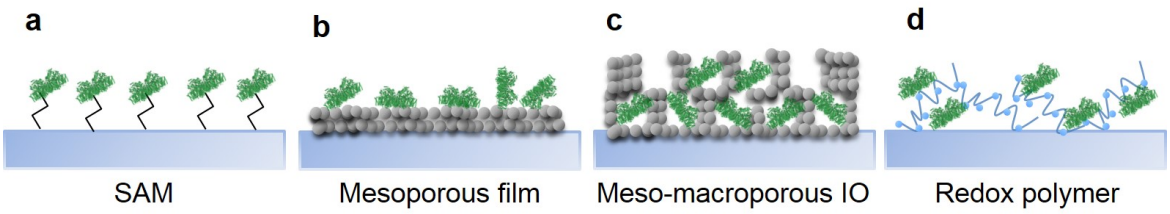

Figure 1.8 **Schematic representation of enzyme immobilisation methods on electrodes.** Representative PSII immobilisation via: **a**, a covalent attachment by SAM, **b**, electrostatic interactions on mesoporous films, **c**, electrostatic interactions on 3-D macro-mesoporous IO films, and **d**, entrapment in a redox polymer matrix.

1.7.1 Self-assembled monolayers

A traditional approach for the immobilisation of photosynthetic reaction centres is to align the proteins on chemically-modified Au, graphite or ITO electrodes functionalised with linkers

(Fig. 1.8a) such as quinonoid, [136, 137] *N*-hydroxy-succinimidyl ester, [138] nickel nitrilotriacetic acid, [55, 139–141] 3-aminopropyltriethoxysilane, [142] cytochrome *c*, [143, 144] carboxylic acid/amino groups, [145] lipid bilayers [146, 147] and ferricyanide-intercalated layered double hydroxide. [148] However, the magnitude of the photocurrent is limited by the attachment of a single monolayer of photosynthetic reactions centres that can be assembled on the electrode. Those systems have typically utilised red light illumination at applied bias potential (E_{app}) of ∼0.5 V vs. SHE. The photocurrent densities and turnover frequencies (TOFs) for the ITO-modified electrodes were 0.43 μA cm^{-2} (TOF = 0.61 s^{-1}) for DET and 4.5 μA cm^{-2} (TOF = 4.6 s^{-1}) for MET. For the Au-modified photoanodes, the photocurrent densities of 2.4 μA cm^{-2} for DET and 14 μA cm^{-2} for MET were reported. The PSII loading for all SAM-modified electrodes was in the range of 0.29-2.0 pmol cm^{-2}. For comparison, the second photosynthetic enzyme, PSI has typically been employed to construct hybrid photocathodes, and immobilised on SAM-functionalised Au [149, 150] and carbon nanotube (CNT) [151] electrodes, and interfaced with HER catalysts, [152] Pt NPs [153, 154] and H_2ases. [155, 156] Similarly, [NiFeSe]-H_2ases have been immobilised on Au, [157, 158] TiO_2-coated Si [159] and CNT scaffolds to serve as hybrid cathodes. [160]

1.7.2 Structured electrodes

An emerging and effective enzyme immobilisation strategy involves the adoption of highly structured electrode morphologies [134, 161, 162] to increase the available surface area for enzyme adsorption. [36, 145, 163] A robust and highly active PSII variant from *T. elongatus* [164–166] was first integrated into mesoporous ITO (≈3 μm thicknesses, 50 nm mesopores) electrodes (Fig. 1.8b) prepared by a doctor blading method. [163] Under red light irradiation and E_{app} of 0.5 V vs. SHE, photocurrent densities of 1.6 μA cm^{-2} (TOF = 0.18 s^{-1}) for DET and 22 μA cm^{-2} (TOF = 3.2 s^{-1}) for MET were reached. Increased PSII loading of 76 pmol cm^{-2} was reported.

In a recent benchmark system, a PSII-based photoanode was wired to a [NeFeSe]-H_2ase-based cathode for overall water splitting. [36] Both enzymes were adsorbed on a hierarchically-structured IO-ITO electrodes (Fig. 1.8c) that incorporated macroporosity (for enhanced enzyme and substrate penetration and diffusion) and mesoporosity (to enhance the effective surface area and enzyme anchoring) with high thickness. [36] As a result, up to 16,000-fold and 30-fold increase in PSII loading was observed compared to conventional flat and mesoporous electrodes, respectively. [167, 168] PSII loading increased linearly with the electrode thickness from 36 pmol cm^{-2} (4 μm films) to 1020 pmol cm^{-2} (80 μm films). However, insufficient wiring at the PSII-electrode interface was still apparent, with DET photocurrents of 20 μA cm^{-2} being observed in contrast to 1 mA cm^{-2} for MET under

red light irradiation at E_{app} of 0.5 V vs. SHE. A further limitation of the electrode was poor PSII photostability, with the electrode exhibiting a photocurrent half-life time of only a few minutes. PSII has been also integrated into mesoporous TiO_2 scaffolds, but generated photocurrents were limited by the mismatched energy levels between the Q_B in PSII and the CB of TiO_2, resulting in ineffective electron transfer. [169, 170] IO-ITO and IO-TiO_2 architectures has since been employed as hosts for PSI, [150, 171] H_2ase [172] and other enzymes. [173–175]

1.7.3 Redox polymers

A strategy to enhance the loading of electrically-wired enzymes onto electrodes is to entrap them in a redox-active polymer matrix on an electrode surface (Fig. 1.8d). [176, 177] In this approach, an enzyme of any orientation can in principle be efficiently wired to the electrode by the redox-active centres that are homogeneously distributed in the matrix, which can mediate charge transfer via an electron hopping mechanism. [178] In contrast to conjugated conductive polymers, redox polymers are characterised by spatially- and electrostatically-localised redox-active moieties, which can be attached to the polymer backbone either by electrostatic interactions or covalent bonding. Few examples of the latter include: poly(tetracyanoquinodimethane, poly(viologens), poly(tetrathiafulvalene), quinone polymers, poly(vinylferrocene) and [Os-(2,2'-bipyridyl)$_2$(4-vinylpyridine)$_n$Cl]Cl. [179] The properties of a redox polymer, including the formal redox potential of the redox site, hydrophilicity, pH-dependence, solubility and cross-linking ability can be tuned by modifying the structure and compositional ratio of monomers incorporated into the backbone. A key role of redox polymers is to provide electrical wiring to the electrode with increased electron transfer efficiency, but also to serve as a stabilisation network decreasing photodegradation and preventing partial protein denaturation (Fig. 1.8c). Independently of the total loading at the electrode surface, the amount of electroactive enzyme is defined by the rate of charge transfer via electron hopping, which limits the maximum (photo-)electrocatalytic response that can be detected. [180] On modified flat electrodes where enzymes are entrapped in redox polymers, the current generation typically arises from catalysts present within a thin layer (a few μm thick) at the electrode/hydrogel interface; the remaining catalysts in the outer layers of the film are electro-inactive and do not contribute to current generation. [181] To minimise the energy losses, the formal potential ($E_{1/2}$) of a redox hydrogel has to be tuned to be more positive than the potential of the electron acceptor at the anode, or more negative than the potential of the electron donor at the cathode. [181]

Metal complex-modified redox polymers

Ru and Os complex-based redox polymers have been successfully exploited in biophotovoltaics and shown to be the most efficient electron mediator candidates for modified biophotoelectrodes. [182–184] The benchmark PSII-based photoanode using this approach consisted of a flat Au electrode on which PSII was embedded in an Os complex-based polymer ($E_{1/2}$ = 0.395 - 0.505 V vs. SHE), stabilised by poly(ethylene glycol)diglycidyl ether cross-linker. [167] Photocurrents of up to 45 μA cm^{-2} at E_{app} of 0.5 V vs. SHE were reported for this photoanode upon red light illumination. Despite its advantages, the performance of this system was limited by the intrinsic properties of the polymeric matrix on flat electrode surfaces. Coupling of PSII-based photoanode to PSI-based photocathode was also demonstrated, where Os complex-modified redox hydrogels with matching $E_{1/2}$ were employed as electrical contacts to the Au electrodes. [181] Other studies of photosynthetic systems with Os complex-modified redox polymers involved immobilisation of PSI, [185, 186] cyanobacteria cells [187] and thylakoid membranes [188] on electrodes. All those systems demonstrated enhanced photocurrent responses, provided by more efficient electron transfer between a biological guest and an electrode surface. On the other hand, cobaltocene-modified redox polymers, with more negative $E_{1/2} = -0.58$ vs. SHE, have been utilised to for CO_2 reduction in FDH-based biocathodes. [189]

Metal-free-modified redox polymers

A need for metal-free redox polymer synthesis has led to increased interest in fully-organic redox polymers with phenothiazine-modified hydrogels viewed as attractive candidates for anodes, [190] and viologen- and quinone-modified polymers for cathodes. [191, 192] The advantage of utilisation of phenothiazine-based over Os complex-based polymers for PSII-photoanodes is associated with lower losses of the harvested energy due to $E_{1/2}$ of the hydrogels better matching the Q_B. Recently, a series of toluidine blue, nile blue, azure blue and neutral red modified redox hydrogels was investigated for PSII photocurrent generation at E_{app} of 0.5 V vs. SHE and red light illumination. [168] The toluidine blue-modified redox polymer with $E_{1/2}$ close to 0 V vs. SHE and highly hydrophilic backbone character exhibited the highest photocurrent densities in the range of 1.5 μA cm^{-2} with no additional cross-linker stabilisation, increased further to 10 μA cm^{-2} on the addition of dithiol cross-linker. In terms of biocathode design, methyl viologen-modified redox polymers with $E_{1/2} = -0.45$ vs. SHE have proven to be promising solid state electron mediators.

1.8 Bias-free PF-PEC design

The water-splitting PEC cell design is often based on the DSSC architecture described earlier. The DSSC (Grätzel cell) is a regenerative liquid-junction PEC cell in which the anode and cathode reactions are the reverse of each other (Fig. 1.9a). In a photosynthetic cell, such as water-splitting PEC prototype (Fujishima-Honda cell), an aqueous electrolyte is used, O_2 is evolved at the TiO_2 photoanode, and H^+ is reduced to H_2 at the dark cathode (Fig. 1.9b). The water-splitting dye-sensitised PEC cell can be thought of as a hybrid of the Grätzel and Fujishima-Honda cell. An OER catalyst, bound to or co-adsorbed with the sensitiser, replaced the I^-/I_3^- redox couple. As the photoexcited electrons in the TiO_2 are not sufficiently reducing to generate H_2 from water, a minimum applied bias voltage (U) of 200-300 mV is needed (Fig. 1.9c). [119]

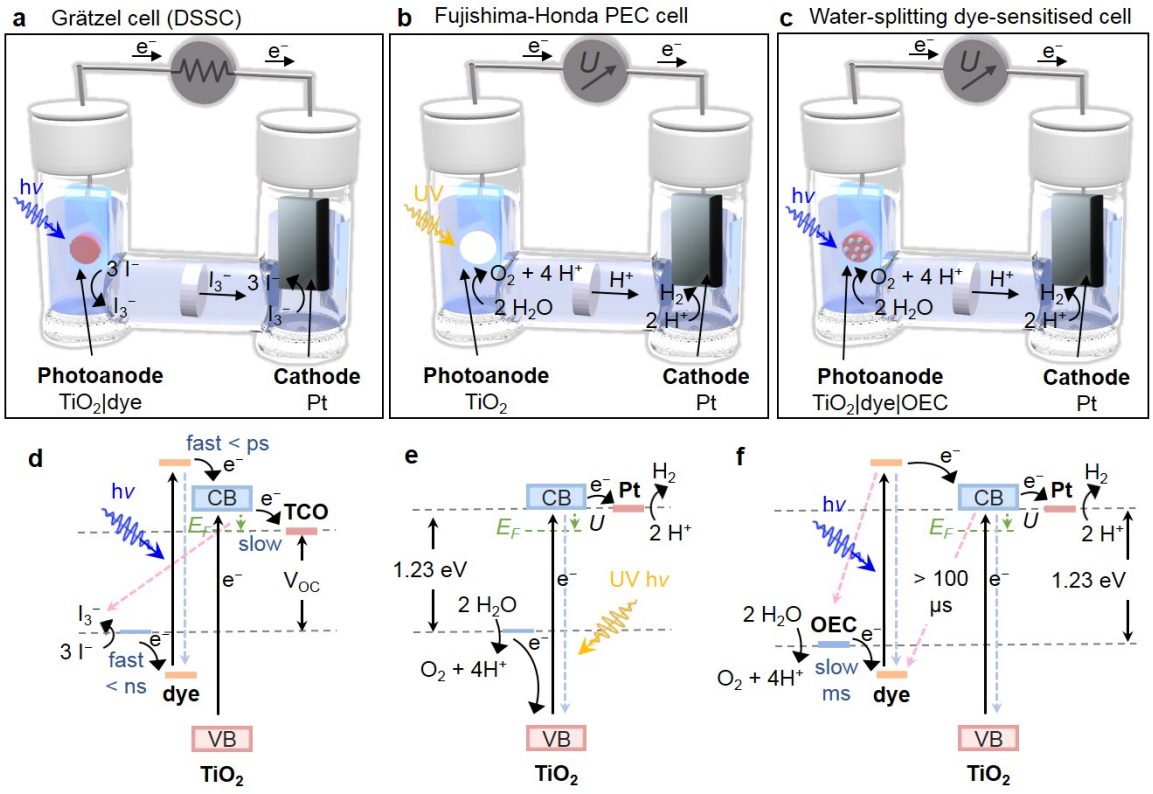

Figure 1.9 **Schematic representation of regenerative and photosynthetic PEC cell designs.** **a**, Regenerative Grätzel cell (DSSC), **b**, photosynthetic water-splitting Fujishima-Honda cell, **c**, photosynthetic water-splitting dye-sensitised cell. The relevant electrochemical potential diagrams for these three kinds of PEC cells: **d**, the Grätzel cell (DSSC), **e**, the Fujishima-Honda cell and **f**, a water-splitting dye-sensitised cell. Abbreviations: OEC, oxygen-evolution catalyst.

In the Grätzel cell, the quantum yield is high, a consequence of fast (< ps) electron injection from the photoexcited dye into the TiO_2 CB, followed by reduction of the oxidised dye by I^- (ns) (Fig. 1.9d). In the Fujishima-Honda cell types based on wide band gap semiconductor electrodes, light absorption creates strongly oxidising VB holes that rapidly oxidise water (Fig. 1.9e). The quantum yield for water oxidation can be high, especially at high applied voltage, where excitons are efficiently separated, but utilisation of the solar spectrum is ineffective. In contrast, in the water-splitting dye-sensitised PEC cells, catalytic water oxidation is typically slow (ms) because of the weak driving force for the reaction (Fig. 1.9f). While the TOFs of the benchmark OER catalysts are sufficient to sustain water electrolysis at 1 sun irradiance, they are too slow to compete effectively with back electron transfer (100s μs). Consequently, water splitting dye-sensitised PEC cells operate with low quantum yield (2-3%) because of the fast kinetics of charge recombination, which competes effectively with the catalytic oxidation of water. Much of the current photoanode design has focused on improving the quantum yield by slowing down back electron transfer and accelerating the water oxidation process. [119]

In a water-splitting cell containing a single light absorber, the maximum photovoltage (V_{OC}, open circuit voltage) can be estimated from the potential of the O_2/H_2O couple and the E_F of the semiconductor, which at low trap state density and high illumination intensity should be close to the E_{CB}. The maximum photovoltage will be obtained when the cathode reaction is the reverse of the anode reaction, i.e. reduction of O_2. At pH 6.5 the thermodynamic potential for water splitting is 0.84 V vs. SHE and the E_{CB} of TiO_2 is approximately -0.55 V vs. SHE, meaning that the maximum photovoltage that could be generated by the cell is $\sim$1.39 V. In practice, however, the V_{OC} of the best dye-sensitised photoanodes is 1.0 V and a bias of a few 100 mV is needed to reach the maximum power point. [193] This implies that a second, complementary absorber should be added to provide additional photovoltage to drive overall water splitting. As PF-PEC cells operate near neutral pH in aqueous solutions, the inherent potential losses in such systems when the anode and cathode separated by an ion exchange membrane to facilitate separation of H_2 and O_2, is:

$$E_{loss} = \eta_{anode} + \eta_{cathode} + iR_{sol} + E_M + E_{pH} \tag{1.8}$$

The η_{anode} and $\eta_{cathode}$ represent the overpotentials of the anode and cathode, iR_{sol} is the solution resistance, E_M is the membrane resistance, and E_{pH} is the potential loss associated with the pH gradient. Resistance losses due to charge transport through the semiconductor are typically low. In concentrated buffers, the losses from iR_{sol} and E_M are small, provided that the electrode separation is short. However, the E_{pH} can be as large as several hundred

mV, and to minimise membrane polarisation, an efficient diffusional flux must be maintained, and thin permeable membranes are needed. Lastly, the buffer choice can have a significant, and largely underexplored, effect on the efficiency of water oxidation. Inefficient buffering can lead to the anode polarisation effect that has been observed in the majority of the current water-splitting dye-sensitised PEC cells. When the cell is held at a potential sufficient to drive water splitting under light illumination, the initial photocurrent is typically in the range of 0.2-0.3 mA cm^{-2}, corresponding to a quantum yield of $\sim$20%. The steady state photocurrent decays over tens of s, reaching a plateau that is 10-20% of the initial value. The possible causes of this polarisation effect are either a slower electron transfer between oxidised catalyst and sensitiser, or a local pH drop of the solution. [193]

1.8.1 Single-absorber PEC

Previously reported PF-PEC water splitting system with a PSII photoanode [36] relied solely on light absorption by PSII and required an externally applied voltage ($U > 0.6$ V) due to the low electrochemical potential of electrons leaving PSII. This limitation can be resolved by introducing a second light absorber to further promote the energetics of the electrons to be delivered to H_2ase. [12] Similarly, to increase the driving force for CO_2 reduction, NAD-FDHs have been coupled to visible light-absorbers, such as zinc porphyrins, [194–196] Chl *a*, [197] cyanobacterial PSI, [198] $BiVO_4$, [91] Fe_2O_3 [94] and $Ru(bpy)_3^{2+}$ dye, [199] but suffered from low selectivity and sacrificial electron donor dependence.

1.8.2 Dual-absorber (tandem) PEC

To generate sufficient driving force for overall water splitting while maximising solar energy harvesting, complementary dual-absorber/tandem systems can be assembled (Fig. 1.4c), showing the highest theoretical limits for solar-to-hydrogen (STH) efficiency of up to 25%, overcoming 12% efficiency of single-absorber systems. [200] Assuming close to 100% quantum yield and reasonable total losses (700-800 mV) for series resistance and catalyst overpotentials, water-splitting dye-sensitised tandem PEC cells could achieve overall efficiencies in the 10-15% range. For a two-absorber system to work efficiently, the redox levels of the electron transport chain components must be properly aligned. The first oxidised absorber drives water oxidation, while the second reduced absorber drives water reduction. Both absorbers could both be on the same electrode or split to give a photoanode and photocathode. In either configuration, two photons are absorbed to generate one electron for water reduction and one hole for water oxidation. Z-schemes have been demonstrated with photocatalysts, but typically with low (1%) quantum yields. In terms of PF-PEC tandem cells, PSII-based [168,

181] and $BiVO_4$ [201] photoanodes wired to PSI-based photocathodes have been reported for solar-to-electrical conversion, but no fuel production. Moving towards solar H_2 generation, hybrid systems PSII-Ru-dye [54], PSII-Si/Pt [202], PSII-Si [172, 203] and PSII-WO_3 [204] introduced a second, more complementary synthetic absorber to drive the half-cell reactions in a diffusional mediator-limited design.

The kinetic optimisation of tandem cells is difficult due to the requirement for current matching and the increased probability of charge recombination in more complex photosystems. The concept is so far largely underinvestigated in dye-sensitised water-splitting PEC cells. It can be concluded that only a tandem PEC cell design with minimal resistance losses could be capable of accumulating enough driving force for an overall water splitting or CO_2 reduction powered solely by solar light without an applied bias voltage.

1.9 Project objectives

As elaborated in *Chapter 1*, natural photosynthesis stores sunlight in chemical energy carriers, but it has not evolved for the efficient synthesis of fuels, such as H_2. Semi-artificial photosynthesis combines the strengths of natural photosynthesis with synthetic chemistry and materials science to develop model systems that overcome Nature's limitations, such as non-complementary light absorption of the Z-scheme and low-yielding pathways of the CBB cycle. For this purpose, it is of interest to solar technologies to develop semi-artificial *in vitro* systems providing a design protocol for unassisted PEC cells for water splitting and CO_2 reduction, and an extended toolbox of biotic and abiotic components to re-engineer photosynthetic pathways (Fig. 1.10a). At the start of this project, semi-artificial PF-PEC design using PSII as a light harvester (i) suffered from ineffective biotic-abiotic interface assembly and inefficient electrical wiring to the electrode surface, (ii) has not achieved an unassisted overall water splitting and (iii) has not been coupled to drive CO_2 reduction. The aim of this work was first to expand the range of 3-D hierarchically-structured inverse opal electrodes with tuneable properties to maximise biological component loading for PF-PEC applications (Fig. 1.10b). Then, the goal was to enhance the electrical wiring at the enzyme-electrode interface in a PSII-based photoanode by using a redox polymer. The subsequent aim was to develop a new tandem PSII−dye photoanode that could provide enough driving force to achieve unassisted overall water splitting when coupled to a H_2ase-based cathode. The final objective was to extend the scope of the project to solar-driven CO_2 reduction by coupling the tandem PSII−dye photoanode to a FDH-based cathode. The project is presented in the chapters of this thesis as outlined below.

In *Chapter 2*, a range of tailor-made tuneable hierarchically-structured electrodes is developed, constituting a versatile platform to accommodate a wide range of biotic guests for semi-artificial PF-PEC cells. In *Chapter 3*, a rational approach for a PSII-based electrode assembly is described, integrating redox polymers with high surface area hierarchically-structured electrodes, reaching a new PSII-based benchmark photoanode using an Os complex-modified hydrogel. In *Chapter 4*, a tandem platform is reported that integrates a dye-sensitised TiO_2 photoanode with the natural machineries, PSII and H_2ase, to split water using solar energy without additional applied bias. In *Chapter 5*, a semi-artificial tandem device is presented, which performs solar-driven CO_2 reduction to formate with a W-dependent FDH coupled to PSII, using water as an electron donor. Finally, in *Chapter 6*, the conclusions of this work are summarised and future directions for the continuation of this project are addressed.

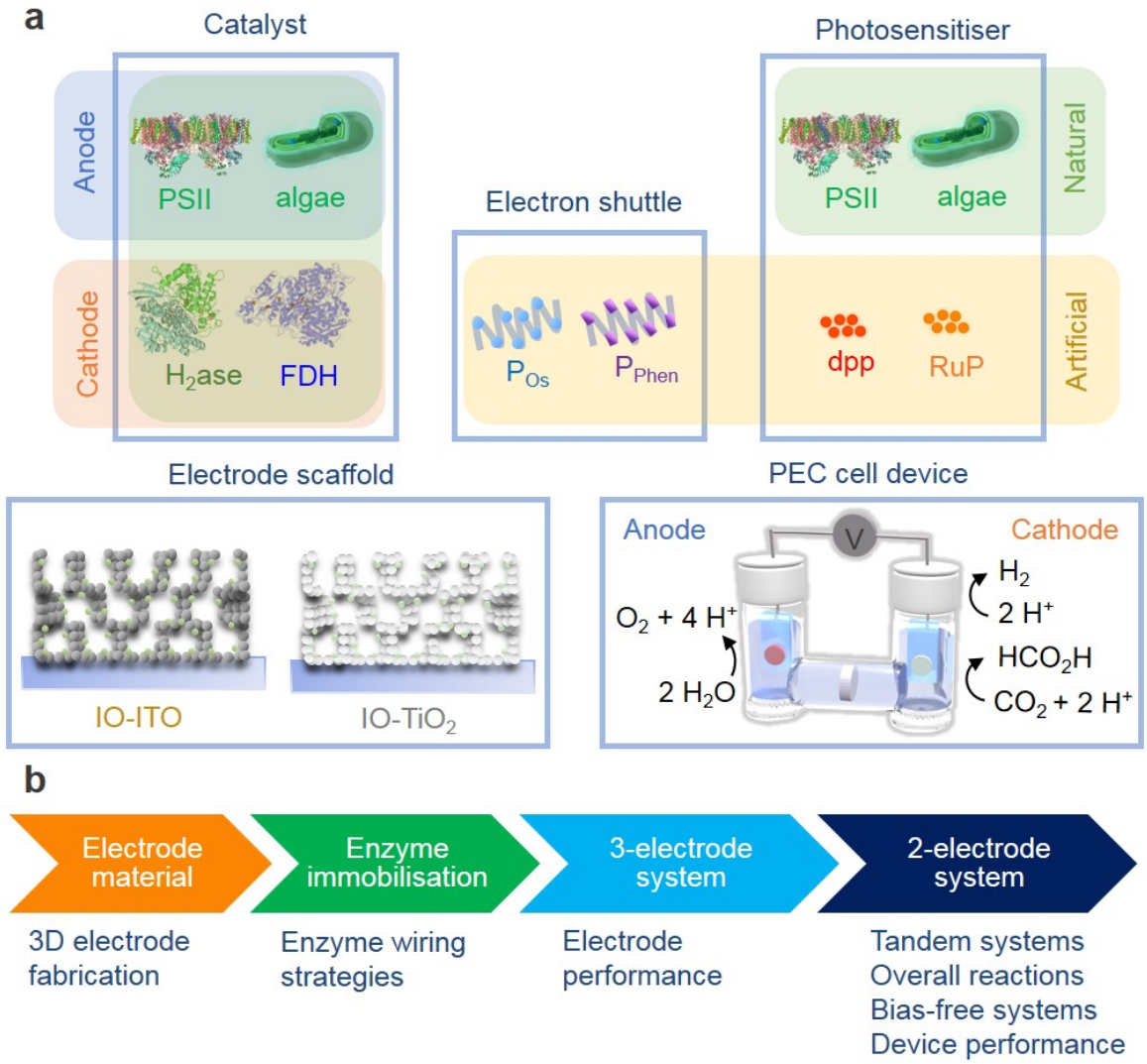

Figure 1.10 **Schematic representation of the project outline and objectives. a**, Toolbox of biological (green shading) and synthetic (yellow shading) components presented in this study. Representative biocatalysts for oxidation (blue shading) and reduction (orange shading) reactions, redox shuttles, photosensitisers, electrode scaffolds and relevant PEC cell reactions are shown (species size not drawn to scale). **b**, Rational all-integrated PEC cell assembly, from the material and electrode to three-electrode setup characterisation and two-electrode setup overall reaction and device performance characterisation. Abbreviations: P_{Os}, poly(1-vinylimidazole-*co*-allylamine)-[Os(bipy)$_2$Cl]Cl polymer; P_{Phen}, phenothiazine-modified polymer; dpp, diketopyrrolopyrrole dye; RuP, [Ru(bpy)$_2$(4,4'-(PO$_3$H$_2$)$_2$bpy)](Br)$_2$ dye.

References

(1) D. G. Nocera and N. S. Lewis, *Proc. Natl. Acad. Sci. U. S. A.*, 2006, **103**, 15729–15735.

(2) International Energy Agency, *2017 Key World Energy Statistics*, tech. rep., Paris, 2017, pp. 6–72.

(3) Y. Tachibana, L. Vayssieres and J. R. Durrant, *Nat. Photonics*, 2012, **6**, 511–518.

(4) C. C. L. McCrory, S. Jung, I. M. Ferrer, S. M. Chatman, J. C. Peters and T. F. Jaramillo, *J. Am. Chem. Soc.*, 2015, **137**, 4347–4357.

(5) R. Hill and F. Bendall, *Nature*, 1960, **186**, 136–137.

(6) D. Walker, *New Phytol.*, 1992, **121**, 325–345.

(7) A. W. Rutherford, *TIBS*, 1989, **14**, 227–232.

(8) T. Noguchi, *Plant Cell Physiol.*, 2002, **43**, 1112–1116.

(9) J. Barber and P. D. Tran, *J. R. Soc. Interface*, 2013, **10**, 20120984.

(10) J. Yon-Kahn and G. Hervé, *Molecular and Cellular Enzymology*, Springer-Verlag Berlin Heidelberg, 1st Edition, 2010, vol. 1, pp. 22–24.

(11) O. Kruse, J. Rupprecht, J. H. Mussgnug, G. C. Dismukes and B. Hankamer, *Photochem. Photobiol. Sci.*, 2005, **4**, 957–969.

(12) B. Esper, A. Badura and M. Rögner, *Trends Plant Sci.*, 2006, **11**, 543–549.

(13) M. Calvin and A. A. Benson, *Science*, 1948, **107**, 476–80.

(14) J. A. Bassham, A. A. Benson, L. D. Kay, A. Z. Harris, A. T. Wilson and M. Calvin, *J. Am. Chem. Soc.*, 1954, **76**, 1760–1770.

(15) X.-G. Zhu, S. P. Long and D. R. Ort, *Annu. Rev. Plant Biol.*, 2010, **61**, 235–261.

(16) H. Yu, X. Li, F. Duchoud, D. S. Chuang and J. C. Liao, *Nat. Commun.*, 2018, **9**, 1–10.

(17) B. J. Walker, A. VanLoocke, C. J. Bernacchi and D. R. Ort, *Annu. Rev. Plant Biol.*, 2016, **67**, 107–129.

(18) T. J. Erb and J. Zarzycki, *Curr. Opin. Biotechnol.*, 2018, **49**, 100–107.

(19) C. A. Cotton, C. Edlich-Muth and A. Bar-Even, *Curr. Opin. Biotechnol.*, 2018, **49**, 49–56.

(20) D. Gust, T. A. Moore and A. L. Moore, *Acc. Chem. Res.*, 2001, **34**, 40–48.

(21) D. Gust, T. A. Moore and A. L. Moore, *Acc. Chem. Res.*, 2009, **42**, 1890–1898.

(22) K. Kalyanasundaram and M. Grätzel, *Curr. Opin. Biotechnol.*, 2010, **21**, 298–310.

(23) M. Grätzel, *Nature*, 2001, **414**, 338–344.

(24) A. J. Bard and M. A. Fox, *Acc. Chem. Res.*, 1995, **28**, 141–145.

(25) A. J. Bard and L. R. Faulkner, *Electrochemical Methods: Fundamentals and Applications*, Wiley, New York, 2nd Edition, 2001, pp. 534–579.

(26) T. Hisatomi, J. Kubota and K. Domen, *Chem. Soc. Rev.*, 2014, **43**, 7520–7535.

(27) S. Mukhopadhyay, R. J. Staples and W. H. Armstrong, *Chem. Commun.*, 2002, **4**, 864–865.

(28) Y. Gorlin and T. Jaramillo, *J. Am. Chem. Soc.*, 2010, **132**, 13612–13614.

(29) Y. Gao, R. H. Crabtree and G. W. Brudvig, *Inorg. Chem.*, 2012, **51**, 4043–4050.

(30) Y. Xu, G. Eilers, M. Borgström, J. Pan, M. Abrahamsson, A. Magnuson, R. Lomoth, J. Bergquist, T. Polívka, L. Sun, V. Sundström, S. Styring, L. Hammarström and B. Åkermark, *Chem. Eur. J.*, 2005, **11**, 7305–7314.

(31) P. W. Menezes, A. Indra, N. R. Sahraie, A. Bergmann, P. Strasser and M. Driess, *ChemSusChem*, 2015, **8**, 164–167.

(32) S. Ott, M. Kritikos, B. Åkermark, L. Sun and R. Lomoth, *Angew. Chem. Int. Ed.*, 2004, **43**, 1006–1009.

(33) A. Magnuson, O. J. Anderlund, P. Lindblad, R. Lomoth, T. Polikova, S. Ott, K. Stensjo, S. Styring, V. Sundström and L. Hammarström, *Acc. Chem. Res.*, 2009, **42**, 10.

(34) K. K. Sakimoto, A. B. Wong and P. Yang, *Science*, 2016, **351**, 74–77.

(35) O. Yehezkeli, R. Tel-vered, J. Wasserman, A. Trifonov, D. Michaeli, R. Nechushtai and I. Willner, *Nat. Commun.*, 2012, **3**, 742–748.

(36) D. Mersch, C.-Y. Lee, J. Z. Zhang, K. Brinkert, J. C. Fontecilla-Camps, A. W. Rutherford and E. Reisner, *J. Am. Chem. Soc.*, 2015, **137**, 8541–8549.

(37) D. R. Ort, S. S. Merchant, J. Alric, A. Barkan, R. E. Blankenship, R. Bock, R. Croce, M. R. Hanson, J. M. Hibberd, S. P. Long, T. A. Moore, J. Moroney, K. K. Niyogi, M. A. J. Parry, P. P. Peralta-Yahya, R. C. Prince, K. E. Redding, M. H. Spalding, K. J. van Wijk, W. F. J. Vermaas, S. von Caemmerer, A. P. M. Weber, T. O. Yeates, J. S. Yuan and X. G. Zhu, *Proc. Natl. Acad. Sci. U. S. A.*, 2015, **112**, 8529–8536.

(38) J. H. Montoya, L. C. Seitz, P. Chakthranont, A. Vojvodic, T. F. Jaramillo and J. K. Nørskov, *Nat. Mater.*, 2016, **16**, 70–81.

(39) T. W. Woolerton, S. Sheard, Y. S. Chaudhary and F. A. Armstrong, *Energy Environ. Sci.*, 2012, **5**, 7470–7490.

(40) C. Liu, B. C. Colón, M. Ziesack, P. A. Silver and D. G. Nocera, *Science*, 2016, **352**, 1210–1213.

(41) C. Léger and P. Bertrand, *Chem. Rev.*, 2008, **108**, 2379–2438.

(42) G. Leblanc, E. Gizzie, S. Yang, D. E. Cliffel and G. K. Jennings, *Langmuir*, 2014, **30**, 10990–11001.

(43) M. Kato, J. Z. Zhang, N. Paul and E. Reisner, *Chem. Soc. Rev.*, 2014, **43**, 6485–6497.

(44) S. K. Ravi and S. C. Tan, *Energy Environ. Sci.*, 2015, **8**, 2551–2573.

(45) S. H. Lee, D. S. Choi, S. K. Kuk and C. B. Park, *Angew. Chem. Int. Ed.*, 2018, **57**, 7958–7985.

(46) M. Rögner, *Biochem. Soc. Trans.*, 2013, **41**, 1254–1259.

(47) W. Khetkorn, R. P. Rastogi, A. Incharoensakdi, P. Lindblad, D. Madamwar, A. Pandey and C. Larroche, *Bioresour. Technol.*, 2017, **243**, 1194–1206.

(48) H. Michel, *Angew. Chem. Int. Ed.*, 2012, **51**, 2516–2518.

(49) M. Sensi, C. Baffert, L. Fradale, C. Gauquelin, P. Soucaille, I. Meynial-Salles, H. Bottin, L. De Gioia, M. Bruschi, V. Fourmond, C. Léger and L. Bertini, *ACS Catal.*, 2017, **7**, 7378–7387.

(50) G. Ananyev and G. C. Dismukes, *Photosynth. Res.*, 2005, **84**, 355–365.

(51) D. J. Vinyard, G. M. Ananyev and G. C. Dismukes, *Annu. Rev. Biochem.*, 2013, **82**, 577–606.

(52) R. Tel-Vered and I. Willner, *ChemElectroChem*, 2014, **1**, 1778–1797.

(53) O. Yehezkeli, R. Tel-Vered, D. Michaeli, I. Willner and R. Nechushtai, *Photosynth. Res.*, 2014, **120**, 71–85.

(54) K. K. Rao, D. O. Hall, N. Vlachopoulos, M. Grätzel, M. C. W. Evans and M. Seibert, *J. Photochem. Photobiol. B*, 1990, **5**, 379–389.

(55) A. Badura, B. Esper, K. Ataka, C. Grunwald, C. Wöll, J. Kuhlmann, J. Heberle and M. Rögner, *Photochem. Photobiol.*, 2006, **82**, 1385–1390.

(56) N. Terasaki, M. Iwai, N. Yamamoto, T. Hiraga, S. Yamada and Y. Inoue, *Thin Solid Films*, 2008, **516**, 2553–2557.

(57) V. M. Friebe and R. N. Frese, *Curr. Opin. Electrochem.*, 2017, **5**, 126–134.

(58) S. A. Trammell, A. Spano, R. Price and N. Lebedev, *Biosens. Bioelectron.*, 2006, **21**, 1023–1028.

(59) J. Zhao, N. Ma, B. Liu, Y. Zhou, C. Xu and J. Kong, *J. Photochem. Photobiol. A Chem.*, 2002, **152**, 53–60.

(60) K. B. Lam, E. A. Johnson and L. Lin, *IEEE*, 2004, **15**, 220–223.

(61) J. O. Calkins, Y. Umasankar, H. O'Neill and R. P. Ramasamy, *Energy Environ. Sci.*, 2013, **6**, 1891–1900.

(62) S. Larom, D. Kallmann, G. Saper, R. Pinhassi, A. Rothschild, H. Dotan, G. Ankonina, G. Schuster and N. Adir, *Photosynth. Res.*, 2015, **126**, 161–169.

(63) A. J. McCormick, P. Bombelli, D. J. Lea-Smith, R. W. Bradley, A. M. Scott, A. C. Fisher, A. G. Smith and C. J. Howe, *Energy Environ. Sci.*, 2013, **6**, 2682–2690.

(64) G. Longatte, F. Rappaport, F. A. Wollman, M. Guille-Collignon and F. Lemaître, *Electrochim. Acta*, 2017, **236**, 337–342.

(65) K. Tanaka, M. Kaneko, M. Ishikawa, S. Kato, H. Ito, T. Kamachi, K. Kamiya and S. Nakanishi, *ChemPhysChem*, 2017, **18**, 878–881.

(66) J. Z. Zhang, P. Bombelli, K. P. Sokol, A. Fantuzzi, A. W. Rutherford, C. J. Howe and E. Reisner, *J. Am. Chem. Soc.*, 2018, **140**, 6–9.

(67) M. Guiral-Brugna, M. T. Giudici-Orticoni, M. Bruschi and P. Bianco, *J. Electroanal. Chem.*, 2001, **510**, 136–143.

(68) S. Morra, F. Valetti, S. J. Sadeghi, P. W. King, T. Meyer and G. Gilardi, *Chem. Commun.*, 2011, **47**, 10566.

(69) A. J. Healy, H. A. Reeve, A. Parkin and K. A. Vincent, *Electrochim. Acta*, 2011, **56**, 10786–10790.

(70) A. Ciaccafava, C. Hamon, P. Infossi, V. Marchi, M. T. Giudici-Orticoni and E. Lojou, *Phys. Chem. Chem. Phys.*, 2013, **15**, 16463–16467.

(71) M. Sensi, M. del Barrio, C. Baffert, V. Fourmond and C. Léger, *Curr. Opin. Electrochem.*, 2017, **5**, 135–145.

(72) C. Wombwell, C. A. Caputo and E. Reisner, *Acc. Chem. Res.*, 2015, **48**, 2858–2865.

(73) E. Reisner, D. J. Powell, C. Cavazza, J. C. Fontecilla-Camps and F. A. Armstrong, *J. Am. Chem. Soc.*, 2009, **131**, 18457–18466.

(74) M. C. Marques, C. Tapia, O. Gutiérrez-Sanz, A. R. Ramos, K. L. Keller, J. D. Wall, A. L. De Lacey, P. M. Matias and I. A. Pereira, *Nat. Chem. Biol.*, 2017, **13**, 544–550.

(75) R. Kebeish, M. Niessen, K. Thiruveedhi, R. Bari, H. J. Hirsch, R. Rosenkranz, N. Stäbler, B. Schönfeld, F. Kreuzaler and C. Peterhänsel, *Nat. Biotechnol.*, 2007, **25**, 593–599.

(76) M. W. Keller, G. J. Schut, G. L. Lipscomb, A. L. Menon, I. J. Iwuchukwu, T. T. Leuko, M. P. Thorgersen, W. J. Nixon, A. S. Hawkins, R. M. Kelly and M. W. W. Adams, *Proc. Natl. Acad. Sci. U. S. A.*, 2013, **110**, 5840–5845.

(77) M. d. Mattozzi, M. Ziesack, M. J. Voges, P. A. Silver and J. C. Way, *Metab. Eng.*, 2013, **16**, 130–139.

(78) P. M. Shih, J. Zarzycki, K. K. Niyogi and C. A. Kerfeld, *J. Biol. Chem.*, 2014, **289**, 9493–9500.

(79) N. E. Kreel and F. R. Tabita, *PLoS One*, 2015, **10**, 1–25.

(80) N. Antonovsky, S. Gleizer, E. Noor, Y. Zohar, E. Herz, U. Barenholz, L. Zelcbuch, S. Amram, A. Wides, N. Tepper, D. Davidi, Y. Bar-On, T. Bareia, D. G. Wernick, I. Shani, S. Malitsky, G. Jona, A. Bar-Even and R. Milo, *Cell*, 2016, **166**, 115–125.

(81) T. Schwander, S. Burgener and T. J. Erb, *Science*, 2016, **354**, 900–904.

(82) S. W. Ragsdale and E. Pierce, *Biochim. Biophys. Acta*, 2008, **1784**, 1873–1898.

(83) B. Loges, A. Boddien, H. Junge and M. Beller, *Angew. Chem. Int. Ed.*, 2008, **47**, 3962–3965.

(84) B. Kumar, M. Llorente, J. Froehlich, T. Dang, A. Sathrum and C. P. Kubiak, *Ann. Rev. Phys. Chem.*, 2012, **63**, 541–569.

(85) T. Reda, C. M. Plugge, N. J. Abram and J. Hirst, *Proc. Natl. Acad. Sci. U. S. A.*, 2008, **105**, 10654–10658.

(86) S. Kuwabata, R. Tsuda, K. Nishida and H. Yoneyama, *Chem. Lett.*, 1993, **22**, 1631–1634.

(87) S. Kuwabata, R. Tsuda and H. Yoneyama, *J. Am. Chem. Soc.*, 1994, **116**, 5437–5443.

(88) S. Schlager, L. M. Dumitru, M. Haberbauer, A. Fuchsbauer, H. Neugebauer, D. Hiemetsberger, A. Wagner, E. Portenkirchner and N. S. Sariciftci, *ChemSusChem*, 2016, **9**, 631–635.

(89) Y. Amao and N. Shuto, *Res. Chem. Intermed.*, 2014, **40**, 3267–3276.

(90) H. Hwang, Y. J. Yeon, S. Lee, H. Choe, M. G. Jang, D. H. Cho, S. Park and Y. H. Kim, *Bioresour. Technol.*, 2015, **185**, 35–39.

(91) S. Y. Lee, S. Y. Lim, D. Seo, J. Y. Lee and T. D. Chung, *Adv. Energy Mater.*, 2016, **6**, 1502207.

(92) S. Kim, M. K. Kim, S. H. Lee, S. Yoon and K. D. Jung, *J. Mol. Catal. B Enzym.*, 2014, **102**, 9–15.

(93) S. Srikanth, M. Maesen, X. Dominguez-Benetton, K. Vanbroekhoven and D. Pant, *Bioresour. Technol.*, 2014, **165**, 350–354.

(94) D. H. Nam, S. K. Kuk, H. Choe, S. Lee, J. W. Ko, E. J. Son, E. G. Choi, Y. H. Kim and C. B. Park, *Green Chem.*, 2016, **18**, 5989–5993.

(95) S. H. Kim, G. Y. Chung, S. H. Kim, G. Vinothkumar, S. H. Yoon and K. D. Jung, *Electrochim. Acta*, 2016, **210**, 837–845.

(96) L. Zhang, J. Liu, J. Ong and S. F. Y. Li, *Chemosphere*, 2016, **162**, 228–234.

(97) L. Zhang, J. Ong, J. Liu and S. F. Y. Li, *Renew. Energy*, 2017, **108**, 581–588.

(98) A. Graentzdoerffer, D. Rauh, A. Pich and J. R. Andreesen, *Arch. Microbiol.*, 2003, **179**, 116–130.

(99) T. Hartmann and S. Leimkühler, *FEBS J.*, 2013, **280**, 6083–6096.

(100) K. Schuchmann and V. Müller, *Science*, 2013, **342**, 1382–1386.

(101) A. Bassegoda, C. Madden, D. W. Wakerley, E. Reisner and J. Hirst, *J. Am. Chem. Soc.*, 2014, **136**, 15473–15476.

(102) L. B. Maia, L. Fonseca, I. Moura and J. J. G. Moura, *J. Am. Chem. Soc.*, 2016, **138**, 8834–8846.

(103) X. Yu, D. Niks, A. Mulchandani and R. Hille, *J. Biol. Chem.*, 2017, **292**, 16872–16879.

(104) K. Sakai, Y. Kitazumi, O. Shirai, K. Takagi and K. Kano, *Electrochem. Commun.*, 2017, **84**, 75–79.

(105) W. E. Robinson, A. Bassegoda, E. Reisner and J. Hirst, *J. Am. Chem. Soc.*, 2017, **139**, 9927–9936.

(106) K. Sakai, Y. Kitazumi, O. Shirai and K. Kano, *Electrochem. Commun.*, 2016, **65**, 31–34.

(107) K. Sakai, Y. Kitazumi, O. Shirai, K. Takagi and K. Kano, *Electrochem. Commun.*, 2016, **73**, 85–88.

(108) J. McKone and N. S. Lewis, in *Photoelectrochemical Water Splitting: Materials, Processes and Architectures*, ed. H.-J. Lewerenz and L. Peter, Royal Society of Chemistry, Cambridge, RSC Energy, 2013, pp. 52–82.

(109) J. Nowotny, T. Bak, M. K. Nowotny and L. R. Sheppard, *Int. J. Hydrogen Energy*, 2007, **32**, 2609–2629.

(110) K. J. Young, L. A. Martini, R. L. Milot, R. C. S. Iii, V. S. Batista, C. A. Schmuttenmaer, R. H. Crabtree and G. W. Brudvig, *Coord. Chem. Rev.*, 2012, **256**, 2503–2520.

(111) B. O'Regan and M. Grätzel, *Nature*, 1991, **353**, 737–740.

(112) P. Wang, S. M. Zakeeruddin, J. E. Moser, M. K. Nazeeruddin, T. Sekiguchi and M. Grätzel, *Nat. Mater.*, 2003, **2**, 402–407.

(113) M. Grätzel, *Inorg. Chem.*, 2005, **44**, 6841–6851.

(114) L. Han, A. Islam, H. Chen, C. Malapaka, B. Chiranjeevi, S. Zhang, X. Yang and M. Yanagida, *Energy Environ. Sci.*, 2012, **5**, 6057–6060.

(115) Y. Cao, Y. Liu, S. M. Zakeeruddin, A. Hagfeldt and M. Grätzel, *Joule*, 2018, **2**, 1108–1117.

(116) J. Burschka, N. Pellet, S. J. Moon, R. Humphry-Baker, P. Gao, M. K. Nazeeruddin and M. Grätzel, *Nature*, 2013, **499**, 316–319.

(117) M. Hambourger, G. Kodis, M. D. Vaughn, G. F. Moore, D. Gust, A. L. Moore and T. A. Moore, *Dat. Trans.*, 2009, **45**, 9979–9989.

(118) W. Song, Z. Chen, M. K. Brennaman, J. J. Concepcion, A. O. T. Patrocinio, N. Y. M. Iha and T. J. Meyer, *Pure Appl. Chem.*, 2011, **83**, 749–768.

(119) P. Xu, N. S. McCool and T. E. Mallouk, *Nano Today*, 2017, **14**, 42–58.

(120) J. J. Concepcion, J. W. Jurss, M. K. Brennaman, P. G. Hoertz, N. Yukie, M. Iha, J. L. Templeton and T. J. Meyer, *Acc. Chem. Res.*, 2009, **42**, 1954–1965.

(121) D. L. Ashford, W. Song, J. J. Concepcion, C. R. K. Glasson, M. K. Brennaman, M. R. Norris, Z. Fang, J. L. Templeton and T. J. Meyer, *J. Am. Chem. Soc.*, 2012, **134**, 19189–19198.

(122) G. F. Moore, S. J. Konezny, H.-e. Song, R. L. Milot, J. D. Blakemore, M. L. Lee, V. S. Batista, C. A. Schmuttenmaer, R. H. Crabtree and G. W. Brudvig, *J. Phys. Chem. C*, 2012, **116**, 4892–4902.

(123) Y. Zhao, J. R. Swierk, J. D. Megiatto, B. Sherman, W. J. Youngblood and D. Qin, *Proc. Natl. Acad. Sci. U. S. A.*, 2012, **109**, 15612–15616.

(124) L. Alibabaei, M. K. Brennaman, M. R. Norris, B. Kalanyan, W. Song and M. D. Losego, *Proc. Natl. Acad. Sci. U. S. A.*, 2013, **110**, 20008–20013.

(125) F. Liu, T. Cardolaccia, B. J. Hornstein, J. R. Schoonover and T. J. Meyer, *J. Am. Chem. Soc.*, 2007, **129**, 2446–2447.

(126) Y.-G. Guo, S. Xin and L.-Y. Wan, in *Electrochem. Nanofabrication Princ. Appl.* Ed. D. Wei, Pan Stanford Publishing, Singapore, 2011, pp. 251–261.

(127) Y. Dong, Y. Wang, T. Cai, L. Kou, G. Yang and Z. Yan, *Ceram. Int.*, 2014, **40**, 11213–11219.

(128) J. C. Lytle, H. Yan, N. S. Ergang, W. H. Smyrl and A. Stein, *J. Mater. Chem.*, 2004, **14**, 1616–1622.

(129) E. Arsenault, N. Soheilnia and G. a. Ozin, *ACS Nano*, 2011, **5**, 2984–2988.

(130) Y. Liu, K. Peters, B. Mandlmeier, A. Müller, K. Fominykh, J. Rathousky, C. Scheu and D. Fattakhova-Rohlfing, *Electrochim. Acta*, 2014, **140**, 108–115.

(131) R. Lakes, *Nature*, 1993, **361**, 511–515.

(132) Y. H. Sun, P. P. Dong, X. Lang and J. M. Nan, *Chinese Chem. Lett.*, 2014, **25**, 915–918.

(133) D. Lee and C. L. Grigoropoulos, in *Hierarchical Nanostructures for Energy Devices*, ed. S. H. Ko and C. P. Grigoropoulos, Royal Society of Chemistry, Cambridge, RSC Nanoscience, 2015, pp. 175–200.

(134) Y. Li, Z.-Y. Fu and B.-L. Su, *Adv. Funct. Mater.*, 2012, **22**, 4634–4667.

(135) W. Liu, A. Wang, J. Tang, S.-L. Chen, G. Yuan, K. Zhao, C. Li and X. Liu, *Microporous Mesoporous Mater.*, 2015, **204**, 143–148.

(136) E. Y. Katz, A. Y. Shkuropatov, O. I. Vagabova and V. A. Shuvalov, *Biochim. Biophys. Acta - Bioenerg.*, 1989, **976**, 121–128.

(137) M. Miyachi, S. Ikehira, D. Nishiori, Y. Yamanoi, M. Yamada, M. Iwai, T. Tomo, S. I. Allakhverdiev and H. Nishihara, *Langmuir*, 2017, **33**, 1351–1358.

(138) E. Katz, *J. Electroanal. Chem.*, 1994, **365**, 157–164.

(139) C. Nakamura, M. Hasegawa, Y. Yasuda and J. Miyake, *Appl. Biochem. Biotechnol.*, 2000, **84-86**, 401–408.

(140) S. A. Trammell, L. Wang, J. M. Zullo, R. Shashidhar and N. Lebedev, *Biosens. Bioelectron.*, 2004, **19**, 1649–1655.

(141) S. A. Trammell, I. Griva, A. Spano, S. Tsoi, L. M. Tender, J. Schnur and N. Lebedev, *J. Phys. Chem. C*, 2007, **111**, 17122–17130.

(142) M. Kondo, M. Amano, T. Joke, S. Ishigure, T. Noji, T. Dewa, Y. Amao and M. Nango, *Res. Chem. Intermed.*, 2014, **40**, 3287–3293.

(143) N. Lebedev, A. Spano, S. Trammell, I. Griva, S. Tsoi and J. M. Schnur, *Proc. SPIE 6656, Organic Photovoltaics VIII*, 2007, **6656**, 665614.

(144) H. Yaghoubi, Z. Li, D. Jun, E. Lafalce, X. Jiang, R. Schlaf, J. T. Beatty and A. Takshi, *J. Phys. Chem. C*, 2014, **118**, 23509–23518.

(145) M. Kato, T. Cardona, A. W. Rutherford and E. Reisner, *J. Am. Chem. Soc.*, 2013, **135**, 10610–10613.

(146) Y. Zhang, N. M. Magdaong, M. Shen, H. a. Frank and J. F. Rusling, *ChemistryOpen*, 2015, **4**, 111–114.

(147) T. Laftsoglou and L. J. Jeuken, *Chem. Commun.*, 2017, **53**, 3801–3809.

(148) M. Kato, H. Sato, I. Yagi and M. Sugiura, *Electrochim. Acta*, 2018, **264**, 386–392.

(149) P. N. Ciesielski, A. M. Scott, C. J. Faulkner, B. J. Berron, D. E. Cliffel and G. K. Jennings, *ACS Nano*, 2008, **2**, 2465–2472.

(150) K. R. Stieger, S. C. Feifel, H. Lokstein, M. Hejazi, A. Zouni and F. Lisdat, *J. Mater. Chem. A*, 2016, **4**, 17009–17017.

(151) D. Ciornii, S. C. Feifel, M. Hejazi, A. Kölsch, H. Lokstein, A. Zouni and F. Lisdat, *Physi. Status Solidi*, 2017, **214**, 1700017.

(152) L. M. Utschig, S. C. Silver, K. L. Mulfort and D. M. Tiede, *J. Am. Chem. Soc.*, 2011, **133**, 16334–16337.

(153) R. A. Grimme, C. E. Lubner, D. A. Bryant and J. H. Golbeck, *J. Am. Chem. Soc.*, 2008, **130**, 6308–6309.

(154) I. J. Iwuchukwu, M. Vaughn, N. Myers, H. O'Neill, P. Frymier and B. D. Bruce, *Nat. Nanotechnol.*, 2010, **5**, 73–79.

(155) H. Krassen, A. Schwarze, Ba, K. Ataka, O. Lenz and J. Heberle, *ACS Nano*, 2009, **3**, 4055–4061.

(156) C. E. Lubner, A. M. Applegate, P. Knorzer, A. Ganago, D. A. Bryant, T. Happe and J. H. Golbeck, *Proc. Natl. Acad. Sci. U. S. A.*, 2011, **108**, 20988–20991.

(157) C. Gutiérrez-Sánchez, D. Olea, M. Marques, V. M. Fernández, I. A. Pereira, M. Vélez and A. L. Lacey, *Langmuir*, 2011, **27**, 6449–6457.

(158) J. Riethausen, O. Rüdiger, W. Gärtner, W. Lubitz and H. S. Shafaat, *ChemBioChem*, 2013, **14**, 1714–1719.

(159) C. Y. Lee, H. S. Park, J. C. Fontecilla-Camps and E. Reisner, *Angew. Chem. Int. Ed.*, 2016, **55**, 5971–5974.

(160) S. Gentil, S. M. Che Mansor, H. Jamet, S. Cosnier, C. Cavazza and A. Le Goff, *ACS Catal.*, 2018, **8**, 3957–3964.

(161) P. Trogadas, V. Ramani, P. Strasser, T. F. Fuller and M.-O. Coppens, *Angew. Chem. Int. Ed.*, 2015, **54**, 2–29.

(162) K. R. Phillips, G. T. England, S. Sunny, E. Shirman, T. Shirman, N. Vogel and J. Aizenberg, *Chem. Soc. Rev.*, 2016, **45**, 281–322.

(163) M. Kato, T. Cardona, A. W. Rutherford and E. Reisner, *J. Am. Chem. Soc.*, 2012, **134**, 8332–8335.

(164) K. N. . Ferreira, T. M. . Iverson, K. Maghlaoui, J. Barber and S. Iwata, *Science*, 2004, **303**, 1831–1838.

(165) J. Kern, B. Loll, C. Lüneberg, D. DiFiore, J. Biesiadka, K.-D. Irrgang and A. Zouni, *Biochim. Biophys. Acta - Bioenerg.*, 2005, **1706**, 147–157.

(166) M. Broser, A. Gabdulkhakov, J. Kern, A. Guskov, F. Müh, W. Saenger and A. Zouni, *J. Biol. Chem.*, 2010, **285**, 26255–26262.

(167) A. Badura, D. Guschin, B. Esper, T. Kothe, S. Neugebauer, W. Schuhmann and M. Rögner, *Electroanalysis*, 2008, **20**, 1043–1047.

(168) V. Hartmann, T. Kothe, S. Pöller, E. El-Mohsnawy, M. M. Nowaczyk, N. Plumeré, W. Schuhmann and M. Rögner, *Phys. Chem. Chem. Phys.*, 2014, **16**, 11936–11941.

(169) K. Brinkert, F. Le Formal, X. Li, J. Durrant, A. W. Rutherford and A. Fantuzzi, *Biochim. Biophys. Acta - Bioenerg.*, 2016, **1857**, 1497–1505.

(170) J. Li, X. Feng, J. Fei, P. Cai, J. Huang and J. Li, *J. Mater. Chem. A*, 2016, **4**, 12197–12204.

(171) D. Ciornii, M. Riedel, K. R. Stieger, S. C. Feifel, M. Hejazi, H. Lokstein, A. Zouni and F. Lisdat, *J. Am. Chem. Soc.*, 2017, **139**, 16478–16481.

(172) D. H. Nam, J. Z. Zhang, V. Andrei, N. Kornienko, N. Heidary, A. Wagner, K. Nakanishi, K. P. Sokol, B. Slater, I. Zebger, S. Hofmann, J. C. Fontecilla-Camps, C. B. Park and E. Reisner, *Angew. Chem. Int. Ed.*, 2018, **57**, 10595–10599.

(173) L. Matuschek, G. Göbel and F. Lisdat, *Electrochem. Commun.*, 2017, **81**, 145–149.

(174) M. Riedel and F. Lisdat, *ACS Appl. Mater. Interfaces*, 2018, **10**, 267–277.

(175) M. Riedel, W. J. Parak, A. Ruff, W. Schuhmann and F. Lisdat, *ACS Catal.*, 2018, **8**, 5212–5220.

(176) A. Heller, *Curr. Opin. Chem. Biol.*, 2006, **10**, 664–672.

(177) R. Gracia and D. Mecerreyes, *Polym. Chem.*, 2013, **4**, 2206–2214.

(178) A. Badura, D. Guschin, T. Kothe, M. J. Kopczak, W. Schuhmann and M. Rögner, *Energy Environ. Sci.*, 2011, **4**, 2435–2440.

(179) G. Inzelt, in *Conduct. Polym.* Ed. F. Scholz, Springer-Verlag, Berlin Heidelberg, 2nd Edition, 2012, pp. 7–83.

(180) P. N. Bartlett and K. F. E. Pratt, *J. Electroanal. Chem.*, 1995, **397**, 61–78.

(181) T. Kothe, N. Plumeré, A. Badura, M. M. Nowaczyk, D. A. Guschin, M. Rögner and W. Schuhmann, *Angew. Chem. Int. Ed.*, 2013, **52**, 14233–14236.

(182) T. Ikeda, C. R. Leidner and R. W. Murray, *J. Electroanal. Chem.*, 1982, **138**, 343–365.

(183) A. Heller, *Acc. Chem. Res.*, 1990, **23**, 128–134.

(184) A. Heller, *J. Phys. Chem.*, 1992, **96**, 3579–3587.

(185) D. R. Baker, R. F. Simmerman, J. J. Sumner, B. D. Bruce and C. A. Lundgren, *Langmuir*, 2014, **30**, 13650–13655.

(186) C. Tapia, R. D. Milton, G. Pankratova, S. D. Minteer, H. E. Åkerlund, D. Leech, A. L. De Lacey, M. Pita and L. Gorton, *ChemElectroChem*, 2017, **4**, 90–95.

(187) K. Hasan, H. Bekir Yildiz, E. Sperling, P. Ó Conghaile, M. a. Packer, D. Leech, C. Hägerhäll and L. Gorton, *Phys. Chem. Chem. Phys.*, 2014, **16**, 24676–24680.

(188) H. Hamidi, K. Hasan, S. C. Emek, Y. Dilgin, H.-E. Åkerlund, P.-Å. Albertsson, D. Leech and L. Gorton, *ChemSusChem*, 2015, **8**, 990–993.

(189) M. Yuan, S. Sahin, R. Cai, S. Abdellaoui, D. P. Hickey, S. D. Minteer and R. D. Milton, *Angew. Chem. Int. Ed.*, 2018, 6582–6586.

(190) A. A. Golriz, T. Suga, H. Nishide, R. Berger and J. S. Gutmann, *RSC Adv.*, 2015, **5**, 22947–22950.

(191) O. Yehezkeli, R. Tel-Vered, D. Michaeli, R. Nechushtai and I. Willner, *Small*, 2013, **9**, 2970–2978.

(192) S. Sahin, R. Cai, R. D. Milton, S. Abdellaoui, F. C. Macazo and S. D. Minteer, *J. Electrochem. Soc.*, 2018, **165**, 109–113.

(193) J. R. Swierk and T. E. Mallouk, *Chem. Soc. Rev.*, 2013, **42**, 2357–2387.

(194) R. Miyatani and Y. Amao, *Biotechnol. Lett.*, 2002, **24**, 1931–1934.

(195) Y. Amao, S. Takahara and Y. Sakai, *Int. J. Hydrogen Energy*, 2014, **39**, 20771–20776.

(196) S. Ikeyama and Y. Amao, *Sustain. Energy Fuels*, 2017, **1**, 1730–1733.

(197) I. Tsujisho, M. Toyoda and Y. Amao, *Catal. Commun.*, 2006, **7**, 173–176.

(198) M. Ihara, Y. Kawano, M. Urano and A. Okabe, *PLoS One*, 2013, **8**, 1–8.

(199) T. Noji, T. Jin, M. Nango, N. Kamiya and Y. Amao, *ACS Appl. Mater. Interfaces*, 2017, **9**, 3260–3265.

(200) S. Hu, C. Xiang, S. Haussener, A. D. Berger and N. S. Lewis, *Energy Environ. Sci.*, 2013, **6**, 2984–2993.

(201) J. H. Kim, Y. Jo, J. H. Kim, J. W. Jang, H. J. Kang, Y. H. Lee, D. S. Kim, Y. Jun and J. S. Lee, *ACS Nano*, 2015, **9**, 11820–11829.

(202) W. Wang, H. Wang, Q. Zhu, W. Qin, G. Han, J.-r. Shen and X. Zong, *Angew. Chem. Int. Ed.*, 2016, **55**, 9229–9233.

(203) R. I. Pinhassi, D. Kallmann, G. Saper, H. Dotan, A. Linkov, A. Kay, V. Liveanu, G. Schuster, N. Adir and A. Rothschild, *Nat. Commun.*, 2016, **7**, 12552.

(204) H. Pang, G. Zhao, G. Liu, H. Zhang, X. Hai and S. Wang, *Small*, 2018, **14**, 1800104.

Chapter 2

Hierarchically-structured electrodes for semi-artificial photosynthesis

The contents of this chapter have been published in peer-reviewed articles: J. Am. Chem. Soc., 2018, 140, 6−9 (10 µm macropore diameter IO-ITO electrodes for cyanobacteria cell immobilisation), Nano Lett., 2018, accepted (0.75 and 3 µm macropore IO-ITO electrode macro/mesoporosity study) and Angew. Chem. Int. Ed., 2018, 57, 10595−10599 (0.75 µm macropore IO-TiO_2 electrodes for H_2ase immobilisation). Results presented were obtained by the author of this thesis except as outlined here: Dr. Tarek Kandiel is acknowledged for characterising the ITO NPs by TEM.

2.1 Introduction

The design of PF-PEC cells relies on suitable electrode materials and architectures that serve as a host structure for the incorporation of biotic guests. In comparison to synthetic systems, semi-artificial PEC cells exploit the integration and operation of enzymes and whole cells *in vitro*. Due to the large size of biological components, 3-D interconnected porous electrodes constitute ideal host morphology, allowing to achieve high thicknesses, while not being constrained by diffusional mass transfer of reagents and products. [1] Additional hierarchical structuring, introducing another level of porosity, would address the issues of current state-of-the-art non-hierarchical (flat, nanostructured and mesoporous) electrodes, incompatible to host biological species. [2, 3] Those limitations include: low electrode thickness, low effective surface area and guest loading, poor guest stability and electrical wiring to the electrode surface and incapability of effective immobilisation of microsize species on the surface.

Despite the intensive work and significant progress in nanostructured electrode synthesis for artificial PEC cells, the design of 3-D porous hierarchically-structured electrodes for photo- and redox-active guest species in semi-artificial PF-PEC cells has been underexplored. At the start of this project, hierarchically-structured macro-mesoporous inverse opal (IO) indium tin oxide (IO-ITO) electrodes with 750 nm pore diameter have been introduced for the improved integration of enzymes, such as photosystem II (PSII) and hydrogenase (H_2ase), for PF-PEC water splitting. [4] These electrodes were shown to be advantageous compared to state-of-the-art electrodes used in PFE due to their large surface area of sorption, high loading capacity, transparency and hydrophilicity.

Here, a broadened range of tailor-made hierarchically-structured IO electrodes for semi-artificial photosynthesis is fabricated (Fig. 2.1). Increasing the macroporosity could expand the IO-ITO electrode application to host the whole algae and cyanobacteria cells. Tuning the mesporosity could lead towards more controlled and systematic study of enzyme−electrode interface and interactions. Introducing a stable and cost-effective material, such as TiO_2 could broaden the IO applicability. Tailoring of IO architecture would allow to: (i) establish a range of materials with tuneable morphologies and pore sizes to fit a wide range of biotic guests for semi-artificial PEC cells and (ii) develop a versatile platform for the future PF-PEC electrode design.

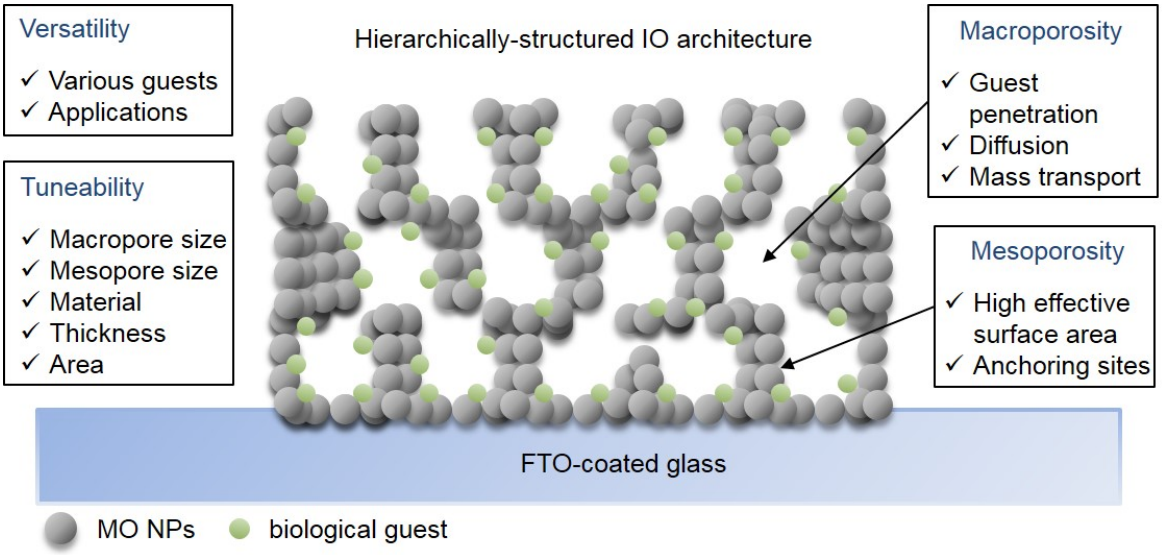

Figure 2.1 **Scheme of hierarchically-structured IO macro-mesoporous tailor-made host morphology for biological guests.** The key architecture features are indicated: versatility, tuneability, macroporosity and mesoporosity. MO, metal oxide; FTO, fluorine-doped tin oxide.

2.2 Results and discussion

2.2.1 IO electrode fabrication

The first goal of this project was to assemble IO-ITO electrodes to accommodate a variety of different guests. Herein, new types of hierarchically-structured macro-mesoporous IO-ITO electrodes with 3 and 10 μm pore diameter were developed for the incorporation of larger guest species, such as redox polymers and cyanobacteria cells, respectively. Amongst various methods that have been developed in the past for the synthesis of three-dimensionally ordered macroporous (3-DOM) structures of amorphous or crystalline metal oxides, [5, 6] the polystyrene (PS) spheres colloidal crystal template is a scalable and low-cost bottom-up approach and was thus employed in this study. [7] This method involves the evaporation-induced self-assembly of PS beads to yield a sacrificial opal template, which directs the deposition or infiltration of functional materials to obtain the IO architecture (Fig. 2.2). Assuming that the PS colloidal suspension is stable over evaporation time, the assembly of PS spheres into a face-centred cubic (fcc) crystal lattice starts when the polystyrene volume fraction $\phi_{PS} \geq 0.494$ and is complete at $\phi_{PS} \geq 0.545$ (where: $\phi_{PS} + \phi_{solvent} = 1$). [8] Upon solvent evaporation, the strong capillary forces, supported by the van der Waals interactions, act on the nearby PS beads to bring them together. The formation of the fcc ordering is driven by the free volume entropy increase. The IO electrode structure developed here is aperiodic to some extent, resulting in additional enhancement in light harvesting due to scattering inside the porous scaffold.

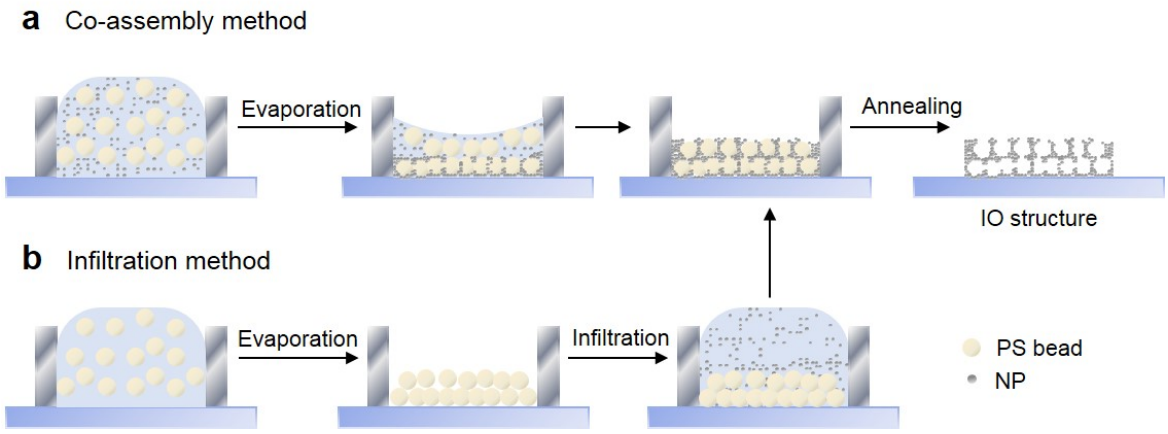

Figure 2.2 **Scheme of IO macro-mesoporous structure formation via PS bead evaporation-induced self-assembly. a**, co-assembly method. **b**, infiltration method.

The resultant hierarchical structure combines meso- and macroporous morphological features of the mesoporous films and IO open framework (Fig. 2.2), respectively. The macro-

pore size can be tuned by choosing suitable monodispersed PS beads that are commercially available. The mesoporosity can be achieved by employing commercially available metal oxide nanoparticles (NPs) as a matrix material. The significantly smaller size of ITO NPs ($\leq$ 50 nm) relative to the PS beads ensured minimised structure shrinkage and associated cracking upon removal of PS opal template by annealing. The drop-casting deposition method was used to achieve readily tuneable high thickness films. The most effective fabrication route was found to be dependent on the desired pore size of the IO structure. The co-assembly method, employed previously to fabricate IO-ITO electrodes with 750 nm pore size, [4] was found to be also effective for PS spheres with 3 μm diameter, and thus was successfully implemented. The infiltration method introduced in this work resulted in better morphology for bigger pore size (10 μm in diameter) IO films, which can be attributed to significantly faster sedimentation of PS beads due to the gravitational effect.

Co-assembly method

A general scheme for the assembly of the IO-mesoporous electrodes by the co-assembly method is outlined in Fig. 2.3. In brief, the co-assembly of the PS colloidal template with the metal oxide NPs was achieved by mixing both suspensions together to form a homogeneous precursor mixture, which was then deposited on a conductive substrate by drop-casting. The PS template was removed by annealing at 500 °C. The IO-mesoporous electrode structures were optimised in terms of a solvent choice for the metal oxide NPs dispersion, evaporation temperature of the PS$-$NPs precursor mixture and a relative concentration of ITO NPs to PS beads. Once the structure was optimised, the maximum film thickness exhibiting sufficient stability was determined by the multiple PS$-$NPs precursor drop-casting cycles.

Infiltration method

A general scheme for the assembly of the IO-mesoporous electrodes by the infiltration method is outlined in Fig. 2.4. In this more conventional method, the PS colloidal template is assembled first, and subsequently infiltrated with the metal oxide NPs colloidal suspension. In the last step, the PS sacrificial template is removed by annealing. The IO-ITO structure was optimised in terms of a solvent choice for the ITO NPs dispersion, ITO NPs dispersion concentration, PS beads suspension concentration, sedimentation time and self-assembly sintering temperature, ITO NPs evaporation temperature and relative concentration of ITO NPs to PS beads. Once the structure was optimised, the maximum stable film thickness was assessed by the multiple deposition cycles.

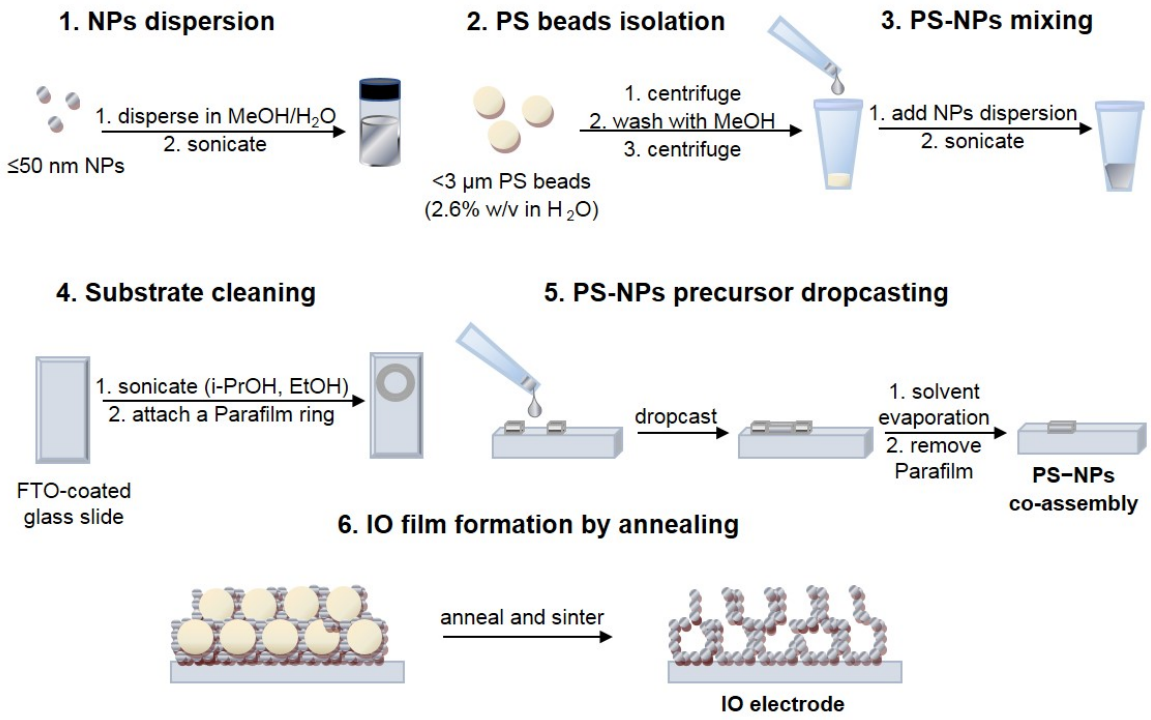

Figure 2.3 **General scheme of the IO-mesoporous electrode preparation by the co-assembly method.**

2.2.2 IO morphology tuning: macroporosity

3 μm pore diameter ITO-IO

The IO-ITO electrode with 3 μm pore diameter was fabricated via a modified co-assembly method, adapted from previously reported procedure for 0.75 μm pore diameter IO-ITO. [4] The morphology of the electrode was characterised by scanning electron microscopy (SEM, Fig. 2.5a) and showed a uniform, almost crack-free surface with good 3-D interconnections between the pores and no ITO NPs overlayer. The pore and effective channel diameter were determined to be 3 μm and 1 μm, respectively, indicative of no significant electrode shrinkage upon PS bead template removal. The mesopores, serving as anchoring sites for the guest species, were on the size scale of 50 nm, well-fitting to the enzymes such as PSII and H_2ase, or small polymers, following analogous host-guest binding rule as complementarity and preorganisation principles. The IO-ITO film thickness could be tuned between 10 μm and 80 μm (corresponding to 27 PS layers), with no structural collapse observed, as shown by the SEM (Fig. 2.5a).

The best solvent for the ITO NPs dispersion was found to be a MeOH/H_2O mixture (10:1 v/v ratio), resulting in a highly homogeneous PS−NPs precursor suspension (Fig. A.1 and

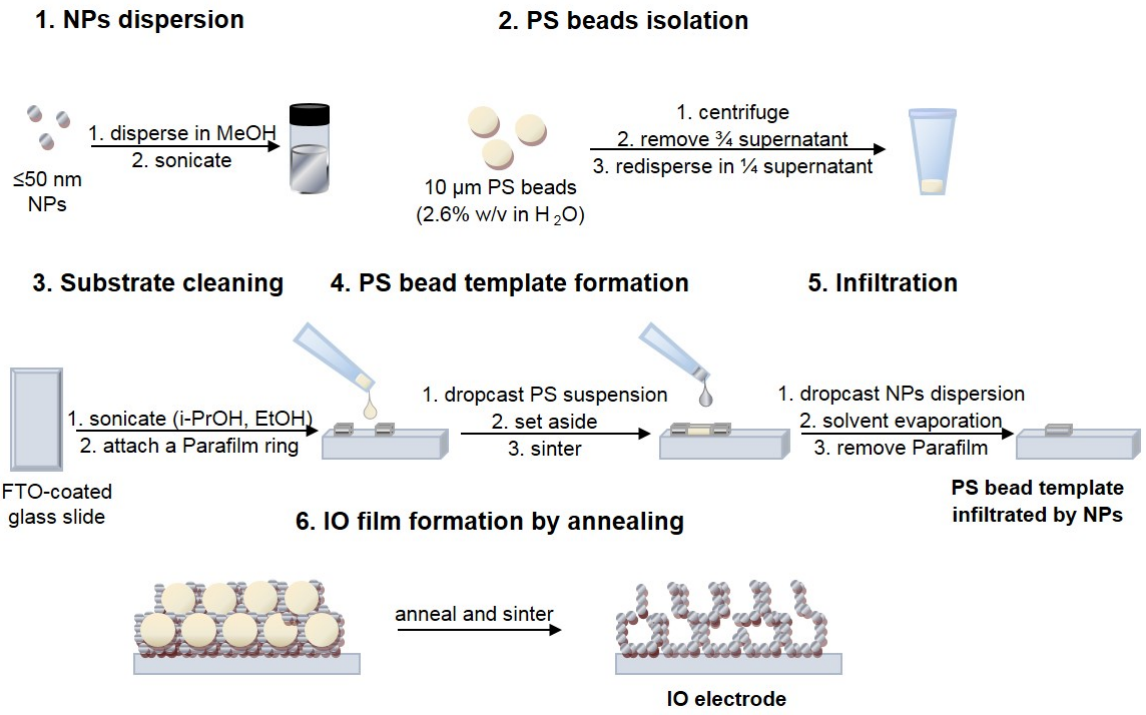

Figure 2.4 **General scheme of the IO-mesoporous electrode preparation by the infiltration method.**

Fig. A.2). Increasing the MeOH ratio led to increased film uniformity due to low wetting angle and surface tension, [9] but also resulted in higher PS bead template disorder and poorer interconnections (Fig. A.2). When the deposition temperature was increased, the interconnections were only slightly more pronounced and the ITO NPs overlayer appeared, due to faster solvent evaporation (low boiling point of MeOH) and more disordered co-assembly formation. [9] Increasing the H_2O ratio increased PS bead self-assembly order, but decreased the overall film uniformity and was accompanied by the accumulation of ITO NPs overlayer at the electrode edge (Fig. A.2). This effect was attributed to high wetting angle and adhesion between the dispersive medium (strong capillary forces and high surface tension of H_2O) and the inner side of a template confining the electrode surface. Further excess of H_2O ratio or rise of deposition temperature resulted in structure shattering, explained by enhanced evaporative self-assembly formation until the stress-induced cracking occurred over larger lateral dimensions. [7]

Deposition and evaporation of a drop-cast PS−NPs precursor suspension at room temperature (20 °C) resulted in the best and most stable film morphology (Fig. A.2). Elevated evaporation temperatures gave rise to increased structure disorder, less pronounced interconnections and overlayer formation, due to increased entropy of the system. On the other

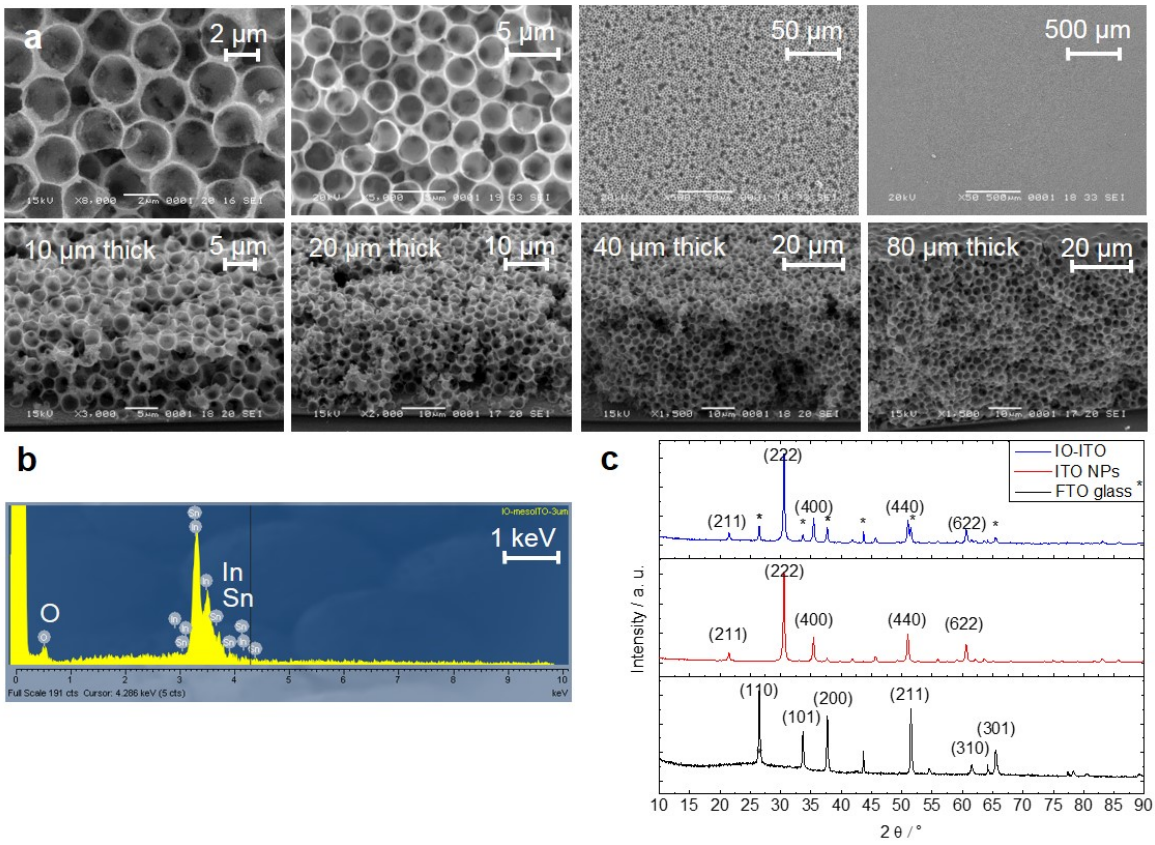

Figure 2.5 **Physical characterisation of the 3 μm pore diameter IO-ITO electrode. a**, SEM top view images (top) and cross-sections (bottom) of films with the thickness of 10, 20, 40 and 80 μm recorded at 60° tilt angle. **b**, EDX elemental analysis of the electrode. **c**, PXRD pattern of the electrode material compared to the matrix material ITO NPs before the annealing and the FTO glass substrate.

hand, higher order, but also associated higher extent of cracking and shattering of the IO structure was observed at lower evaporation temperature. [10] The relative concentration of [ITO NPs]:[PS beads] was systematically varied (Fig. A.3) until the optimum ratio of 1.35:1 by mass was found, giving the most stable IO framework with no overlayer formation or structural collapse due to either an excess or deficiency of ITO NPs, respectively.

As the ITO NPs ($In_{1.86}Sn_{0.105}O_3$, 90% In_2O_3 and 10% SnO_2) used as a matrix material were provided by a commercial supplier, the theoretical initial composition corresponded to 78.00% In, 17.52% O and 4.48% Sn by weight. The energy dispersive X-ray (EDX) spectroscopy elemental analysis (Fig. 2.5b) revealed a composition of 76.55% In, 18.03% O and 5.42% Sn by weight, suggesting no significant changes after ITO NPs annealing. The powder X-ray diffraction (PXRD) pattern analysis of the electrodes (Fig. 2.5c) confirmed relatively pure and crystalline single-phase $In_{1.84}Sn_{0.12}O_3$ solid solution of cubic bixbyite type structure and the la 3 space group. [11] Cleaning of the IO-ITO electrodes via UV-ozone treatment to enhance surface hydrophilicity resulted in no further composition changes.

10 μm pore diameter ITO-IO

When the IO-ITO macropore diameter was increased to 10 μm, the co-assembly method was demontrated to generate poor IO electrode morphology (Fig. A.4). On the other hand, the infiltration method was more effective in generating multilayered IO assembly (Fig. A.5), due to fast sedimentation of large PS spheres and more effective infiltration of bigger interstitials within the PS beads template. Electrode morphology was characterised by the SEM (Fig. 2.6a), with the pore and channel diameter of 10 μm and 3 μm, respectively.

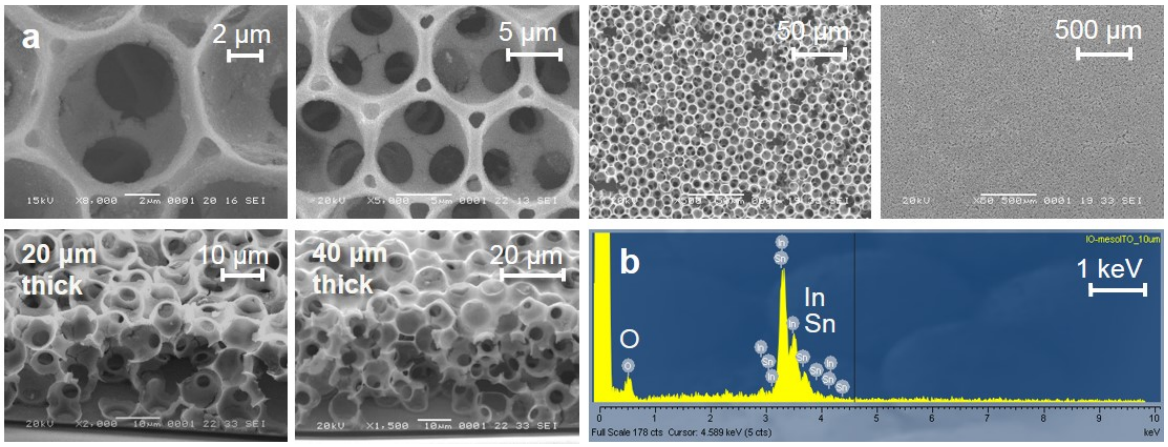

Figure 2.6 **Physical characterisation of the 10 μm pore diameter IO-ITO electrode. a**, SEM top view images (top) and cross-sections (bottom) of films with the thickness of 20 and 40 μm recorded at 60° tilt angle and **b**, EDX elemental analysis of the electrode.

The PS beads were supplied in de-ionised water with residual anionic surfactant ($\leq 0.1\%$ sodium dodecyl sulphate) stabilising the colloidal dispersion. To avoid aggregate formation, the PS spheres were used in an aqueous medium provided, without any further purification. To obtain the most uniform template, initial PS beads suspension was concentrated by four times its initial value by centrifugation, deposited on a substrate, set aside to settle and sediment for minimum 30 min, and partially sintered at 90 °C for 5 min. Pure MeOH used as a dispersive medium resulted in the most homogeneous ITO NPs suspension (Fig. A.5). The desired interconnection size could be tuned by varying the sintering temperature between 70 °C and 130 °C (Fig. A.6), above which a partial decomposition of PS beads was observed. Deposition and solvent evaporation at room temperature (20 °C) under the cover allowed slow infiltration by the matrix material dispersion with no overlayer and minimised defect and colloid vacancy formation (Fig. A.7).

The optimum ratio of [ITO NPs]:[PS beads] was determined as 1.40:1 by mass (Fig. A.8). The IO-ITO film thickness could be tuned between 20 and 40 μm by adjusting deposited PS suspension volume, represented in Fig. 2.6a. At higher thicknesses the electrode was found to be increasingly unstable with many larger cracks and partially peeled off the substrate. The EDX elemental analysis (Fig. 2.6b) confirmed the composition of 72.71% In, 21.20% O and 6.09% Sn by weight, suggesting no significant changes after ITO NPs annealing. The PXRD characterisation resulted in the same pattern as in Fig. 2.5c.

2.2.3 Morphology tuning: mesoporosity

The function of mesoporous features of the IO-ITO electrode is to increase the effective surface area and aid enzyme binding. Depending on the protein size, further electrode structure optimisation could lead to the maximisation of guest species loading. Here, a range of IO-ITO electrodes with various size of mesoporous features was fabricated (Fig. 2.7a) for the future study of the enzyme integration dependence on the mesopore size.

To vary the mesostructure, a range of monodispersed ITO NPs with average diameters of 10 nm, 20 nm and 40 nm (Fig. 2.7b) was synthesised using a simple hydrothermal method, and compared to the previously used commercially-available polydispersed ≤ 50 nm ITO NPs (Sigma Aldrich). The PXRD characterisation (Fig. 2.7c) of the synthesised monodispersed ITO NPs resulted in the same pattern as for the commercial polydispersed ITO NPs, confirming high purity and crystallinity single-phase $In_{1.84}Sn_{0.12}O_3$ of cubic bixbyite structure.

The IO-ITO electrodes fabricated using 0.75 μm PS beads and the above set of ITO NPs, show different mesoporosity on their scaffolds (Fig. 2.7a). All the electrodes were optimised to have a controlled film thickness of 20 μm. The IO-ITO electrode made of 10 nm ITO

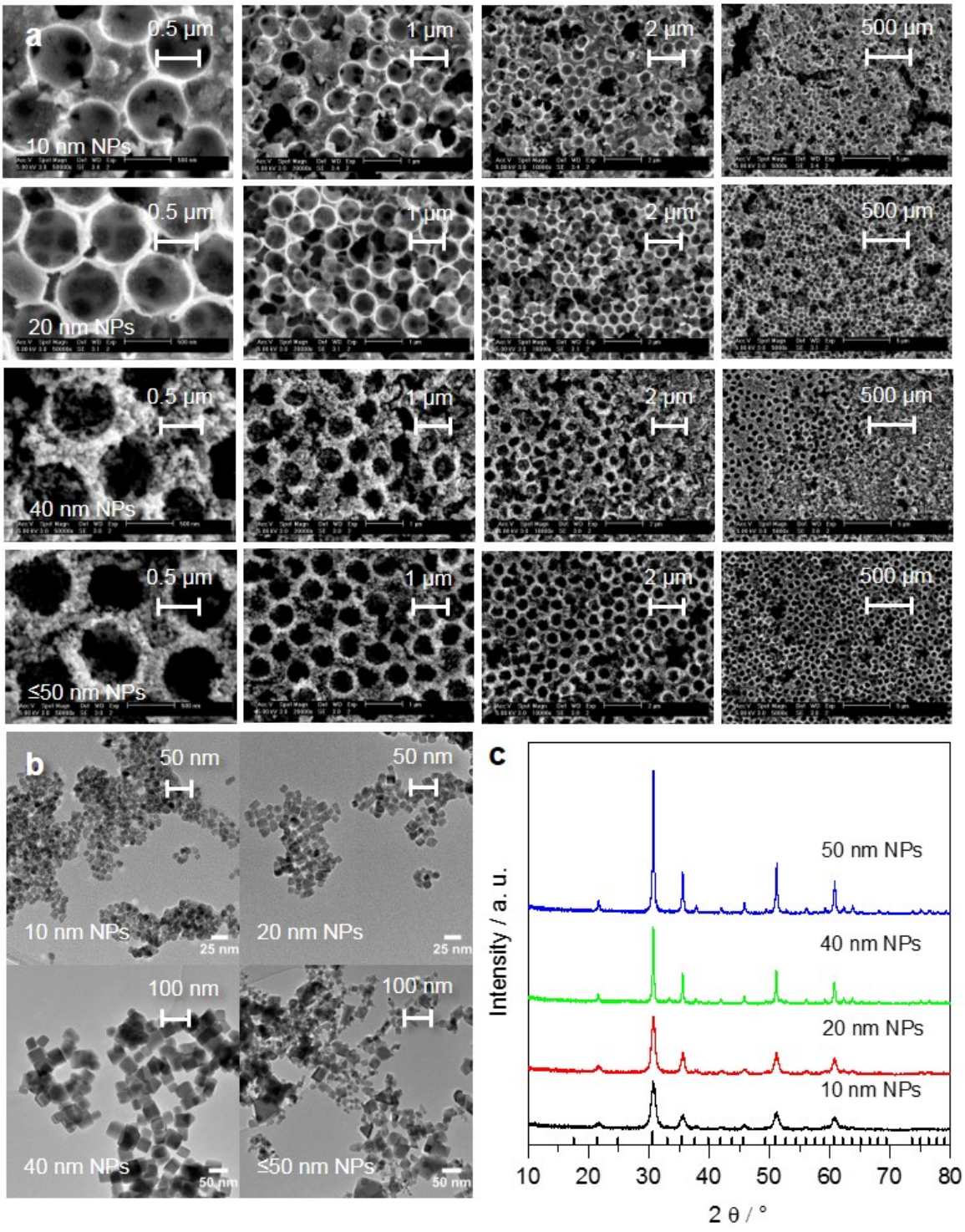

Figure 2.7 **Physical characterisation of the IO-ITO electrode assembled using 10, 20, 40 and $\leq$ 50 nm diameter ITO NPs. a**, SEM top view images of the IO-ITO electrodes using monodispersed 10 nm (top row), 20 nm (second row), 40 nm (third row) and polydispersed $\leq$ 50 nm diameter ITO NPs (forth row). **b**, TEM images of the constituent 10, 20, 40 and $\leq$ 50 nm diameter ITO NPs. TEM recorded by Dr. Tarek Kandiel. **c**, PXRD pattern of the constituent 10, 20, 40 and $\leq$ 50 nm diameter ITO NPs.

NPs was largely smooth, whereas the structure based on 20 nm ITO NPs showed increasing roughness. The 40 nm ITO NPs and $\leq$ 50 nm ITO NPs based electrodes have a distinct granular texture with large cavities (Fig. 2.7a). Those electrodes show an increasing size of macroporous features, from 10 nm to 50 nm, in agreement with the ITO NPs used as a building block, respectively. The low-resolution SEM images of IO-ITO electrodes show a relatively uniform surface, with the homogeneity and crack-free areas increasing from 10 nm ITO NPs to $\leq$ 50 nm ITO NPs based electrodes. The $\leq$ 50 nm ITO NPs IO-ITO exhibited the most homogeneous, robust and ordered morphology, which can be justified by the polydispersity of ITO NPs with various diameters that filled in the PS bead template voids more effectively.

2.2.4 Morphology tuning: material

0.75 μm pore diameter IO-TiO_2

The IO-TiO_2 electrode with 0.75 μm pore diameter was also developed for the future design of the dye-sensitised tandem PSII−dye photoanode, inspired by previously reported immobilisation of chromophores with PSII on TiO_2 electrodes. [12] The optimised IO-TiO_2 electrode was characterised by SEM (Fig. 2.8a), with pore and channel diameter of 750 nm and 150 nm, respectively.

The best solvent for the P25-TiO_2 NPs colloidal suspension was found to be the H_2O/MeOH mixture (4:1 v/v ratio) (Fig. A.9 and Fig. A.10), which was attributed to the hydrophilic nature of the metal oxide NP surface, due to the likely presence of the -O-H^+ sites. The presence of MeOH in the dispersive medium helped to achieve more homogeneous PS−NPs suspension and uniform IO-TiO_2 films. The most stable and crack-free electrode morphology was obtained by the deposition and evaporation of a PS−NPs precursor at room temperature (20 °C). The optimum relative concentration of the [TiO_2 NPs]:[PS beads] was determined as 0.75:1 by mass (Fig. A.11). Tuneable IO-Ti_2 film thickness between 2 μm and 80 μm (corresponding to 107 PS layers) could be achieved, as shown by the SEM (Fig. 2.8a). The EDX elemental analysis (Fig. 2.8b) confirmed the composition of 56.59% Ti and 43.41% O by weight. The P25-TiO_2 NPs were provided by a commercial supplier and the theoretical initial composition corresponded to 59.95% Ti and 40.05% O by weight, suggesting no significant changes after NPs annealing. The PXRD characterisation of the electrodes (Fig. 2.8c) confirmed crystalline TiO_2 of a major phase tetragonal anatase type structure and the $I4_1$/amd space group. [13]

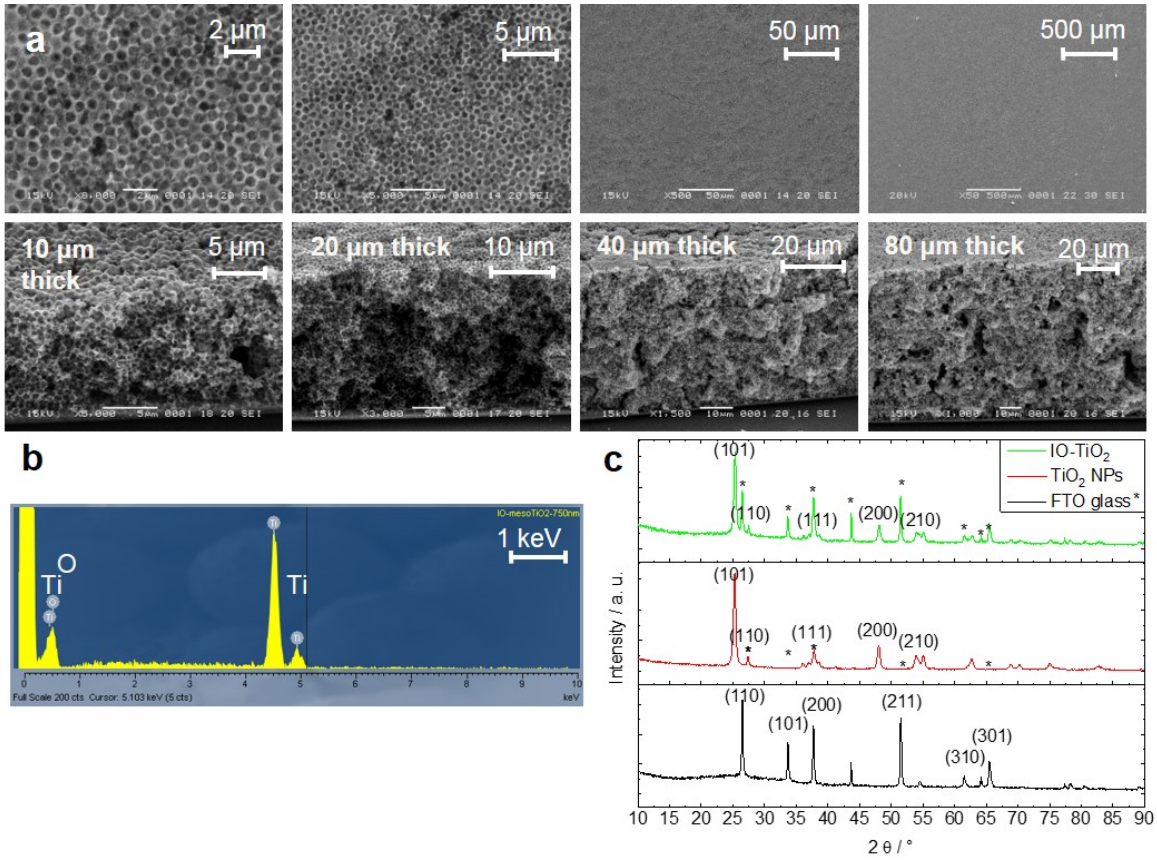

Figure 2.8 **Physical characterisation of the 0.75 μm pore diameter IO-TiO_2 electrode.** **a**, SEM top view images (top) and cross-sections (bottom) of films with the thickness of 10, 20, 40 and 80 μm recorded at 60° tilt angle. **b**, EDX elemental analysis of the electrode. **c**, PXRD pattern of the electrode material compared to the matrix material P25 TiO_2 NPs before the annealing and the FTO glass substrate.

2.2.5 Summary

Here, in *Chapter 2*, the tuneability and versatility of hierarchically-structured IO electrodes was demonstrated and new types of IO electrodes were developed for the subsequent studies. The co-assembly and infiltration methods were explored to tune the macroporosity of IO-ITO electrodes by changing the PS bead template, giving rise to 3 μm and 10 μm pore diameter architectures (Fig. 2.9a). The IO-ITO mesporosity was tuned by employing various size monodispersed ITO NPs (Fig. 2.9b). Fabrication of the 0.75 μm pore diameter IO-TiO_2 electrode introduced a stable cost-effective material (Fig. 2.9c). The thickness of all electrodes was easily adjusted with the multiple PS−NPs deposition cycles. The IO electrodes were characterised by the SEM, EDX and PXRD.

2.3 Conclusions

In this work, new types of hierarchically-structured meso-macroporous IO-ITO and IO-TiO_2 electrodes with different macropore and channel sizes, tuneable film thickness and mesoporous features were developed and optimised via a simple bottom-up colloidal co-assembly method. The most effective fabrication route was found to be dependent on the desired macropore size of the IO structure. Developed IO-ITO electrodes were found to be a versatile platform for the incorporation of various dimension guest species, demonstrated by deployment of designed electrodes in the subsequently developed PF-PEC systems, using a variety of enzymes, including PSII (*Chapter 3-5*) H_2ase (*Chapter 4*) and FDH (*Chapter 5*), as well as redox polymers (*Chapter 3-5*) and photosynthetic cells. This study provides tools that enable to move towards better control over electrode architectures. The systematic approach enables to find correlation between the host electrode architecture and biological guest dimensions.

2.4 Experimental section

2.4.1 Materials

All chemicals ethylene glycol (99% Fischer Chemical), NaOH (Sigma Aldrich), anhydrous $InCl_3$ (99.99% trace metals basis, Sigma Aldrich), $SnCl_4{\cdot}5H_2O$ (98%, Sigma Aldrich), PS beads (Polysciences, Inc., 750 nm, 3 μm and 10 μm diameter, 2.6% w/v suspension in H_2O), ITO NPs (Sigma Aldrich; $\leq$ 50 nm diameter), P25-TiO_2 NPs (Evonik; 21 nm diameter), FTO-coated glass slides (8 Ω sq^{-1}; Sigma Aldrich) and Parafilm® (Sigma Aldrich) were

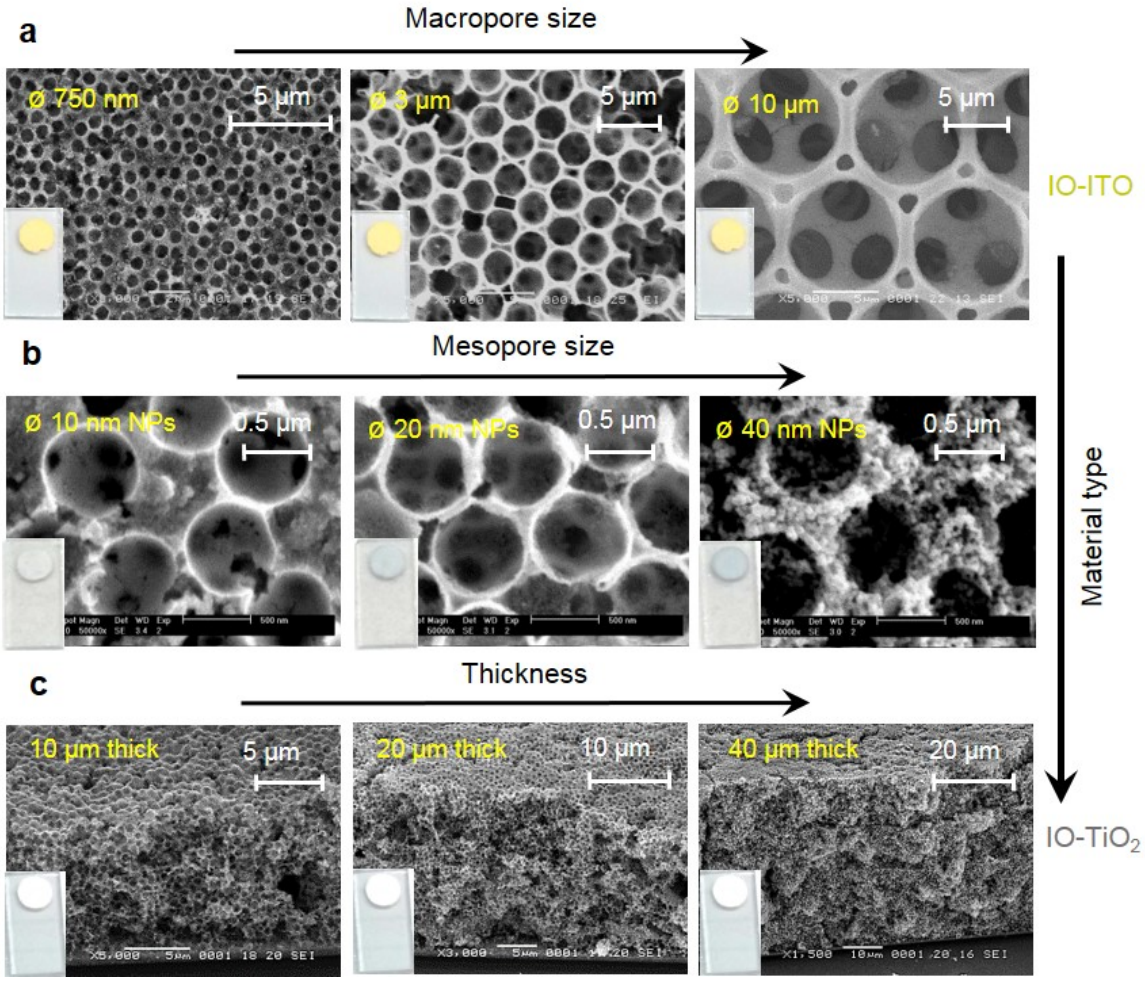

Figure 2.9 **Summary of the morphology tuning of the IO electrode in terms of: macroporosity, mesoporosity, thickness and material. a**, SEM top view images (top row) of the IO-ITO electrodes showing the macropore diameter tuning (0.75, 3 and 10 μm). **b**, SEM top view images (second row) of the IO-ITO electrodes showing the mesoporous feature tuning (10, 20 and 40 nm). **c**, SEM cross-section images (third row) of the IO-TiO_2 electrodes showing the material and thickness tuning (10, 20 and 40 μm). Insets: photographs of assembled IO-ITO and IO-TiO_2 electrodes (geometrical surface area A = 0.25 cm^{-2}) on the FTO-glass substrate (2 x 1 cm) before annealing.

purchased from commercial suppliers and used without further purification unless otherwise noted. Methanol, absolute ethanol, and 2-propanol were purchased from Sigma Aldrich.

2.4.2 Physical characterisation

The surface morphology of the electrodes was analysed by SEM (Philips SFEG XL30; acceleration voltage 5 kV; WD 5 mm) and EDX spectroscopy attached to the SEM. PXRD analysis was carried out using an X-ray diffractometer (X'Pert PRO, PANalytical B.V., The Netherlands). A centrifuge (5804 Eppendorf), furnace (ELF 11/14B/301, Carbolite), ultrasonicator (DT102H, Sonorex Digitec, Bandelin, Monmouth Scientific) and UV/Ozone cleaner (ProCleaner Plus, BioForce Nanosciences) were used for electrode preparation.

2.4.3 Synthesis of monodispersed ITO NPs

The monodisperse ITO NPs were synthesised by a solvothermal method. [14, 15] Typically, anhydrous $InCl_3$ (4.5 mmol) and $SnCl_4 \cdot 5H_2O$ (0.5 mmol) were dissolved in ethylene glycol (4 mL). To this mixture, a NaOH solution in ethylene glycol (2.5 M, 6 mL) was added under continuous stirring at 0 °C. The final NaOH concentration was 1.5 M. After 15 min of stirring, the suspension was transferred into a Teflon-lined autoclave and heated at 250 °C for 12 h to obtain ITO NPs with an average size of 10 nm or for 96 h to obtain 20 nm ITO NPs. After cooling to room temperature, the product was washed three times with ethanol and twice with water/ethanol mixture (50% v/v) then once with acetone and dried under vacuum at room temperature. For 40 nm ITO nanoparticles, the same recipe was used except that NaOH concentration was adjusted to be 1.0 M and the annealing time was 96 h.

2.4.4 Preparation of IO electrodes

FTO-coated glass substrates (2 x 1 cm) were cleaned by sonication in two 30 min steps in 2-propanol and absolute ethanol, and subsequently stored at 150 °C. A Parafilm ring (diameter, $\varnothing$ = 0.56 cm) was placed onto the FTO substrate to define the geometrical surface area of 0.25 cm^2 for the IO-ITO/TiO_2 films.

2.4.5 Co-assembly method

IO-ITO electrodes

A mixed dispersion of ITO NPs and PS beads was prepared as follows: ITO NPs (35 mg) were sonicated for 3 h in a MeOH:H_2O mixture (300 μL; 6:1 or 10:1 v/v for 750 nm or 3

μm pore size, respectively). The PS beads suspension (1 mL) was centrifuged (10,000 r.p.m., 3 min) and the supernatant was removed. The PS beads precipitate was then re-dispersed in MeOH (1 mL), followed by centrifugation (10,000 r.p.m., 0.5 min) and extraction of the supernatant. The NPs dispersion (300 μL) was added to the PS beads precipitate and sonicated in water (< 10 °C) for 10 min until a homogeneous PS−NPs precursor dispersion was obtained. The as-prepared PS−NPs precursor dispersion was dropcast (5 μL) at room temperature (RT) onto the pre-defined area on the FTO substrate, resulting in a 12 μm thick film. The volume of the drop-cast precursor dispersion could be adjusted depending on the desired film thickness. After solvent evaporation, the electrodes were annealed at a 1 °C min^{-1} ramp rate from RT to 500 °C and then sintered for 20 min. The IO-ITO electrodes were cleaned using an UV/Ozone cleaner to ensure a contamination-free hydrophilic electrode surface for improved enzyme adsorption prior the PEC experiments. [4]

IO-TiO_2 electrodes

A mixed dispersion of P25-TiO_2 NPs and PS beads was prepared as follows: TiO_2 NPs (30 mg) were sonicated for 3 h in a MeOH:H_2O mixture (300 μL; 1:4 v/v). The PS beads suspension (1 mL) was isolated and washed as described above for the IO-ITO electrodes. The NPs dispersion (180 μL) was added to the PS beads precipitate and the same procedure as described in the section above was followed. The PS−NPs precursor dispersion drop-casting (5 μL, RT) onto the pre-defined area on the FTO substrate resulted in a 20 μm thick film.

2.4.6 Infiltration method

A PS beads template was prepared as follows: the PS beads suspension (1 mL) was centrifuged (10,000 r.p.m., 3 min) and concentrated by four times its initial value by removing $\frac{3}{4}$ of the supernatant (750 μL). The as-prepared PS beads solution was drop-cast (5 μL, RT) onto the FTO substrate, set aside to settle (RT, 30 min) and sintered (90 °C, 5 min), resulting in a 12 μm thick film. The volume of the drop-cast PS beads dispersion could be adjusted depending on the desired film thickness. ITO NPs (35 mg) were sonicated for 3 h in MeOH (300 μL). The as-prepared ITO NPs dispersion was drop-cast (6.25 μL, RT) onto the as-prepared PS beads template and slowly evaporated (RT) under the Petri dish cover. After solvent evaporation, the electrodes were annealed and cleaned using the same procedure as described above for the IO-ITO electrodes.

References

(1) K. R. Phillips, G. T. England, S. Sunny, E. Shirman, T. Shirman, N. Vogel and J. Aizenberg, *Chem. Soc. Rev.*, 2016, **45**, 281–322.

(2) Y. Li, Z.-Y. Fu and B.-L. Su, *Adv. Funct. Mater.*, 2012, **22**, 4634–4667.

(3) P. Trogadas, V. Ramani, P. Strasser, T. F. Fuller and M.-O. Coppens, *Angew. Chem. Int. Ed.*, 2015, **54**, 2–29.

(4) D. Mersch, C.-Y. Lee, J. Z. Zhang, K. Brinkert, J. C. Fontecilla-Camps, A. W. Rutherford and E. Reisner, *J. Am. Chem. Soc.*, 2015, **137**, 8541–8549.

(5) A. Stein, *Microporous Mesoporous Mater.*, 2001, **44-45**, 227–239.

(6) V. Guliants, M. Carreon and Y. Lin, *J. Memb. Sci.*, 2004, **235**, 53–72.

(7) B. Hatton, L. Mishchenko, S. Davis, K. H. Sandhage and J. Aizenberg, *Proc. Natl. Acad. Sci. U. S. A.*, 2010, **107**, 10354–10359.

(8) P. N. Pusey and W. van Megen, *Nature*, 1986, **320**, 340–342.

(9) K. Sefiane, S. David and M. E. R. Shanahan, *J. Phys. Chem. B*, 2008, **112**, 11317–11323.

(10) S. Rakers, L. F. Chi and H. Fuchs, *Languir*, 1997, **13**, 7121–7124.

(11) N. Nadaud, N. Lequeux, M. Nanot, J. Jové and T. Roisnel, *J. Solid State Chem.*, 1998, **135**, 140–148.

(12) K. K. Rao, D. O. Hall, N. Vlachopoulos, M. Grätzel, M. C. W. Evans and M. Seibert, *J. Photochem. Photobiol. B*, 1990, **5**, 379–389.

(13) W. Li, C. Ni, H. Lin, C. P. Huang and S. I. Shah, *J. Appl. Phys.*, 2004, **96**, 6663–6668.

(14) Y. Endo, T. Sasaki, K. Kanie and A. Muramatsu, *Chem. Lett.*, 2008, **37**, 1278–1279.

(15) T. Sasaki, Y. Endo, M. Nakaya, K. Kanie, A. Nagatomi, K. Tanoue, R. Nakamura and A. Muramatsu, *J. Mater. Chem.*, 2010, **20**, 8153–8157.

Chapter 3

Rational wiring of photosystem II to hierarchical indium tin oxide electrodes using redox polymers

The content of this chapter has been published in a peer-reviewed article: Energy Environ. Sci., 2016, 9, 3698−3709. Results presented were obtained by the author of this thesis except as outlined here: Dr. Adrian Ruff in the group of Prof. Wolfgang Shuhmann at Ruhr-Universität Bochum, Germany is acknowledged for characterising the P_{Os} and P_{Phen} redox polymers by ^{1}H NMR, UV-Vis spectroscopy and DLS.

3.1 Introduction

The immobilisation of photosynthetic proteins onto electrodes is of importance to a range of current and future innovations, including biosensors, [1–3] biophotovoltaic systems [4–7] and photoelectrochemical (PEC) platforms. [8, 9] Photosystem II (PSII) is a photosynthetic enzyme with the ability to photocatalyse water oxidation, a bottleneck reaction in artificial photosynthesis, at theoretical rates of up to 250 mol O_2 (mol PSII monomer)$^{-1}$ s^{-1}. [10, 11] As such, there is considerable interest in the integration of PSII as a guest into electrode scaffolds, [12, 13] in particular to improve our fundamental understanding of the protein function and also in PEC cells for proof-of-principle solar electricity/fuel generation. [14–17]

Several strategies for the integration of PSII into electrodes are currently employed, each with unique advantages. Before these approaches can be discussed, some knowledge of the mechanism behind PSII water oxidation is required. Briefly, light is absorbed by pigments within PSII, and funnelled into the reaction centre complex where charge formation and

separation at the P680 primary electron donor site occurs. The photogenerated electrons are then transferred via pheophytin and plastoquinone A (Q_A) to the terminal electron acceptor plastoquinone B (Q_B), which is located on the stromal side of the enzyme. Holes generated at the P680 are transferred in the lumenal direction, via a redox-active tyrosine side chain (Tyr_Z) to the oxygen-evolving complex (OEC), where water is oxidised to liberate H^+ and O_2. [18, 19] If the PSII is adsorbed in the correct orientation on an electrode, direct electron transfer from the Q_A/Q_B to the electrode can take place. [9, 20] However, a Q_B mimic, such as 2,6-dichloro-1,4-benzoquinone (DCBQ), is typically required as a diffusional mediator between the insufficiently wired PSII and the electrode to substantially enhance photocurrent generation. [19]

A traditional approach for the immobilisation of photosynthetic reaction centres is to align the proteins on chemically-modified electrodes functionalised with linkers such as quinonoid, [21] *N*-hydroxy-succinimidyl ester, [22] nickel nitrilotriacetic acid, [23, 24] cytochrome *c* [25, 26] and carboxylic acid/amino groups. [27] However, the magnitude of the photocurrent is limited by the attachment of a single monolayer of photosynthetic reactions centres that can be assembled on the electrode.

A strategy to enhance the loading of electrically wired PSII onto electrodes is to entrap PSII in a redox-active polymer matrix on an electrode surface. [28, 29] In this approach, PSII of any orientation can in principle be efficiently wired to the electrode by the redox-active moieties that are homogeneously distributed in the matrix, which can mediate charge transfer via an electron hopping mechanism. [30] The benchmark system using this approach consists of a flat gold electrode on which PSII is embedded in an Os complex-based polymer ($E_{1/2}$ = 0.395 - 0.505 V versus the standard hydrogen electrode; vs. SHE). [31] Photocurrents of up to 45 μA cm^{-2} at an applied potential (E_{app}) of 0.5 V vs. SHE were reported for this biophotoanode. Despite its advantages, the performance of this system was limited by the intrinsic properties of the polymeric matrix. Independently of the total loading at the electrode surface, the amount of electroactive enzyme is defined by the rate of charge transfer via electron hopping, which limits the maximum (photo-)electrocatalytic response that can be detected. [32] On modified flat electrodes where enzymes are entrapped in redox polymers, the current generation typically arises from catalysts present within a thin layer (a few micrometer thick) at the electrode/hydrogel interface; the remaining catalysts in the outer layers of the film are electro-inactive and do not contribute to current generation. [33]

An emerging and effective enzyme immobilisation strategy involves the adoption of highly structured electrode morphologies [34–36] to increase the available surface area for enzyme adsorption. [9, 27, 37] In a recent benchmark system, PSII was adsorbed on a hierarchically-structured indium tin oxide (ITO) electrode that incorporated macroporosity

(for enhanced enzyme and substrate penetration) and mesoporosity (to enhance the effective surface area and enzyme anchoring) with high thickness. [9] As a result, a 16,000-fold increase in PSII loading was observed compared to conventional flat electrodes. [6, 31] However, insufficient wiring at the PSII-electrode interface was still apparent, with non-mediated photocurrents of 20 μA cm^{-2} being observed in contrast to 1 mA cm^{-2} in the presence of a freely diffusing mediator. A further limitation of the electrode was poor PSII photostability, with the electrode exhibiting a photocurrent half-life time of only a few minutes.

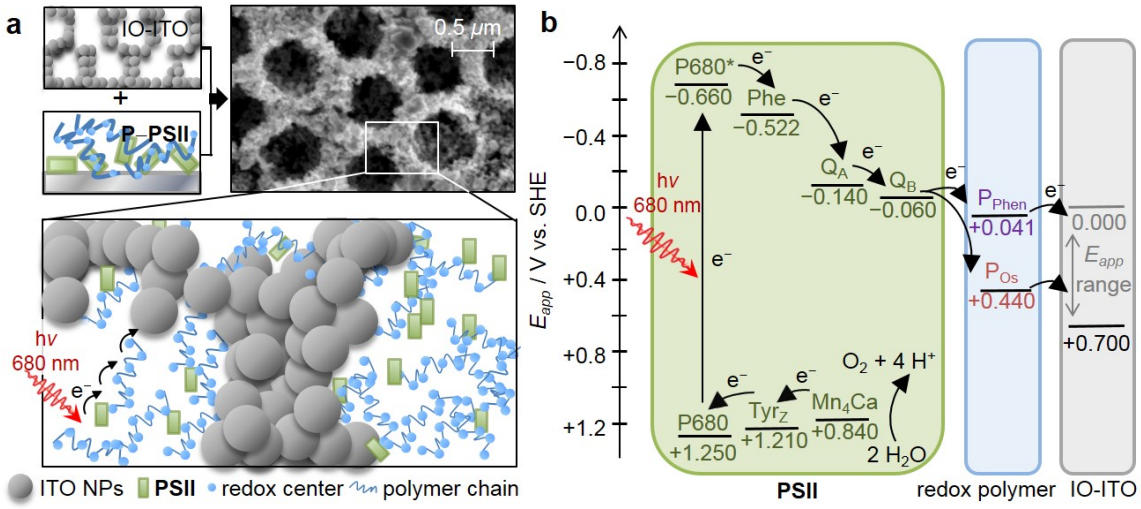

Figure 3.1 **Semi-artificial IO-ITO|polymer−PSII photoanode. a**, Schematic representation of PSII wired via a redox polymer network to a hierarchically-structured IO-ITO electrode (species size not drawn to scale), indicating the electron transfer from photoexcited PSII to the electrode via the redox-active centres. The SEM image of IO-ITO is also shown. **b**, Energy level diagram showing electron transfer pathways between PSII, the redox polymer (P_{Phen} or P_{Os}, at pH 6.5) and the IO-ITO electrode (E_{app} refers to the applied electrochemical potential, which determines the Fermi level at the ITO electrode). Abbreviations: P680, primary electron donor site; Phe, pheophytin; Q_A/Q_B, electron acceptor plastoquinones; Tyr_Z, tyrosine; Mn_4Ca, oxygen-evolving complex. The figure adapted from Sokol et. al., *Energy Environ. Sci.*, 2016, **9**, 3698−3709.

Here, we report a high performing PSII−electrode system that combines the best aspects of two advanced enzyme immobilisation strategies: the use of a redox polymer matrix to enable efficient PSII wiring, and the use of high surface area hierarchically-structured ITO electrodes to enable high loading of both the polymer and the PSII (Fig. 3.1a). The highly structured electrode scaffold increases the polymer−electrode interface and reduces the average charge transfer distance between the PSII and the electrode surface via the polymeric matrix. This enables the wiring of a large population of PSII to the electrode, which

translates to high effective loading. We first compared the performance of two promising redox polymers differing in chemical and redox properties as electron conducting matrices for PSII in inverse opal mesoporous ITO (IO-ITO) electrodes (Fig. 3.1b). We then focused on the optimisation of the lead ITO−polymer−PSII system to ultimately deliver high photocurrents in the absence of diffusional mediators, at an extended operating lifetime.

3.2 Results and discussion

3.2.1 Synthesis and characterisation of IO-ITO and polymers

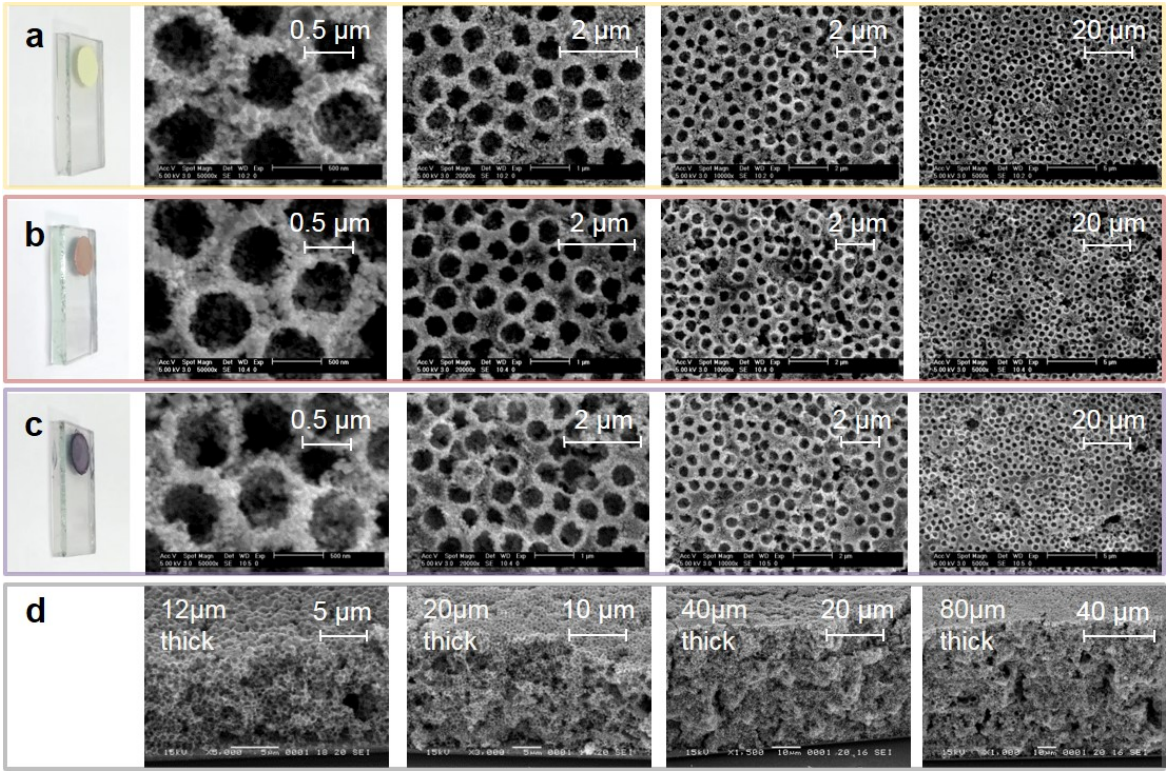

Figure 3.2 **Modified IO-ITO electrode characterisation.** Photographic and scanning electron microscopy (SEM) images of **a**, the unmodified IO-ITO electrode, **b**, IO-ITO|P_{Os}−PSII and **c**, IO-ITO|P_{Phen}−PSII with an IO-ITO film thickness of 20 μm in all cases. The hierarchical ITO morphology stays intact during the integration of PSII and polymer. **d**, Unmodified IO-ITO electrodes with 12, 20, 40 and 80 μm film thickness measured at 60° tilt angle are shown. The figure adapted from Sokol et. al., *Energy Environ. Sci.*, 2016, **9**, 3698−3709.

This study uses a hierarchical IO-ITO electrode, which has previously demonstrated a high loading capacity for the large enzymes, PSII and hydrogenase (Fig. 3.2a). [9] The macropores with diameter of 750 nm and channels of 150 nm are also suitable for the

penetration of macromolecular polymers; the mesopores with a diameter of approximately 50 nm provide a high effective surface area of $\sim 115 \times 10^6$ m^2 m^{-3} for polymer/enzyme adsorption. [9] The tunability of the film thickness (up to 80 μm, Fig. 3.2d) provides extra flexibility in the optimisation of guest loading. The PSII used was isolated from the thermophilic cyanobacterium *Thermosynechococcus elongatus* given that cyanobacterial PSII is relatively well characterised, [38–40] and it exhibits high activity and relative robustness. [41, 42]

The polymers chosen for this study include the Os complex-modified polymer (1-vinylimidazole-*co*-allylamine)-[Os(bpy)$_2$Cl]Cl (P_{Os}) (Fig. 3.3a), which has demonstrated effective integration of PSII on flat electrodes; [31] and the purely organic phenothiazine-modified polymer (P_{Phen}, phenothiazine moiety = toluidine blue) (Fig. 3.3b), which has a better matched redox potential with the Q_A/Q_B cofactors and has also demonstrated favourable wiring of PSII to flat electrodes. [6] Both polymers are compatible with PSII and are stable under the acidic pH conditions for photocurrent measurements. [6, 43] The chemical structure, purity and size of the polymers were confirmed by ^{1}H NMR (Fig. B.1), UV-vis spectroscopy (Fig. B.2) and dynamic light scattering (DLS, Fig. B.3), respectively. The ^{1}H NMR spectra of the polymer backbones correspond to the expected structure (Fig. B.1). Based on the integral ratio between methyl groups of terminal isopropyl units and the intra-chain imidazole unit, as well as the two signals assigned to the polymer chain, a molecular weight of $\sim 26 \pm 3$ kDa was estimated for the P_{Os} backbone. For the backbone of the P_{Phen} polymer, analysis of the molecular weight via NMR spectroscopy was not possible due to overlapping signals in the spectrum of the backbone.

The total number of Os complexes in P_{Os} was quantified using UV-vis spectroscopy in dimethyl sulfoxide (DMSO) (0.74 ± 0.04 mmol g^{-1} polymer, Fig. B.2), which is consistent with inductively-coupled plasma atomic emission spectroscopy (ICP-AES) measurements (0.67 ± 0.05 mmol Os g^{-1} polymer). *Cis*-[Os^{II}Cl(1-(*n*-butyl)-imidazole)(bipy)$_2$](PF$_6$) (Fig. B.2c), which can be regarded as the freely diffusing analogue to the Os complex moiety in the P_{Os}, was used as a reference for characterisation by UV-vis spectroscopy. The spectrum of the freely diffusing complex and the polymer exhibit the same spectral features (Fig. B.2a). Thus, for the calculation of the total number of Os complexes within the polymer, we assume that both species exhibit the same extinction coefficients. From the UV-vis studies, the ratio of non-complexed imidazole units to Os complex moieties was calculated to be ~7:1, which corresponds to a molecular weight of $\sim 44 \pm 5$ kDa for P_{Os}. The same analysis was performed with the freely diffusing toluidine blue (Fig. B.2c) and P_{Phen}. The spectral shapes of both species are again similar (Fig. B.2d), but the extinction coefficient of the toluidine blue moiety is increased upon covalent attachment to the polymer backbone (the primary

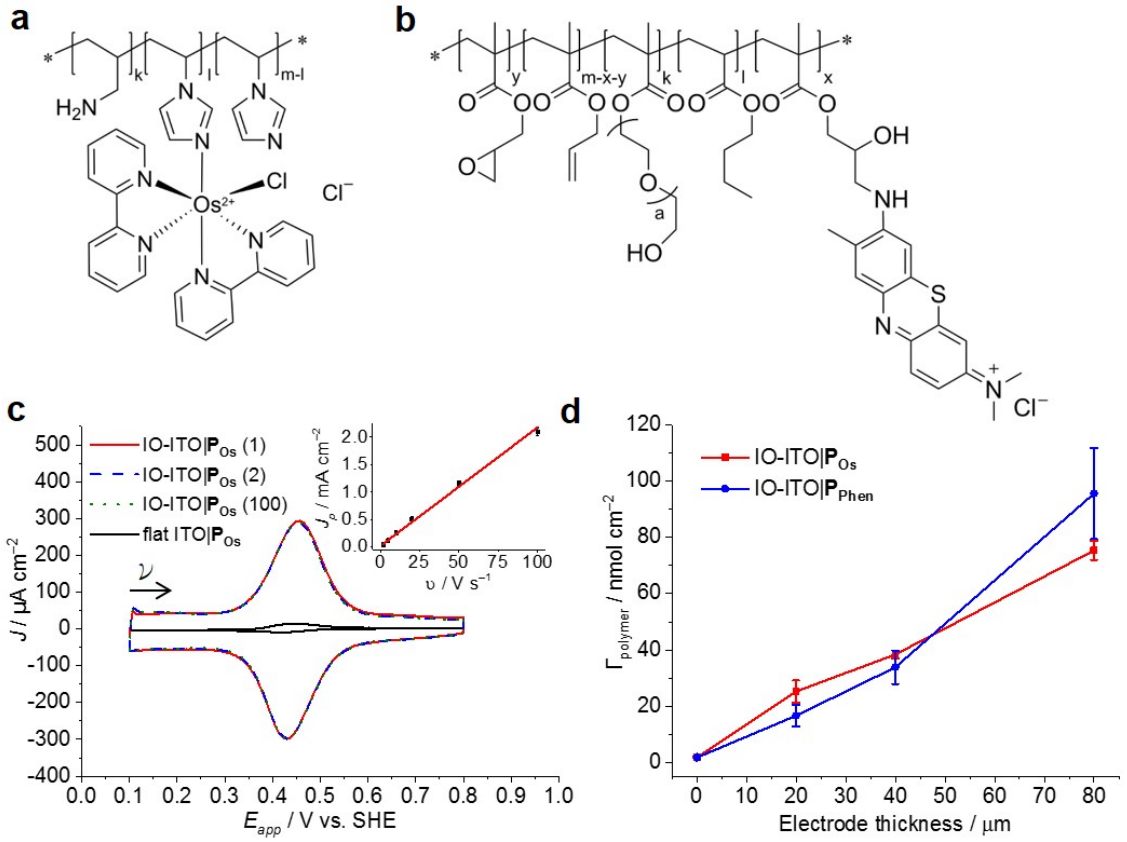

Figure 3.3 **Redox polymer electrochemical characterisation.** **a**, Chemical structures of the P_{Os} and **b**, P_{Phen} polymers. **c**, Cyclic voltametry (CV) scans of P_{Os} adsorbed on 20 μm thick IO-ITO (adsorbed 25 $\pm$ 4 nmol Os cm^{-2}) showing high stability on the electrode surface. The first scan (red solid trace) and the 100th scan (dark green dotted trace; dark, 10 mV s^{-1}) are shown. The second scan (blue dashed trace) was the only scan measured during irradiation (λ = 685 nm; E_e = 10 mW cm^{-2}). A CV scan with P_{Os}-modified flat ITO (black solid trace; dark, 10 mV s^{-1}) is shown for comparison (adsorbed 1.7 $\pm$ 0.2 nmol Os cm^{-2}). The inset shows a linear dependence of the peak current density J_p with the scan rate ν, confirming electron transfer of a surface-confined redox species. **d**, Linear dependence of the redox-active centres loading for both polymers P_{Os} and P_{Phen} (up to 75 $\pm$ 3 and 96 $\pm$ 16 nmol cm^{-2}, respectively) with the electrode thickness. The error bars correspond to the standard deviation (N = 4). Conditions: MES electrolyte solution (pH = 6.5, T = 25 °C). The figure adapted from Sokol et. al., *Energy Environ. Sci.*, 2016, **9**, 3698−3709.

amine in the toluidine blue monomer is converted to a secondary or even to a tertiary amine upon reaction with the epoxide functionality of the polymer backbone of P_{Phen}). Thus, the estimation of the exact number of toluidine blue species was not possible (calculated values exceed the theoretical values).

The hydrodynamic particle diameter of P_{Os} and P_{Phen} was determined using DLS (Fig. B.3) to be 16 $\pm$ 1 nm and $\sim$500 nm (broad distribution), respectively, which indicate the agglomeration of smaller polymer chains. Since both polymer solutions were filtered through a membrane with 200 nm pore size, it was concluded that the P_{Phen} polymer chains form weak agglomerates that can be easily disassembled. The estimated sizes and agglomeration properties of P_{Os} and P_{Phen} are expected to allow them to enter into the IO-ITO structure either by diffusional transport or by convection due to the capillary forces induced by pore filling and H_2O evaporation.

3.2.2 Integration of PSII and polymer into IO-ITO electrodes

To optimise the assembly of a IO-ITO|polymer−PSII electrodes the initial screening of polymer−PSII deposition method, IO-ITO electrode macropore diameter, polymer−PSII concentration ratio and polymer−PSII incubation time was conducted. The co-deposition method (1-step deposition of polymer−PSII mixture/blend) was found more effective than 2-step deposition methods (polymer deposition followed by PSII and PSII deposition followed by polymer) for both, IO-ITO|P_{Os}−PSII and IO-ITO|P_{Phen}−PSII (Fig. B.4). The optimal polymer−PSII ratio was found to be 1 μL polymer (10 mg mL^{-1}) to 1 μL PSII (2.6 mg mL^{-1} Chl *a*) for both IO-ITO|P_{Os}−PSII (Fig. B.5) and IO-ITO|P_{Phen}−PSII (Fig. B.6). The 0.75 μm macropore electrode entrapped more polymer−PSII blend and generated higher photocurrents than 3 μm and 10 μm macropore IO-ITO electrodes and was used in this study (Fig. B.5 and Fig. B.6). Lastly, the polymer−PSII blend incubation/drying time screening showed that 15 min was sufficient to obtain optimal photocurrent generation at high PSII loading (Fig. B.7).

The polymers (1 μL, 10 mg mL^{-1}) were drop-cast onto the IO-ITO and allowed to adsorb for 15 min at room temperature. The redox properties of the adsorbed polymers on the IO-ITO electrode (IO-ITO|polymer) were characterised using cyclic voltammetry (CV; Fig. 3.3 and Fig. 3.4). The redox waves of P_{Os} and P_{Phen} were attributed to the $Os^{3+/2+}$ ($1e^-$ transfer process) and $Phen^+$/PhenH ($2e^-/H^+$ transfer) redox couples, respectively. [6] The positive reduction potential of the P_{Os} polymer ($E_{1/2}$ = 0.44 V vs. SHE) is expected to provide a large driving force for electron transfer from the Q_A and Q_B ($E_{1/2}$ = −0.14 V and −0.06 V vs. SHE, respectively) [19] to the redox centres of the polymer (Fig. 3.1b). However, electron transfer between Q_A/Q_B and the Os complexes results also in a substantial potential

loss (>0.4 V). [5] The P_{Phen} hydrogel exhibits a less positive reduction potential ($E_{1/2}$ = 0.04 V vs. SHE), which matches the Q_B more closely (Fig. 3.1b). The reversibility of the electron transfer process for the surface-adsorbed redox polymers is evident in the almost symmetrical shape in the CV scans of P_{Os} and P_{Phen}, which show minimal peak separation between the oxidation and reduction potentials (ΔE_p = 0.02 ± 0.01 and 0.01 ± 0.005 V for P_{Os} and P_{Phen}, respectively). Furthermore, an anodic to cathodic peak current ratio close to unity (I_{pa}/I_{pc} = 0.97 and 0.83 for P_{Os} and P_{Phen}, respectively) can be observed, and the current density is linearly proportional to the scan rate up to 100 mV s^{-1} (Fig. 3.3c inset and Fig. 3.4). [44] The observed slight increase in the ΔE_p at scan rates > 10 mV s^{-1} (Fig. 3.4) was attributed to the rate limiting charge transfer between the polymer and the electrode surface. [45] In particular, P_{Phen} showed small shoulder waves at high scan rates that could arise from the slow $2e^-/H^+$ transfer rate at the iminium cation site. The voltammetric features of P_{Os}, even at the relatively fast scan rates used here, are characteristic for surface-confined species. The corresponding diffusion layer thicknesses of the electron (δ, calculated from Eq. 3.1) give an estimate of the film thickness that is accessible to the electrochemical process assuming planar semi-infinite diffusion. Based on the previously reported apparent electron diffusion coefficient of the electron for P_{Os} (D_e of 4.00 ± 0.47 × 10^{-9} cm^2 s^{-1}) [43] the δ value corresponding to the scan rate of 100 mV s^{-1} is 320 nm. Hence, the diffusional range of the electrons within P_{Os} is in the range of the IO macropore radius (375 nm; Fig. 3.2a) even at fast scan rates. As such, the IO structure should increase the total polymer loading that can participate in electron transfer in a given geometric surface area by taking advantage of the thick 3-D architecture.

No photocurrent originating from the IO-ITO|polymer electrodes during irradiation (λ = 685 nm, E_e = 10 mW cm^{-2}) was observed (Fig. 3.3c). The surface coverage (Γ) of the electrochemically-active redox centres connected to the electrode surface was calculated for each polymer using Eq. 3.2; the total charge was calculated by integrating the area under the CV curve minus the background. A substantial enhancement in polymer loading (Fig. 3.4) was observed for IO-ITO compared to flat electrodes. The polymer loading increased approximately linearly with the electrode thickness (Fig. 3.3d). Loadings of 1.7 ± 0.2 nmol cm^{-2} and 1.7 ± 0.5 nmol cm^{-2} were observed for flat ITO electrodes with the adsorbed polymers, P_{Os} and P_{Phen}, respectively, which is comparable to previously reported values (1.8 ± 0.1 nmol cm^{-2}) on flat glassy carbon electrodes. [43] IO-ITO electrodes with a thickness of 20, 40 and 80 μm gave rise to a 15-, 23- and 45-fold increase in Γ_{Os} (25 ± 4, 38 ± 1 and 75 ± 3 nmol cm^{-2}) and 10-, 19- and 55-fold increase in Γ_{Phen} (17 ± 4, 34 ± 5 and 96 ± 16 nmol cm^{-2}) compared to a flat ITO electrode, respectively (Table. 3.1). The number of electrochemically-active Os complexes on 20 μm thick IO-ITO was found to be ∼85

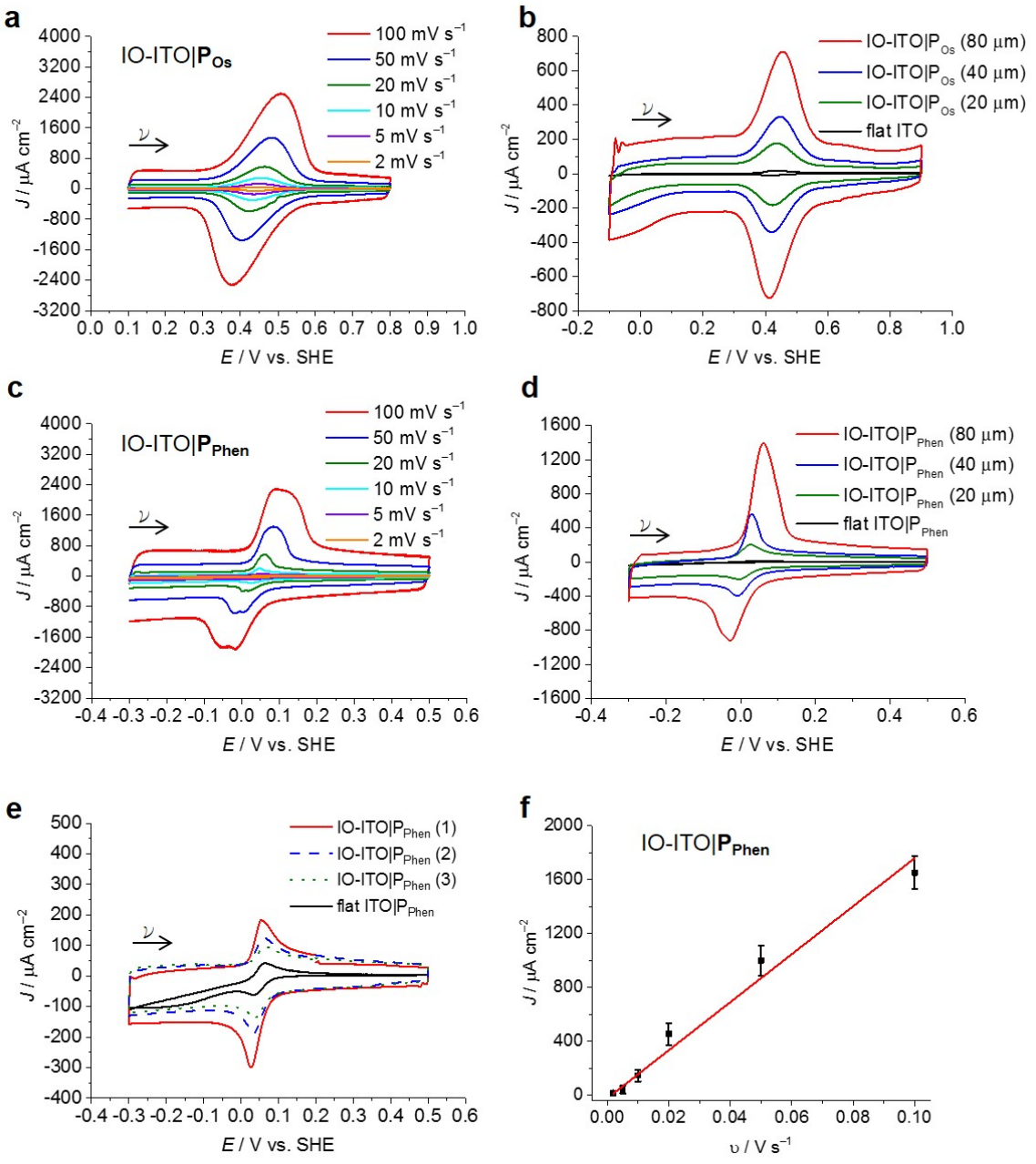

Figure 3.4 **Electrochemical characterisation of the redox hydrogels on IO-ITO electrodes. a**, CV scans of P_{Os} adsorbed on 20 μm thick IO-ITO as a function of the scan rate (ν). **b**, CV scans (ν = 10 mV s^{-1}) with P_{Os} on IO-ITO electrodes with varying thicknesses. **c**, CV scans of P_{Phen} adsorbed on 20 μm thick IO-ITO as a function of ν. **d**, CV scans (ν = 10 mV s^{-1}) with P_{Phen} on IO-ITO electrodes with varying thicknesses. **e**, The first three cycles of CV scans (ν = 10 mV s^{-1}) of P_{Phen} adsorbed on 20 μm thick IO-ITO compared to P_{Phen} on flat ITO. **f**, The linear dependence of the peak current density of IO-ITO|P_{Phen} with ν. The amount of P_{Os} and P_{Phen} (10 μg μL^{-1}) deposited: 1 μL on flat ITO and 1 μL per 20 μm thickness of IO-ITO electrodes. Conditions: MES electrolyte (pH = 6.5, T = 25 °C), no light irradiation. The figure adapted from Sokol et. al., *Energy Environ. Sci.*, 2016, **9**, 3698−3709.

$\pm$ 10% of the total number of immobilised Os atoms, quantified by ICP-AES and UV-vis spectroscopy. The IO-ITO|P_{Os} electrode exhibited high stability, showing no significant desorption or decomposition after 100 CV cycles at 10 mV s^{-1} scan rate (Fig. 3.3c). The IO-ITO|P_{Phen} electrode exhibited lower stability (63% and 38% Γ_{Phen} remaining after the second and third CV cycle at 10 mV s^{-1} scan rate, respectively, Fig. 3.4e). The imidazole functionality in the P_{Os} is also likely to have a strong affinity for the ITO surface and act as an anchoring group, analogous to histidine-tagged enzymes. [46] The toluidine blue centres of the P_{Phen} (heterocyclic N and S atoms pKa < 7) are most likely deprotonated and polymer backbone groups (amine functions pKa > 7) are protonated at pH 6.5. The hydrogel nature of the polymers allows the diffusion of small molecules throughout the network, although the lack of anchoring groups in P_{Phen} prevents stable loading.

Table 3.1 **PF-PEC summary with IO-ITO|polymer−PSII electrodes.**

Electrode thickness / μm	**Polymer−PSII system**	J_{max}	TOF_{PSII}	$\tau_{1/2}$	EQE_{680nm}	Γ_{PSII}	$\Gamma_{polymer}$
		/ μA cm^{-2}	/ mol O_2 (mol PSII)$^{-1}$ s^{-1}	/ min	/ %	/ pmol cm^{-2}	/ nmol cm^{-2}
Flat	PSII	0.011 ± 0.009	n/d	n/d.	0.0002 ± 0.0001	0.064 ± 0.007	n/a
	PSII + DCBQ	0.81 ± 0.05	n/d	n/d.	0.015 ± 0.002	”	n/a
	P_{Os}−PSII	13 ± 3	n/d	n/d	0.2 ± 0.1	0.13 ± 0.03	1.7 ± 0.2
	P_{Os}−PSII +DCBQ	28 ± 5	n/d	n/d	0.5 ± 0.1	”	”
20	PSII	15 ± 3.7	0.33 ± 0.06	2.2 ± 0.2	0.3 ± 0.1	162 ± 17	n/a
	PSII + DCBQ	246 ± 18	4.1 ± 0.3	2.2 ± 0.3	4.5 ± 0.6	”	n/a
	P_{Os}−PSII	217 ± 16	4.0 ± 0.4	3.3 ± 0.4	3.9 ± 0.5	144 ± 21	25 ± 4
	P_{Os}−PSII +DCBQ	359 ± 16	6.7 ± 0.7	8.3 ± 0.5	6.5 ± 0.8	”	”
	P_{Phen}−PSII	40 ± 5	0.7 ± 0.1	n/d	0.7 ± 0.1	149 ± 7	17 ± 4
	P_{Phen}−PSII +DCBQ	225 ± 11	3.3 ± 0.5	n/d	4.1 ± 0.5	”	”
40	PSII	25 ± 5	0.33 ± 0.06	n/d	0.5 ± 0.1	399 ± 39	n/a
	PSII + DCBQ	309 ± 33	2.0 ± 0.3	n/d	5.6 ± 0.7	”	n/a
	P_{Os}−PSII	381 ± 31	3.6 ± 0.3	4.2 ± 0.4	6.9 ± 0.9	336 ± 60	38 ± 1
	P_{Os}−PSII +DCBQ	513 ± 29	4.8 ± 0.4	9.4 ± 0.5	9.3 ± 1.2	”	”
80	PSII	33 ± 5	0.16 ± 0.06	n/d	0.6 ± 0.1	867 ± 80	n/a
	PSII + DCBQ	577 ± 21	1.7 ± 0.3	n/d	10.5 ± 1.4	”	n/a
	P_{Os}−PSII	271 ± 14	2.4 ± 0.1	4.3 ± 0.4	4.9 ± 0.6	280 ± 17	75 ± 3
	P_{Os}−PSII +DCBQ	451 ± 25	4.3 ± 0.4	10.8 ± 0.5	8.2 ± 1.1	”	”

Abbreviations: J_{max}, maximum photocurrent density (the baseline-corrected photocurrent peak density after the third light exposure); TOF_{PSII}, theoretical initial PSII-based turnover frequency (assuming 100% Faradaic efficiency); $\tau_{1/2}$, photocurrent density half-life time; EQE, external quantum efficiency; Γ_{PSII}, PSII loading and $\Gamma_{polymer}$, redox-active centres loading on flat ITO or IO-ITO electrodes. n/a, not applicable; n/d, not determined. Conditions: light illumination (λ = 685 nm, E_e = 10 mW cm^{-2}) at E_{app} = 0.5 V vs. SHE (pH = 6.5, T = 25 °C). The table adapted from Sokol et. al., *Energy Environ. Sci.*, 2016, **9**, 3698−3709.

Following the assembly and characterisation of the IO-ITO|P_{Os} and IO-ITO|P_{Phen} electrodes, PSII was introduced into the electrode system. PSII (1 μL, 2.6 mg Chl *a* mL^{-1}) and the redox polymer (1 μL, 10 mg mL^{-1}) were mixed together and immediately drop-cast on the IO-ITO electrode (20 μm thick) as a uniform blend, then allowed to adsorb in the dark for 15 min at room temperature. The amount of PSII entrapped in the polymer matrix inside the electrode (Γ_{PSII}) was quantified based on the absorption amplitude of Chl *a* (λ_{max} = 665 nm, Eq. 3.3), extracted from PSII using MeOH (Fig. B.8a). UV-vis spectra of polymer solutions (0.02 mg mL^{-1}) in the electrolyte solution and MeOH (Fig. B.8b) showed a negligible absorption at the irradiation wavelength used in PF-PEC (λ = 685 nm). Exceptionally high PSII loadings were observed for IO-ITO|P_{Os}−PSII (144 ± 21 pmol cm^{-2}), IO-ITO|P_{Phen}−PSII (149 ± 7 pmol cm^{-2}) and IO-ITO|PSII (162 ± 17 pmol cm^{-2}) (Fig. B.8c). The slightly higher PSII loading in the PSII-only system could be explained by more space being available (that could be filled by the enzymes) in the absence of polymers. The SEM images of the IO-ITO electrodes taken before and after P_{Os}−PSII and P_{Phen}−PSII deposition (Fig. 3.2) indicate no evident channel or pore blockages.

The effective assembly of PSII with the polymers can be attributed to favourable non-covalent interactions between the protein shell and the polymers. The hydrophilic nature of the polymers is bestowed primarily by the cationic Os complex/phenothiazine dye, with some contributions by the multiple polar functional side groups (P_{Os}: imidazole and amine groups; P_{Phen}: polyethylene glycol side chains and OH-functions). At pH 6.5, P_{Os} is expected to behave as a cationic polyelectrolyte since the primary amine (pKa 10) and imidazole groups (pKa 7) are protonated. This also contributes to the close to optimal polymer solvation and swelling, supported by high D_e value previously observed. [43]

3.2.3 PF-PEC with IO-ITO|polymer−PSII electrodes

PF-PEC measurements were performed at 25 °C using an IO-ITO|polymer−PSII working, a Pt wire counter and a Ag/AgCl (3 M KCl) reference electrode. The electrolyte solution was adjusted to pH 6.5 and contained $CaCl_2$ (20 mM), $MgCl_2$ (15 mM), KCl (50 mM) and 2-(N-morpholino)ethane sulfonic acid (MES, 40 mM). The action spectra of the IO-ITO|PSII, IO-ITO|P_{Os}−PSII and IO-ITO|P_{Phen}−PSII photoelectrodes were recorded to determine appropriate wavelengths of light for photocurrent generation (Fig. B.9a and Fig. 3.5a). In a typical experiment, the wavelength was decreased in steps of 20 nm starting from 760 nm at an applied potential of 0.5 V vs. SHE and the photoresponse was measured at each wavelength. The maximum photocurrent was observed at 680 nm, which matches the UV-vis absorption spectrum of PSII and supports the integrity of PSII in its native state during the immobilisation on the IO-ITO electrodes. [21, 47] The action spectra of the control samples

IO-ITO, IO-ITO|P_{Os} and IO-ITO|P_{Phen} corresponded to the UV-vis absorption spectra of the respective polymers (Fig. B.8b) and confirmed no significant contribution to the photocurrent generation from the polymers (Fig. B.9a and Fig. 3.5b).

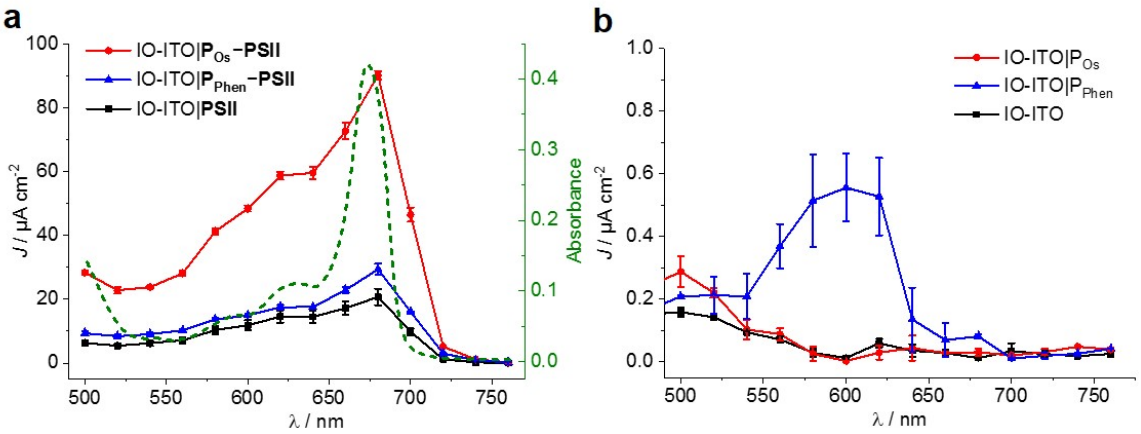

Figure 3.5 **Photocurrent action spectra of IO-ITO|polymer−PSII photoanodes. a**, Action spectra (solid traces) showing the photocurrent density (left Y axis) vs. irradiation wavelength of the IO-ITO|PSII (black), IO-ITO|P_{Os}−PSII (red) and IO-ITO|P_{Os}−PSII (blue) photoelectrodes (20 μm thickness) recorded with monochromatic light (λ = 420 to 760 nm) measured in 20 nm steps (E_e = 3.25 to 6.26 mW cm^{-2}). Plot based on data points recorded in Fig. B.9a. The error bars correspond to the standard deviation (N = 3). The UV-vis absorption spectrum of the PSII (1 μL, 2.6 mg Chl a mL^{-1}) in MES electrolyte solution (0.5 mL) (dashed green line, right Y axis) matches the photocurrent response of PSII on the electrodes. **b**, Control experiments with bare (PSII-free) IO-ITO (black), IO-ITO|P_{Os} (red) and IO-ITO|P_{Phen} (blue) electrodes showing no significant photocurrent density contribution. Plot based on data points recorded in Fig. B.9b. Short irradiation times (chopped 30 s dark and 10 s light irradiation time) are used in all experiments to prevent excessive PSII photodegradation over time. Conditions: E_{app} = 0.5 V vs. SHE, MES electrolyte solution (pH = 6.5, T = 25 °C). The figure adapted from Sokol et. al., *Energy Environ. Sci.*, 2016, **9**, 3698−3709.

Stepped-potential chronoamperometry with chopped red-light irradiation (λ = 685 nm, E_e = 10 mW cm^{-2}) was performed to characterise the onset potential (E_{onset}) of photocurrents in each IO-ITO|polymer−PSII system (Fig. B.10). In a typical experiment, the applied potential was gradually increased in steps of 0.1 V in the anodic direction. A summary of the photoresponse as a function of the E_{app} is shown in Fig. 3.6. The IO-ITO|P_{Phen}−PSII system showed an E_{onset} value of ∼0.1 V vs. SHE, which is slightly more positive than expected, possibly due to other minor interference charge transfer pathways. [48] However, the E_{onset} of IO-ITO|P_{Phen}−PSII is still clearly more negative than that of the IO-ITO|P_{Os}−PSII electrode (E_{onset} = ∼0.3 V vs. SHE; Fig. 3.6 inset), which is consistent with the lower $E_{1/2}$ of P_{Phen}

($E_{1/2}$ = 0.04 V vs. SHE) compared to the P_{Os} ($E_{1/2}$ = 0.44 V vs. SHE). The photocurrents for both the IO-ITO|P_{Os}−PSII and IO-ITO|P_{Os}−PSII electrodes reach a plateau at ∼0.5 V vs. SHE. No photoactivity and negligible dark current were observed for the IO-ITO|P_{Os} and IO-ITO|P_{Phen} electrodes (Fig. B.10d). Upon prolonged irradiation at more positive potentials (E_{app} > 0.6 - 0.7 V vs. SHE), a drop in photocurrent was observed. This drop in photocurrent is irreversible, as shown by the low photoresponse given by a backward scan in the negative direction (at 0.5 V vs. SHE, Fig. 3.7a). CV scans of the IO-ITO|P_{Os}−PSII electrode (Fig. 3.7b) confirmed the stability and homogeneity of the integrated PSII−polymer film on the electrode surface in the dark. However, CV scans performed with red light irradiation (Fig. 3.7c) show a significant decrease in photocurrents after 3 potential sweep cycles over the range 0.1 - 0.8 V vs SHE, which is indicative of P_{Os}−PSII film photodegradation (PSII-limiting system). [49]

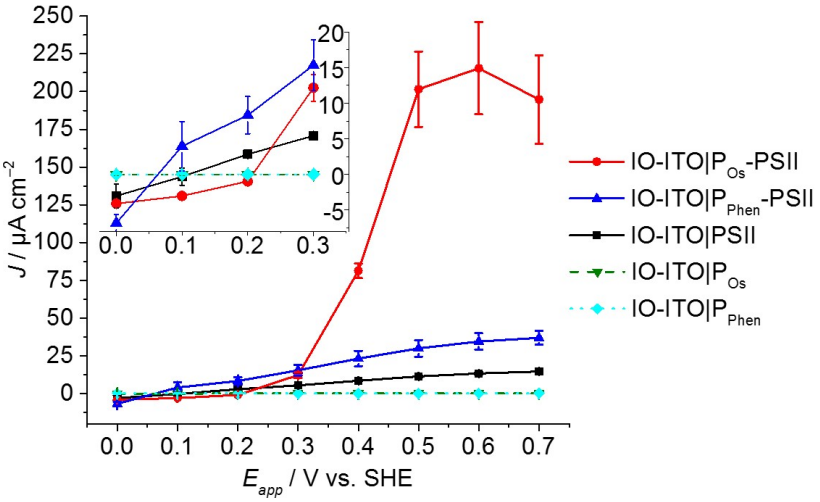

Figure 3.6 **Photocurrent density as a function of the applied potential (E_{app}) for the IO-ITO|polymer−PSII photoanodes.** Data points determined by stepped potential chronoamperometry (see Fig. B.10 for raw data). The inset shows a magnified region of the plot close to the onset potentials of the polymers. The photoresponse for PSII-free IO-ITO|polymer electrodes are shown for comparison. The error bars correspond to the standard deviation (N = 4). Conditions: MES electrolyte solution (pH = 6.5, T = 25 °C).

To investigate the quality of the wiring between the PSII and the ITO electrode in the IO-ITO|polymer−PSII systems, chronoamperometry at an applied potential of 0.5 V vs. SHE was performed in the presence and absence of the diffusional mediator, DCBQ, with chopped light irradiation (Fig. 3.8). Typical photocurrent densities for optimised 20 μm thick IO-ITO|PSII, IO-ITO|P_{Os}−PSII, and IO-ITO|P_{Phen}−PSII electrodes in the absence of a diffusional mediator (Fig. 3.8a) were approximately 15, 230 and 45 μA cm^{-2}, respectively, which compares favourably with PF-PEC of previously reported PSII-electrodes. [9, 19]

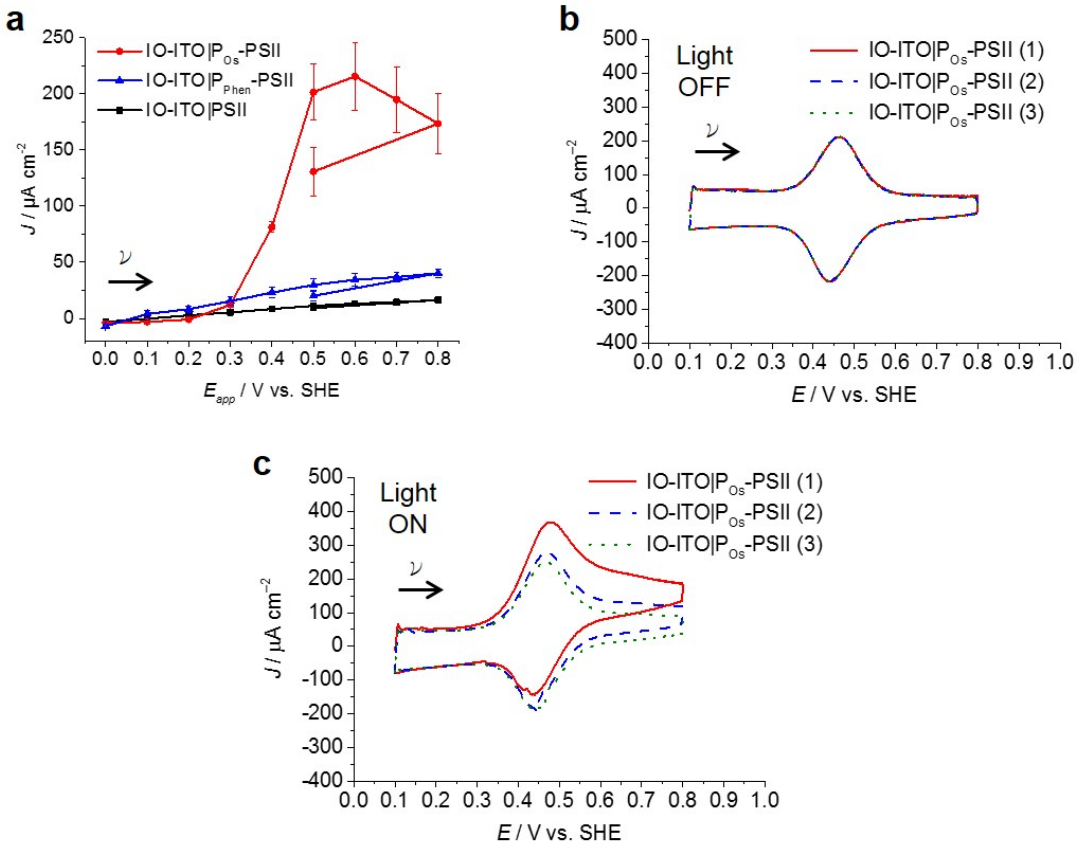

Figure 3.7 **Characterisation of electrochemical stability of the IO-ITO|polymer−PSII photoanode during irradiation.** **a**, Photocurrent density vs. E_{app} for the IO-ITO|polymer−PSII photoanodes with a measurement re-taken at 0.5 V vs. SHE following the scan to determine the extent of PSII degradation. **b**, CV scans of P_{Os}−PSII (1 μL of 10 μg μL^{-1} P_{Os} mixed with 1 μL of 2.6 μg μL^{-1} Chl *a* in PSII) adsorbed on 20 μm thick IO-ITO (Γ_{PSII} = 144 $\pm$ 21 pmol cm^{-2} and Γ_{Os} = 25 $\pm$ 4 nmol cm^{-2}) during the first three scan cycles in the dark, and **c**, during irradiation (λ = 685 nm; E_e = 10 mW cm^{-2}) at a scan rate 10 mV s^{-1}. Conditions: MES electrolyte solution (pH = 6.5, T = 25 °C). The figure adapted from Sokol et. al., *Energy Environ. Sci.*, 2016, **9**, 3698−3709.

Bare IO-ITO and IO-ITO|polymer electrodes exhibited photocurrent densities below 100 nA cm^{-2}.

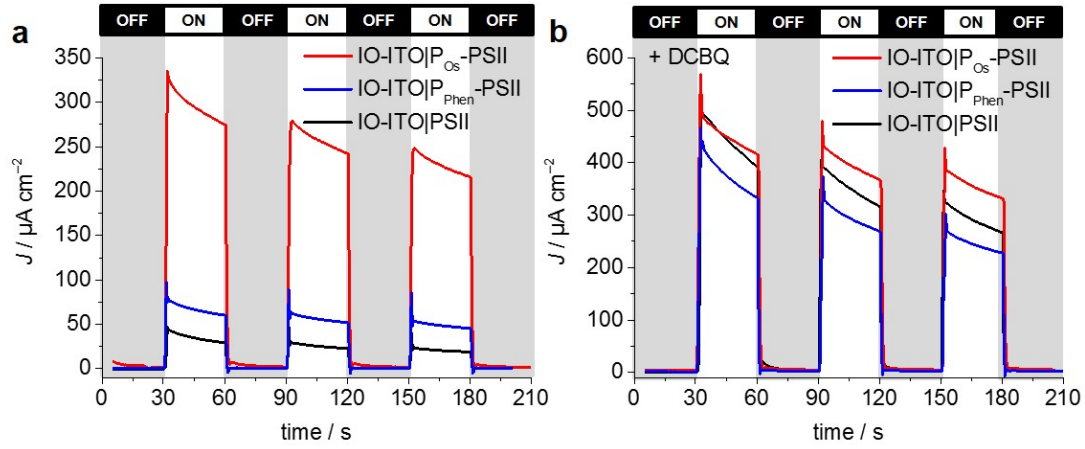

Figure 3.8 **Photocurrent density of the IO-ITO|polymer−PSII and IO-ITO|PSII 20 μm thick electrodes.** Measured with chopped illumination (λ = 685 nm; E_e = 10 mW cm^{-2}) at E_{app} = 0.5 V vs. SHE. **a**, No diffusional mediator was present and **b**, DCBQ (1 mM) was present in the electrolyte solution. The reported photocurrent densities were defined as the right shoulder of the third peak. The PSII loading for each modified electrode (see Fig. B.8) was comparable: 162 ± 17 pmol cm_{-2} (IO-ITO|PSII), 144 ± 21 pmol cm^{-2} (IO-ITO|P_{Os}−PSII) and 149 ± 7 pmol cm^{-2} (IO-ITO|P_{Phen}−PSII). The figure adapted from Sokol et. al., *Energy Environ. Sci.*, 2016, **9**, 3698−3709.

The relatively large photoresponse observed for the IO-ITO|P_{Os}−PSII system is indicative of efficient electronic communication between PSII and the electrode. An external quantum efficiency (EQE) of 4.4% (derived using Eq. 3.4) was obtained for the IO-ITO|P_{Os}−PSII system, which is 15-fold higher than for IO-ITO|PSII (EQE = 0.3%) and the highest reported so far for a diffusional mediator-free PSII-electrode. [9, 19] The photoresponse in the IO-ITO|P_{Phen}−PSII system (EQE = 0.8%) is improved compared to IO-ITO|PSII, however the enhancement is not as great as the IO-ITO|P_{Os}−PSII system, which indicates that the P_{Phen} is less efficient at wiring PSII to the electrode, possibly because of its significantly lower driving force for electron transfer.

The addition of DCBQ (0.36 V vs. SHE) [9] to the IO-ITO|P_{Os}−PSII system gave rise to a further 1.5-fold photocurrent density increase (375 μA cm^{-2}, EQE = 7.7%, Fig. 3.8b). Similarly, the addition of DCBQ to the IO-ITO|P_{Phen}−PSII system gave rise to a 6-fold photocurrent density increase (236 μA cm^{-2}, EQE = 4.6%). The addition of DCBQ to the IO-ITO|PSII system gave rise to an 18-fold increase in photoresponse (265 μA cm^{-2}, EQE = 5.1%). This observation demonstrates that a significantly higher proportion of PSII was electrically connected to the electrode in the IO-ITO|P_{Os}−PSII system compared to

IO-ITO|P_{Phen}−PSII, and that the IO-ITO|polymer−PSII electrodes were better connected than the IO-ITO|PSII system. Addition of bifunctional cross-linkers (PEGDGE for P_{Os} [31] and 2,2'-(ethylenedioxy)diethanethiol for P_{Phen} [6]), to the IO-ITO|polymer−PSII systems resulted in no further photocurrent increase. This may be attributed to the stabilisation of the PSII−polymer matrix inside the 3-D-interconnected porous electrode framework. [9]

These results indicate favourable interactions between the P_{Os} and PSII, most likely between the side groups of the polymer (positively-charged Os^{3+} complex, primary amine and imidazolium units) and the polar residues of PSII, [39, 50] in particular the negatively charged region at the stromal side of PSII and near the Q_A site. [37, 51] In addition, a high number of electrochemically-active Os centres is estimated to be in close proximity to each PSII unit (based on the Os centre to PSII ratios ($\Gamma_{Os/PSII} \sim 175$) co-adsorbed on the electrodes), which explains the favourable photoelectrochemical response of the system discussed earlier. The P_{Phen} can also interact with PSII via its hydrophilic side chains and residual epoxide groups to give rise to possible cross-linking. [39, 50] However, the P_{Phen} is expected to have weaker interactions with the ITO electrode surface (Fig. 3.4e), and is more likely to undergo polymer aggregation, as indicated by DLS, to result in significantly lower polymer entrapment and retention of PSII. The estimated number of toluidine blue units per PSII unit is 108, which is significantly lower than in the IO-ITO|P_{Os}−PSII system.

3.2.4 Comparison of P_{Os} and P_{Phen}

In the preceding experiments, PF-PEC was used to systematically compare the performance of two benchmark polymers for PSII entrapment when they are integrated into high surface area electrodes. The P_{Os} exhibited physically stable integration and long-term immobilisation without significant activity losses in 20 μm thick IO-ITO electrodes. When embedded with PSII, the IO-ITO|P_{Os}−PSII electrodes delivered high photocurrent densities that were at least 5-fold higher than systems connected by P_{Phen} (Fig. 3.8a). Despite the fact that P_{Phen} is free of noble metals and has a better matched $E_{1/2}$ to the Q_A and Q_B (giving rise to earlier onset potentials for water oxidation), it exhibits lower adsorption stability on 20 μm thick IO-ITO electrodes. The IO-ITO|P_{Phen}−PSII systems showed lower overall photoresponses compared to IO-ITO|P_{Os}−PSII, which can also be rationalised by their more negative redox potential values (providing less driving force) and slower (H^+ diffusion-dependent) electron hopping process (2 e^-/H^+ vs. 1 e− transfer, respectively). Overall, IO-ITO|P_{Os}−PSII electrodes demonstrated higher performance and more efficient wiring between the PSII and the ITO electrode.

3.2.5 IO-ITO|P_{Os}−PSII performance

To determine the photoresponse enhancement with film thickness in IO-ITO|polymer−PSII, IO-ITO electrodes with varying thickness (from 20 to 80 μm) were prepared and studied by PF-PEC. The focus was placed on the optimisation of the top performing IO-ITO|P_{Os}−PSII systems.

The maximum loadings of PSII and P_{Os} on IO-ITO electrodes of different thicknesses are shown in Fig. 3.9a. P_{Os} and PSII loadings increase linearly as the thickness rises from 0 to 80 μm. In comparison, an adsorbent saturation point was reached for IO-ITO|P_{Os}−PSII electrodes beyond 40 μm. This was attributed to the accumulation of moderately viscous P_{Os}−PSII aggregates over deposition time, which limits the penetration depth of the P_{Os} due to the formation of channel blockages. No significant losses due to desorption upon long-term (60 min) immersion in the electrolyte solution with constant light irradiation were observed.

The dependence of photocurrent density on the IO-ITO|P_{Os}−PSII electrode thickness is shown in Fig. 3.9b. A saturation photocurrent density of 381 $\pm$ 31 μA cm^{-2} (EQE = 6.9 $\pm$ 0.9%) for 40 μm thick electrodes was observed, which correlates with the maximum PSII loading reached at this thickness. Upon DCBQ addition, a further 1.35-fold photocurrent density increase was detected (513 $\pm$ 29 μA cm^{-2}, EQE = 9.3 $\pm$ 1.2%). The IO-ITO|PSII electrode exhibited almost ideal linear increase in photocurrent densities with the ITO film thickness, which is also consistent with the trend of PSII loading in IO-ITO|PSII electrodes. Maximum photocurrent values of 33 $\pm$ 5 and 577 $\pm$ 21 μA cm^{-2} from 80 μm thick electrodes were observed in the absence and presence of DCBQ, respectively. The comparable maximum photocurrent densities reached by the IO-ITO|P_{Os}−PSII electrode in the absence of DCBQ and the IO-ITO|PSII electrode in the presence of DCBQ indicate efficient wiring of the PSII to the ITO surface by the P_{Os} matrix.

The theoretical turnover frequency TOF_{PSII} of water oxidation was estimated (assuming 100% Faradaic efficiency) according to Eq. 3.5 for the IO-ITO|P_{Os}−PSII electrodes of different thicknesses as shown in Fig. 3.9c. The maximum TOF_{PSII} of 4.0 $\pm$ 0.4 s^{-1} was achieved using 20 μm thick IO-ITO|P_{Os}−PSII electrodes, which could be increased to 6.7 $\pm$ 0.7 s^{-1} by the addition of DCBQ. This is a 1.7-fold increase compared to the IO-ITO|PSII system in the presence of DCBQ, and indicates that the mediated IO-ITO|P_{Os}−PSII system is overall more efficiently wired than the mediated IO-ITO|PSII system due to the presence of the P_{Os} matrix.

The long-term photostability of the IO-ITO|P_{Os}−PSII system was evaluated at a relatively mild E_{app} = 0.5 V vs. SHE and the results are presented in Fig. 3.9d. To determine the photocurrent half-life time ($\tau_{1/2}$), the photocurrent generated by IO-ITO|P_{Os}−PSII electrode

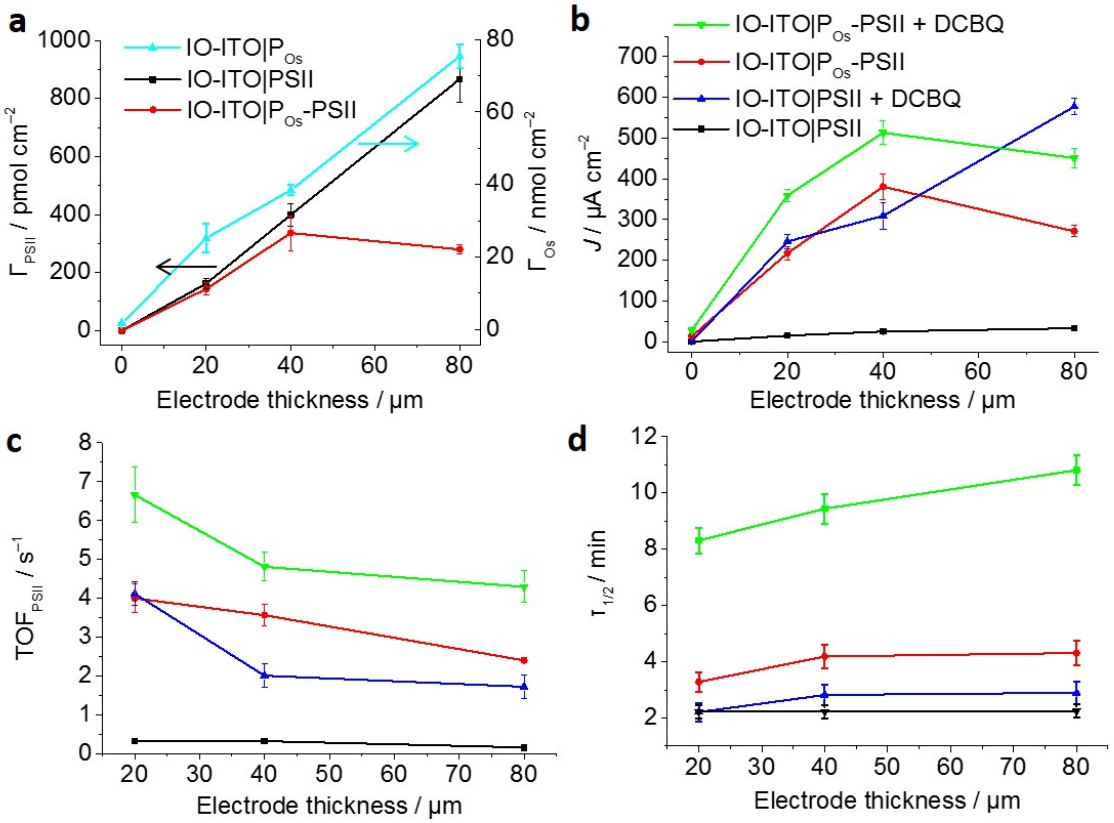

Figure 3.9 **Characterisation of the IO-ITO|P$_{Os}$−PSII photoanode as a function of the electrode thickness. a**, PSII loading quantified by the amplitude of absorption at $\lambda = 665$ nm, and $Os^{3/2+}$ redox centres loading determined by CV (Fig. 3.4b); **b**, photocurrent densities, **c**, corresponding TOF_{PSII} values and **d**, photocurrent half-life times ($\tau_{1/2}$) measured upon light illumination ($\lambda = 685$ nm; $E_e = 10$ mW cm^{-2}) at a fixed potential of 0.5 V vs. SHE without any additional diffusional mediator and upon addition of 1 mM of freely diffusing DCBQ mediator in MES electrolyte solution (pH = 6.5, T = 25 °C). The error bars correspond to the standard deviation (N = 4). The figure adapted from Sokol et. al., *Energy Environ. Sci.*, 2016, **9**, 3698−3709.

under continuous light irradiation for 60 min was recorded starting at the third photoresponse peak (Fig. 3.10). Across the entire thickness range, the IO-ITO|P_{Os}−PSII systems exhibited a 2-fold $\tau_{1/2}$ increase (maximum of 4.3 ± 0.4 min) compared to the IO-ITO|PSII systems (2.2 ± 0.2 min) in the absence of DCBQ. In the presence of DCBQ, further enhancement of the $\tau_{1/2}$ can be seen to reach ∼10 min in 80 μm thick IO-ITO|P_{Os}−PSII electrodes. After 60 min of constant light irradiation, ∼7% and 11% of the initial photocurrent was detected from the IO-ITO|P_{Os}−PSII electrode, without and with DCBQ addition, respectively. In contrast, less than 2% of the initial photocurrent was detected from the IO-ITO|PSII electrode. This can in part be attributed to the physical stabilisation of the PSII by the polymer matrix and the IO-ITO electrode architecture. The increased $\tau_{1/2}$ in the IO-ITO|P_{Os}−PSII system can also be partly attributed to reduced accumulation of pigments in the excited state due to more efficient electron transfer between PSII and the Os centres in P_{Os}. [49] The higher efficiency in charge transfer would result in dampened formation of reactive oxygen species and deterioration of the D1 subunit in PSII. [52]

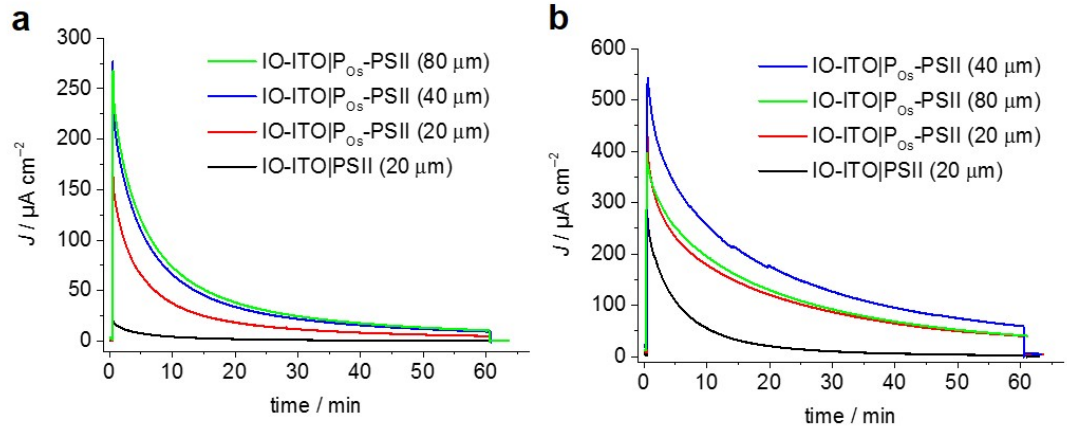

Figure 3.10 **Photostability of the IO-ITO|P_{Os}−PSII photoanode.** Photocurrent decay of IO-ITO|P_{Os}−PSII photoanodes with different film thicknesses during 1 h continuous illumination (λ = 685 nm; E_e = 10 mW cm^{-2}) at 0.5 V vs. SHE **a**, without any additional mediator and **b**, in the presence of a redox mediator (1 mM DCBQ). Conditions: MES electrolyte solution (pH = 6.5, T = 25 °C). The figure adapted from Sokol et. al., *Energy Environ. Sci.*, 2016, **9**, 3698−3709.

Finally, the photocurrent generated by the IO-ITO|P_{Os}−PSII electrode is high enough to enable the quantification of O_2 evolution (Fig. 3.11). Controlled-potential electrolysis at E_{app} = 0.5 V vs. SHE was carried out in a two-compartment cell in the glovebox employing an optimised 40 μm thick IO-ITO|P_{Os}−PSII electrode upon light irradiation for 60 min (λ = 660 nm, E_e = 10 mW cm^{-2}). The passage of 0.12 ± 0.03 C cm^{-2} charge was measured and the evolution of 0.24 ± 0.03 μmol O_2 cm^{-2} was detected by a fluorescence O_2 sensor, which

corresponded to 85 ± 9% Faradaic efficiency. A turnover number TON_{PSII} of 946 ± 96 mol O_2 (mol PSII)$^{-1}$, and an initial PSII-based TOF_{PSII} of 3.6 ± 0.3 mol O_2 (mol PSII)$^{-1}$ s^{-1} was calculated based on quantified O_2 and PSII using Eq. 3.6 and Eq. 3.5, respectively. Previously, the generation of 0.23 ± 0.01 C cm^{-2} charge and the evolution of 0.45 ± 0.01 μmol O_2 cm^{-2} (75 ± 4% Faradaic efficiency), corresponding to TON_{PSII} of 4,200 ± 200 mol O_2 (mol PSII)$^{-1}$ and TOF_{PSII} of 12.9 ± 0.4 mol O_2 (mol PSII)$^{-1}$ s^{-1} were reported for the IO-ITO|PSII system in the presence of DCBQ. [9] The absence of diffusion-limited mediators enables an all-integrated electrode design and eliminates problems such as those associated with concentration-dependent electron transfer. It also overcomes the issue of diffusional mass transport that may interfere with processes at the counter electrode and limit the performance of PSII-based PEC assemblies. Lastly, this electrode prototype allows all catalytic/electroactive material to be confined inside the porous electrode architecture, minimising the presence of high concentration catalytic/electroactive material in the bulk solution.

3.3 Conclusions

The present study has introduced a new benchmark PSII-based electrode, which was developed as a result of a rational design process that incorporated the best aspects of two leading enzyme immobilisation strategies. We integrated the stabilisation and efficient electronic wiring of enzymes within redox polymer matrices with the high loading capacity of hierarchically-structured electrodes. This enabled the demonstration of high photocurrent densities, TOFs and levels of evolved O_2 that could be obtained for a PSII-driven PF-PEC system without the requirement for diffusional additives in the bulk solution. The photocurrents arising from PSII reported here also compare favourably with those reported for other wired photosynthetic proteins such as bacterial reaction centres [53] or photosystem I. [4, 43, 54]

The development of this IO-ITO|polymer−PSII system provides the basic concepts needed for the future design of enzyme-driven semi-artificial photosynthetic systems, including PEC tandem systems that incorporate other reaction centre or pigment-based proteins. We anticipate that this approach will also serve as an inspiration in the design of synthetic PEC water-splitting architectures. In the future, we expect that improvements in polymer design will lead to favourable changes to the electrode stability, electron hopping efficiency and formal redox potentials to better match the energy levels of the protein terminal electron acceptors. Lastly, hierarchical IO electrodes have demonstrated the potential to be highly ver-

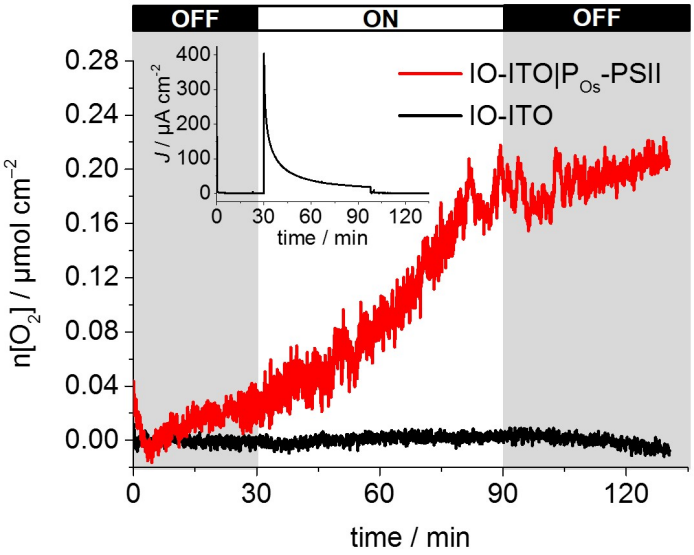

Figure 3.11 **Quantification of O_2 evolution for the 40 μm thick IO-ITO|P_{Os}−PSII electrode.** Continuous light illumination (λ = 660 nm, E_e = 10 mW cm^{-2}) was applied between 30 and 90 min with continuous stirring at E_{app} = 0.5 V vs. SHE (pH = 6.5, T = 25 °C, red line). The Faradaic yield (85 ± 9%) was determined. The corresponding chronoamperogram is shown in the inset. A control experiment in the absence of PSII is also shown (black curve). Quantification of O_2 was performed with a calibrated fluorescence O_2 sensor inside an anaerobic glovebox to avoid leakage of atmospheric O_2. The probe was placed inside the cell headspace, the background signal was left to stabilise over 30 min, the cell was then illuminated for 1 h, followed by the light being switched off for another 40 min, until the O_2 produced in the solution equilibrated with the headspace. The probe was protected from direct irradiation and the background signal was subtracted from all measurements. The reported O_2 values were corrected for dissolved O_2 using Henry's Law. The figure adapted from Sokol et. al., *Energy Environ. Sci.*, 2016, **9**, 3698−3709.

satile as a host system and may be used in various applications outside of PF-PEC, including batteries, fuel cells and solar cells.

3.4 Experimental section

3.4.1 Materials

All chemicals 1-vinylimidazole, 2,2'-bipyridine, allyl amine, K_2OsCl_6, butyl acrylate, allyl methacrylate, poly(ethylene glycol) methacrylate (M_n = 500 g mol^{-1}), 2,2'-azobis(2-methylpropionitrile), toluidine blue (all Sigma Aldrich), , DCBQ (Sigma Aldrich), MES (Alfa Aesar), $CaCl_2$ (Breckland Scientific), $MgCl_2$ (Fisher Scientific), KCl (Alfa Aesar), polystyrene beads (Polysciences, Inc., 750 nm diameter, 2.6% w/v suspension in H_2O), ITO nanoparticles (NPs) (Sigma Aldrich; $\leq$ 50 nm diameter) and fluorine-doped tin oxide (FTO) coated glass slides (8 Ω sq^{-1}; Sigma Aldrich) were purchased from commercial suppliers and used without further purification unless otherwise noted. Methanol, absolute ethanol, 2-propanol, dimethyl sulfoxide (high performance liquid chromatography grade) were purchased from Sigma Aldrich. Poly(ethylene glycol) diglycidyl ether (PEGDGE) (Polyscience, USA) and 2,2'-(ethylenedioxy)diethanethiol) (Sigma Aldrich) were purchased from commercial suppliers. PSII was isolated from the thermophilic cyanobacterium *Thermosynechococcus elongatus* and purified according to a previously reported procedure, [41] resulting in purified PSII with an average oxygen-evolving activity of approximately 5,300 μmol O_2 h^{-1} mg^{-1} of chlorophyll *a* (Chl *a*). A stock PSII solution containing 2.6 mg Chl *a* mL^{-1} (83 μM PSII monomer) was stored in a liquid N_2 Dewar.

3.4.2 Polymer synthesis

The synthetic approaches to obtain the poly(1-vinylimidazole-*co*-allylamine) backbone, the Os precursor cis-[$Os^{II}Cl_2(bpy)_2$] (bpy = 2,2'-bipyridine) and the Os complex cis-[Os^{II}Cl(1-(*n*-butyl)-imidazole)$(bpy)_2$](PF_6) were described previously. [5, 31] The poly(1-vinylimidazole-*co*-allylamine)-[$Os(bpy)_2Cl$]Cl (P_{Os}) [31] and phenothiazine-modified polymer (P_{Phen}, phenothiazine moiety = toluidine blue) [6] were synthesised and characterised according to previously reported procedures, with P_{Os} prepared with slight modifications. In brief, after stirring a mixture of *cis*-[$OsCl_2(bpy)_2$] and the poly(1-vinylimidazole-*co*-allylamine) backbone (1:1.65 weight ratio) dissolved in ethanol for 5 days at 90 °C, the product (P_{Os}) was precipitated upon addition of diethyl ether. The precipitate was separated by centrifugation, thoroughly washed with diethyl ether and dried under vacuum to obtain a reddish powder. Aqueous stock solutions of P_{Os} (10 mg mL^{-1}) and P_{Phen} (10 mg mL^{-1}) were used.

3.4.3 Physical characterisation

The surface morphology of the electrodes was analysed by scanning electron microscopy (SEM; SFEG XL30, Philips). A centrifuge (5804, Eppendorf), furnace (ELF 11/14B/301, Carbolite), ultrasonicator (DT102H, Sonorex Digitec, Bandelin, Monmouth Scientific) and UV/Ozone cleaner (ProCleaner Plus, BioForce Nanosciences) were used for electrode preparation. UV-vis absorption spectra were recorded on a UV-vis spectrophotometer (Cary 50, Varian; or Cary 60, Agilent), using cuvettes with an optical path length of 1 cm. Nuclear magnetic resonance (NMR) experiments were conducted with a spectrometer (200 DPX, Bruker) with a proton resonance frequency of 200.13 MHz (the residual solvent peak was used as internal standard). All DLS measurements (Zetasizer Nano ZS, Malvern Panalytical) were carried out using a 633 nm laser wavelength and a 173° backscatter measurement angle. The buffers were filtered through 450 nm membrane filters (polypropylene membranes bearing a borosilicate prefilter, Alltech) before dissolution of the polymers for DLS measurements; cuvettes were rinsed with buffer solution prior to measurements. For the filtration of polymer suspensions, non-pyrogenic 200 nm polyethersulfone membranes (Filtropur S, Sarstedt) were used.

3.4.4 Preparation of IO-ITO|PSII electrodes

The IO-ITO electrodes were fabricated according to a previously reported co-assembly procedure. [9] A standard IO-ITO electrode macropore diameter of 750 nm, film thickness of 20 μm and geometrical surface area of 0.25 cm^2 were used, unless stated otherwise. An amount of 4.2 μL of the described polystyrene−ITO dispersion on a 0.25 cm^2 geometrical surface area corresponds to a 10 μm thick IO-ITO structure. To obtain higher film thicknesses, the polystyrene−ITO mixture (4.2 μL) was deposited several times with a 4 h drying period in between. All current densities (μA cm^{-2}) are reported with respect to the geometrical surface area. The IO-ITO electrodes were cleaned using an UV/Ozone cleaner to ensure a contamination-free hydrophilic electrode surface for improved enzyme adsorption prior the PEC experiments. The IO-ITO|PSII modified electrodes were prepared as follows: a PSII stock solution (1 μL, 2.6 mg Chl *a* mL^{-1}) was drop-cast onto the IO-ITO electrode and incubated in the dark for 15 min at room temperature. It was determined that 1 μL of PSII stock solution provided an excess of PSII for 20 μm thick IO-ITO and ensured full enzyme coverage on the electrode surface. Prior to electrochemical studies, the IO-ITO|PSII electrode was rinsed (3 $\times$ 500 μL) with the electrolyte solution to remove all unbound enzyme from the electrode surface.

3.4.5 Preparation of IO-ITO|polymer−PSII electrodes

A PSII to polymer ratio of 1:1 (v/v) was defined based on 1 μL PSII stock solution (2.6 mg Chl *a* mL^{-1}) and 1 μL polymer solution (10 mg mL^{-1}). The PSII to polymer ratio was optimised on a 20 μm thick IO-ITO electrode by keeping the PSII solution volume (1 μL) and concentration (2.6 mg Chl *a* mL^{-1}) constant, and varying the polymer solution concentration at constant volume (1 μL). The optimal PSII to polymer ratio was found to be 1 μL of PSII solution (2.6 mg Chl *a* mL^{-1}) to 1 μL of the polymer solution (10 mg mL^{-1}) per 20 μm thickness of IO-ITO. The IO-ITO|polymer−PSII electrodes were prepared as follows: the PSII stock solution (1 μL) was mixed with a redox polymer solution (1 μL) and the polymer−PSII mixture was drop-cast (2 μL) onto the IO-ITO electrode (20 μm thick) and incubated in the dark for 15 min at room temperature. Prior to electrochemical studies, the IO-ITO|polymer−PSII electrode was rinsed (3 × 500 μL) with the electrolyte solution.

3.4.6 Determination of PSII and polymer loading on IO-ITO

The amount of PSII on the IO-ITO surface was quantified by scratching off the IO-ITO from the glass substrate and washing with MeOH (500 μL) to extract Chl *a* from the electrode surface into a centrifuge vial. The vial was centrifuged (10,000 r.p.m., 1 min), and the UV-vis spectrum of the supernatant was recorded (Fig. B.8a). The band with an absorption maximum of λ_{max} = 665 nm assigned to Chl *a* (extinction coefficient ε = 79.95 (Chl *a* mg)$^{-1}$ mL cm^{-1}) [55] was used to calculate the amount of PSII monomers assuming 35 Chl *a* molecules per PSII monomer. [39] The Os complex loading in the P_{Os} polymer was determined by UV-vis spectroscopy in DMSO, using the freely diffusing Os complex analogue, *cis*-[Os^{II}Cl(1-(*n*-butyl)-imidazole)$(bpy)_2$](PF_6) for calibration, and confirmed by ICP-AES, obtained by washing off the P_{Os} from the IO-ITO electrode with aq. conc. HNO_3 solution and measuring the concentration of the $Os^{3/2+}$ metal ions relative to Os ICP standard (1 mg Os mL^{-1} in 20% HCl, Ricca Chemical).

3.4.7 Protein film photoelectrochemistry (PF-PEC) measurements

All electrochemical experiments (with the exceptions of O_2 quantification and action spectra measurements) were performed with an Ivium Compactstat potentiostat with a purpose-built monochromatic red-light LED lamp (λ = 685 nm), collimated by two plano-convex lenses (THORLABS N-BK7 A Coated, ∅ = 7.5 cm, f = 5.0 cm). A light intensity flux (irradiance) (E_e) of 10 mW cm^{-2} was used, unless stated otherwise. Chronoamperometry and cyclic voltammetry (CV) measurements were carried out in a water-jacketed glass one-compartment

cell at 25 °C with a three-electrode setup using an IO-ITO working, a Pt wire counter and a Ag/AgCl (3 M KCl) reference electrode. Measurements of the IO-ITO|polymer−PSII system were carried out in 4 mL aqueous pH 6.5 electrolyte solution containing $CaCl_2$ (20 mM), $MgCl_2$ (15 mM), KCl (50 mM) and MES (40 mM). For the mediated photocurrent measurements, a DCBQ solution in DMSO (40 μL, 100 mM) was added to give a final concentration of 1 mM in the electrolyte solution. The following correction factor was used to convert the reduction potential to SHE: $E_{SHE} = E_{Ag/AgCl} + 0.197$ V (25 °C). IO-ITO|polymer−PSII electrodes were typically exposed to cycles of 30 s dark and 30 s light irradiation in the PF-PEC measurements. The photocurrent response was defined as the baseline-corrected photocurrent peak after the third light exposure, accounting for charging effects and to avoid overestimation. [19] The action spectra were recorded using a Xenon lamp Solar Light Simulator (300 W) coupled to a monochromator (MSH300; both from LOT Quantum design). The light intensity was measured as a function of wavelength with a photodiode detector (SEL033/F/QNDS1/W) and power meter (ILT1400). For the O_2 evolution measurements, an Ivium Modulight LED module (λ = 660 nm; E_e = 10 mW cm^{-2}) and a gas-tight two-compartment glass cell with the IO-ITO|polymer−PSII working electrode separated from the counter electrode by a glass frit were employed in an anaerobic (O_2 level <1 ppm) MBraun glovebox. The error analysis was based on the standard deviations resulting from at least three experiments.

3.4.8 Product analysis

Quantification of O_2 was performed with a calibrated fluorescence O_2 sensor (Neofox; Ocean Optics FOSPHOR probe) inside an MBraun glovebox to avoid leakage of atmospheric O_2. The probe was placed inside the cell headspace, protected from direct irradiation and the background signal was subtracted from all measurements using the OriginPro 9.0 software. The reported O_2 values were corrected for dissolved O_2 using Henry's Law.

3.4.9 Equations

$$\delta = \frac{D_e RT}{nF\nu} \tag{3.1}$$

where δ, diffusion layer thickness of the electrons (m); D_e, apparent electron diffusion coefficient (m^2 s^{-1}); R, ideal gas constant (8.314 J K^{-1} mol^{-1}); T, temperature (K); n, number of electrons transferred; F, Faraday constant (96,485.332 C mol^{-1}) and ν, scan rate (V s^{-1}). [44]

$$\Gamma = \frac{Q}{nFA} \tag{3.2}$$

where Γ, surface coverage of the electrochemically-active redox centres (mol m^{-2}); Q, total charge passed (C) and A, geometric electrode area (m^2). [44]

$$\Gamma_{PSII} = \frac{(16.29Abs^{665-750} - 8.54Abs^{652-750})V_{MeOH} \times 10^6 gmL^{-1}}{35M_{Chla} \times A} \tag{3.3}$$

where Γ_{PSII}, surface coverage of immobilised PSII (mol m^{-2}); Abs^{λ}, background (λ = 750 nm) corrected UV-vis absorption of Chl a at a given λ; V_{MeOH}, MeOH volume (mL) and M_{Chla}, molecular mass of Chl a (893.5 g mol^{-1}). [55]

$$EQE = \frac{I_e}{E_\lambda} = \frac{\frac{J}{F}}{\frac{\lambda E_e}{N_A hc}} = \frac{hcJ}{e\lambda E_e} \tag{3.4}$$

where EQE, external quantum efficiency (defined as the number of incident photons converted to electrons at a selected irradiation wavelength); I_e, electron flux at the external circuit (mol m^{-2} s^{-1}); I_λ, incident photon flux (mol m^{-2} s^{-1}); h, Plank constant (6.626×10^{-34} J s); c, speed of light (3.00×10^8 m s^{-1}); J, photocurrent density (A m^{-2}); e, electron charge (1.602×10^{-19} C); N_A, Avogadro constant (6.022×10^{23} mol^{-1}); λ, irradiation wavelength (m) and E_e, light intensity flux (irradiance) (W m^{-2}). [14]

$$TOF_{PSII} = \frac{I}{4neN_A n_{PSII}} \tag{3.5}$$

where TOF_{PSII}, theoretical initial PSII-based O_2 evolution turnover frequency (assuming 100% Faradaic efficiency, except where O_2 was quantified) (mol O_2 (mol PSII)$^{-1}$ s^{-1}); I, photocurrent response (A) and n_{PSII}, amount of immobilised PSII (mol). [9]

$$TON_{PSII} = \frac{n_{O_2}}{n_{PSII}} \tag{3.6}$$

where TON_{PSII}, PSII-based O_2 evolution turnover number (mol O_2 (mol PSII)$^{-1}$), n_{O_2}, amount of evolved O_2 (mol) and n_{PSII}, amount of immobilised PSII (mol).

References

(1) M. T. Giardi, M. Koblížek and J. Masojídek, *Biosens. Bioelectron.*, 2001, **16**, 1027–1033.

(2) M. Koblížek, J. Malý, J. Masojídek, J. Komenda, T. Kučera, M. T. Giardi, A. K. Mattoo and R. Pilloton, *Biotechnol. Bioeng.*, 2002, **78**, 110–116.

(3) D. J. K. Swainsbury, V. M. Friebe, R. N. Frese and M. R. Jones, *Biosens. Bioelectron.*, 2014, **58**, 172–178.

(4) A. Mershin, K. Matsumoto, L. Kaiser, D. Yu, M. Vaughn, M. K. Nazeeruddin, B. D. Bruce, M. Grätzel and S. Zhang, *Sci. Rep.*, 2012, **2**, 1–7.

(5) T. Kothe, N. Plumeré, A. Badura, M. M. Nowaczyk, D. A. Guschin, M. Rögner and W. Schuhmann, *Angew. Chem. Int. Ed.*, 2013, **52**, 14233–14236.

(6) V. Hartmann, T. Kothe, S. Pöller, E. El-Mohsnawy, M. M. Nowaczyk, N. Plumeré, W. Schuhmann and M. Rögner, *Phys. Chem. Chem. Phys.*, 2014, **16**, 11936–11941.

(7) N. T. Nguyen, T. Yatabe, K. S. Yoon and S. Ogo, *J. Biosci. Bioeng.*, 2014, **118**, 386–391.

(8) O. Yehezkeli, R. Tel-Vered, D. Michaeli, R. Nechushtai and I. Willner, *Small*, 2013, **9**, 2970–2978.

(9) D. Mersch, C.-Y. Lee, J. Z. Zhang, K. Brinkert, J. C. Fontecilla-Camps, A. W. Rutherford and E. Reisner, *J. Am. Chem. Soc.*, 2015, **137**, 8541–8549.

(10) G. Ananyev and G. C. Dismukes, *Photosynth. Res.*, 2005, **84**, 355–365.

(11) D. J. Vinyard, G. M. Ananyev and G. C. Dismukes, *Annu. Rev. Biochem.*, 2013, **82**, 577–606.

(12) R. Tel-Vered and I. Willner, *ChemElectroChem*, 2014, **1**, 1778–1797.

(13) O. Yehezkeli, R. Tel-Vered, D. Michaeli, I. Willner and R. Nechushtai, *Photosynth. Res.*, 2014, **120**, 71–85.

(14) K. K. Rao, D. O. Hall, N. Vlachopoulos, M. Grätzel, M. C. W. Evans and M. Seibert, *J. Photochem. Photobiol. B*, 1990, **5**, 379–389.

(15) A. Badura, B. Esper, K. Ataka, C. Grunwald, C. Wöll, J. Kuhlmann, J. Heberle and M. Rögner, *Photochem. Photobiol.*, 2006, **82**, 1385–1390.

(16) N. Terasaki, M. Iwai, N. Yamamoto, T. Hiraga, S. Yamada and Y. Inoue, *Thin Solid Films*, 2008, **516**, 2553–2557.

(17) O. Yehezkeli, R. Tel-vered, J. Wasserman, A. Trifonov, D. Michaeli, R. Nechushtai and I. Willner, *Nat. Commun.*, 2012, **3**, 742–748.

(18) J. Barber and P. D. Tran, *J. R. Soc. Interface*, 2013, **10**, 20120984.

(19) M. Kato, J. Z. Zhang, N. Paul and E. Reisner, *Chem. Soc. Rev.*, 2014, **43**, 6485–6497.

(20) S. A. Trammell, A. Spano, R. Price and N. Lebedev, *Biosens. Bioelectron.*, 2006, **21**, 1023–1028.

(21) E. Y. Katz, A. Y. Shkuropatov, O. I. Vagabova and V. A. Shuvalov, *Biochim. Biophys. Acta - Bioenerg.*, 1989, **976**, 121–128.

(22) E. Katz, *J. Electroanal. Chem.*, 1994, **365**, 157–164.

(23) C. Nakamura, M. Hasegawa, Y. Yasuda and J. Miyake, *Appl. Biochem. Biotechnol.*, 2000, **84-86**, 401–408.

(24) S. A. Trammell, L. Wang, J. M. Zullo, R. Shashidhar and N. Lebedev, *Biosens. Bioelectron.*, 2004, **19**, 1649–1655.

(25) N. Lebedev, S. A. Trammell, A. Spano, E. Lukashev, I. Griva and J. Schnur, *J. Am. Chem. Soc.*, 2006, **128**, 12044–12045.

(26) H. Yaghoubi, Z. Li, D. Jun, E. Lafalce, X. Jiang, R. Schlaf, J. T. Beatty and A. Takshi, *J. Phys. Chem. C*, 2014, **118**, 23509–23518.

(27) M. Kato, T. Cardona, A. W. Rutherford and E. Reisner, *J. Am. Chem. Soc.*, 2013, **135**, 10610–10613.

(28) A. Heller, *Curr. Opin. Chem. Biol.*, 2006, **10**, 664–672.

(29) R. Gracia and D. Mecerreyes, *Polym. Chem.*, 2013, **4**, 2206–2214.

(30) A. Badura, T. Kothe, W. Schuhmann, M. Rögner, R. Matthias, W. Schuhmann and M. Rögner, *Energy Environ. Sci.*, 2011, **4**, 3263–3274.

(31) A. Badura, D. Guschin, B. Esper, T. Kothe, S. Neugebauer, W. Schuhmann and M. Rögner, *Electroanalysis*, 2008, **20**, 1043–1047.

(32) P. N. Bartlett and K. F. E. Pratt, *J. Electroanal. Chem.*, 1995, **397**, 61–78.

(33) V. Fourmond, S. Stapf, H. Li, D. Buesen, J. Birrell, O. Rüdiger, W. Lubitz, W. Schuhmann, N. Plumeré and C. Léger, *J. Am. Chem. Soc.*, 2015, **137**, 5494–5505.

(34) Y. Li, Z.-Y. Fu and B.-L. Su, *Adv. Funct. Mater.*, 2012, **22**, 4634–4667.

(35) P. Trogadas, V. Ramani, P. Strasser, T. F. Fuller and M.-O. Coppens, *Angew. Chem. Int. Ed.*, 2015, **54**, 2–29.

(36) K. R. Phillips, G. T. England, S. Sunny, E. Shirman, T. Shirman, N. Vogel and J. Aizenberg, *Chem. Soc. Rev.*, 2016, **45**, 281–322.

(37) M. Kato, T. Cardona, A. W. Rutherford and E. Reisner, *J. Am. Chem. Soc.*, 2012, **134**, 8332–8335.

(38) A. R. Holzwarth, M. G. Müller, M. Reus, M. Nowaczyk, J. Sander and M. Rögner, *Proc. Natl. Acad. Sci. U. S. A.*, 2006, **103**, 6895–6900.

(39) Y. Umena, K. Kawakami, J.-R. Shen and N. Kamiya, *Nature*, 2011, **473**, 55–60.

(40) L. Rapatskiy, N. Cox, A. Savitsky, W. M. Ames, J. Sander, M. M. Nowaczyk, M. Rögner, A. Boussac, F. Neese, J. Messinger and W. Lubitz, *J. Am. Chem. Soc.*, 2012, **134**, 16619–16634.

(41) H. Kuhl, J. Kruip, A. Seidler, A. Krieger-liszkay, M. Bu, D. Bald, A. J. Scheidig and M. Ro, *J. Biol. Chem.*, 2000, **275**, 20652–20659.

(42) J. Kern, B. Loll, C. Lüneberg, D. DiFiore, J. Biesiadka, K.-D. Irrgang and A. Zouni, *Biochim. Biophys. Acta - Bioenerg.*, 2005, **1706**, 147–157.

(43) T. Kothe, S. Pöller, F. Zhao, P. Fortgang, M. Rögner, W. Schuhmann and N. Plumeré, *Chem. Eur. J.*, 2014, **20**, 11029–11034.

(44) A. J. Bard and L. R. Faulkner, *Electrochemical Methods: Fundamentals and Applications*, Wiley, New York, 2nd Edition, 2001, pp. 534–579.

(45) E. Laviron, *J. Electroanal. Chem. Interfacial Electrochem.*, 1979, **101**, 19–28.

(46) N. Lebedev, A. Spano, S. Trammell, I. Griva, S. Tsoi and J. M. Schnur, *Proc. SPIE 6656, Organic Photovoltaics VIII*, 2007, **6656**, 665614.

(47) Y. Y.-H. Lai, M. Kato, D. Mersch and E. Reisner, *Faraday Discuss.*, 2014, **176**, 199–211.

(48) J. Z. Zhang, K. P. Sokol, N. Paul, E. Romero, R. Van Grondelle, E. Reisner, K. P. Sokol, E. Romero, R. Van Grondelle and E. Reisner, *Nat. Chem. Biol.*, 2016, **12**, 1046–1052.

(49) P. Cai, X. Feng, J. Fei, G. Li, J. J. Li, J. Huang and J. J. Li, *Nanoscale*, 2015, **7**, 10908–10911.

(50) M. Suga, F. Akita, K. Hirata, G. Ueno, H. Murakami, Y. Nakajima, T. Shimizu, K. Yamashita, M. Yamamoto, H. Ago and J.-r. Shen, *Nature*, 2014, **517**, 99–103.

(51) S. Khan, J. S. Sun and G. W. Brudvig, *J. Phys. Chem. B*, 2015, **119**, 7722–7728.

(52) E.-M. Aro, I. Virgin and B. Andersson, *Biochim. Biophys. Acta - Bioenerg.*, 1993, **1143**, 113–134.

(53) V. M. Friebe, J. D. Delgado, D. J. K. Swainsbury, J. M. Gruber, A. Chanaewa, R. Van Grondelle, E. Von Hauff, D. Millo, M. R. Jones and R. N. Frese, *Adv. Funct. Mater.*, 2016, **26**, 285–292.

(54) A. Badura, D. Guschin, T. Kothe, M. J. Kopczak, W. Schuhmann and M. Rögner, *Energy Environ. Sci.*, 2011, **4**, 2435–2440.

(55) R. Porra, W. A. Thompson and P. E. Kriedemann, *Biochim. Biophys. Acta - Bioenerg.*, 1989, **975**, 384–394.

Chapter 4

Bias-free photoelectrochemical water splitting with photosystem II on a dye-sensitised photoanode wired to hydrogenase

The content of this chapter has been published in a peer-reviewed article: Nat. Energy, 2018, 3, 944-951. The results presented were obtained by the author of this thesis, except as outlined here: Dr. Nikolay Kornienko is acknowledged for characterising the PSII−dye photoanodes by HAADF-STEM and RRDE.

4.1 Introduction

Semi-artificial photosynthesis bridges the rapidly progressing fields of synthetic biology and artificial photosynthesis, offering a platform for developing and understanding solar fuel generation. [1–4] Synthetic biology has vastly opened up the way Nature can be manipulated to streamline functionality and to build artificial biological systems, but its complex machineries and metabolic pathways limit engineering flexibility. [5] Artificial photosynthesis utilises synthetic, often biomimetic, components to convert and store solar energy, but is often constrained by inefficient catalysis and costly/toxic materials. [6] Semi-artificial photosynthesis aims to integrate the high efficiency and selectivity of enzymes with the controllability of synthetic materials to photocatalyse endergonic reactions in the absence of competing processes. [7] It also allows the construction of biologically-inaccessible pathways with a high level of control and flexibility. [3] The catalytic activity of redox enzymes

can be harnessed when adsorbed on electrodes by protein film electrochemistry (PFE) and photoelectrochemistry (PF-PEC). [8, 9] A key challenge is to design biotic-abiotic interfaces that effectively wire together the biological and synthetic components to operate at their optimum.

Solar-driven water splitting into H_2 and O_2 is the most prominent model reaction in artificial photosynthesis. [10] Inefficient catalysis (particularly, kinetically slow O_2 evolution and formation of partially-oxidised side products) is a major limitation in synthetic systems, resulting in the requirement of large overpotentials and energy conversion losses. [6] Oxygenic organisms convert solar energy using a photosynthetic Z-scheme containing two light absorbers, photosystem (PS) I and II. [11] In this tandem configuration, the first excitation in PSII drives water oxidation to O_2 and produces a proton gradient, whereas the second excitation in PSI generates a low potential electron to drive CO_2 fixation into sugars. [12] Alternatively, H_2 can be produced from microalgae and cyanobacteria, via electron transfer from ferredoxin to a [FeFe]-hydrogenase ([FeFe]-H_2ase), reducing protons to H_2. [13] Efficiencies for photobiological H_2 production are low for several reasons. [14, 15] First, PSII and PSI overlap in light absorption and compete for a small fraction of the solar spectrum. Second, high light intensities limit efficient electron flux up- and down-stream of PSII. Third, *in vivo* H_2 production relies on O_2-sensitive [FeFe]-H_2ases, preventing sustained water splitting. Fourth, CO_2 fixation is preferred over proton reduction leading to low H_2 yields. Overcoming these limitations offers scope for enhancing H_2 production with biological components.

We have previously reported a PEC water splitting system with a PSII photoanode wired to a [NiFeSe]-H_2ase cathode. [3] However, this system relied solely on light absorption by PSII and required an externally applied voltage due to the low electrochemical potential of electrons leaving PSII. This limitation can be resolved by introducing a second light absorber to further promote the energetics of the electrons to be delivered to H_2ase. [16] To generate sufficient driving force for overall water splitting while maximising solar energy harvesting, complementary dual-absorber/tandem systems can be assembled, showing theoretical limits for solar-to-hydrogen (STH) efficiency of up to 25%. [17] PSII [18, 19] and $BiVO_4$ [20] photoanodes wired to PSI photocathodes have been reported to produce electricity, but no chemical fuel. Tandem systems containing PSII have not been combined with enzymatic fuel synthesis. [21–23]

Herein, a semi-artificial system for unassisted photocatalytic water splitting with PSII and H_2ase is presented (Fig. 4.1). This PEC system does not require an external energy input as dual light absorption is realised by a tandem photoanode consisting of PSII wired to a dye-sensitised TiO_2, providing sufficient voltage to reduce protons using a H_2ase cathode.

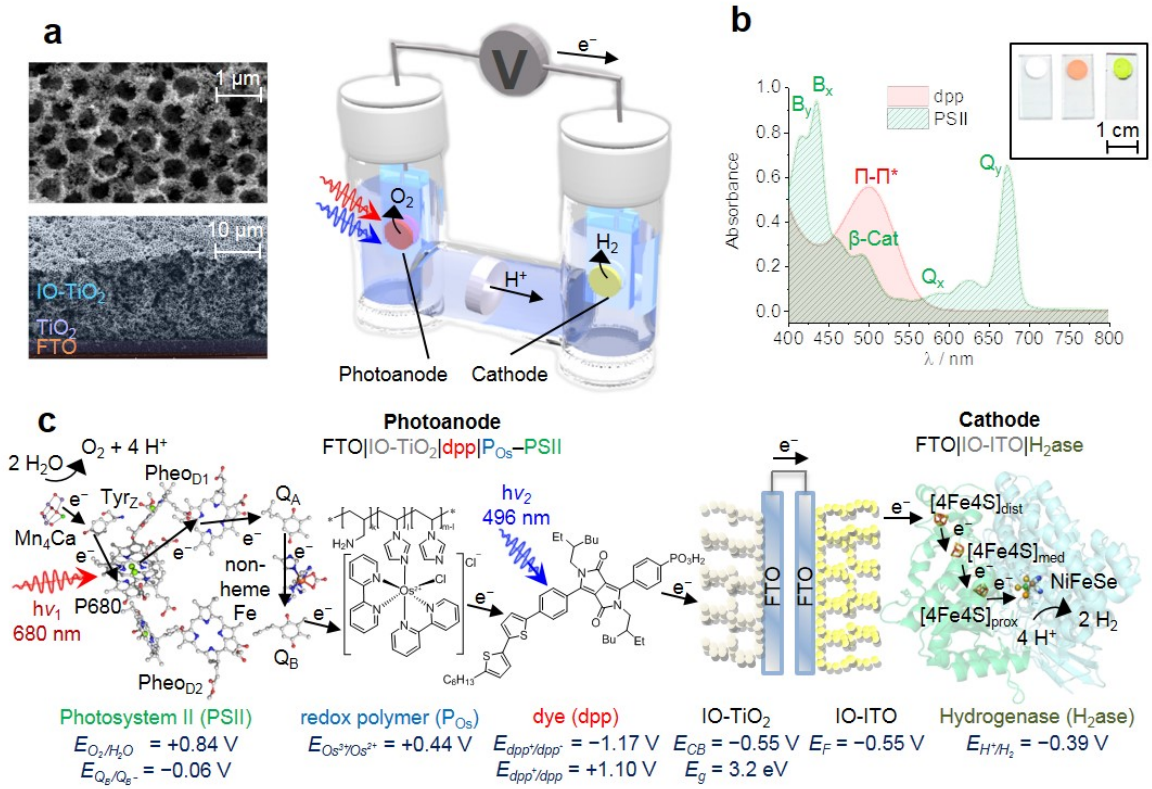

Figure 4.1 **Semi-artificial tandem PEC system for unassisted overall water splitting. a**, Schematic representation of a PEC cell with IO-TiO_2|dpp|P_{Os}−PSII photoanode wired to IO-ITO|H_2ase cathode. SEM images of IO-TiO_2 photoanode architecture (top view and cross-section at 60° tilt angle). **b**, Solution UV-vis spectra of dpp (0.15 μM in THF) and PSII (0.005 mg Chl *a* mL^{-1} in H_2O) with the photographic images of IO-TiO_2, IO-TiO_2|dpp and IO-TiO_2|PSII, quoting from left to right (inset). Absorptions: $B_{y/x}$, chlorophyll *a* Soret-bands; β-Cat, β-carotene; $Q_{x/y}$, chlorophyll *a* lowest-energy bands; $\Pi - \Pi^*$, dpp Π-orbital intramolecular charge transfer. **c**, Electron-transfer pathway between PSII, P_{Os}, dpp, IO-TiO_2, IO-ITO and H_2ase (species size not drawn to scale) and the relevant redox potentials. Abbreviations: Mn_4Ca, oxygen-evolving complex (OEC); Tyr_Z, tyrosine; P680, pigment/primary electron donor; Pheo, pheophytin; Q_A/Q_B, plastoquinones; [NiFeSe], H_2ase active site; [4Fe4S], iron-sulfur clusters; E_g, energy band gap; E_F, Fermi energy level; all potentials reported vs. SHE at pH 6.5. Atom labels (PSII): C (grey), O (red), N (blue), Mn (violet), Ca (green), Mg (light green). Atom labels (H_2ase): S (yellow), Fe (brown), Ni (green), Se (light orange). The figure adapted from Sokol et. al., *Nat. Energy*, 2018, **3**, 944-951.

This PEC design is inspired by dye-sensitised solar cells, [24, 25] and allows replacing PSI by a rationally-designed diketopyrrolopyrrole (dpp) dye with an absorption complementary to PSII. Efficient electronic communication between PSII and dpp was achieved by using the redox polymer poly(1-vinylimidazole-*co*-allylamine)-[Os(bpy)$_2$Cl]Cl (P_{Os}; bpy = 2,2'-bipyridine), which bypasses possible limitations from inefficient interfacial electron transfer. Simultaneously, the hydrogel character of the redox polymer provides a solvated environment for the biocatalyst. A hierarchically-structured inverse opal TiO_2 (IO-TiO_2) scaffold was employed to provide high surface area for effective integration of polymer/PSII.

4.2 Results and discussion

4.2.1 Assembly of the tandem PSII−dye photoanode

The components and assembly of the PEC tandem cell is depicted in Fig. 4.1 and the principle of operation as a semi-artificial Z-scheme is shown in Fig. 4.2. Hierarchically-structured IO-TiO_2 electrodes were assembled on a TiO_2 layer-protected fluorine tin oxide (FTO)-coated glass substrate via a modified co-assembly method (Fig. C.1). [3] The TiO_2 protection layer was used to prevent direct contact of electroactive components (PSII and P_{Os}) with the FTO. The optimal thickness of the IO-TiO_2 film was determined to be 20 μm, based on preliminary electrochemical screening, and was utilised throughout this work. [4] Scanning electron microscopy (SEM) revealed a diameter of 750 nm for the TiO_2 macropores with connecting channels of 150 nm and a mesoporous skeleton with a porosity of approximately 50 nm. The macroporosity permits the penetration of the bulky PSII and P_{Os} ($\sim$20 nm and 16 nm in size, respectively), [3, 4] whereas the mesoporous structure provides enhanced effective surface area for guest adsorption.

Dye-sensitisation of the IO-TiO_2 photoanodes (geometrical surface area, A = 0.25 cm^2) was performed by soaking IO-TiO_2 in a tetrahydrofuran (THF) solution of dpp [26, 27] overnight (Fig. 4.3). The resulting IO-TiO_2|dpp electrodes had a dpp surface loading of 72 $\pm$ 4 nmol cm^{-2} (estimated by spectrophotometry; Fig. C.2), consistent with previously reported loadings of molecular species on mesoporous metal oxide scaffolds. [28] The organic dpp dye was selected for its complementary absorption spectrum to PSII and for its ability to act as an efficient visible-light photosensitiser for TiO_2 in aqueous media, chemisorbing via its phosphonic acid anchoring group. [27] For comparison, electrodes were also prepared using the ruthenium bis(2,2'-bpy)(4,4'-bis(phosphonic acid)-2,2'-bpy) dibromide dye (RuP), [29–32] which is commonly used as a benchmark in aqueous dye-sensitised schemes (Fig. 4.2c and Fig. 4.3).

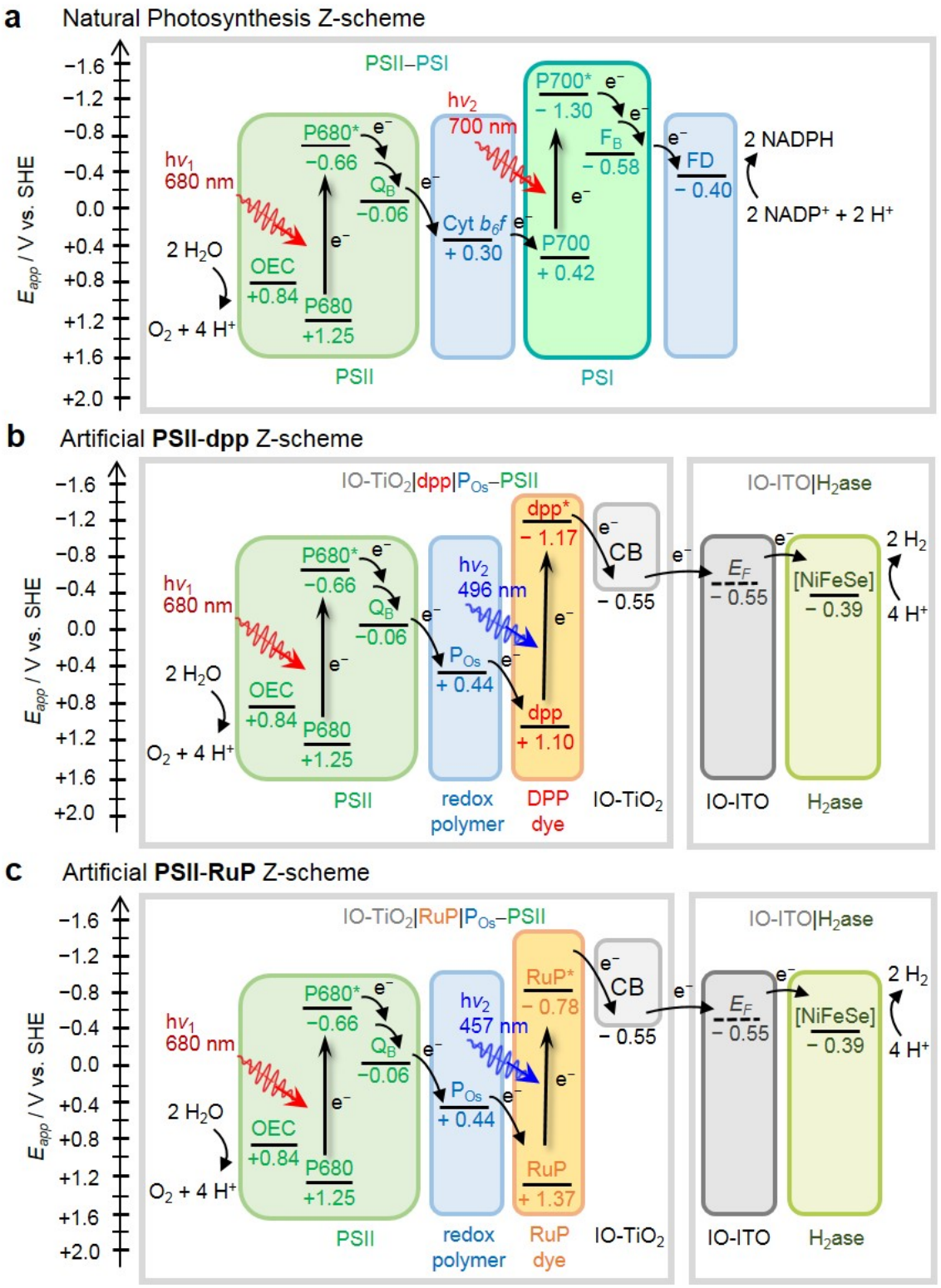

Figure 4.2 **Energy level diagrams. a**, The simplified photosynthetic Z-scheme. **b**, Electron-transfer between PSII, the redox polymer (P_{Os}), the dye (dpp) and the conduction band (CB) of IO-TiO_2 electrode. **c**, Electron-transfer between PSII, P_{Os}, the dye (RuP) and the IO-TiO_2. Abbreviations: E_F, Fermi level; Mn_4Ca, oxygen-evolving complex (OEC); Tyr_Z, tyrosine; P680, pigment/primary electron donor; Pheo, pheophytin; Q_A/Q_B, plastoquinones A and B; [NiFeSe], H_2ase active site; Cyt b_6f, cytochrome b_6f; P700, pigment/primary donor in PSI; F_B, iron sulphur clusters; FD, ferredoxin, $NADP^+$, nicotinamide adenine dinucleotide phosphate. The figure adapted from Sokol et. al., *Nat. Energy*, 2018, **3**, 944-951.

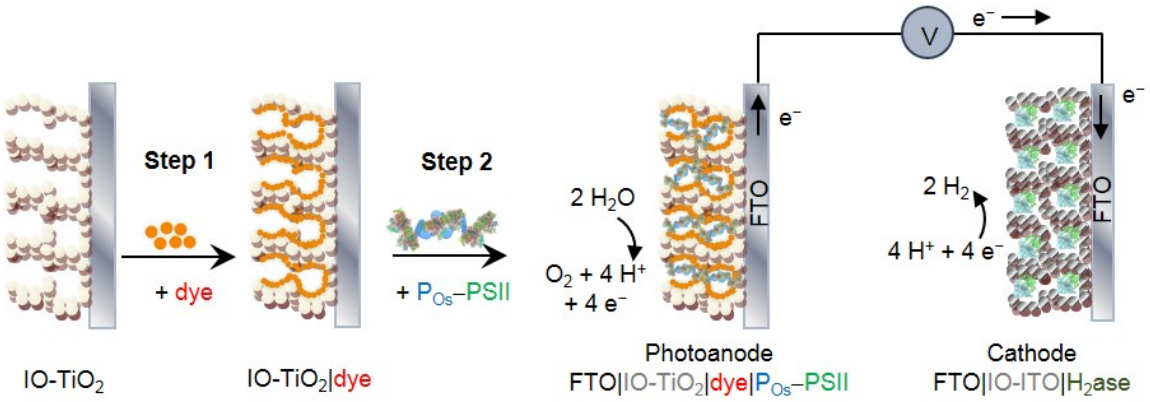

Figure 4.3 **Schematic representation of biotic/abiotic Z-scheme assembly.** Dye deposition (step 1) followed by integration of polymer−PSII blend (step 2) into the IO-TiO_2 electrode. The IO-TiO_2|dye|polymer−PSII photoanode is wired to a IO-ITO|H_2ase cathode (species size not drawn to scale). The figure adapted from Sokol et. al., *Nat. Energy*, 2018, **3**, 944-951.

The macroporous voids of the IO-TiO_2|dpp electrodes were subsequently filled with a blend of PSII and P_{Os} to give the fully-integrated IO-TiO_2|dpp|P_{Os}−PSII tandem photoanode. PSII chosen for this study was isolated from the thermophilic cyanobacterium *Thermosynechococcus elongatus* as a well characterised, [33, 34] highly active and relatively robust PSII variant. [35, 36] Loadings of 24 ± 4 nmol cm^{-2} and 143 ± 25 pmol cm^{-2} were determined by inductively-coupled plasma optical emission spectroscopy (ICP-OES) and Ultraviolet-visible (UV-vis) spectrophotometry for P_{Os} and PSII, respectively (Fig. C.2). The redox polymer P_{Os} mediates electron transfer between PSII and the IO-TiO_2|dpp surface, enhancing their electrical connection, and physically stabilises PSII on the electrode. [4, 37] The integration of all biotic and abiotic components in the hybrid photoanode was further confirmed by high angular annular dark field scanning transmission electron microscopy (HAADF-STEM) (Fig. 4.4).

The UV-vis absorption spectra of dpp, P_{Os} and PSII in solution and individually adsorbed on IO-TiO_2 electrodes were recorded (Fig. 4.2 and Fig. 4.5). IO-TiO_2|PSII displays absorption maxima (λ_{max}) at 450 nm ($B_{x/y}$ Soret bands) and 680 nm (Q_y band), [38] whereas IO-TiO_2|dpp showed a broad absorption from 475 to 575 nm. Thus, the absorption spectra of the co-sensitised IO-TiO_2 electrode demonstrate panchromatic light absorption and highlight the light harvesters' complementarity desired for a semi-artificial Z-scheme. For comparison, the spectrum of RuP (λ_{max} = 457 nm) significantly overlaps with PSII (λ_{max} of $B_{x/y}$ band at 450 nm). The IO-TiO_2|P_{Os} spectrum consisted of a broad and weak absorption, in line with the modest molar absorption of P_{Os} (ε = 8.72 mM^{-1} cm^{-1} at 531 nm), [4] which

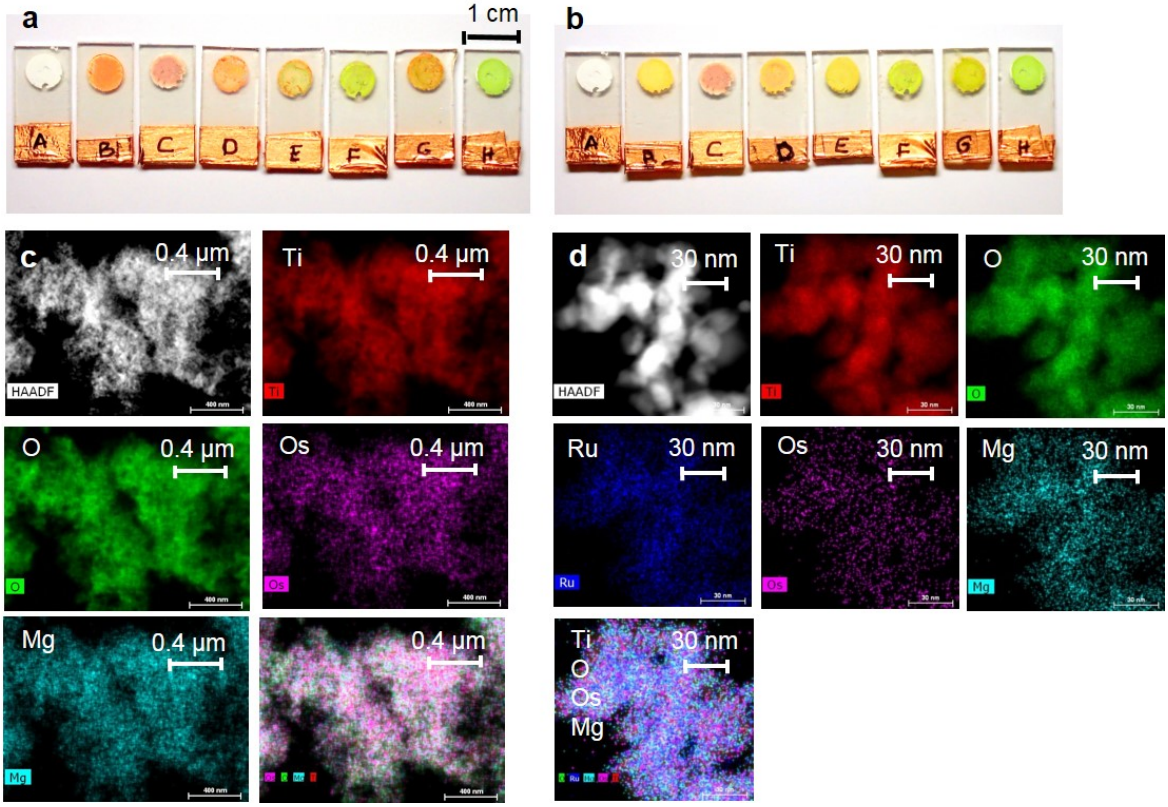

Figure 4.4 **Characterisation of PSII−dye photoanodes by HAADF-STEM. a**, Photographic images of the dpp-sensitised and **b**, RuP-sensitised electrodes, respectively. Sample sets: IO-TiO_2 (A), IO-TiO_2|dye (B), IO-TiO_2|P_{Os} (C), IO-TiO_2|dye|P_{Os} (D), IO-TiO_2|dye|PSII (E), IO-TiO_2|P_{Os}−PSII (F), IO-TiO_2|dye|P_{Os}−PSII (G) and IO-TiO_2|PSII (H). **c**, High-angle annular dark-field scanning transmission electron microscopy (HAADF-STEM) images with EDX elemental analysis indicating the presence of Ti, O (IO-TiO_2), Os (P_{Os}) and Mg (PSII) in the IO-TiO_2|dpp|P_{Os}−PSII, and also **d**, Ru in the IO-TiO_2|RuP|P_{Os}−PSII. Data recorded by Dr. Nikolay Kornienko. The figure adapted from Sokol et. al., *Nat. Energy*, 2018, **3**, 944-951.

is not expected to substantially affect light conversion efficiency in the fully assembled IO-TiO_2|dpp|$_{Os}$−PSII tandem system.

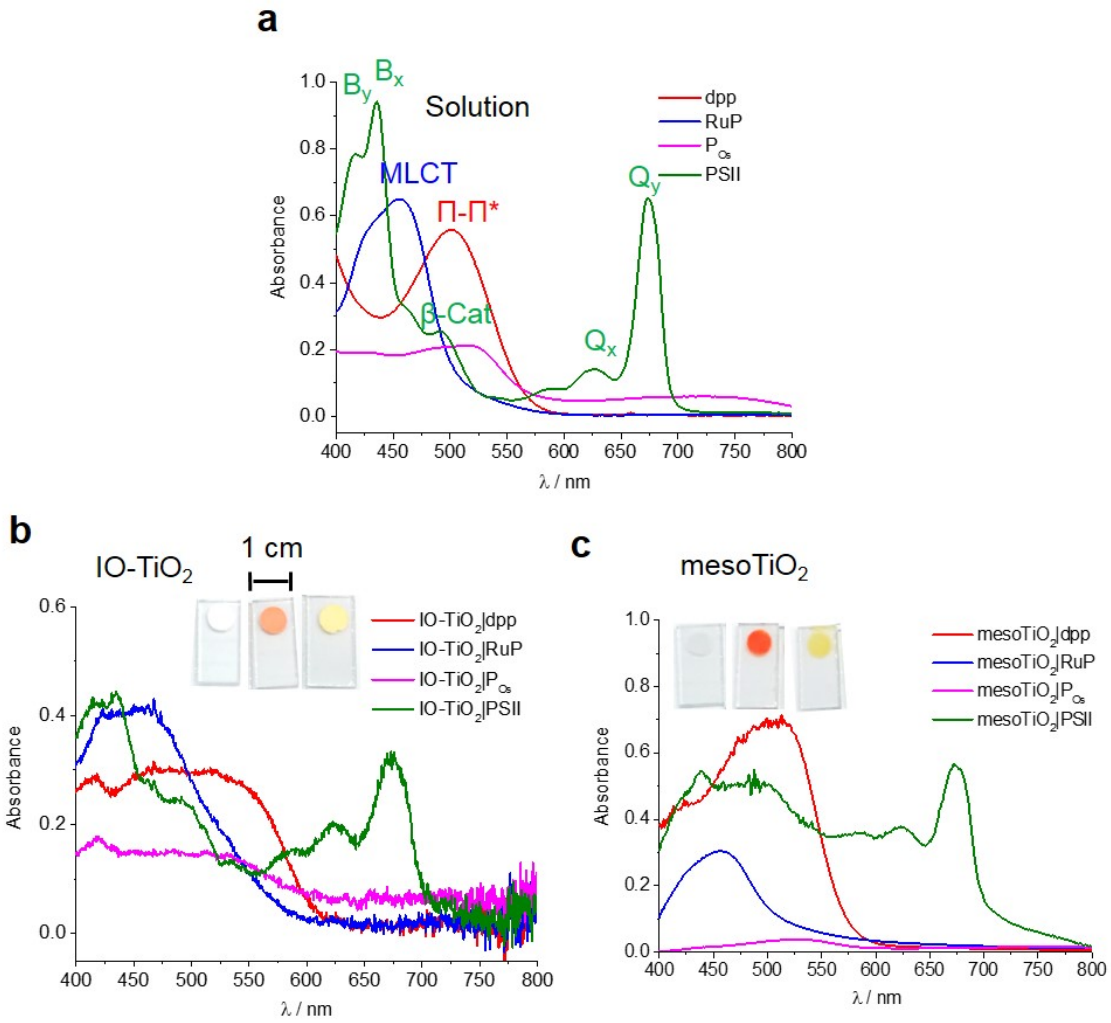

Figure 4.5 **Optical properties of PSII−dye photoanode.** **a**, UV-vis absorption spectra in the electrolyte solution (except dpp recorded in THF). **b**, Background-corrected dpp, RuP, P_{Os} and PSII immobilised on the on the IO-TiO_2 electrodes (integrating sphere). **c**, Mesoporous TiO_2 electrodes (transmittance mode). The broader and red-shifted absorption profile absorption of immobilised dpp compared to dpp in THF solution (λ_{max} = 496 nm) may be due to partial aggregation of dpp on the IO-TiO_2 surface. The figure adapted from Sokol et. al., *Nat. Energy*, 2018, **3**, 944-951.

4.2.2 Photoelectrochemistry

The photocurrent response (J) of IO-TiO_2|dpp|P_{Os}−PSII was recorded by PF-PEC at an applied potential (E_{app}) in a three-electrode configuration. Stepped-potential chronoamperometry under periodic illumination with UV-filtered simulated solar light was used (1.5 AM filter; irradiance E_e = 100 mW cm^{-2}; λ_{max} > 420 nm, Fig. 4.6). Photogenerated electrons in PSII are transferred to the electron acceptor plastoquinone B (Q_B) (Fig. 4.1). [9] The holes are collected at the oxygen-evolving complex (OEC), where water is oxidised to liberate protons and gaseous O_2. The conduction band (CB) of IO-TiO_2 receives electrons from the photoexcited dpp which is thereby oxidised (dpp^+), giving rise to anodic photocurrent. The Os^{3+}-complex embedded in P_{Os} mediates the electrons between reduced Q_B and oxidised dpp to close the electric circuit between the two light absorbers.

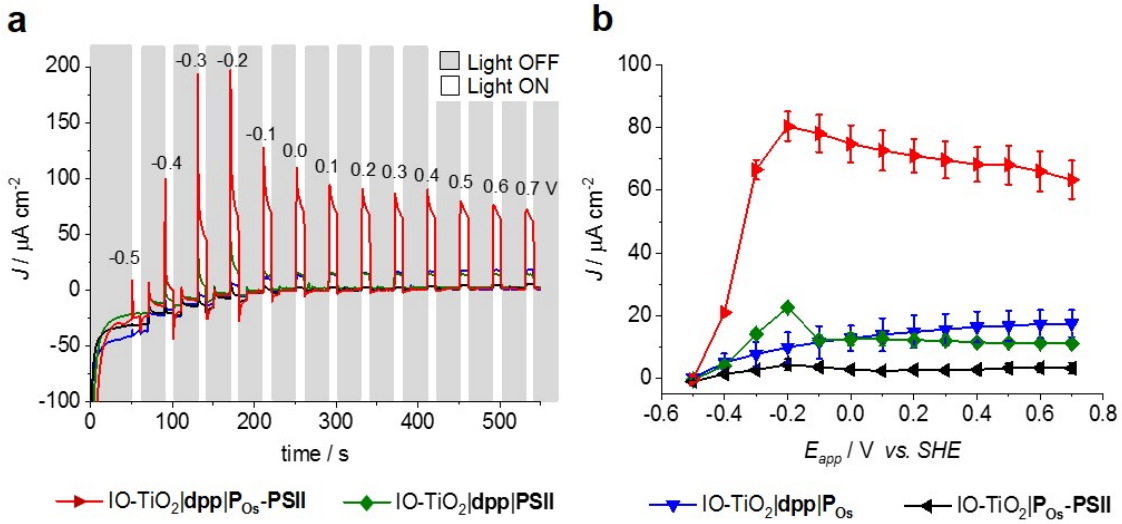

Figure 4.6 **PF-PEC of tandem PSII−dye photoanode.** **a**, Chronoamperometry (0.1 V potential steps with 30 s dark and 10 s light cycles) for the determination of onset potential (E_{onset}) and limiting photocurrent for IO-TiO_2|dpp|P_{Os}−PSII photoanode. E_{app} values (shown on top of the lines) are reported vs. SHE. Short irradiation times were used to minimise PSII photodegradation. **b**, Photocurrent density (J) plotted as function of E_{app} determined by stepped-potential chronoamperometry in **a**. Values of J were taken at the end of illumination (baseline-corrected for background dark current). Error bars correspond to the standard deviation (N = 3). Control experiments omitting one of the components of the tandem photoanode are also presented in **a** and **b** (see figure legend). Conditions: PSII electrolyte solution, pH = 6.5, T = 25 °C. Counter and reference electrodes were a Pt wire and Ag/AgCl (3 M KCl), respectively. The figure adapted from Sokol et. al., *Nat. Energy*, 2018, **3**, 944-951.

The photoanodic current onset potential (E_{onset}) of approximately -0.5 V vs. standard hydrogen electrode (SHE) is consistent with the reported anatase TiO_2 conduction band (CB) edge of approximately -0.6 vs. SHE [39] (Fig. 4.6 and Fig. C.3). The IO-TiO_2|dpp|$P_{Os}-$PSII tandem electrode exhibits a shift of more than 0.5 V towards negative potential compared to single-absorber photoanodes with immobilised PSII, [3, 4, 40] which makes it a promising candidate for bias-free overall water splitting. Potential independent steady-state photocurrents (80 μA cm^{-2}) were observed at $E_{app} > -0.2$ V vs. SHE (Fig. 4.6b) and attributed to water oxidation. [3, 4] Prolonged irradiation at $E_{app} > -0.2$ V vs. SHE results in an irreversible drop in photocurrent, most likely due to PSII photodegradation (irreversible light-induced D1 subunit damage). [4]

Control experiments omitting one component of the tandem photoanode exhibited only a marginal photoactivity. The small background photoresponse for IO-TiO_2|dpp|PSII and IO-TiO_2|dpp|P_{Os} (Fig. 4.6, and similar for IO-TiO_2|dpp, Fig. C.3a,b) can be assigned to stoichiometric electron transfer from photoexcited dpp (dpp*) to TiO_2 without regeneration and photocatalytic turnover of the dye. Low photocurrent in the absence of P_{Os} (IO-TiO_2|dpp|PSII) supports insufficient direct electronic interaction between PSII and dpp without the redox polymer. [4] No significant photocurrents were observed in the absence of dpp (IO-TiO_2|$P_{Os}-$PSII, Fig. 4.6; IO-TiO_2, IO-TiO_2|P_{Os}, IO-TiO_2|PSII, Fig. C.3a,b) consistent with the more positive reduction potentials of PSII's Q_B and P_{Os} relative to the CB of TiO_2, resulting in unfavourable electron transfer. The presented semi-artificial system therefore demonstrates the successful assembly of a functional biotic-abiotic interface for controlled electron-transfer in an artificial Z-scheme. A PSII tandem system based on IO-TiO_2|RuP was also assembled and exhibited a similar behaviour (Fig. C.3c,d). To maximise the performance of the tandem systems, screening of dye loading (Fig. C.4), P_{Os}/PSII ratio (Fig. C.5) and IO-TiO_2 thickness (Fig. C.6) was conducted.

4.2.3 Photocurrent action spectrum

The photocurrent response as a function of irradiation wavelength (the photocurrent action spectrum) was recorded for IO-TiO_2|dye|$P_{Os}-$PSII and relevant control samples (Fig. 4.7a) to characterise the complementary light absorption of the tandem photoanode (Fig. 4.2). In a typical experiment, the wavelength was decreased from 760 to 420 nm (λ_{scan}) at E_{app} = 0.5 V vs. SHE whilst measuring the photocurrent. The action spectra were corrected to equal photon flux at each wavelength and normalised (Fig. C.7 and Fig. C.8).

In agreement with the photocurrent responses under full visible light irradiation (Fig. 4.6), IO-TiO_2, IO-TiO_2|P_{Os}, IO-TiO_2|PSII and IO-TiO_2|$P_{Os}-$PSII gave negligible photocurrents upon monochromatic light illumination across all wavelengths (Fig. 4.7a). PSII-free elec-

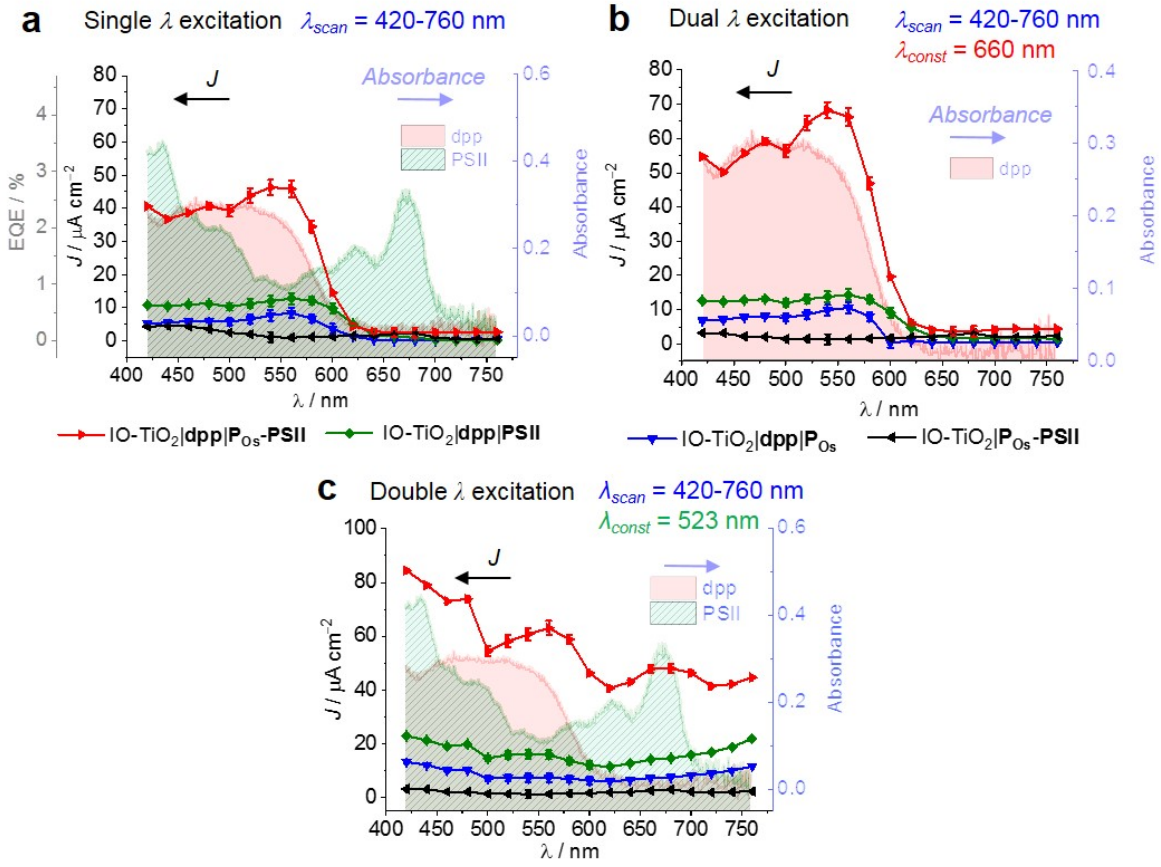

Figure 4.7 **Photocurrent action spectra of tandem PSII−dye photoanode.** **a**, Single-wavelength action spectra of the IO-TiO_2|dpp|P_{Os}−PSII recorded with monochromatic light (λ_{scan}) measured in 20 nm steps from 760 nm to 420 nm (E_e = 6 mW cm^{-2}). The second left y-axis (grey) shows the corresponding external quantum efficiency (EQE) values. **b**, Dual-wavelength action spectra recorded with monochromatic light measured in 20 nm steps (E_e = 6 mW cm^{-2}) and a second simultaneous irradiation at a constant wavelength (λ_{const}) = 660 nm (E_e = 4 mW cm^{-2}) and **c**, λ_{const} = 523 nm (E_e = 4 mW cm^{-2}). The action spectra were normalised to equal photon flux at 500 nm (0.26 mmol m^{-2} s^{-1}). The control experiments (with IO-TiO_2|dpp|PSII, IO-TiO_2|dpp|P_{Os} and IO-TiO_2|P_{Os}−PSII photoanodes) are also given. The right y-axis (blue) refers to the UV-vis spectra of background-corrected dpp and PSII immobilised on the IO-TiO_2 electrodes (shaded in red and turquoise in the background). Conditions for all experiments: PSII electrolyte solution, pH = 6.5, T = 25 °C, E_{app} = 0.5 V vs. SHE. The error bars correspond to the standard deviation (N = 3). The figure adapted from Sokol et. al., *Nat. Energy*, 2018, **3**, 944-951.

trodes loaded with dpp (IO-TiO_2|dpp, IO-TiO_2|dpp|P_{Os}) gave small photocurrent responses concurrent with the absorption spectrum of dpp, consistent with the assignment of background current due to dpp photooxidation (see above). For the functional IO-TiO_2|dpp|P_{Os}−PSII tandem system, the photocurrent onset was observed at λ_{scan} = 620 nm, with a maximum photocurrent at approximately 560 nm. This photoresponse is consistent with the spectral overlap of PSII with dpp and the required simultaneous excitation of both photoactive components. [41] The absence of photocurrent at $\lambda_{scan} > 620$ nm is consistent with the requirement of dpp excitation for electron injection into the CB of TiO_2 and P_{Os} oxidation. An external quantum efficiency (EQE) [21] of 2.7% was obtained at λ_{max}= 560 nm (E_e = 6 mW cm^{-2}).

Dual-wavelength action spectra were also recorded by coupling excitation by the scanned monochromatic light (λ_{scan}) to simultaneous irradiation at a fixed wavelength to continuously excite either PSII (λ_{const}= 660 nm, Fig. 4.7b and Fig. C.8b) or dpp (λ_{const} = 523 nm, Fig. C.8c). Continuous excitation of PSII (thereby probing dpp) in IO-TiO_2|dpp|P_{Os}−PSII (Fig. 4.7b) led to an action spectrum profile (with regard to λ_{scan}) similar to the UV-vis spectrum of dpp and the single-wavelength excitation experiment. In comparison to the latter, a maximum at λ_{scan} = 550 nm was also observed, but with a 40% higher photocurrent magnitude. The overall photocurrent cross-section using dual-excitation (Fig. 4.7b) was approximately two times higher compared to cross-sections of individual components (Fig. 4.7a), confirming the functional and efficient dual-absorber tandem mechanism in the IO-TiO_2|dpp|P_{Os}−PSII (Fig. 4.2).

Continuous excitation of dpp (probing PSII) (Fig. C.8c) resulted in a general increase in photocurrent across all wavelengths (760 to 420 nm) compared to the single-wavelength excitation action spectrum. A new photocurrent maximum was detected at 680 nm, corresponding to the PSII Q_y band. A photocurrent maximum at 550 nm remained, corresponding to higher intensity excitation of the PSII/dpp spectral overlap region, leading to higher photocurrent compared to the single-wavelength experiment. Absorption at 480 nm, corresponding to excitation of the PSII β-carotene, and $\leq$ 420 nm, corresponding to excitation of the B_x and B_y bands, were also observed. Action spectra of the RuP-sensitised photoanodes recorded for comparison (Fig. C.9 and Fig. C.10) also correlated with the UV-vis absorption spectrum of RuP (Fig. 4.5) and exhibited analogous features.

4.2.4 Bias-free overall water splitting via artificial Z-scheme

The negative E_{onset} and broad absorption spectrum of the IO-TiO_2|dpp|P_{Os}−PSII tandem photoanode make it a suitable light absorber for bias-free (unassisted) overall water splitting. To achieve this long-standing goal, [16, 42] the photoanode was wired to a previously reported indium tin oxide (ITO)-based IO-ITO|H_2ase cathode, [3] which utilises a reversible

biological electrocatalyst for H_2 production integrated in a hierarchically-structured ITO electrode. The *Desulfomicrobium baculatum* [NiFeSe]-H_2ase was used for its high proton reduction activity, O_2 tolerance under reductive conditions and marginal inhibition by H_2, offering advantageous properties for water splitting compared to O_2-sensitive [FeFe]-H_2ases available in algal H_2 production. [43] ITO has been shown to be a suitable electrode material for the wiring of [NiFeSe]-H_2ases in a direct electron transfer regime, and the IO-ITO|H_2ase electrode exhibited high current densities for proton reduction (> 400 μA cm^{-2}) and E_{onset} of -0.35 V vs. SHE (pH 6.5; N_2 atmosphere). [3]

Comparison of the voltammetric responses of IO-TiO_2|dpp|P_{Os}−PSII and IO-ITO|H_2ase measured individually (Fig. 4.8) indicate that E_{onset} of the anodic (-0.50 V vs. SHE) and cathodic (-0.35 V vs. SHE) current responses overlap by approximately 0.15 V. [42, 44] Thus, a two-electrode PEC cell consisting of the two enzyme-modified electrodes should be capable of bias-free solar-driven water splitting, assuming only minor resistive solution/membrane losses. [45] Comparison of the current densities indicates that IO-TiO_2|dpp|P_{Os}−PSII should primarily limit the current response when wired to IO-ITO|H_2ase.

A semi-artificial PEC device was therefore assembled consisting of a IO-TiO_2|dpp|P_{Os}−PSII photoanode connected to a IO-ITO|H_2ase cathode separated by a glass frit membrane in a two-electrode, two-compartment cell. Fig. 4.9 demonstrates the ability of the system to achieve bias-free solar-driven water splitting. Chronoamperometry measurements with longer irradiation times (Fig. 4.9a) were performed to minimise the charging effects below an applied voltage (U_{app}) of 0 V. At more positive voltages, the charging effects were decreased and photocurrent responses stabilised. Upon irradiation with UV-filtered simulated solar light, a current density of 28 $\pm$ 5 μA cm^{-2} was achieved at U_{app} = 0 V (Fig. 4.9b). Voltage independent steady-state photocurrents (122 $\pm$ 21 μA cm^{-2}) were reached at U_{app} = 0.3 V. The photocurrent magnitudes were similar to a two-electrode system with a Pt cathode instead of IO-ITO|H_2ase (Fig. 4.10), consistent with photocurrent limitation by IO-TiO_2|dpp|P_{Os}−PSII. A two-electrode system with a IO-TiO_2|H_2ase cathode was also assembled and exhibited a similar behaviour, albeit with less charging due to the matched Fermi levels of IO-TiO_2 (Fig. C.11).

Overall water splitting with the IO-TiO_2|dpp|P_{Os}−PSII ‖ IO-ITO|H_2ase PEC cell was studied at U_{app} = 0.0 and 0.3 V (Fig. 4.11a). At zero bias (U_{app} = 0 V), the initial photocurrent decayed from 130 μA cm^{-2} to 5 μA cm^{-2} after 1 h irradiation, leading to an average half-life time ($\tau_{1/2}$) of 6.5 min. At U_{app} = 0.3 V, the photocurrent decayed from 140 μA cm^{-2} to 15 μA cm^{-2} after 1 h irradiation with a $\tau_{1/2}$ of $\sim$8 min. These lifetimes are similar to previously reported PSII-based photoanodes, [3, 4] and consistent with the stability of PSII *in vivo* ($\tau_{1/2}$ of $\sim$20 min). [9] The relative stability of the IO-TiO_2|dpp|P_{Os}−PSII system

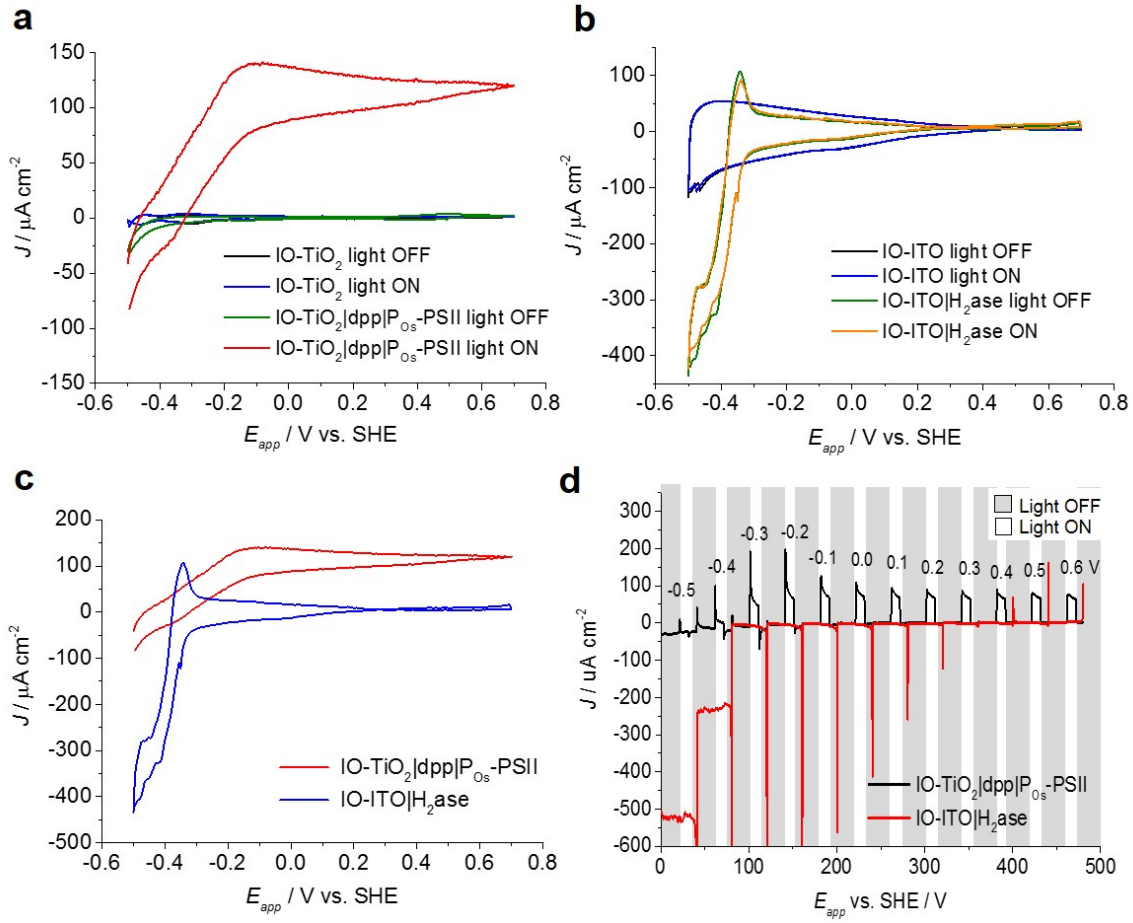

Figure 4.8 **Characterisation of IO-TiO_2|dpp|P_{Os}−PSII photoanode and IO-ITO|H_2ase cathode.** **a**, Cyclic voltammetry (CV) scans (ν = 10 mV s^{-1}) in the dark and upon light irradiation of IO-TiO_2 and IO-TiO_2|dpp|P_{Os}−PSII, and of **b**, IO-TiO_2 and IO-ITO|H_2ase, showing the E_{onset} potentials. **c**, CV scans (ν = 10 mV s^{-1}) of the IO-TiO_2|dpp|P_{Os}−PSII and IO-ITO|H_2ase under illumination, indicating the E_{onset} overlap (reproduced from **a** and **b**). **d**, Stepped-potential (ΔE_{app} = 0.1 V) chronoamperometry, showing the anodic response of IO-TiO_2|dpp|P_{Os}−PSII for water oxidation and the cathodic response of IO-ITO|H_2ase for proton reduction. Conditions: PSII electrolyte solution, pH = 6.5, T = 25 °C, continuous stirring, N_2 atmosphere. Light illumination (1 sun; 1.5 AM filter; E_e = 100 mW cm^{-2}; λ > 420 nm). The error bars correspond to the standard deviation (N = 3). A three-electrode configuration was employed with a Ag/AgCl (3 M KCl) reference and Pt wire counter electrode, respectively. The figure adapted from Sokol et. al., *Nat. Energy*, 2018, **3**, 944-951.

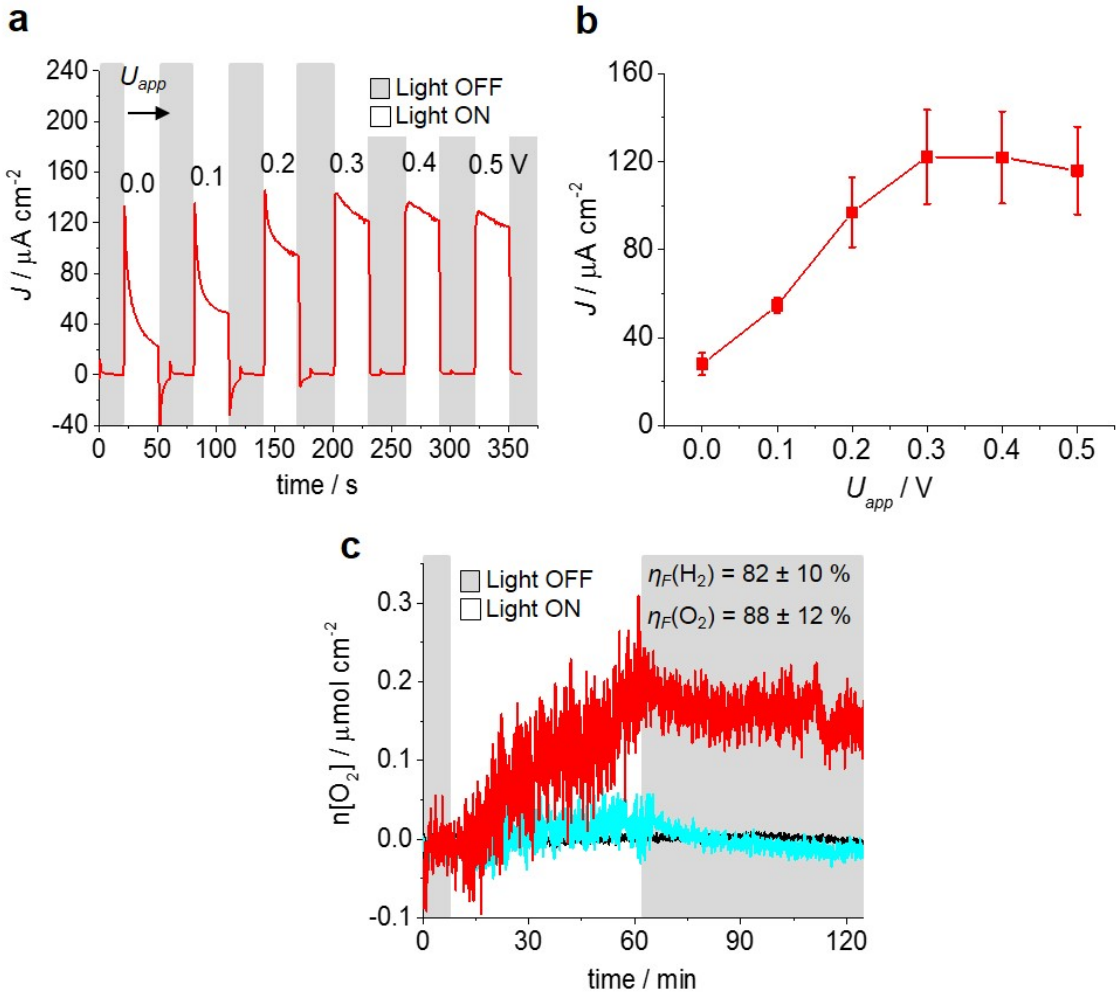

Figure 4.9 **Overall water splitting in semi-artificial PEC cell.** **a**, Chronoamperometry (0.1 V voltage steps with 30 s dark and 30 s light cycles) of the two-electrode IO-TiO_2|dpp|P_{Os}−PSII || IO-ITO|H_2ase cell. Applied voltage (U_{app}) values are shown on top of the lines. **b**, Photocurrent density as a function of U_{app} based on stepped-voltage (ΔU_{app} = 0.1 V) chronoamperometry measurements for IO-TiO_2|dpp|P_{Os}−PSII || IO-ITO|H_2ase determined in **a**. Values of J were taken at the end of illumination (baseline-corrected for background dark current). Error bars correspond to the standard deviation (N = 3). **c**, Quantification of O_2 evolution (η_F = 88 ± 12%; N = 6) of the photoanode after continuous 1 h illumination (AM 1.5G filter; E_e = 100 mW cm^{-2}; $\lambda > 420$ nm) with continuous stirring at U_{app} = 0.3 V (red curve). The amount of H_2 (η_F = 82 ± 10%; N = 6) was quantified by GC analysis. Control experiments in absence of PSII (cyan trace) and without irradiation (black trace) are also shown. Conditions: PSII electrolyte solution, pH = 6.5, T = 25 °C, continuous stirring, N_2 atmosphere. The figure adapted from Sokol et. al., *Nat. Energy*, 2018, **3**, 944-951.

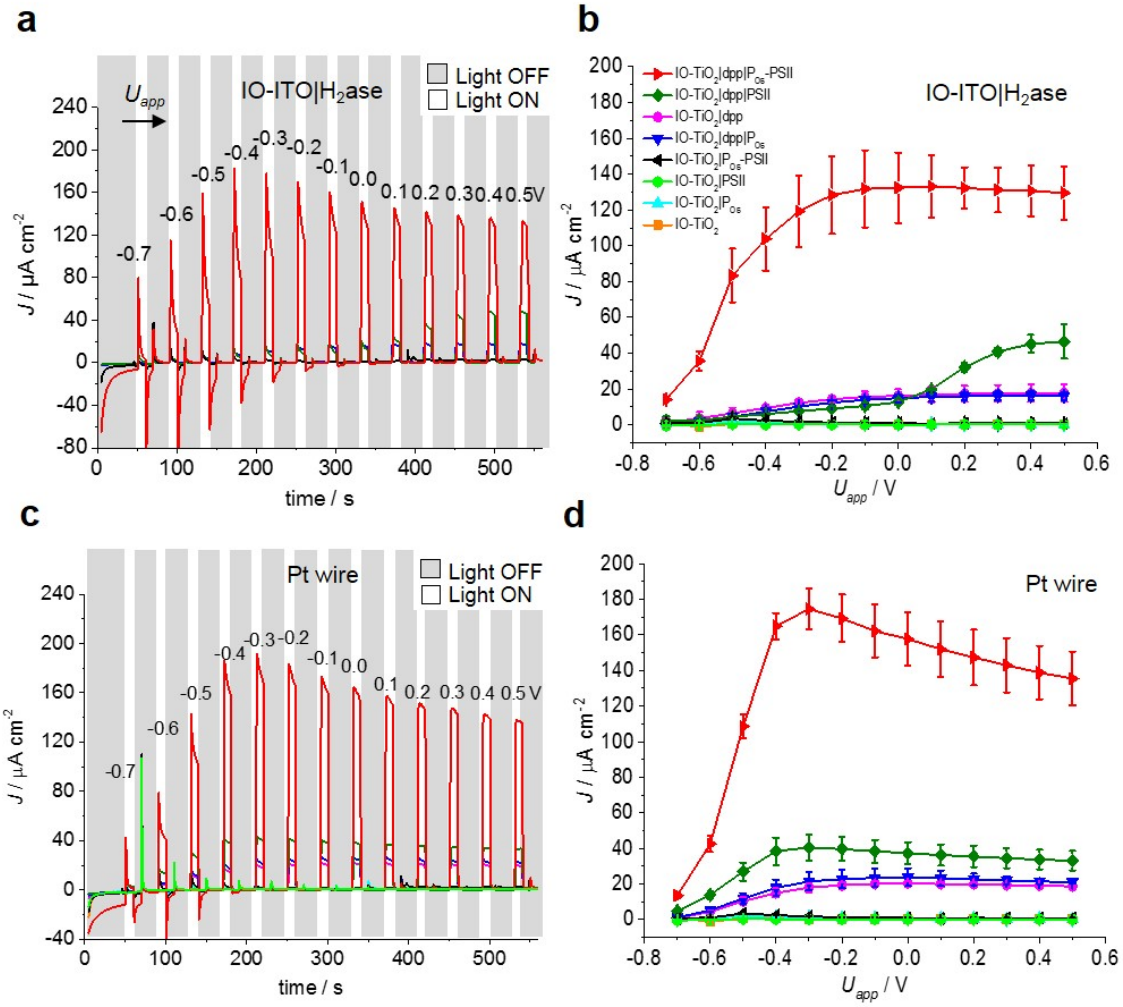

Figure 4.10 **PF-PEC of tandem bias-free two-electrode system. a**, Stepped-voltage (ΔU_{app} = 0.1 V) chronoamperometry (U_{app} = −0.7 to 0.5 V) of the IO-TiO_2|dpp|P_{Os}−PSII photoanode wired to IO-ITO|H_2ase cathode. **b**, Photocurrent density as a function of U_{app} of the IO-TiO_2|dpp|P_{Os}−PSII wired to IO-ITO|H_2ase, based on the stepped-voltage chronoamperometry determined in **a**. **c**, Stepped-voltage (ΔU_{app} = 0.1 V) chronoamperometry (U_{app} = −0.7 to 0.5 V) of the IO-TiO_2|dpp|P_{Os}−PSII photoanode wired to Pt wire cathode. **d**, Corresponding photocurrent density as a function of U_{app} of the IO-TiO_2|dpp|P_{Os}−PSII wired to Pt. Conditions: PSII electrolyte solution, pH = 6.5, T = 25 °C, continuous stirring, N_2 atmosphere. Light illumination (1 sun; 1.5 AM filter; E_e = 100 mW cm^{-2}; $\lambda > 420$ nm). The error bars correspond to the standard deviation (N = 3). The figure adapted from Sokol et. al., *Nat. Energy*, 2018, **3**, 944-951.

can be attributed to the efficient electron transfer between TiO_2−dpp−P_{Os}−PSII, physical stabilisation of PSII by the polymer and reduced accumulation of excited states in Chl *a* within PSII. [46] However, it is important to emphasise that the current hybrid enzyme system is a proof-of-concept device, and its practical applicability is intrinsically limited by the photodegradation pathways of PSII *in vitro*.

After 1 h of continuous light irradiation at U_{app} = 0.0 V, H_2 was detected (0.06 μmol H_2 cm^{-2}) with a Faradaic efficiency (η_F) of 76%, but reliable O_2 analysis was prevented by the detection limit of the apparatus. At U_{app} = 0.3 V, O_2 and H_2 were quantified (Fig. 4.9c) with η_F of 88 ± 12% and 82 ± 10%, respectively (Table. 4.1) and a STH conversion efficiency of 0.14 ± 0.02% was obtained. [47] A PSII-based TOF of 2.5 ± 0.3 mol O_2 (mol PSII)$^{-1}$ s^{-1} was calculated based on quantified O_2 and PSII. [3, 4] Previously, similar η_F values were reported for benchmark PSII-photoanodes: diffusional-mediated IO-ITO|PSII [3] and IO-ITO|P_{Os}−PSII, [4] but required significantly higher driving force (U_{app} = 0.9 V and E_{app} = 0.5 V vs. SHE, respectively). Negligible photocurrents were detected in control experiments (Fig. 4.11b; Table. 4.1). O_2 evolution was also confirmed using a rotating ring-disc electrode (RRDE) setup (Fig. C.12).

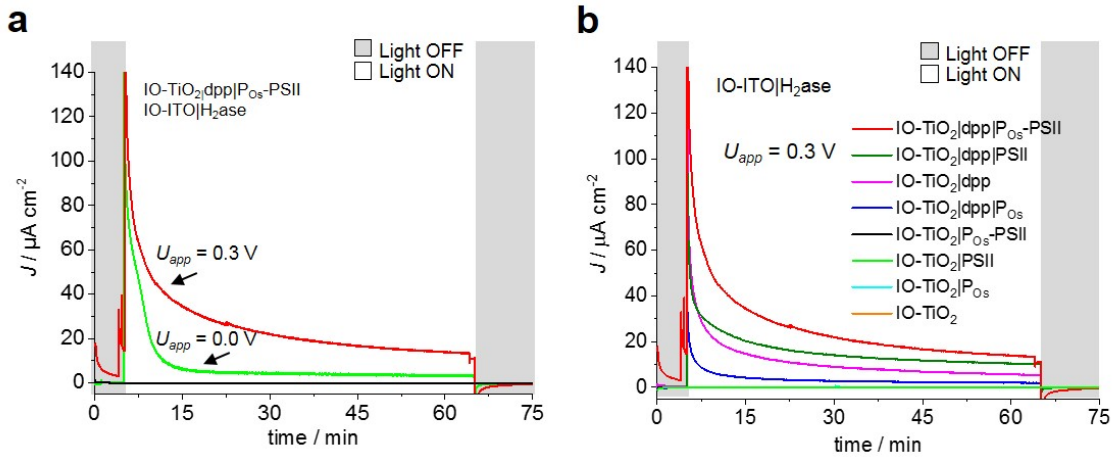

Figure 4.11 **Controlled potential electrolysis in two-electrode system. a**, Chronoamperograms of the IO-TiO_2|dpp|P_{Os}−PSII photoanode during continuous 1 h light illumination wired in a two-electrode configuration to a IO-ITO|H_2ase cathode at U_{app} = 0.0 V and 0.3 V. **b**, Chronoamperograms of the IO-TiO_2|dpp|P_{Os}−PSII photoanode and controls during continuous 1 h light illumination wired in a two-electrode configuration to a IO-ITO|H_2ase cathode at U_{app} = 0.3 V. Conditions: PSII electrolyte solution, pH = 6.5, T = 25 °C, continuous stirring, N_2 atmosphere. Light illumination (1 sun; 1.5 AM filter; E_e = 100 mW cm^{-2}; $\lambda > 420$ nm). We assign a significant contribution from capacitance/charging of the components (primarily ITO, TiO_2 and P_{Os}) to the initial decay, and the second phase to thermodynamic equilibration of the cathode with the anode (Fig. 4.8). The former, the anodic (charging during irradiation) and cathodic (discharging in the dark) current spikes observed at negative voltages (Fig. 4.10), suggest high capacitance and reversible polarisation (charge accumulation) of the cell. The latter may be due to (i) a local increase in H_2 concentration inside the IO-ITO electrode, which causes a cathodic shift of E_{onset} for the bidirectional H_2ase catalyst according to the Nernst equation, and/or (ii) reduction of accumulated O_2 inside the IO-TiO_2 by the photoanode components. The figure adapted from Sokol et. al., *Nat. Energy*, 2018, **3**, 944-951.

Table 4.1 **PF-PEC summary with IO-TiO_2|dpp|P_{Os}−PSII photoanodes.**

IO-TiO_2 system	Three-electrode configuration[1]			Two-electrode configuration[2]		
	E_{onset} / V	$J_{ph}(E_{app}$ = **−0.2 V**) / μA cm^{-2}	EQE_{420nm} / % EQE_{560nm} / % EQE_{680nm} / %	$J_{ph}(U_{app}$ = **0 V**) / μA cm^{-2}	TOF_{PSII} / mol O_2 (mol PSII)$^{-1}$ s^{-1}	$\tau_{1/2}$ / min
dpp|P_{Os}−PSII	−0.5	80.4 ± 4.7	2.5 2.7 0.5	132.4 ± 19.1	2.27 ± 0.29	6.5 (0.0 V) 8.0 (0.3 V)
dpp|PSII	−0.5	22.6 ± 0.2	0.3 0.4 0.0	25.9 ± 16.1	0.49 ± 0.30	1.0
dpp|P_{Os}	−0.5	9.9 ± 4.9	0.5 0.6 0.1	17.6 ± 5.1	n/a	0.8
P_{Os}−PSII	−0.2	2.8 ± 0.9	0.1 0.1 0.1	4.0 ± 3.8	0.08 ± 0.08	0.5
dpp	−0.5	9.1 ± 3.2	0.4 0.6 0.0	19.0 ± 11.3	n/a	0.8
P_{Os}	−0.2	1.0 ± 0.1	n/a	0.3 ± 0.1	n/a	0.0
PSII	−0.2	0.6 ± 0.1	0.1 0.0 0.0	2.6 ± 2.2	0.04 ± 0.04	0.5
blank	−0.1	−0.2 ± 0.1	n/a	1.6 ± 1.35	n/a	0.0

Abbreviations: J_{ph}, photocurrent density (baseline-corrected peak after 10 s light exposure); TOF_{PSII}, initial PSII-based TOF (assuming η_F = 100%); Γ_{PSII}, PSII loading, Γ_{dpp}, dye loading and $\Gamma_{P_{Os}}$, redox-active centres loading. n/a, not applicable; n/d, not determined. The Γ_{dpp} = 72 ± 4 and $\Gamma_{P_{Os}}$ = 24 ± 4 nmol cm^{-2}. The Γ_{PSII} = 132 ± 12 (P_{Os}−PSII), 138 ± 20 (dpp|PSII) and 143 ± 25 pmol cm^{-2} (dpp|P_{Os}−PSII). Conditions: PSII electrolyte solution, pH = 6.5, T = 25 °C, stirring. Illumination conditions (AM 1.5G filter, E_e = 100 mW cm^{-2}, λ > 420 nm), except for the EQE measurements (E_e = 6 mW cm^{-2}, λ monochromatic). [1] Counter and reference electrodes were a Pt wire and Ag/AgCl (3 M KCl), respectively. The E_{app} values are reported vs. SHE. [2] Counter electrode (cathode) was an IO-ITO|H_2ase. The table adapted from Sokol et. al., *Nat. Energy*, 2018, **3**, 944-951.

4.3 Conclusions

The reported enzyme-based tandem PEC system consisting of an IO-TiO_2|dpp|P_{Os}−PSII photoanode connected to a IO-ITO|H_2ase cathode achieves the long-standing goal of a bias-free *in vitro* system for overall water splitting using PSII (O_2 generation) connected to H_2ase (H_2 generation). This semi-artificial design addresses key limitations in biology as PEC wiring of PSII to H_2ase via an abiotic dye allows for: (i) panchromatic solar light absorption by using a synthetic green-light absorber (in contrast to non-complementary absorption by PSI), (ii) quantitative use of electrons extracted from PSII for H_2 production (and thereby avoiding inefficient metabolic pathways), and (iii) separation of H_2 and O_2 gas in separate compartments (as opposed to inhibiting an O_2-sensitive H_2ase).

The tandem system produced H_2 and O_2 from water with high Faradaic efficiencies in 2:1 ratio and presents an effective strategy for constructing biotic-abiotic interfaces. Future work will involve investigating other dyes and replacing TiO_2 with a semiconductor with a more negative CB potential to enhance driving force for more efficient catalysis or CO_2 reduction chemistry. Moreover, our study provides a blueprint for advancing future semi-artificial systems capable of bias-free photocatalysis and a toolbox for developing proof-of-concept model systems for solar energy conversion.

4.4 Experimental section

4.4.1 Materials

All chemicals: 2-(N-morpholino)ethane sulfonic acid (MES, Alfa Aesar), tetrabutylammonium hydroxide (TBAOH, Sigma Aldrich), $CaCl_2$ (Breckland Scientific), $MgCl_2$ (Fisher Scientific), KCl (Alfa Aesar), KOH (Breckland Scientific), polystyrene (PS) beads (Polysciences Inc., 750 nm diameter, 2.6% w/v suspension in H_2O), titanium dioxide (TiO_2) nanoparticles (NPs) (Evonik Industries, Aeroxide® P25 TiO_2 nanoparticles; 21 nm diameter; 80/20 anatase/rutile w/w), indium tin oxide (ITO) NPs (Sigma Aldrich; $\leq$ 50 nm diameter), fluorine-doped tin oxide (FTO) coated glass slides (8 Ω sq^{-1}; Sigma Aldrich) and Parafilm® (Sigma Aldrich) were purchased from commercial suppliers and used without further purification unless otherwise noted. Methanol, absolute ethanol, 2-propanol, dimethyl sulfoxide, tetrahydrofuran (high performance liquid chromatography grade) were purchased from Sigma Aldrich. PSII was isolated from the thermophilic cyanobacterium *Thermosynechococcus elongatus* according to a previously reported procedure, [35] with an average oxygen-evolving activity of approximately 5,300 μmol O_2 h^{-1} mg^{-1} of chlorophyll *a* (Chl *a*). A stock PSII solution containing 2.6 mg Chl *a* mL^{-1} (83 μM PSII) was stored in a

liquid N_2 Dewar. [NiFeSe]-H_2ase from *Desulfomicrobium baculatum* was purified using a previously published method, [48] with a specific activity of 2,115 μmol H_2 min^{-1} mg^{-1}. Stock solutions of H_2ase (8 μM, in 20 mM Tris/HCl buffer, pH 7.0) were stored in 10-20 μL aliquots at -40 °C in an anaerobic glovebox and used immediately after thawing.

4.4.2 Polymer and dye synthesis

Poly(1-vinylimidazole-*co*-allylamine)-[Os(bpy)$_2$Cl]Cl (P_{Os}) [37] was synthesised according to previously reported procedures. [4] In brief, an ethanolic solution of cis-[$OsCl_2$(bpy)$_2$] and poly(1-vinylimidazole-*co*-allylamine) backbone (1/1.65 weight ratio) was stirred for 5 days at 90 °C. P_{Os} was then precipitated by addition of diethyl ether, collected by centrifugation and dried under vacuum to obtain a reddish powder. An aqueous solution of P_{Os} (10 mg mL^{-1}) was used in all experiments. The diketopyrrolopyrrole-based dye (dpp) was synthesised using a previously reported procedure. [27] Briefly, pseudo-Stobbe condensation of 1-bromo-4-cyanobenzene with diethyl succinate was followed by lactam N-alkylation then desymmetrisation of the intermediate via Suzuki–Miyaura cross-coupling. The phosphonic acid anchoring group was then added via Hirao cross-coupling using diethyl phosphite followed by hydrolysis. To obtain ruthenium bis(2,2'-bpy)(4,4'-bis(phosphonic acid)-2,2'-bpy) dibromide (RuP), Me_3SiBr was added to a solution of [Ru(bpy)$_2$(4,4'-(PO_3Et_2)$_2$bpy)](PF_6)$_2$ in dry dimethylformamide and the mixture was heated in the dark at 60 °C for 18 h under Ar then concentrated under vacuum. Methanol was added and the solution was stirred at room temperature for 3 h. The product was precipitated by adding diethyl ether and dried under vacuum to afford [Ru(bpy)2(4,4'-(PO_3H_2)$_2$bpy)](Br)$_2$ (RuP). [29] Both dpp and RuP were characterised as previously reported.

4.4.3 Instrumentation

The surface morphology of the electrodes was analysed by scanning electron microscopy (SEM; SFEG XL30, Philips; acceleration voltage 5 kV; WD 5 mm), energy dispersive X-ray (EDX) spectroscopy attached to the SEM, scanning transmission electron microscopy (STEM; 60-300, TitanX with High Angle Annular Dark Field (HAADF) detector; acceleration voltage 300 kV) and powder X-Ray diffraction (PXRD; Empyrean 2, PANalytics). A centrifuge (5804, Eppendorf), furnace (ELF 11/14B/301, Carbolite), ultrasonicator (DT102H, Sonorex Digitec, Bandelin, Monmouth Scientific) and UV/Ozone cleaner (ProCleaner Plus, BioForce Nanosciences) were used for electrode preparation. UV-vis absorption spectra were recorded on a spectrofluorometer (FS5, Edinburgh Instruments; integrating sphere reflectance mode) and spectrophotometer (Varian Cary 50, Agilent), using cuvettes with an optical path

length of 1 cm (transmittance mode). With the integrating sphere, the measurement was performed by concentrating the light reflected from the electrode on the detector using a polytetrafluoroethylene-coated sphere (120 mm in diameter). The relative reflectance was measured with respect to the reflectance of the reference standard white board, which is taken to be 100%.

4.4.4 Preparation of IO-TiO_2 electrodes

The IO-TiO_2 electrodes were fabricated according to a method adopted from a previously reported procedure for the synthesis of IO-ITO. [3, 4] FTO-coated glass slides (2 $\times$ 1 cm) were cleaned by sonication in two 30 min steps in 2-propanol and absolute ethanol. First, to ensure no direct contact of the electroactive components (PSII and P_{Os}) with the FTO layer, it was coated with a layer of mesoporous TiO_2 (mesoTiO_2). TiO_2 NPs (50 mg) were dispersed via sonication for 20 min in a MeOH/water mixture (300 μL, 5:1 v/v). The suspension (10 μL) was deposited onto a 0.50 cm^2 area defined by a Parafilm® ring on an FTO slide and doctor bladed to give a 3 μm thick mesoTiO_2 layer. The IO-TiO_2 layer was then deposited on top of the mesoTiO_2 layer. TiO_2 NPs (30 mg) were dispersed in a water/MeOH mixture (300 μL, 4:1 v/v) via sonication (3 h). The PS bead dispersion (1 mL) was centrifuged (10,000 r.p.m., 3 min), and the supernatant was removed. The pellet was redispersed in MeOH (1 mL) before being centrifuged again (10,000 r.p.m., 0.5 min). The supernatant was removed and the TiO_2 NPs dispersion was added to the PS pellet. The pellet was dispersed into the solution by sonication (10 min, < 10 °C). The resulting PS-TiO_2 NPs dispersion was drop-cast (5 μL) onto a 0.25 cm^2 area defined by a Parafilm ring on an FTO slide. Following evaporation of the solvent, the electrodes were annealed at a 1 °C min^{-1} ramp rate from room temperature to 500 °C and sintered for 20 min giving a 20 μm thick IO-TiO_2 film. The electrodes were allowed to cool to room temperature and cleaned with an UV/ozone cleaner (15 min) and characterised by SEM and HAADF-STEM, elemental mapping using EDX, and powder XRD (Fig. C.1).

4.4.5 Preparation of IO-TiO_2|dye electrodes

IO-TiO_2 electrodes with a pore diameter of 750 nm, 20 μm film thickness and a geometrical surface area of 0.25 cm^2 were used in all experiments, unless stated otherwise. The IO-TiO_2|dye modified electrodes were prepared by soaking IO-TiO_2 electrodes in solutions of dpp or RuP (0.15 mM in THF/H_2O, respectively) overnight in the dark. To remove excess dye prior to enzyme/polmer deposition, the IO-TiO_2|dpp electrodes were rinsed with THF,

followed by water, then air-dried. Similarly, the IO-TiO_2|RuP electrodes were rinsed with water and air-dried.

4.4.6 Preparation of IO-TiO_2|dye|P_{Os}−PSII electrodes

The IO-TiO_2|dye|P_{Os}−PSII electrodes were prepared by depositing a blend of PSII (1 μL, 2.6 mg Chl *a* mL^{-1}) stock solution and P_{Os} (1 μL, 10 mg mL^{-1}) onto the IO-TiO_2|dye electrode (20 μm thick) and incubating the electrodes in the dark for 15 min at room temperature. Prior to electrochemical studies, the IO-TiO_2|dye|P_{Os}−PSII electrode was rinsed (3 × 500 μL) with the PSII buffer electrolyte solution (composition given below) to remove loosely bound species from the electrode surface.

4.4.7 Determination of PSII, P_{Os} and dye loading on IO-TiO_2

The amount of PSII on the IO-TiO_2 surface was quantified by scratching off the IO-TiO_2 from the FTO glass substrate and washing it with MeOH (500 μL) to extract Chl *a* (originating from PSII) from the electrode surface into a centrifuge vial. The vial was centrifuged (10,000 r.p.m., 1 min), and the UV-vis spectrum of the supernatant was recorded (Fig. C.2b). The band with an absorption maximum of λ_{max} = 665 nm assigned to Chl *a* (extinction coefficient ε = 79.95 (Chl *a* mg)$^{-1}$ mL cm^{-1}) [49] was used to calculate the amount of PSII monomers [49] assuming 35 Chl *a* molecules per PSII monomer. [33] The Os complex loading in the P_{Os} was determined by ICP-OES obtained by washing off the P_{Os} from the IO-TiO_2 electrode with aqueous concentrated HNO_3 solution (70% w/w) and measuring the concentration of the $Os^{3+/2+}$ metal ions relative to Os ICP standard (1 mg Os mL^{-1} in 20% HCl, Ricca Chemical). The dpp/RuP loadings were quantified by scratching off the IO-TiO_2|dye from the glass substrate and washing with TBAOH (0.1 M) in MeOH (500 μL) to extract the dye from the electrode surface into a centrifuge vial. The vial was centrifuged (10,000 r.p.m., 1 min) and the UV-vis spectrum of the supernatant was recorded (Fig. C.2a). The amount of dye desorbed into solution was estimated using the Beer-Lambert Law.

4.4.8 Preparation of IO-ITO|H_2ase electrodes

[NiFeSe]-H_2ase was immobilised on ozone cleaned IO-ITO electrodes (20 μm film thickness, geometrical surface area, A = 0.25 cm^2) by depositing the enzyme solution (5 μL) on the electrode surface, followed by incubation for approximately 5 min. The loading of [NiFeSe]-H_2ase (40 pmol) was adjusted to the electrode thickness, as reported previously. [3]

4.4.9 Protein film photoelectrochemistry (PF-PEC) measurements

Chronoamperometry and cyclic voltammetry (CV) measurements were performed using an Ivium Compactstat potentiostat and a gas-tight two-compartment glass cell with a water jacket for temperature control (T = 25 °C). A three-electrode setup was employed with an IO-TiO_2 (or IO-ITO) working electrode, a Ag/AgCl (3 M KCl) reference electrode and a Pt wire counter electrode separated by a glass frit in another compartment. The cell was filled with a PSII electrolyte solution (12 mL, pH 6.5) consisting of $CaCl_2$ (20 mM), $MgCl_2$ (15 mM), KCl (50 mM), chosen based on electrolyte screening (Fig. C.13). All current densities (μA cm^{-2}) are reported with respect to the geometrical surface area of the electrodes. Experimentally measured potentials are reported vs. SHE using the conversion $E_{SHE} = E_{Ag/AgCl} + 0.197$ V (25 °C).

Bias-free PEC overall water splitting and O_2 and H_2 quantification was studied using a two-electrode configuration with an IO-TiO_2 photoanode containing PSII and an IO-ITO|H_2ase cathode. In all experiments involving IO-ITO|H_2ase cathode, MES (40 mM) was added to the PSII electrolyte solution as it was found to retain H_2ase electroactivity and only caused negligible photocurrents from MES oxidation.

PEC experiments were performed using a Xe lamp (150 W, Newport) Solar Light Simulator (LOT Quantum Design, light intensity flux (irradiance) (E_e) 100 mW cm^{-2}, AM 1.5G filter, $\lambda > 420$ nm filter). Action spectra were recorded with a Xe lamp (300 W, Newport) Solar Light Simulator (LOT Quantum Design) coupled to a monochromator (MSH300, LOT Quantum Design). For dual excitation experiments, an Ivium modulight LED module (λ = 460/523/660 nm; 4 mW cm^{-2}) was used as a second light source. Light intensity was measured as a function of wavelength with a thermal sensor (S302C, Thorlabs) and power meter console (PM100D, Thorlabs)

IO-TiO_2|dye|P_{Os}−PSII electrodes were exposed to dark and light cycles in the PF-PEC measurements. The photocurrent response was defined as the baseline-corrected (dark current-subtracted) photocurrent peak shoulder edge after a light exposure, to avoid overestimation of photocurrent. [9] Action spectra were corrected to equal photon flux at each wavelength and normalised (taking the peak at 500 nm as unity). Error bars are ± sample standard deviation estimated from at least three experiments. All data processing was performed using OriginPro 9.1 software.

RRDE experiments were performed using Ag/AgCl (3 M KCl) reference and glassy carbon counter electrodes. The disk/ring apparatus was embedded in a cylindrical polyether ether ketone housing. A Pt ring electrode surrounded a glassy carbon disk electrode on which a mesoporous TiO_2 layer was deposited prior to depositing additional components (dpp, P_{Os}, PSII). The electrodes were placed in a single-compartment cell under continuous purging

with N_2. The ring-disk electrode was rotated at 400 r.p.m. for O_2 evolution measurements and the collection efficiency of the ring electrode was calibrated under conditions similar to those of the experiment (Fig. C.12).

4.4.10 Product analysis

Quantification of O_2 was performed using a fluorescence-based O_2 sensor (Neofox FOSFOR-R probe, Ocean Optics) inside an anaerobic glovebox (Belle Technology) to avoid ingress of atmospheric O_2. The probe was placed inside the anodic compartment headspace of a two-compartment cell, protected from direct irradiation. The results are reported as the average of six measurements and the background signal was subtracted from all measurements. The reported O_2 values were corrected for dissolved O_2 using Henry's Law ($K_H(O_2)$ = 769.23 L atm mol^{-1} at 25 °C). H_2 was analysed by taking aliquots of the headspace gas (50 μL) after electrolysis and quantified using gas chromatography (GC; 7890 Agilent, carrier gas N_2, flow rate 0.7 mL min^{-1}, molecular sieve column, thermal conductivity detector). Calibration runs were performed to quantify the volume of H_2 evolved. The reported Faradaic efficiencies were corrected by subtracting the dpp dye background current estimated from control experiments from the experimental data.

References

(1) K. K. Sakimoto, A. B. Wong and P. Yang, *Science*, 2016, **351**, 74–77.

(2) O. Yehezkeli, R. Tel-vered, J. Wasserman, A. Trifonov, D. Michaeli, R. Nechushtai and I. Willner, *Nat. Commun.*, 2012, **3**, 742–748.

(3) D. Mersch, C.-Y. Lee, J. Z. Zhang, K. Brinkert, J. C. Fontecilla-Camps, A. W. Rutherford and E. Reisner, *J. Am. Chem. Soc.*, 2015, **137**, 8541–8549.

(4) K. P. Sokol, D. Mersch, V. Hartmann, J. Z. Zhang, M. M. Nowaczyk, M. Rögner, A. Ruff, W. Schuhmann, N. Plumeré and E. Reisner, *Energy Environ. Sci.*, 2016, **9**, 3698–3709.

(5) D. R. Ort, S. S. Merchant, J. Alric, A. Barkan, R. E. Blankenship, R. Bock, R. Croce, M. R. Hanson, J. M. Hibberd, S. P. Long, T. A. Moore, J. Moroney, K. K. Niyogi, M. A. J. Parry, P. P. Peralta-Yahya, R. C. Prince, K. E. Redding, M. H. Spalding, K. J. van Wijk, W. F. J. Vermaas, S. von Caemmerer, A. P. M. Weber, T. O. Yeates, J. S. Yuan and X. G. Zhu, *Proc. Natl. Acad. Sci. U. S. A.*, 2015, **112**, 8529–8536.

(6) Y. Tachibana, L. Vayssieres and J. R. Durrant, *Nat. Photonics*, 2012, **6**, 511–518.

(7) T. W. Woolerton, S. Sheard, Y. S. Chaudhary and F. A. Armstrong, *Energy Environ. Sci.*, 2012, **5**, 7470–7490.

(8) C. Léger and P. Bertrand, *Chem. Rev.*, 2008, **108**, 2379–2438.

(9) M. Kato, J. Z. Zhang, N. Paul and E. Reisner, *Chem. Soc. Rev.*, 2014, **43**, 6485–6497.

(10) A. J. Bard and M. A. Fox, *Acc. Chem. Res.*, 1995, **28**, 141–145.

(11) Govindjee, D. Shevela and L. O. Björn, *Photosynth. Res.*, 2017, **133**, 5–15.

(12) J. Barber and P. D. Tran, *J. R. Soc. Interface*, 2013, **10**, 20120984.

(13) W. Khetkorn, R. P. Rastogi, A. Incharoensakdi, P. Lindblad, D. Madamwar, A. Pandey and C. Larroche, *Bioresour. Technol.*, 2017, **243**, 1194–1206.

(14) O. Kruse, J. Rupprecht, J. H. Mussgnug, G. C. Dismukes and B. Hankamer, *Photochem. Photobiol. Sci.*, 2005, **4**, 957–969.

(15) H. Michel, *Angew. Chem. Int. Ed.*, 2012, **51**, 2516–2518.

(16) B. Esper, A. Badura and M. Rögner, *Trends Plant Sci.*, 2006, **11**, 543–549.

(17) S. Hu, C. Xiang, S. Haussener, A. D. Berger and N. S. Lewis, *Energy Environ. Sci.*, 2013, **6**, 2984–2993.

(18) T. Kothe, N. Plumeré, A. Badura, M. M. Nowaczyk, D. A. Guschin, M. Rögner and W. Schuhmann, *Angew. Chem. Int. Ed.*, 2013, **52**, 14233–14236.

(19) V. Hartmann, T. Kothe, S. Pöller, E. El-Mohsnawy, M. M. Nowaczyk, N. Plumeré, W. Schuhmann and M. Rögner, *Phys. Chem. Chem. Phys.*, 2014, **16**, 11936–11941.

(20) Y. Kim, D. Shin, W. J. Chang, H. L. Jang, C. W. Lee, H.-E. Lee and K. T. Nam, *Adv. Funct. Mater.*, 2015, **25**, 2369–2377.

(21) K. K. Rao, D. O. Hall, N. Vlachopoulos, M. Grätzel, M. C. W. Evans and M. Seibert, *J. Photochem. Photobiol. B*, 1990, **5**, 379–389.

(22) W. Wang, H. Wang, Q. Zhu, W. Qin, G. Han, J.-r. Shen and X. Zong, *Angew. Chem. Int. Ed.*, 2016, **55**, 9229–9233.

(23) R. I. Pinhassi, D. Kallmann, G. Saper, H. Dotan, A. Linkov, A. Kay, V. Liveanu, G. Schuster, N. Adir and A. Rothschild, *Nat. Commun.*, 2016, **7**, 12552.

(24) B. O'Regan and M. Grätzel, *Nature*, 1991, **353**, 737–740.

(25) P. Xu, N. S. McCool and T. E. Mallouk, *Nano Today*, 2017, **14**, 42–58.

(26) J. Warnan, L. Favereau, Y. Pellegrin, E. Blart, D. Jacquemin and F. Odobel, *J. Photochem. Photobiol. A Chem.*, 2011, **226**, 9–15.

(27) J. Warnan, J. Willkomm, J. N. Ng, R. Godin, S. Prantl, J. R. Durrant and E. Reisner, *Chem. Sci.*, 2017, **8**, 3070–3079.

(28) N. M. Muresan, J. Willkomm, D. Mersch, Y. Vaynzof and E. Reisner, *Angew. Chem. Int. Ed.*, 2012, **51**, 12749–12753.

(29) F. Lakadamyali, A. Reynal, M. Kato, J. R. Durrant and E. Reisner, *Chem. Eur. J.*, 2012, **18**, 15464–15475.

(30) R. R. Knauf, M. K. Brennaman, L. Alibabaei, M. R. Norris and J. L. Dempsey, *J. Phys. Chem. C*, 2013, **117**, 25259–25268.

(31) F. Li, K. Fan, L. Wang, Q. Daniel, L. Duan and L. Sun, *ACS Catal.*, 2015, **5**, 3786–3790.

(32) J. Willkomm, K. L. Orchard, A. Reynal, E. Pastor, J. R. Durrant and E. Reisner, *Chem. Soc. Rev.*, 2016, **45**, 9–23.

(33) Y. Umena, K. Kawakami, J.-R. Shen and N. Kamiya, *Nature*, 2011, **473**, 55–60.

(34) L. Rapatskiy, N. Cox, A. Savitsky, W. M. Ames, J. Sander, M. M. Nowaczyk, M. Rögner, A. Boussac, F. Neese, J. Messinger and W. Lubitz, *J. Am. Chem. Soc.*, 2012, **134**, 16619–16634.

(35) H. Kuhl, J. Kruip, A. Seidler, A. Krieger-Liszkay, M. Bünker, D. Bald, A. J. Scheidig and M. Rögner, *J. Biol. Chem.*, 2000, **275**, 20652–20659.

(36) J. Kern, B. Loll, C. Lüneberg, D. DiFiore, J. Biesiadka, K.-D. Irrgang and A. Zouni, *Biochim. Biophys. Acta - Bioenerg.*, 2005, **1706**, 147–157.

(37) A. Badura, D. Guschin, B. Esper, T. Kothe, S. Neugebauer, W. Schuhmann and M. Rögner, *Electroanalysis*, 2008, **20**, 1043–1047.

(38) M. O. Senge, A. A. Ryan, K. A. Letchford, S. A. MacGowan and T. Mielke, *Symmetry*, 2014, **6**, 781–843.

(39) R. Beranek, *Adv. Phys. Chem.*, 2011, **2011**, 80–83.

(40) J. Z. Zhang, K. P. Sokol, N. Paul, E. Romero, R. Van Grondelle, E. Reisner, K. P. Sokol, E. Romero, R. Van Grondelle and E. Reisner, *Nat. Chem. Biol.*, 2016, **12**, 1046–1052.

(41) R. Razeghifard and T. J. Wydrzynski, *Artificial Photosynthesis: From Basic Biology to Industrial Application*, ed. A. F. Collings and C. Critchley, John Wiley & Sons, 2007, pp. 138–140.

(42) E. Reisner, D. J. Powell, C. Cavazza, J. C. Fontecilla-Camps and F. A. Armstrong, *J. Am. Chem. Soc.*, 2009, **131**, 18457–18466.

(43) C. Wombwell, C. A. Caputo and E. Reisner, *Acc. Chem. Res.*, 2015, **48**, 2858–2865.

(44) M. Hambourger, M. Gervaldo, D. Svedruzic, P. W. King, D. Gust, M. Ghirardi, A. L. Moore and T. A. Moore, *J. Am. Chem. Soc.*, 2008, **130**, 2015–2022.

(45) R. H. Coridan, A. C. Nielander, S. A. Francis, M. T. McDowell, V. Dix, S. M. Chatman and N. S. Lewis, *Energy Environ. Sci.*, 2015, **8**, 2886–2901.

(46) P. Cai, X. Feng, J. Fei, G. Li, J. J. Li, J. Huang and J. J. Li, *Nanoscale*, 2015, **7**, 10908–10911.

(47) H. Dotan, N. Mathews, T. Hisatomi, M. Grätzel and A. Rothschild, *J. Phys. Chem. Lett.*, 2014, **5**, 3330–3334.

(48) E. Hatchikian, M. Bruschi and J. Le Gall, *Biochem. Biophys. Res. Commun.*, 1978, **82**, 451–461.

(49) R. Porra, W. A. Thompson and P. E. Kriedemann, *Biochim. Biophys. Acta - Bioenerg.*, 1989, **975**, 384–394.

Chapter 5

Photoreduction of CO_2 with a formate dehydrogenase driven by photosystem II using a semi-artificial Z-scheme architecture

The content of this chapter has been published in a peer-reviewed article: J. Am. Chem. Soc., 2018, 140, 16418–16422. The results presented were obtained by the author of this thesis, except as outlined here: Dr. William Robinson shared the electrochemistry experiments with the author.

5.1 Introduction

In the thylakoid membrane of plants, light-driven water oxidation in the photosynthetic Z-scheme is coupled to CO_2 fixation for sugar synthesis via the dark Calvin-Benson-Bassham (CBB) cycle (Eq. 5.1). [1, 2] Although this solar energy storing reaction is one of the most fundamental processes in biology and essential for life, it also exemplifies inefficiencies of solar-to-fuel conversion. [3] For example, Photosystem II (PSII) and PSI are non-complementary light absorbers, which limits light harvesting efficiency. Ribulose-1,5-bisphosphate carboxylase/oxygenase (RuBisCO) is responsible for CO_2 fixation, but has low turnover rates (1-10 s^{-1}), thereby creating a significant kinetic bottleneck. RuBisCO also reacts with O_2 to produce 2-phosphoglycolate, which must be recycled in energy-demanding, CO_2 evolving, photorespiration. [4, 5] The CBB cycle involves significant adenosine triphosphate (ATP) consumption, which leads to a lower biomass production efficiency compared

to the prokaryotic reductive acetyl-coenzyme A (rAcCoA) pathway. [6] This alternative, light-independent, route to CO_2 fixation uses the energy vector hydrogen as an electron donor to reduce two CO_2 molecules to acetate in a linear sequence of reaction steps. [7]

$$6\,CO_2 + 6\,H_2O + 48\,h\nu \rightarrow C_6H_{12}O_6 + 6\,O_2 \tag{5.1}$$

Addressing the limitations of biological carbon fixation presents several challenges, [8–14] leading research towards *in vitro* (but light-independent) carbon fixation pathways. [15] As bio-inspired alternative, artificial photosynthesis aspires to couple solar light-driven water oxidation and CO_2 reduction to chemical fuels at higher efficiency than natural systems. [16] However, artificial photosynthetic carbon fixation is currently not economically feasible due to a lack of efficient, selective or inexpensive catalysts and light absorbers. [17]

One of the entry points of CO_2 into the rAcCoA pathway is its conversion to formate before transfer to tetrahydrofolate (the second entry point involves its reduction to CO by carbon monoxide dehydrogenase/AcCoA synthase). [7] Coupling this process to light-driven water oxidation is a compelling step towards creating an efficient, artificial photosynthetic carbon fixation pathway. Formate is also a stable intermediate between CO_2 and methanol/methane, a hydrogen carrier and a viable fuel itself. [18, 19] Semi-artificial photosynthesis, in which catalytically efficient redox enzymes are interfaced with synthetic materials, offers a possibility to couple this key entry point of the rAcCoA pathway to light-driven CO_2 reduction and bypass the use of energy-demanding and inefficient ATP.

Mo- and W-dependent formate dehydrogenases (FDHs) are enzymes capable of interconverting CO_2 and formate. [20–28] When adsorbed on an electrode, FDHs from *Syntrophobacter fumaroxidans* [21] and *Escherichia coli* [24, 28] have been shown to perform reversible electrocatalysis with high efficiency through fast interfacial electron transfer. The activity of an Mo-FDH from *E. coli* has been harnessed in fuel cell devices, in which is was immobilised in cobaltocene- and viologen-functionalised redox polymers. [29, 30] Electrochemical CO_2 reduction using a W-FDH has been reported in mediated [31, 32] and unmediated systems. [27] These FDHs contrast with metal-independent FDHs, which reduce CO_2 using nicotinamide adenine dinucleotide (NADH), an unstable, expensive and diffusive cofactor with little driving force. [33–42] To increase the driving force for CO_2 reduction, metal-independent FDHs have been coupled to molecular, [43–46] biological [47, 48] and solid state [38, 41, 49] visible light-absorbers. In addition to the limitations of NADH utilisation, these systems suffered from low selectivity and relied on sacrificial electron donors.

Here, we report a semi-artificial photoelectrochemical (PEC) tandem cell that wires the enzymes PSII to FDH to perform light-driven CO_2 conversion to formate using water as an electron donor (Eq. 5.2). First, we study the CO_2 reduction activity of W-FDH from *Desulfovibrio vulgaris* [50] adsorbed on a hierarchically-structured inverse opal titanium dioxide (IO-TiO_2) scaffold (IO-TiO_2|FDH). The IO-TiO_2|FDH electrode is then wired to a recently reported PSII-based dye-sensitised photoanode IO-TiO_2|dpp|P_{Os}−PSII, which combines PSII isolated from *Thermosynechococcus elongatus*, dpp (phosphonated diketopyrrolopyrrole dye) and P_{Os} [poly(1-vinylimidazole-*co*-allylamine)-[Os(bipy)$_2$Cl]Cl redox polymer] [51] to realise a light-driven rAcCoA pathway by coupling selective CO_2 fixation to light-driven water oxidation (Fig. 5.1).

$$2\,CO_2 + 2\,H_2O + 8\,h\nu \rightarrow 2\,HCO_2^- + O_2 + 2\,H^+ \tag{5.2}$$

5.2 Results and discussion

5.2.1 Tandem PSII−FDH PEC cell design

In this enzyme-catalysed PEC system, photogenerated electrons in PSII, which is embedded in the redox polymer P_{Os}, are transferred to the electron acceptor plastoquinone B (Q_B) (Fig. D.1). The holes are collected at the oxygen-evolving complex (OEC), where water is oxidised to liberate protons and O_2. The Os^{3+} complex in P_{Os} mediates electron transfer between reduced Q_B and oxidised dpp^+. The conduction band (CB) of IO-TiO_2 receives electrons from the photoexcited dpp^*. [51] Electrons are transferred through the external electrical circuit to the IO-TiO_2|FDH cathode and arrive at the CO_2-reducing [WSe]-active site via interfacial electron transfer from the TiO_2 CB to iron-sulfur clusters (Fe_4S_4) which connect the FDH active site to its surface. An analogous system was assembled for comparison using an FDH-modified IO-indium tin oxide (IO-ITO) cathode (IO-ITO|FDH) wired to the IO-TiO_2|dpp|P_{Os}−PSII photoanode (Fig. D.2).

5.2.2 IO-TiO_2|FDH cathode characterisation

Hierarchical macro-mesoporous IO-TiO_2 electrodes (20 μm film thickness; geometrical surface area, A = 0.25 cm^2) were assembled on a fluorine tin oxide (FTO)-coated glass substrate via a previously reported method. [51] An FDH solution (2 μL, 17 μM with 50 mM DL-dithiothreitol, incubated for 10 min) was drop-cast onto IO-TiO_2 to give the

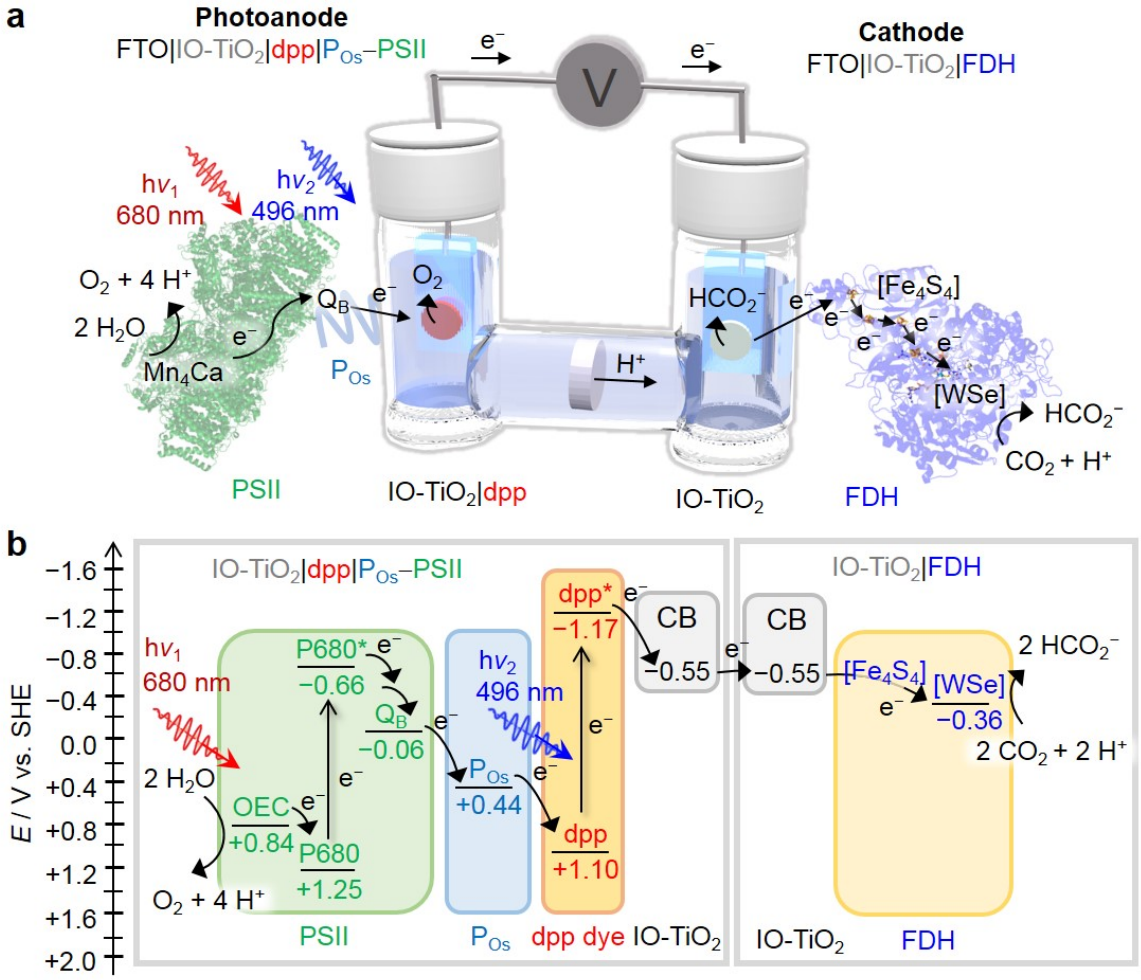

Figure 5.1 **Schematic representation of the semi-artificial photosynthetic tandem PEC cell coupling CO_2 reduction to water oxidation. a,** A blend of P_{Os} and PSII adsorbed on a dpp-sensitised photoanode (IO-TiO_2|dpp|P_{Os}−PSII) is wired to an IO-TiO_2|FDH cathode (species size not drawn to scale). **b,** Energy level diagram showing the electron-transfer pathway between PSII, the redox polymer (P_{Os}), the dye (dpp), the conduction band (CB) of IO-TiO_2 electrodes, four [Fe_4S_4] clusters and the [WSe]-active site in FDH. All potentials are reported vs. SHE at pH 6.5. Abbreviations: Mn_4Ca, oxygen-evolving complex (OEC); P680, pigment/primary electron donor; Q_B, plastoquinone B; [Fe_4S_4], iron-sulfur clusters; [WSe], FDH active site. The figure adapted from Sokol et. al., *J. Am. Chem. Soc.*, 2018, **140**, 16418–16422.

IO-TiO_2|FDH cathode. Anaerobic conditions were employed due to possible O_2 inhibition of FDH and side-reactions of the electrode components with O_2. Cyclic voltammetry (CV) of IO-TiO_2|FDH in a solution of CO_2/$NaHCO_3$ (100 mM, pH 6.5, under 1 atmosphere CO_2), and KCl (50 mM) demonstrated the high CO_2 reduction activity of the electrode (Fig. 5.2a). The current density (J) of IO-TiO_2|FDH was measured as a function of an applied potential (E_{app}) in a three-electrode configuration. The onset potential for CO_2 reduction to formate was observed close to the thermodynamic potential of the CO_2/HCO_2^- couple (-0.36 V vs. standard hydrogen electrode, SHE) at approximately -0.4 V vs. SHE, and a current density of -240 μA cm^{-2} was reached at -0.6 V vs. SHE (see Fig. 5.2b for comparison with an IO-ITO electrode, showing a reversible electrocatalytic wave upon sodium formate addition).

The IO-TiO_2|FDH electrode exhibited good stability, retaining approximately 83% of its initial activity after controlled-potential electrolysis (CPE) over 2 h at $E_{app} = -0.6$ vs. SHE (Fig. 5.2c). The Faradaic efficiency (η_F) of formate production, measured by ion chromatography (IC), was determined as 78 $\pm$ 10% (2.22 $\pm$ 0.23 μmol cm^{-2}). A voltammogram recorded immediately after the CPE experiment indicated similar electrode behaviour as measured before CPE (Fig. 5.2d), though with slightly lower, yet stable, activity. No H_2 production was detectable by gas chromatographic (GC) analysis of the cell headspace, suggesting that the background current was due to charging of the CB of IO-TiO_2 (Fig. 5.2a). [52] The relatively high current densities of the IO-TiO_2|FDH electrode was likely due to high enzyme loading and effective wiring inside the porous hierarchically-structured IO-TiO_2 scaffold. [53, 54] Thus, the cathode proved to be suitable for coupling to PSII-catalysed water oxidation in a two-electrode PEC setup.

5.2.3 Wiring photosynthetic water oxidation to CO_2 reduction

The activity of the IO-TiO_2|dpp|P_{Os}−PSII electrode in CO_2/$NaHCO_3$/KCl electrolyte solution was measured by stepped-potential chronoamperometry under periodic simulated solar illumination (Fig. D.3), showing comparable behaviour to the recently reported PSII-modified dye-sensitised photoanode. [51] The photoanode was electrically wired to the IO-TiO_2|FDH cathode via a potentiostat and the two electrodes were placed in compartments separated by a glass frit membrane in a PEC cell (Fig. 5.1).

Stepped-voltage chronoamperometry under periodic illumination with UV-filtered simulated solar light (AM 1.5G filter; irradiance E_e = 100 mW cm^{-2}; $\lambda > 420$ nm, Fig. 5.3a) was used to study the system's performance. Upon irradiation, a current density of 5.5 $\pm$ 0.4 μA cm^{-2} was achieved at zero applied voltage (U_{app}) = 0 V (Fig. 5.3b inset). Voltage-independent steady-state photocurrents (99 $\pm$ 4 μA cm^{-2}) were reached at $U_{app} > 0.4$ V. Control experiments showed that small background responses were also observed using PSII-

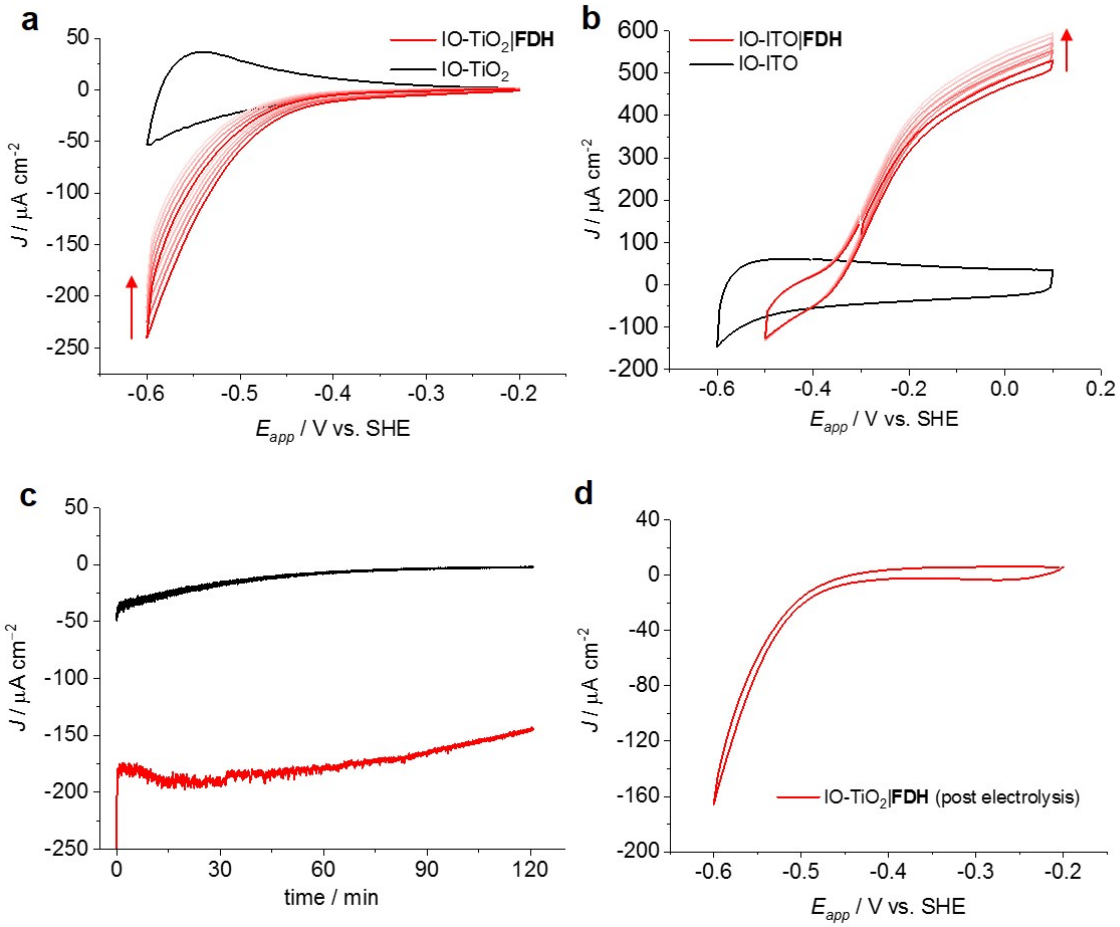

Figure 5.2 **Cyclic voltammetry (CV) of the IO-TiO_2|FDH and IO-ITO|FDH cathode. a**, CV scans (ν = 5 mV s^{-1}) in the dark of IO-TiO_2 (black trace) and IO-TiO_2|FDH (red traces, arrow indicates scan order). **b**, CV scans (ν = 5 mV s^{-1}) in the dark of IO-ITO (black trace) and IO-ITO|FDH (red traces, arrow indicates scan order). Sodium formate added (20 mM). **c**, CPE at $E_{app} = -0.6$ V vs. SHE of the IO-TiO_2 (black trace) and IO-TiO_2|FDH (red trace) electrodes. Formate produced from the IO-TiO_2|FDH electrode was quantified via IC ($\eta_F = 78 \pm 10\%$; N = 3). No formate was detected in the absence of FDH. **d**, CV scan (ν = 5 mV s^{-1}) of the IO-TiO_2|FDH cathode after 2 h electrolysis with continuous stirring at $E_{app} = -0.6$ V vs. SHE, showing the activity retention for CO_2 reduction to formate. Conditions: CO_2/$NaHCO_3$ (100 mM), KCl (50 mM), one atmosphere CO_2, pH = 6.5, T = 25°C, continuous stirring. A three-electrode configuration employed a two-compartment cell with Ag/AgCl (saturated KCl) reference and Pt mesh counter electrodes. The figure adapted from Sokol et. al., *J. Am. Chem. Soc.*, 2018, **140**, 16418–16422.

free IO-TiO_2|dpp photoanodes (Fig. 5.3b, green and black traces) due to electron transfer from photoexcited dpp to TiO_2 without dye regeneration resulting in photobleaching. [51] When FDH was omitted from the system (Fig. 5.3b, blue trace), lower photoresponses were observed than in its presence but the current response was higher than those responses observed in the absence of PSII. This background current is likely due to high capacitance of the high surface area IO-TiO_2 (charging of TiO_2 CB), supported by the cathodic discharging spikes observed upon switching off the light and persisting photocurrents in the chronoamperometry measurements with longer irradiation time (Fig. 5.3c). Substantial capacitance currents over a long timescale consistent with those observed in this study have been previously observed for porous TiO_2 electrodes. [52, 55] At lower applied voltages (U_{app} < 0.4 V), Faradaic current from CO_2 reduction with FDH and some charging of TiO_2 should dominate, whereas at higher applied voltages (U_{app} > 0.5 V), substantial TiO_2 CB charging and possibly electrode degradation (e.g., FTO breakdown) [56, 57] could become significantly competing processes (Fig. D.4a). Stepped-voltage chronoamperometry of the two-electrode system consisting of the IO-TiO_2|dpp|P_{Os}−PSII photoanode wired to the IO-ITO|FDH cathode exhibited similar behaviour, but with significantly more charging at lower applied voltages, further increasing at higher applied voltages, suggesting higher ITO capacitance and possible material degradation (Fig. D.5). [56, 57]

Only a small bias was required to drive the overall reaction (Eq. 5.2) and increasing the electrochemical driving force/decreasing the loss of energy from the photoexcited dye may be achieved by replacing TiO_2 with a semiconductor with a more negative CB potential in future studies. CPE at U_{app} = 0.3 V with the IO-TiO_2|dpp|P_{Os}−PSII || IO-TiO_2|FDH PEC cell under illumination was performed (Fig. 5.3d). The photocurrent decayed from 92 μA cm^{-2} to 7 μA cm^{-2} after 1 h irradiation with a half-life time ($\tau_{1/2}$) of ∼8 min. These values are consistent with a previously reported PSII−H_2ase semi-artificial Z-scheme (average J = 122 μA cm^{-2} and $\tau_{1/2}$ = 8 min). [51] Prolonged irradiation resulted in an irreversible drop in photocurrent, most likely due to PSII photodegradation. [3] Formate was detected (0.185 ± 0.017 μmol cm^{-2}) with a Faradaic efficiency of 70 ± 9%, but reliable O_2 analysis (estimated 0.132 μmol cm^{-2}, 0.01% O_2, assuming quantitative η_F) was prevented by the detection limit of the apparatus. Negligible photocurrents were detected in control experiments omitting FDH. Other products such as H_2 and CO could not be detected in the cathodic chamber. No products (H_2, CO and formate) were observed in control experiments omitting FDH at U_{app} = 0.3 (Figures Fig. 5.3d and Fig. D.4b) and 0.6 V (Figures Fig. D.4a).

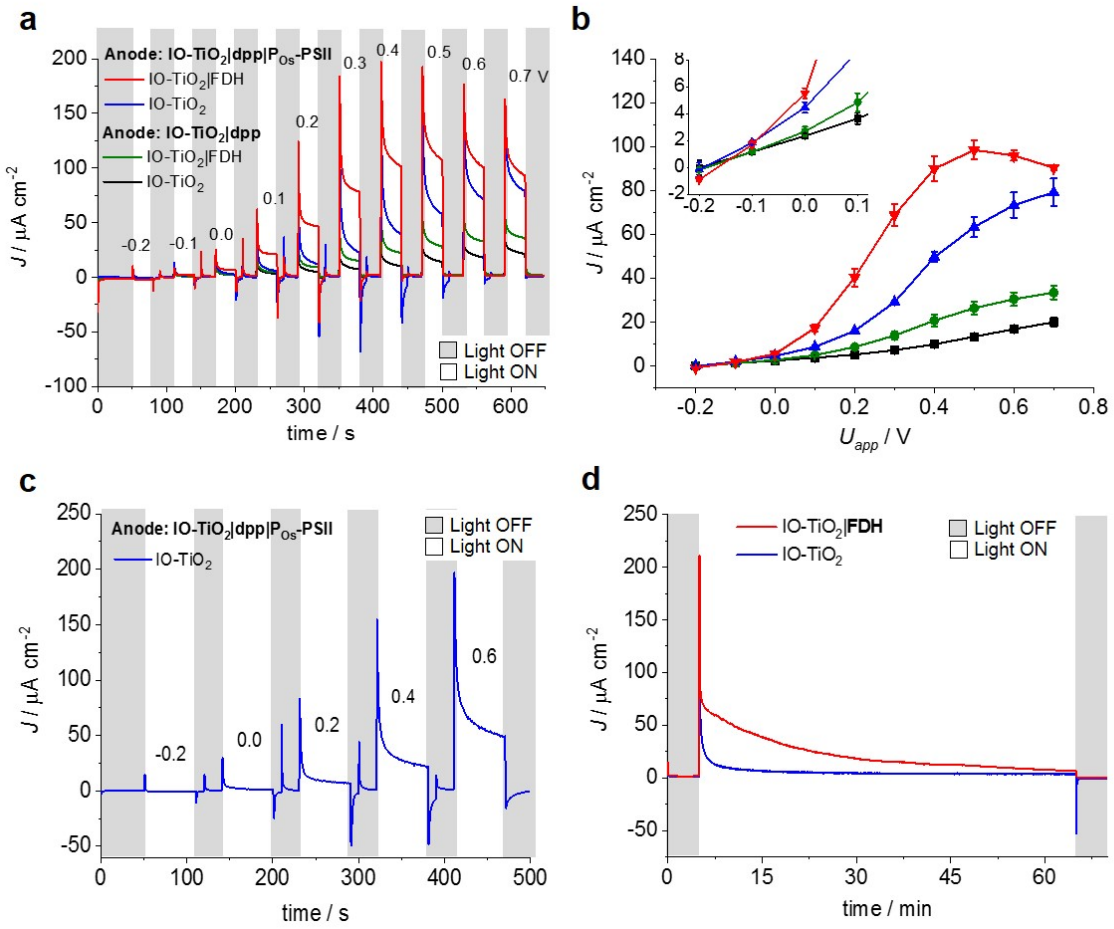

Figure 5.3 **Characterisation of two-electrode PEC cell consisting of IO-TiO_2|FDH cathode wired to IO-TiO_2|dpp|P_{Os}−PSII photoanode.** **a**, Representative stepped-voltage chronoamperometry (0.1 V voltage steps with 30 s dark and 30 s light cycles) of the fully assembled IO-TiO_2|dpp|P_{Os}−PSII || IO-TiO_2|FDH PEC cell (red trace). Control experiments in absence of PSII (green and black trace) and without FDH (blue and black trace) are also shown. Applied voltage (U_{app}) values are shown on top of the traces. **b**, Photocurrent density as a function of U_{app} based on chronoamperometry measurements determined in **a**. Steady-state J values were taken at the end of illumination and baseline-corrected for background dark current. Error bars correspond to the standard deviation (N = 3). Inset: J vs. U_{app} (−0.2 to 0.1 V) zoomed in, indicating close to bias-free capabilities of the device. **c** Stepped-voltage chronoamperometry (0.1 V voltage steps with 30 s dark and 60 s light cycles) of the two-electrode IO-TiO_2|dpp|P_{Os}−PSII || IO-TiO_2 cell. U_{app} values are shown on top of the lines. **d**, CPE (U_{app} = 0.3 V) of the two-electrode PSII−FDH system (red trace) and a similar system in the absence of FDH (blue trace). Formate production was quantified by IC (η_F = 70 ± 9%; N = 3) after 1 h of continuous illumination. No formate was detected in the absence of FDH. Conditions: CO_2/$NaHCO_3$ (100 mM), KCl (50 mM), one atmosphere CO_2, pH = 6.5, T = 25 °C, continuous stirring. Simulated solar light source: (AM 1.5G filter; E_e = 100 mW cm^{-2}; $\lambda > 420$ nm). The figure adapted from Sokol et. al., *J. Am. Chem. Soc.*, 2018, **140**, 16418–16422.

5.3 Conclusions

In summary, we have demonstrated that the IO-TiO_2|dpp|P_{Os}−PSII || IO-TiO_2|FDH PEC cell achieves the biologically and synthetically challenging coupling of solar-driven water oxidation to selective CO_2 reduction with a small additional supply of energy (applied voltage) under mild conditions. The semi-artificial architecture employs efficient enzymes and synthetic components that enable not only complementary light absorption, but also the coupling of unnatural redox partners which is challenging *in vivo*. The PSII−FDH tandem PEC system reported here demonstrates how semi-artificial photosynthesis is a translatable and versatile platform, allowing a variety of electroactive enzymes to be studied electrochemically to gain better understanding of their activity *in vitro*. From a biological perspective, this system can be viewed as an effective model for the light-driven rAcCoA pathway, that bypasses inefficiencies of the Z-scheme and CBB cycle, achieving a metabolically-inaccessible pathway of light-driven CO_2 fixation to formate. From a synthetic point of view, it represents a precious metal-free catalyst proof-of-principle system for solar-driven selective CO_2 to formate conversion using water as an electron donor. Further biologically-relevant electrochemical reactions and redox proteins may be coupled using this approach to introduce a plethora of model systems, which extend solar-driven CO_2 reduction to production of high-value chemicals and value-added precursors.

5.4 Experimental section

5.4.1 Materials

All chemicals: $NaHCO_3$ (Fisher Scientific), CO_2 (BOC), HCO_2Na (Sigma Aldrich), KCl (Sigma Aldrich), DL-Dithiothreitol (DTT, Sigma Aldrich), tetrahydrofuran (high liquid chromatography grade, Sigma Aldrich), polystyrene (PS) beads (Polysciences Inc., 750 nm diameter, 2.6% w/v suspension in H_2O), titanium dioxide (TiO_2) nanoparticles (NPs) (Evonik Industries, Aeroxide® P25 TiO_2 nanoparticles; 21 nm diameter; 80/20 anatase/rutile w/w), indium tin oxide (ITO) NPs (Sigma Aldrich; $\leq$ 50 nm diameter), fluorine-doped tin oxide (FTO) coated glass slides (8 Ω sq^{-1}; Sigma Aldrich) and Parafilm® (Sigma Aldrich) were purchased from commercial suppliers and used without further purification unless otherwise noted. PSII was isolated from the thermophilic cyanobacterium *Thermosynechococcus elongatus* according to a previously reported procedure, [58] with an average oxygen-evolving activity of approximately 5,300 µmol O_2 h^{-1} mg^{-1} of chlorophyll a (Chl *a*). A stock PSII solution containing 2.6 mg Chl *a* mL^{-1} (83 μM PSII) was stored in a liquid N_2 Dewar.

Expression of the tungsten-containing formate dehydrogenase (FDH) from *Desulfovibrio vulgaris* and purification by affinity chromatography followed a previously reported method. [59] Cells expressing StrepII tagged FDH were disrupted in a French pressure cell. The soluble fraction was further clarified by ultra-centrifugation and then directly loaded on a Strep-tactin® gravity flow column (IBA Lifesciences, Germany) equilibrated with Tris-HCl pH 8.0 (100 mM) with 10% (v/v) glycerol, $NaNO_3$ (10 mM) and NaCl (150 mM), hereby referred to as buffer W. After five washing steps with buffer W, the FDH was eluted with buffer W plus d-desthiobiotin (2.5 mM). The buffer of eluted samples was exchanged to Tris-HCl (20 mM), 10% (v/v) glycerol, $NaNO_3$ (10 mM), pH 7.6 for storage. Stock solutions of FDH (34 μM, in a buffer containing 20 mM Tris-HCl, 10% glycerol, 10 mM $NaNO_3$, pH 7.6) were stored at -40 °C in an anaerobic glovebox and used immediately after thawing. The FDH CO_2 reduction activity was determined to be 126 ± 10 μmol HCO_2^- min^{-1} mg^{-1} ($290\ s^{-1}$), by following the oxidation of methyl viologen at 578 nm ($\varepsilon = 9.7\ mM^{-1}\ cm^{-1}$), in phosphate buffer (50 mM) pH 6.9, dithiothreitol (1 mM) and sodium bicarbonate (50 mM).

Poly(1-vinylimidazole-*co*-allylamine)-[Os(bipy)$_2$Cl]Cl (P_{Os}) [60] was synthesised according to previously reported procedures. [54, 61] An aqueous solution of P_{Os} (10 mg mL^{-1}) was used in all experiments. The diketopyrrolopyrrole-based dye (dpp) was synthesised and characterised as reported previously. [62]

5.4.2 Instrumentation

A centrifuge (5804 Eppendorf), furnace (Carbolite, ELF 11/14B/301), ultrasonicator (DT102H, Sonorex Digitec, Bandelin, Monmouth Scientific) and UV/Ozone cleaner (ProCleaner Plus, BioForce Nanosciences) were used for IO-TiO_2 electrode preparation. Enzyme-modified electrodes were prepared in an anaerobic glovebox (MBraun, N_2 filled, <0.1 ppm O_2). Protein film electrochemistry (PFE) and photoelectrochemistry (PF-PEC) were performed using a potentiostat (Compactstat, Ivium) and a gas-tight two-compartment glass cell, prepared and sealed in the glovebox (see above). PF-PEC experiments were performed using a Xe lamp (150 W, Newport) Solar Light Simulator (LOT Quantum Design, light intensity flux (irradiance) (E_e) 100 mW cm^{-2}, AM 1.5G filter, $\lambda > 420$ nm filter). Light intensity was measured with a thermal sensor (S302C, Thorlabs) and power meter console (PM100D, Thorlabs). Ion chromatography (882 compact IC plus, Metrohm) was used to quantify foramate. Gas chromatography (GC; Agilent 7890, carrier gas N_2, flow rate 0.7 mL min^{-1}, molecular sieve column, thermal conductivity detector) was used to test for H_2.

5.4.3 Preparation of IO-TiO_2|dye|P_{Os}−PSII electrodes

IO-TiO_2 electrodes with a pore diameter of 750 nm (20 μm film thickness, geometrical surface area, A = 0.25 cm^2) were fabricated according to previously reported procedure [51] and used in all experiments. IO-TiO_2|dpp modified electrodes were prepared by soaking IO-TiO_2 electrodes in solutions of dpp (0.15 mM in THF) overnight in the dark. The IO-TiO_2|dpp electrodes were then rinsed with THF, followed by water, then air-dried. IO-TiO_2|dpp|P_{Os}−PSII electrodes were prepared in an anaerobic glovebox. A blend of PSII (1 μL, 2.6 mg Chl *a* mL^{-1}) stock solution and P_{Os} (1 μL, 10 mg mL^{-1}) was deposited on the IO-TiO_2|dpp electrode and incubated for 5 min at room temperature. [51]

5.4.4 Preparation of IO-TiO_2|FDH electrodes

FDH (1 μL stock solution) was activated by mixing with DTT (1 μL, 100 mM in water) an incubated (10 min) prior to immobilisation on ozone-cleaned IO-TiO_2 electrodes (20 μm film thickness, geometrical surface area, A = 0.25 cm^2) by depositing the enzyme-DTT solution (2 μL) on the electrode surface, followed by incubation (5 min) under N_2 atmosphere in an anaerobic glovebox.

5.4.5 Protein film electrochemistry and photoelectrochemistry

Cyclic voltammetry was performed in a three-electrode configuration using IO-TiO_2|FDH working electrode, a Ag/AgCl (saturated KCl) reference electrode (BASi, RE-6) and a Pt mesh counter electrode separated by a glass frit in a separate compartment. Each compartment of the cell was filled with 3 mL $NaHCO_3$ (68 mM) and KCl (50 mM) solution, leaving a headspace of 7 mL. The compartments were purged with one atmosphere CO_2, resulting in each compartment containing a solution of KCl (50 mM) and CO_2/$NaHCO_3$ (100 mM) under one atmosphere of CO_2. Continuous stirring without gas purge was applied during the experiment. Stirring induced convection, lowered current limitation by mass transport and aided product dispersion from the electrode surface. Experimentally measured potentials are reported vs. standard hydrogen electrode (SHE), using the conversion $E_{SHE} = E_{Ag/AgCl}$ + 0.197 V (25 °C). [63]

The PF-PEC experiments were performed using a Solar Light Simulator in a two-electrode configuration using an IO-TiO_2|dpp|P_{Os}−PSII (or IO-TiO_2|dpp) photoanode and an IO-TiO_2|FDH (or IO-TiO_2) cathode separated by a glass frit in a separate compartment. Cell solutions were prepared in a similar manner to the 3-electrode experiments described above. IO-TiO_2|dpp|P_{Os}−PSII electrodes were exposed to a 30 s dark and 30 s light cycles, unless

stated otherwise. The photocurrent response was defined as the baseline-corrected (dark current-subtracted) photocurrent after a 30 s light exposure. All current densities (μA cm^{-2}) are reported with respect to the geometrical surface area of the electrodes. Error bars are $\pm$ sample standard deviation estimated from three experiments. All data processing was performed using OriginPro 9.1 software

5.4.6 Product analysis

Formate was analysed by taking aliquots of the electrolyte solution (1 mL from both cell compartments) after electrolysis and quantified using ion chromatography utilising an eluent consisting of Na_2CO_3 (3 mM), $NaHCO_3$ (1 mM) and acetone (50 mL/L). H_2 was analysed by sampling the cell headspace (50 μL) after electrolysis and quantified using gas chromatography. Calibration runs with sodium formate were performed to quantify the amount of formate produced by integration of the formate peak areas. The reported Faradaic efficiencies were corrected by subtracting the IO-TiO_2 background charging current calculated from control experiments.

References

(1) J. A. Bassham, A. A. Benson, L. D. Kay, A. Z. Harris, A. T. Wilson and M. Calvin, *J. Am. Chem. Soc.*, 1954, **76**, 1760–1770.

(2) J. Barber and P. D. Tran, *J. R. Soc. Interface*, 2013, **10**, 20120984.

(3) O. Kruse, J. Rupprecht, J. H. Mussgnug, G. C. Dismukes and B. Hankamer, *Photochem. Photobiol. Sci.*, 2005, **4**, 957–969.

(4) B. J. Walker, A. VanLoocke, C. J. Bernacchi and D. R. Ort, *Annu. Rev. Plant Biol.*, 2016, **67**, 107–129.

(5) T. J. Erb and J. Zarzycki, *Curr. Opin. Biotechnol.*, 2018, **49**, 100–107.

(6) C. A. Cotton, C. Edlich-Muth and A. Bar-Even, *Curr. Opin. Biotechnol.*, 2018, **49**, 49–56.

(7) S. W. Ragsdale and E. Pierce, *Biochim. Biophys. Acta*, 2008, **1784**, 1873–1898.

(8) R. Kebeish, M. Niessen, K. Thiruveedhi, R. Bari, H. J. Hirsch, R. Rosenkranz, N. Stäbler, B. Schönfeld, F. Kreuzaler and C. Peterhänsel, *Nat. Biotechnol.*, 2007, **25**, 593–599.

(9) M. W. Keller, G. J. Schut, G. L. Lipscomb, A. L. Menon, I. J. Iwuchukwu, T. T. Leuko, M. P. Thorgersen, W. J. Nixon, A. S. Hawkins, R. M. Kelly and M. W. W. Adams, *Proc. Natl. Acad. Sci. U. S. A.*, 2013, **110**, 5840–5845.

(10) M. d. Mattozzi, M. Ziesack, M. J. Voges, P. A. Silver and J. C. Way, *Metab. Eng.*, 2013, **16**, 130–139.

(11) P. M. Shih, J. Zarzycki, K. K. Niyogi and C. A. Kerfeld, *J. Biol. Chem.*, 2014, **289**, 9493–9500.

(12) N. E. Kreel and F. R. Tabita, *PLoS One*, 2015, **10**, 1–25.

(13) N. Antonovsky, S. Gleizer, E. Noor, Y. Zohar, E. Herz, U. Barenholz, L. Zelcbuch, S. Amram, A. Wides, N. Tepper, D. Davidi, Y. Bar-On, T. Bareia, D. G. Wernick, I. Shani, S. Malitsky, G. Jona, A. Bar-Even and R. Milo, *Cell*, 2016, **166**, 115–125.

(14) H. Yu, X. Li, F. Duchoud, D. S. Chuang and J. C. Liao, *Nat. Commun.*, 2018, **9**, 1–10.

(15) T. Schwander, S. Burgener and T. J. Erb, *Science*, 2016, **354**, 900–904.

(16) W. Tu, Y. Zhou and Z. Zou, *Adv. Mater.*, 2014, **26**, 4607–4626.

(17) J. H. Montoya, L. C. Seitz, P. Chakthranont, A. Vojvodic, T. F. Jaramillo and J. K. Nørskov, *Nat. Mater.*, 2016, **16**, 70–81.

(18) B. Loges, A. Boddien, H. Junge and M. Beller, *Angew. Chem. Int. Ed.*, 2008, **47**, 3962–3965.

(19) M. F. Kuehnel, D. W. Wakerley, K. L. Orchard and E. Reisner, *Angew. Chem. Int. Ed.*, 2015, **54**, 9627–9631.

(20) A. Graentzdoerffer, D. Rauh, A. Pich and J. R. Andreesen, *Arch. Microbiol.*, 2003, **179**, 116–130.

(21) T. Reda, C. M. Plugge, N. J. Abram and J. Hirst, *Proc. Natl. Acad. Sci. U. S. A.*, 2008, **105**, 10654–10658.

(22) T. Hartmann and S. Leimkühler, *FEBS J.*, 2013, **280**, 6083–6096.

(23) K. Schuchmann and V. Müller, *Science*, 2013, **342**, 1382–1386.

(24) A. Bassegoda, C. Madden, D. W. Wakerley, E. Reisner and J. Hirst, *J. Am. Chem. Soc.*, 2014, **136**, 15473–15476.

(25) L. B. Maia, L. Fonseca, I. Moura and J. J. G. Moura, *J. Am. Chem. Soc.*, 2016, **138**, 8834–8846.

(26) X. Yu, D. Niks, A. Mulchandani and R. Hille, *J. Biol. Chem.*, 2017, **292**, 16872–16879.

(27) K. Sakai, Y. Kitazumi, O. Shirai, K. Takagi and K. Kano, *Electrochem. Commun.*, 2017, **84**, 75–79.

(28) W. E. Robinson, A. Bassegoda, E. Reisner and J. Hirst, *J. Am. Chem. Soc.*, 2017, **139**, 9927–9936.

(29) M. Yuan, S. Sahin, R. Cai, S. Abdellaoui, D. P. Hickey, S. D. Minteer and R. D. Milton, *Angew. Chem. Int. Ed.*, 2018, 6582–6586.

(30) S. Sahin, R. Cai, R. D. Milton, S. Abdellaoui, F. C. Macazo and S. D. Minteer, *J. Electrochem. Soc.*, 2018, **165**, 109–113.

(31) K. Sakai, Y. Kitazumi, O. Shirai, K. Takagi and K. Kano, *Electrochem. Commun.*, 2016, **73**, 85–88.

(32) K. Sakai, Y. Kitazumi, O. Shirai and K. Kano, *Electrochem. Commun.*, 2016, **65**, 31–34.

(33) S. Kuwabata, R. Tsuda, K. Nishida and H. Yoneyama, *Chem. Lett.*, 1993, **22**, 1631–1634.

(34) S. Kuwabata, R. Tsuda and H. Yoneyama, *J. Am. Chem. Soc.*, 1994, **116**, 5437–5443.

(35) S. Schlager, L. M. Dumitru, M. Haberbauer, A. Fuchsbauer, H. Neugebauer, D. Hiemetsberger, A. Wagner, E. Portenkirchner and N. S. Sariciftci, *ChemSusChem*, 2016, **9**, 631–635.

(36) Y. Amao and N. Shuto, *Res. Chem. Intermed.*, 2014, **40**, 3267–3276.

(37) H. Hwang, Y. J. Yeon, S. Lee, H. Choe, M. G. Jang, D. H. Cho, S. Park and Y. H. Kim, *Bioresour. Technol.*, 2015, **185**, 35–39.

(38) S. Y. Lee, S. Y. Lim, D. Seo, J. Y. Lee and T. D. Chung, *Adv. Energy Mater.*, 2016, **6**, 1502207.

(39) S. Kim, M. K. Kim, S. H. Lee, S. Yoon and K. D. Jung, *J. Mol. Catal. B Enzym.*, 2014, **102**, 9–15.

(40) S. Srikanth, M. Maesen, X. Dominguez-Benetton, K. Vanbroekhoven and D. Pant, *Bioresour. Technol.*, 2014, **165**, 350–354.

(41) D. H. Nam, S. K. Kuk, H. Choe, S. Lee, J. W. Ko, E. J. Son, E. G. Choi, Y. H. Kim and C. B. Park, *Green Chem.*, 2016, **18**, 5989–5993.

(42) S. H. Kim, G. Y. Chung, S. H. Kim, G. Vinothkumar, S. H. Yoon and K. D. Jung, *Electrochim. Acta*, 2016, **210**, 837–845.

(43) R. Miyatani and Y. Amao, *Biotechnol. Lett.*, 2002, **24**, 1931–1934.

(44) Y. Amao, S. Takahara and Y. Sakai, *Int. J. Hydrogen Energy*, 2014, **39**, 20771–20776.

(45) S. Ikeyama and Y. Amao, *Sustain. Energy Fuels*, 2017, **1**, 1730–1733.

(46) T. Noji, T. Jin, M. Nango, N. Kamiya and Y. Amao, *ACS Appl. Mater. Interfaces*, 2017, **9**, 3260–3265.

(47) I. Tsujisho, M. Toyoda and Y. Amao, *Catal. Commun.*, 2006, **7**, 173–176.

(48) M. Ihara, Y. Kawano, M. Urano and A. Okabe, *PLoS One*, 2013, **8**, 1–8.

(49) S. K. Kuk, R. K. Singh, D. H. Nam, R. Singh, J. K. Lee and C. B. Park, *Angew. Chem. Int. Ed.*, 2017, **56**, 3827–3832.

(50) S. M. da Silva, J. Voordouw, C. Leitão, M. Martins, G. Voordouw and I. A. Pereira, *Microbiology.*, 2013, **159**, 1760–1769.

(51) K. P. Sokol, W. E. Robinson, J. Warnan, N. Kornienko, M. M. Nowaczyk, A. Ruff, J. Z. Zhang and E. Reisner, *Nat. Energy*, 2018, **3**, 944–951.

(52) T. E. Rosser, M. A. Gross, Y. H. Lai and E. Reisner, *Chem. Sci.*, 2016, **7**, 4024–4035.

(53) D. Mersch, C.-Y. Lee, J. Z. Zhang, K. Brinkert, J. C. Fontecilla-Camps, A. W. Rutherford and E. Reisner, *J. Am. Chem. Soc.*, 2015, **137**, 8541–8549.

(54) K. P. Sokol, D. Mersch, V. Hartmann, J. Z. Zhang, M. M. Nowaczyk, M. Rögner, A. Ruff, W. Schuhmann, N. Plumeré and E. Reisner, *Energy Environ. Sci.*, 2016, **9**, 3698–3709.

(55) J. J. Leung, J. Warnan, D. H. Nam, J. Z. Zhang, J. Willkomm and E. Reisner, *Chem. Sci.*, 2017, **8**, 5172–5180.

(56) J. D. Benck, B. A. Pinaud, Y. Gorlin and T. F. Jaramillo, *PLoS One*, 2014, **9**, 1–13.

(57) S. Geiger, O. Kasian, A. M. Mingers, K. J. Mayrhofer and S. Cherevko, *Sci. Rep.*, 2017, **7**, 3–9.

(58) H. Kuhl, J. Kruip, A. Seidler, A. Krieger-Liszkay, M. Bünker, D. Bald, A. J. Scheidig and M. Rögner, *J. Biol. Chem.*, 2000, **275**, 20652–20659.

(59) M. C. Marques, C. Tapia, O. Gutiérrez-Sanz, A. R. Ramos, K. L. Keller, J. D. Wall, A. L. De Lacey, P. M. Matias and I. A. Pereira, *Nat. Chem. Biol.*, 2017, **13**, 544–550.

(60) A. Badura, D. Guschin, B. Esper, T. Kothe, S. Neugebauer, W. Schuhmann and M. Rögner, *Electroanalysis*, 2008, **20**, 1043–1047.

(61) F. Conzuelo, N. Marković, A. Ruff and W. Schuhmann, *Angew. Chem. Int. Ed.*, 2018, **57**, 13681–13685.

(62) J. Warnan, J. Willkomm, J. N. Ng, R. Godin, S. Prantl, J. R. Durrant and E. Reisner, *Chem. Sci.*, 2017, **8**, 3070–3079.

(63) A. J. Bard and L. R. Faulkner, *Electrochemical Methods: Fundamentals and Applications*, Wiley, New York, 2nd Edition, 2001, pp. 534–579.

Chapter 6

Conclusions

The aim of this thesis was to develop versatile and translatable semi-artificial PEC platforms capable of coupling selective and efficient enzymatic reactions, providing a blueprint for artificial photosynthetic and solar fuel generation devices. Demonstrated model systems established a design protocol for bias-free semi-artificial Z-schemes *in vitro* and an extended toolbox of biotic and abiotic components to re-engineer photosynthetic pathways.

6.1 Summary

First, new types of hierarchically-structured macro-mesoporous IO-ITO and IO-TiO_2 electrodes with varying macropore (0.75, 3 and 10 μm) and channel sizes (0.15, 1 and 3 μm, respectively), tuneable film thickness (2-80 μm) and mesoporous features (10-50 nm) were developed and optimised. The co-assembly and infiltration methods were explored to tune the macroporosity of IO-ITO electrodes by changing the PS bead template, giving rise to 3 μm and 10 μm pore diameter architectures. The IO-ITO mesporosity was tuned by employing various size monodispersed ITO NPs. Fabrication of the 0.75 μm pore diameter IO-TiO_2 electrode introduced a stable cost-effective material. This study provided tools to move towards better control over the IO electrode architecture. The systematic approach enabled to find correlation between the host electrode architecture and biological guest dimensions. [1, 2]

Then, a new benchmark PSII-based photoanode was developed by combining the efficient wiring afforded by redox-active polymers with the high loading provided by the IO-ITO electrodes. [3] Compared to flat electrodes, the hierarchical IO-ITO electrodes enabled up to $\sim$50-fold increase in the immobilisation of an Os complex-based and a phenothiazine-based polymer. When the P_{Os} polymer was co-adsorbed with PSII on the hierarchical IO-ITO to obtain IO-ITO|$P_{Os}-$PSII photoanode, photocurrent densities of up to $\sim$410 μA

cm^{-2} at E_{app} = 0.5 V vs. SHE were observed in the absence of diffusional mediators, demonstrating a substantially improved wiring of PSII to the IO-ITO electrode with the redox polymer. The high photocurrent density allowed for the quantification of O_2 evolution, and a Faradaic efficiency of 85 ± 9% was measured. This assembly strategy provided the basis for high performance PSII-based PEC and all-integrated electrode designs for a wide range of biological and synthetic catalysts.

To generate sufficient driving force for overall water splitting while maximising solar energy harvesting, complementary enzyme-based tandem PEC system was designed, consisting of an IO-TiO_2|dpp|P_{Os}−PSII photoanode connected to a [NiFeSe]-H_2ase-based IO-ITO|H_2ase cathode. [4] The PF-PEC cell achieved the long-standing goal of a bias-free *in vitro* system for overall water splitting using PSII (O_2 generation) connected to H_2ase (H_2 generation). Upon irradiation with UV-filtered simulated solar light, a current density of 28 ± 5 μA cm^{-2} was achieved at U_{app} = 0 V. Voltage independent steady-state photocurrents (122 ± 21 μA cm^{-2}) were reached at U_{app} > 0.3 V. This semi-artificial design addressed key limitations in natural photosynthesis as wiring of PSII to H_2ase via an abiotic dye allowed for: (i) panchromatic solar light absorption by using a synthetic green-light absorber, (ii) quantitative use of electrons extracted from PSII for H_2 production and (iii) separation of H_2 and O_2 in individual compartments. Upon electrolysis over 1 h at U_{app} = 0.3 V, the PSII−H_2ase tandem system produced H_2 and O_2 from water in 2:1 ratio with high Faradaic efficiencies of 88 ± 12% and 82 ± 10%, respectively, and presented a strategy for constructing effective biotic-abiotic interfaces.

Having established the IO-TiO_2|dpp|P_{Os}−PSII photoanode as a versatile platform for the assembly of bias-free semi-artificial Z-schemes for overall water splitting, the direction of the project shifted towards the development of a semi-artificial PEC system for CO_2 reduction to formate with a W-dependent FDH. [5] The applicability of the IO-TiO_2|dpp|P_{Os}−PSII photoanode was expanded beyond water splitting, by wiring to a IO-TiO_2|FDH cathode in a PEC cell. This system achieved the biologically and synthetically challenging coupling of solar-driven water oxidation to selective CO_2 reduction with a small additional applied voltage under mild conditions. Upon irradiation with UV-filtered simulated solar light, a current density of 5.5 ± 0.4 μA cm^{-2} was achieved at U_{app} = 0 V. Voltage independent steady-state photocurrents (99 ± 4 μA cm^{-2}) were reached at U_{app} > 0.4 V. Controlled-potential electrolysis over 1 h at U_{app} = 0.3 V yielded formate with a Faradaic efficiency of 70 ± 9%. This PSII−FDH tandem PEC system demontrated an effective model for the solar-driven rAcCoA pathway, that bypasses inefficiencies of the Z-scheme and CBB cycle.

This study provides a blueprint for advancing future semi-artificial systems capable of bias-free photocatalysis and a toolbox for developing proof-of-concept model systems for

solar energy conversion (Fig. 6.1). On one hand, it allows a variety of electroactive enzymes to be studied electrochemically to gain better understanding of their activity *in vitro*. On the other hand, it enables an electrode material type and morphology to be easily altered, achieving favourable biotic-abiotic interfacial interactions and optimal enzyme loading. Further biologically-relevant electrochemical reactions may be coupled using this approach to introduce a plethora of model systems.

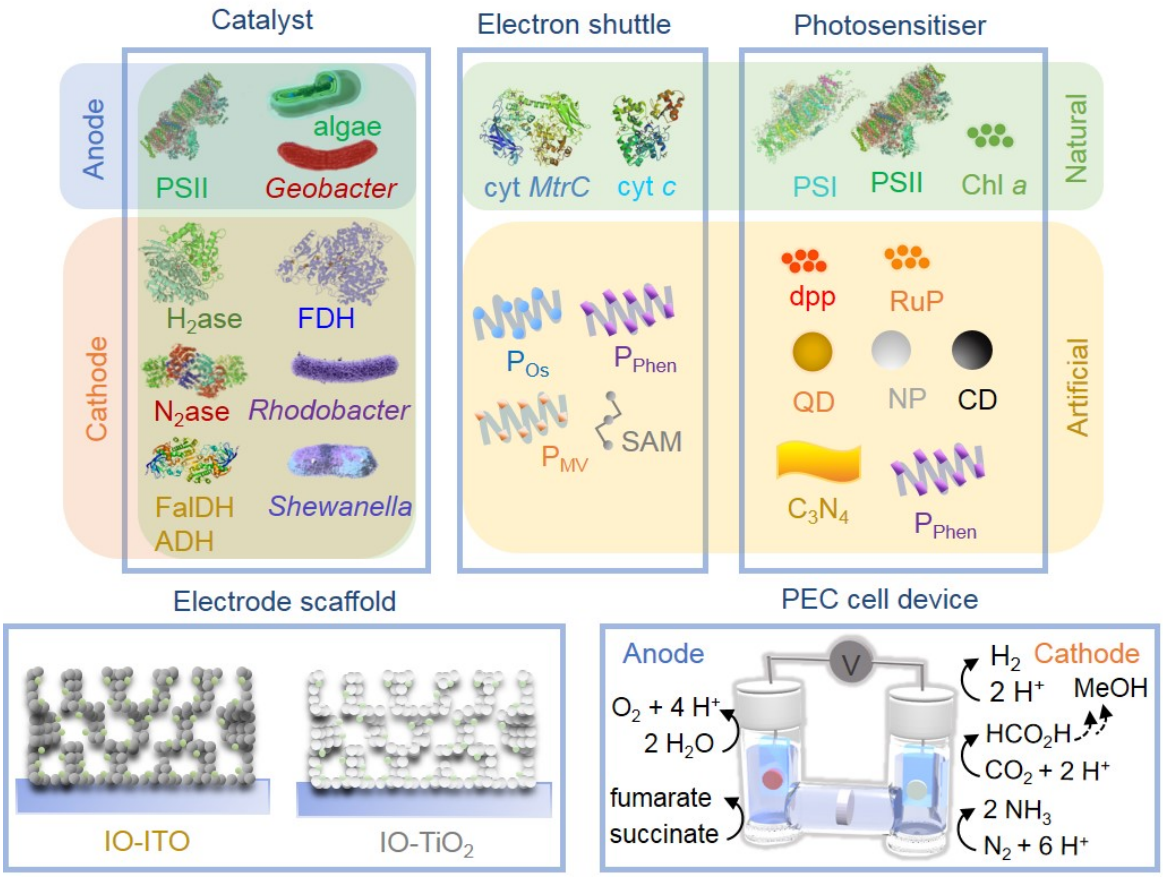

Figure 6.1 **Schematic showing the summary and future outlook on semi-artificial PEC cell design. a**, Toolbox of biological (green shading) and synthetic (yellow shading) components presented in this study and possible future directions. Representative biocatalysts for oxidation (blue shading) and reduction (organge shading) reactions, redox shuttles, photosensitisers, electrode scaffolds and representative PEC cell reactions are shown (species size not drawn to scale). New abbreviations: N_2ase, nitrogenase; FalDH, formaldehyde dehydrogenase; ADH, alcohol dehydrogenase; *Geobacter*, proteobacteria; *Rhodobacter* (*R. sphaeroides* and *R. capsulatus*), purple non-sulfur photosynthetic bacteria; *Shewanella* (*S. oneidensis* MR-1), marine proteobacteria; cyt *MtrC*, cytochrome mitochondrial electron transport chain; cyt *c*, cytochrome *c*; P_{MV}, methyl viologen-modified redox polymer; QD, quantum dot; CD, carbon dot; C_3N_4, carbon nitride.

6.2 Future outlook

Future work could focus on four general aspects: (i) further development of hierarchically-structured IO electrode types and materials, (ii) enhanced immobilisation and in-depth characterisation of biological guest species on electrodes, (iii) performance and technical PEC cell design improvements and (iv) investigation of new enzymes and biotic guests.

6.2.1 Materials

Hierarchical IO electrodes have demonstrated the potential to be highly versatile as a host system and may be used in various applications outside of PF-PEC, including batteries, fuel cells and solar cells. [6] The long-term goal could involve replacement of ITO by more cost-effective materials, including other TCOs such as ATO, FTO or AZO. [7] Development of IO-TiO_2 electrodes with 3 μm and 10 μm pore sizes could allow to accommodate larger photosynthetic guests, including purple bacteria, cyanobacteria or green algae cells. To improve the electrode morphology and gain better control over the assembly process, new synthetic routes for monodispersed TiO_2 NPs [8] with tuneable size could be explored. Increasing the electrochemical driving force and decreasing the loss of energy from the photoexcited dye for more efficient catalysis or CO_2 reduction chemistry in the tandem device could be achieved by replacing TiO_2 with a semiconductor with a more negative CB potential, such as ZrO_2. Mixed-oxide nanocomposites, such as $Al_2O_3-SnO_2$, [9] TiO_2-SnO_2 [10] or TiO_2-ZrO_2, [11] could also be utilised as IO electrode building blocks to increase the V_{OC} of the PEC system. Lastly, the automation of the IO electrode fabrication could make the process more time-efficient and less prone to human error.

6.2.2 Immobilisation and characterisation

Improvements in redox polymer design could lead to favourable changes to the electrode stability, electron hopping efficiency and formal redox potentials to better match the energy levels of the protein electron acceptor/donor. The P_{Os} polymer could be replaced by a metal-free analogue with a formal redox potential slightly less negative than the Q_B site potential of PSII, that could be obtained by tuning the redox-active group structure. A bifunctional dye-modified redox polymer could potentially serve as both, an efficient electron shuttle and the second complementary absorber to PSII in a tandem PEC cell assembly, reducing the number of components and complexity of the system. As for phenothiazine-modified redox polymers, binding stability on the ITO electrode surface was recognised as the major system limitation. A modification in the monomer structure of P_{Phen} or introduction of another monomer with a

functional group forming strong interactions with ITO surface, such as an imidazole group, could enhance the polymer−ITO binding. Interactions with PSII could be enhanced by increasing the hydrophilicity of the polymer chain side-groups. A new generation viologen-modified redox polymers could be utilised to enhance the wiring of H_2ase and FDH to the electrode surface. [12] The long-term future goal should focus on investigating in more depth the electron transfer kinetics between the biotic−abiotic components and interfacial binding interactions by ultrafast spectroscopy *in situ*. Imaging techniques, such as confocal fluorescence microscopy could be used to visualise the localisation and orientation of the components on the electrode surface. Theoretical methods involving Michaelis-Menten kinetics modelling, could be applied to investigate the electrocatalytic mechanism and structure−activity relationships of active-sites. [13, 14]

6.2.3 PEC cell performance and design

The photostability (typical half-life times of ∼8 min) of the PSII-based photoanodes is the major limitation of the semi-artificial PEC systems. As such, all the current hybrid enzyme systems are proof-of-concept devices, and their practical applicability is intrinsically limited by the photodegradation pathways of PSII *in vitro*. [15, 16] The PSII-based photoanode photostability could be extended to some extent by utilising ROS scavengers, removing $^1O_2$ and H_2O_2 from the system. [17] Alternatively, the whole cyanobacteria or green algae cells, characterised with significantly extended photostability, could be explored on electrodes. [1] As for the technical PEC cell design improvements for two-electrode systems, the resistance sources could be further minimised by (i) providing more efficient diffusional flux and introducing thinner (a few μm thick) permeable membranes and (ii) minimising the distance between the active area of two electrodes (or introducing a wire-less artificial leaf design for bias-free systems). [18] As for dye-sensitised PEC systems, the photoanode polarisation effects could be minimised in the future by introducing a better matched biocatalyst−sensitiser pair [19], or an engineered dyad, [20, 21] characterised by a faster electron transfer between the two.

6.2.4 New enzymes and reactions

There is a great scope for the continued development of semi-artificial PEC cells for solar fuel synthesis. A nitrogenase-based cathode could be employed in PF-PEC for N_2 reduction to NH_3. [22] FDH could be combined with formaldehyde dehydrogenase (FalDH) and alcohol dehydrogenase (ADH) on an electrode for enzyme cascade CO_2 reduction to formaldehyde, and ultimately to methanol. [23] Other organisms, including photosynthetic purple bac-

teria (*Rhodobacter sphaeroides* and *Rhodobacter capsulatus*), metal and sulfur-reducing proteobacteria (*Geobacter sulfurreducens*), marine proteobacteria (*Shewanella oneidensis*), cyanobacteria and green algae could be wired to hierarchical IO electrodes. A tandem dye-sensitised assembly could be designed with *Rhodobacter capsulatus* for solar-driven H_2 generation, [24] or with *Rhodobacter sphaeroides* for N_2 fixation to NH_3. Lastly, extended lifetime, efficiency and selectivity for desired reactions could be achieved by bioengineering of organisms and bacteria [25] and constructing artificial metalloproteins containing desired catalytic active-sites, by using for example biotin-streptavidin biotechnology. [26]

References

(1) J. Z. Zhang, P. Bombelli, K. P. Sokol, A. Fantuzzi, A. W. Rutherford, C. J. Howe and E. Reisner, *J. Am. Chem. Soc.*, 2018, **140**, 6–9.

(2) X. Fang, K. P. Sokol, T. A. Kandiel, N. Heidary, J. Z. Zhang and E. Reisner, *Nano Lett.*, 2018, DOI: 10.1021/acs.nanolett.8b04935.

(3) K. P. Sokol, D. Mersch, V. Hartmann, J. Z. Zhang, M. M. Nowaczyk, M. Rögner, A. Ruff, W. Schuhmann, N. Plumeré and E. Reisner, *Energy Environ. Sci.*, 2016, **9**, 3698–3709.

(4) K. P. Sokol, W. E. Robinson, J. Warnan, N. Kornienko, M. M. Nowaczyk, A. Ruff, J. Z. Zhang and E. Reisner, *Nat. Energy*, 2018, **3**, 944–951.

(5) K. P. Sokol, W. E. Robinson, A. R. Oliveira, J. Warnan, M. M. Nowaczyk, A. Ruff, I. A. C. Pereira and E. Reisner, *J. Am. Chem. Soc.*, 2018, **140**, 16418–16422.

(6) K. R. Phillips, G. T. England, S. Sunny, E. Shirman, T. Shirman, N. Vogel and J. Aizenberg, *Chem. Soc. Rev.*, 2016, **45**, 281–322.

(7) V. Müller, M. Rasp, G. Štefanić, J. Ba, S. Günther, J. Rathousky, M. Niederberger and D. Fattakhova-Rohlfing, *Chem. Mater.*, 2009, **21**, 5229–5236.

(8) J. M. Feckl, A. Haynes, T. Bein and D. Fattakhova-Rohlfing, *New J. Chem.*, 2014, **38**, 1996–2001.

(9) G. R. Kumara, K. Tennakone, V. P. Perera, A. Konno, S. Kaneko and M. Okuya, *J. Phys. D. Appl. Phys.*, 2001, **34**, 868–873.

(10) S. Chappel, S. G. Chen and A. Zaban, *Langmuir*, 2002, **18**, 3336–3342.

(11) J. H. Kim, Y. Jo, J. H. Kim, J. W. Jang, H. J. Kang, Y. H. Lee, D. S. Kim, Y. Jun and J. S. Lee, *ACS Nano*, 2015, **9**, 11820–11829.

(12) A. Ruff, J. Szczesny, S. Zacarias, I. A. Pereira, N. Plumeré and W. Schuhmann, *ACS Energy Lett.*, 2017, **2**, 964–968.

(13) G. Longatte, M. Guille-Collignon and F. Lemaître, *ChemPhysChem*, 2017, **18**, 2643–2650.

(14) A. Indra, P. W. Menezes and M. Driess, *ChemSusChem*, 2015, **8**, 776–785.

(15) J. Z. Zhang, K. P. Sokol, N. Paul, E. Romero, R. Van Grondelle, E. Reisner, K. P. Sokol, E. Romero, R. Van Grondelle and E. Reisner, *Nat. Chem. Biol.*, 2016, **12**, 1046–1052.

(16) M. M. Nowaczyk and N. Plumeré, *Nat. Chem. Biol.*, 2016, **12**, 990–991.

(17) N. Kornienko, J. Z. Zhang, K. P. Sokol, S. Lamaison, A. Fantuzzi, R. van Grondelle, A. Rutherford and E. Reisner, *J. Am. Chem. Soc.*, 2018, **140**, 17923–17931.

(18) J. R. Swierk and T. E. Mallouk, *Chem. Soc. Rev.*, 2013, **42**, 2357–2387.

(19) F. Li, K. Fan, B. Xu, E. Gabrielsson, Q. Daniel, L. Li and L. Sun, *J. Am. Chem. Soc.*, 2015, **137**, 9153–9159.

(20) H. Wolpher, S. Sinha, J. Pan, A. Johansson, M. J. Lundqvist, P. Persson, R. Lomoth, J. Bergquist, L. Sun and V. Sundstro, *Inorg. Chem.*, 2007, **46**, 638–651.

(21) H. Li, F. Li, B. Zhang, X. Zhou, F. Yu and L. Sun, *J. Am. Chem. Soc.*, 2015, **137**, 4332–4335.

(22) R. D. Milton and S. D. Minteer, *Chempluschem*, 2017, **82**, 513–521.

(23) S. K. Kuk, R. K. Singh, D. H. Nam, R. Singh, J. K. Lee and C. B. Park, *Angew. Chem. Int. Ed.*, 2017, **56**, 3827–3832.

(24) K. Hasan, S. A. Patil, K. Górecki, D. Leech, C. Hägerhäll and L. Gorton, *Bioelectrochemistry*, 2013, **93**, 30–36.

(25) C. Liu, B. C. Colón, M. Ziesack, P. A. Silver and D. G. Nocera, *Science*, 2016, **352**, 1210–1213.

(26) L. Olshansky, R. Huerta-Lavorie, A. I. Nguyen, J. Vallapurackal, A. Furst, T. D. Tilley and A. S. Borovik, *J. Am. Chem. Soc.*, 2018, **140**, 2739–2742.

Appendix A

Appendix to Chapter 2

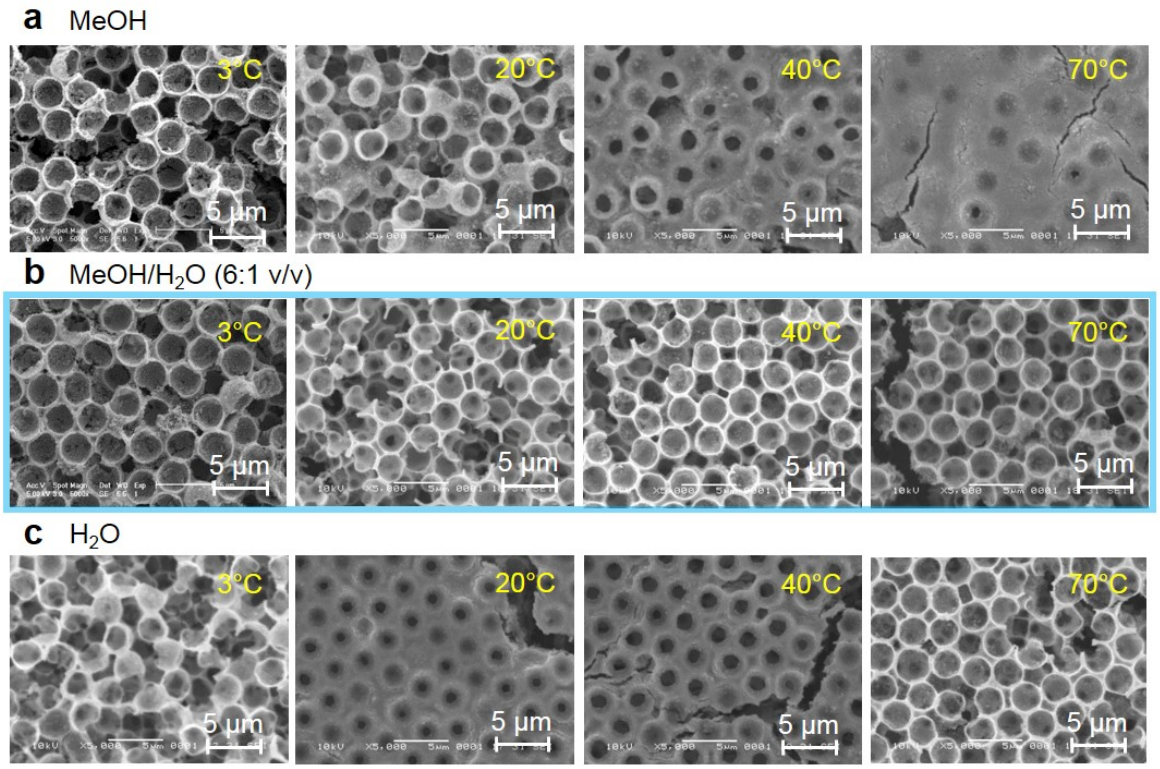

Figure A.1 **Solvent and deposition temperature screening of the 3 μm pore diameter IO-ITO electrode.** SEM top view images of films (10 μm thickness) fabricated via the co-assembly method using **a**, MeOH as a dispersion medium for ITO NPs, **b**, MeOH/H_2O mixture (6:1 v/v) and **c**, H_2O. Deposition temperatures: 3°, 20° (RT), 40° and 70°. [ITO NP]:[PS bead] ratio used = 0.75:1 (w/w). The selected conditions and best electrode morphology are highlighted with a light blue rectangle.

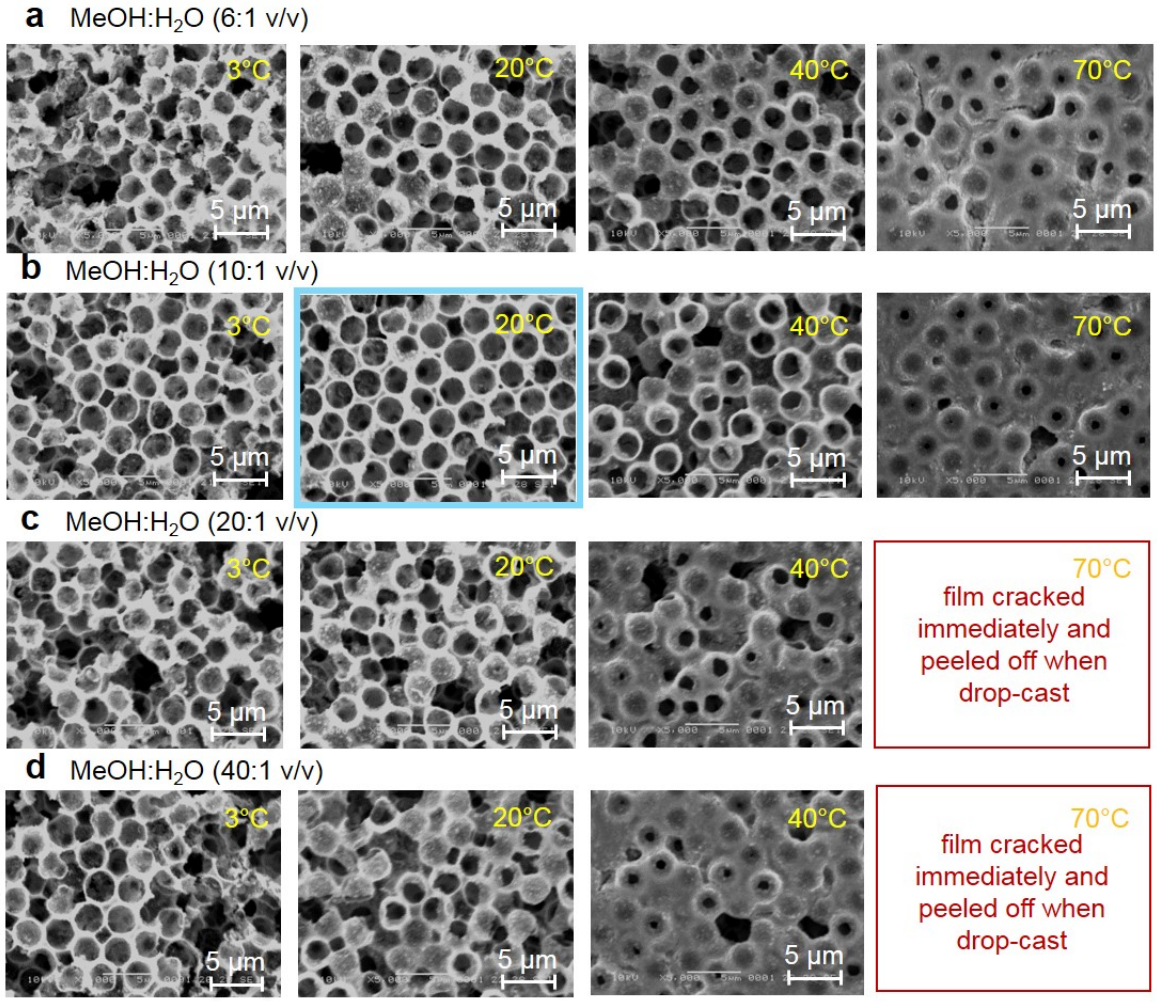

Figure A.2 **MeOH/H_2O ratio and deposition temperature screening of the 3 μm pore diameter IO-ITO electrode.** SEM top view images of films (10 μm thickness) fabricated via the co-assembly method using **a**, MeOH/H_2O mixture (6:1 v/v) as a dispersion medium for ITO NPs, **b**, MeOH/H_2O mixture (10:1 v/v), **c**, MeOH/H_2O mixture (20:1 v/v) and **d**, MeOH/H_2O mixture (40:1 v/v). Deposition temperatures: 3°, 20° (RT), 40° and 70°. [ITO NP]:[PS bead] ratio used = 0.75:1 (w/w). The selected conditions and best electrode morphology are highlighted with a light blue rectangle.

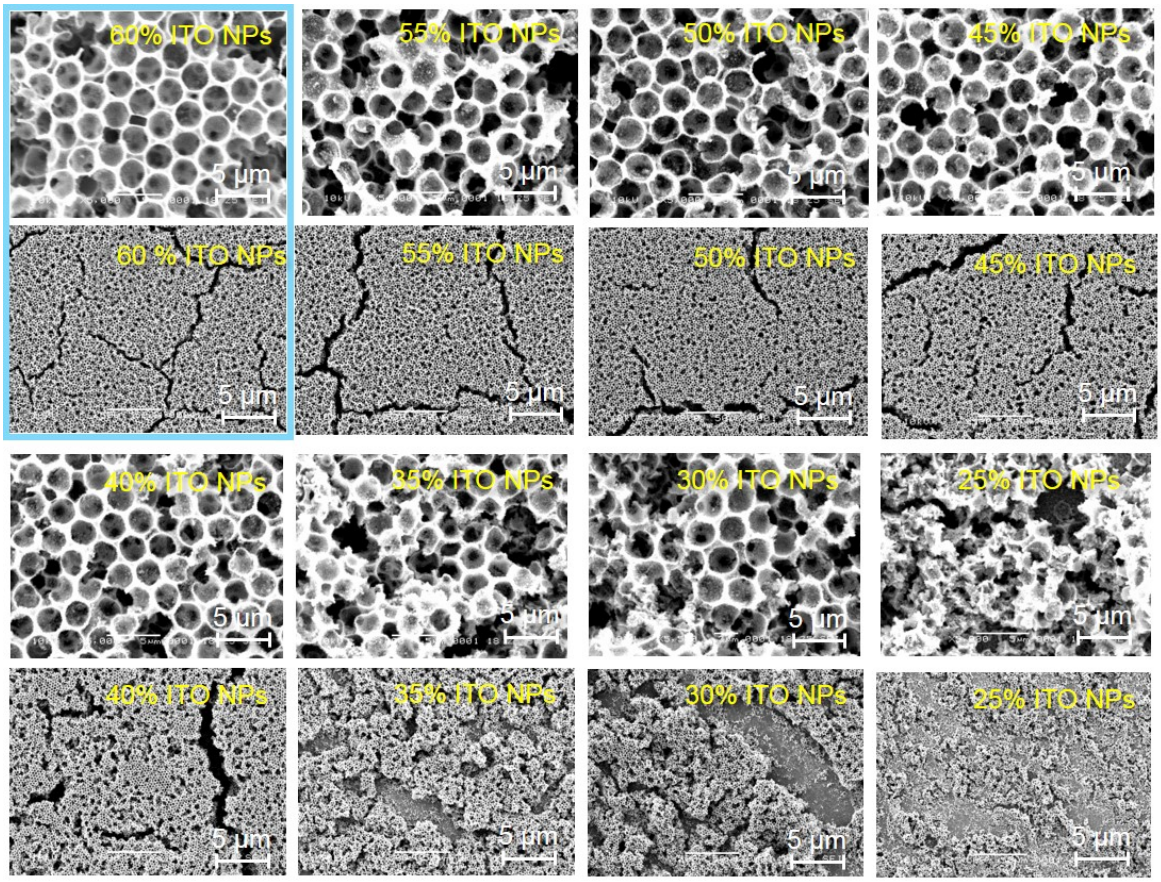

Figure A.3 **[ITO NP]:[PS bead] ratio screening of the 3 μm pore diameter IO-ITO electrode.** SEM top view images of films (10 μm thickness) fabricated via the co-assembly method using varying ITO NP to PS bead ratio (w/w): from 1.35:1 (top left), 1.20:1, 1.05:1, 0.90:1, 0.75:1, 0.60:1, 0.45:1 to 0.30:1 (bottom right). 60% ITO NPs corresponds to 1.35:1 (w/w) ratio. Conditions: MeOH/H_2O mixture (6:1 v/v) as a dispersion medium for ITO NPs, deposition temperature (RT/20°C). The selected conditions and best electrode morphology are highlighted with a light blue rectangle.

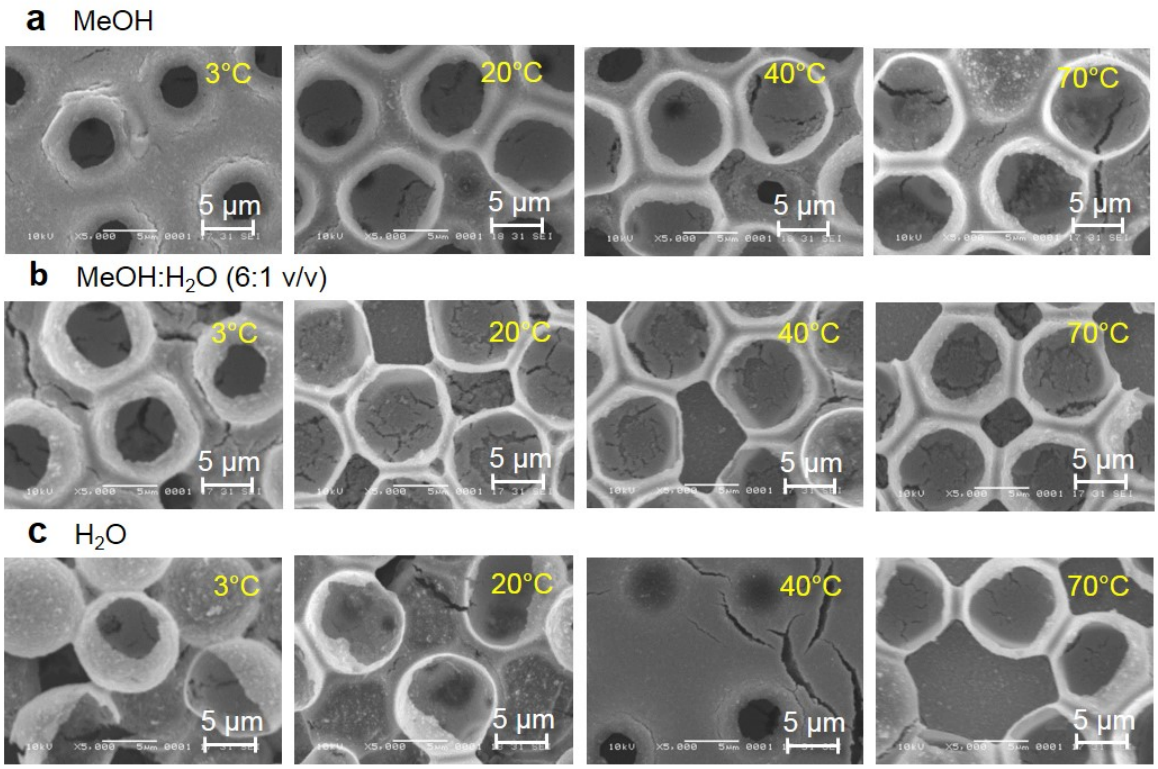

Figure A.4 **Solvent and deposition temperature screening of the 10 μm pore diameter IO-ITO electrode (co-assembly method).** SEM top view images of films (20 μm thickness) fabricated via the co-assembly method using **a**, MeOH as a dispersion medium for ITO NPs, **b**, MeOH/H_2O mixture (6:1 v/v) and **c**, H_2O. Deposition temperatures: 3°, 20° (RT), 40° and 70°. [ITO NP]:[PS bead] ratio used = 2:1 (w/w).

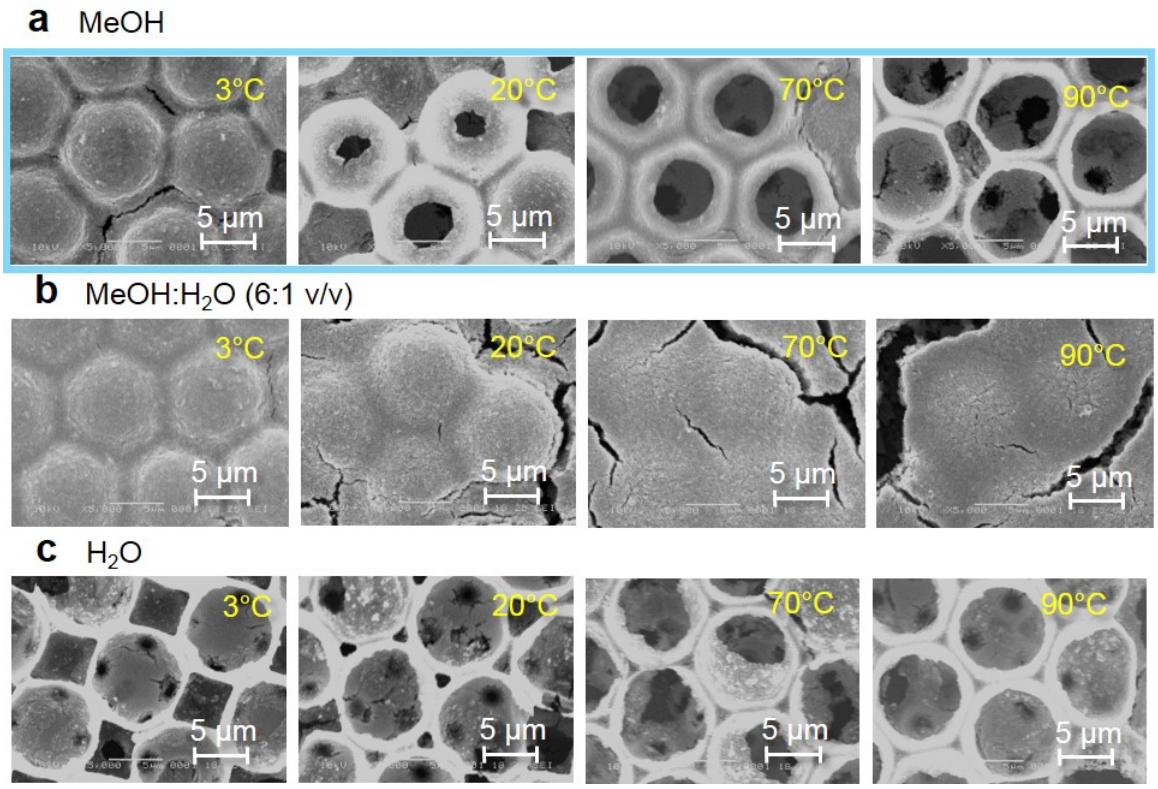

Figure A.5 **Solvent and deposition temperature screening of the 10 μm pore diameter IO-ITO electrode (infiltration method).** SEM top view images of films (20 μm thickness) fabricated via the infiltration method using **a**, MeOH as a dispersion medium for ITO NPs, **b**, MeOH/H_2O mixture (6:1 v/v) and **c**, H_2O. Deposition temperatures of ITO NP dispersion: 3°, 20° (RT), 40° and 70°. PS bead assembly conditions: sintering temperature (90°) and time (5 min). [ITO NP]:[PS bead] ratio used = 2:1 (w/w). The selected conditions and best electrode morphology are highlighted with a light blue rectangle.

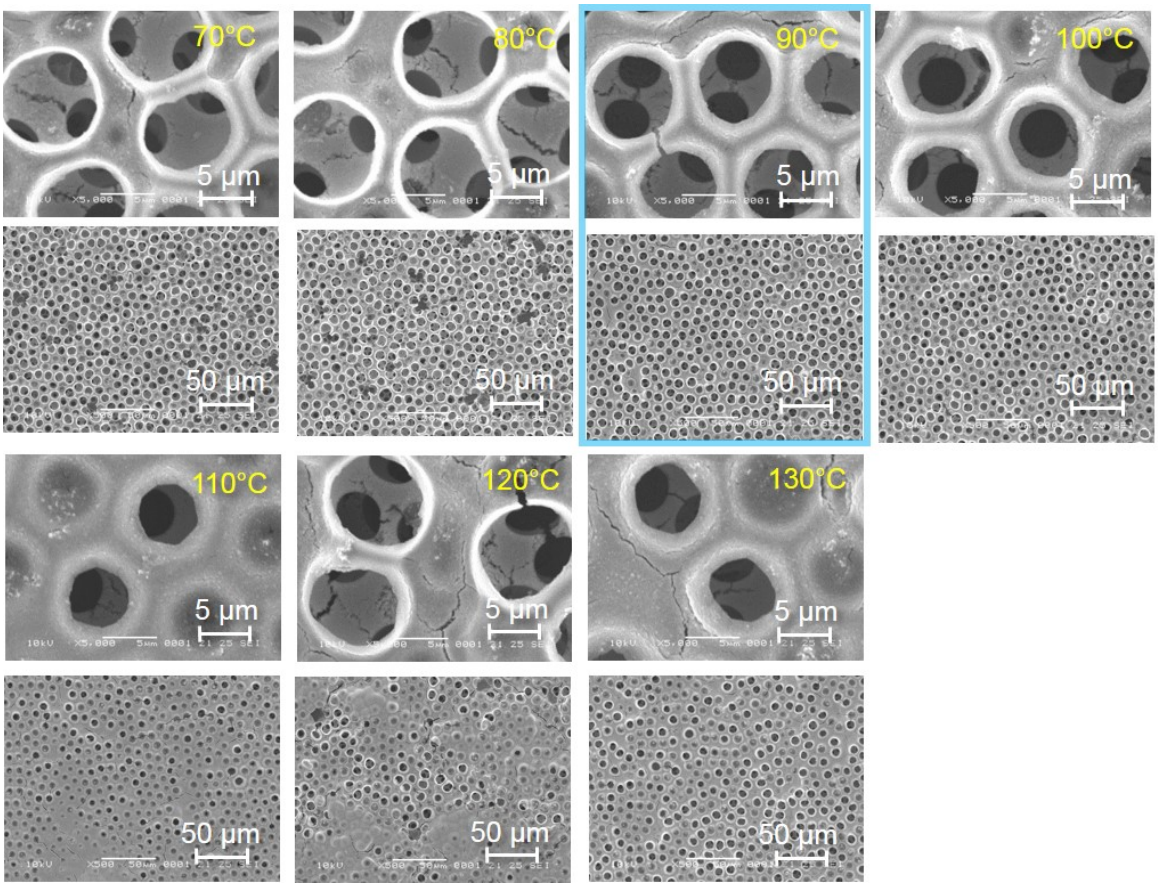

Figure A.6 **PS bead template sintering temperature screening of the 10 μm pore diameter IO-ITO electrode.** SEM top view images of films (20 μm thickness) fabricated via the infiltration method using varying PS bead sintering temperature after deposition: from 90° (top left), 100°, 110°, 120°, 130°, 140° to 150° (bottom right). Conditions: MeOH as a dispersion medium for ITO NPs, deposition temperature (RT/20°C). [ITO NP]:[PS bead] ratio used = 2:1 (w/w). The selected conditions and best electrode morphology are highlighted with a light blue rectangle.

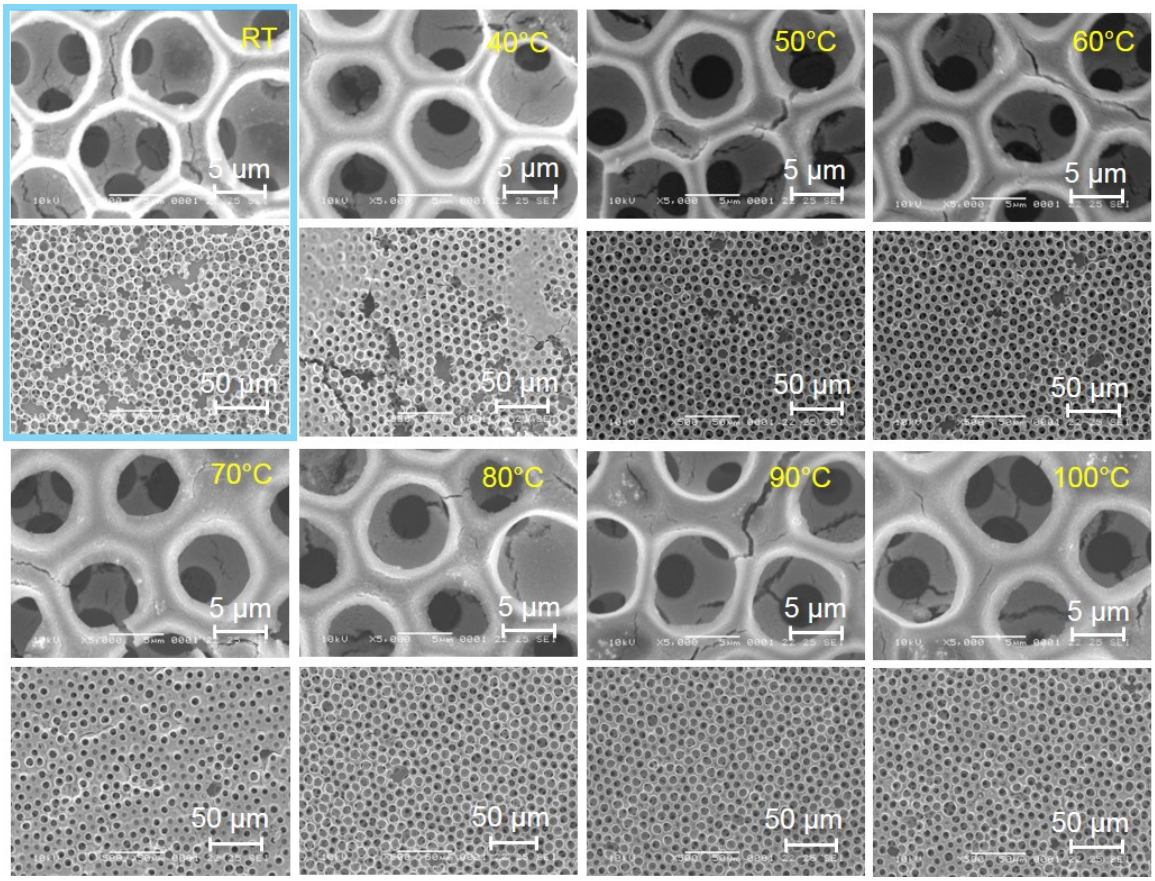

Figure A.7 **ITO NP deposition temperature screening of the 10 μm pore diameter IO-ITO electrode.** SEM top view images of films (20 μm thickness) fabricated via the infiltration method using varying ITO NP disperstion evaporation temperature: from RT/20° (top left), 40°, 50°, 60°, 70°, 80°, 90° to 100° (bottom right). Conditions: MeOH as a dispersion medium for ITO NPs. PS bead assembly conditions: sintering temperature (90°) and time (5 min). [ITO NP]:[PS bead] ratio used = 2:1 (w/w). The selected conditions and best electrode morphology are highlighted with a light blue rectangle.

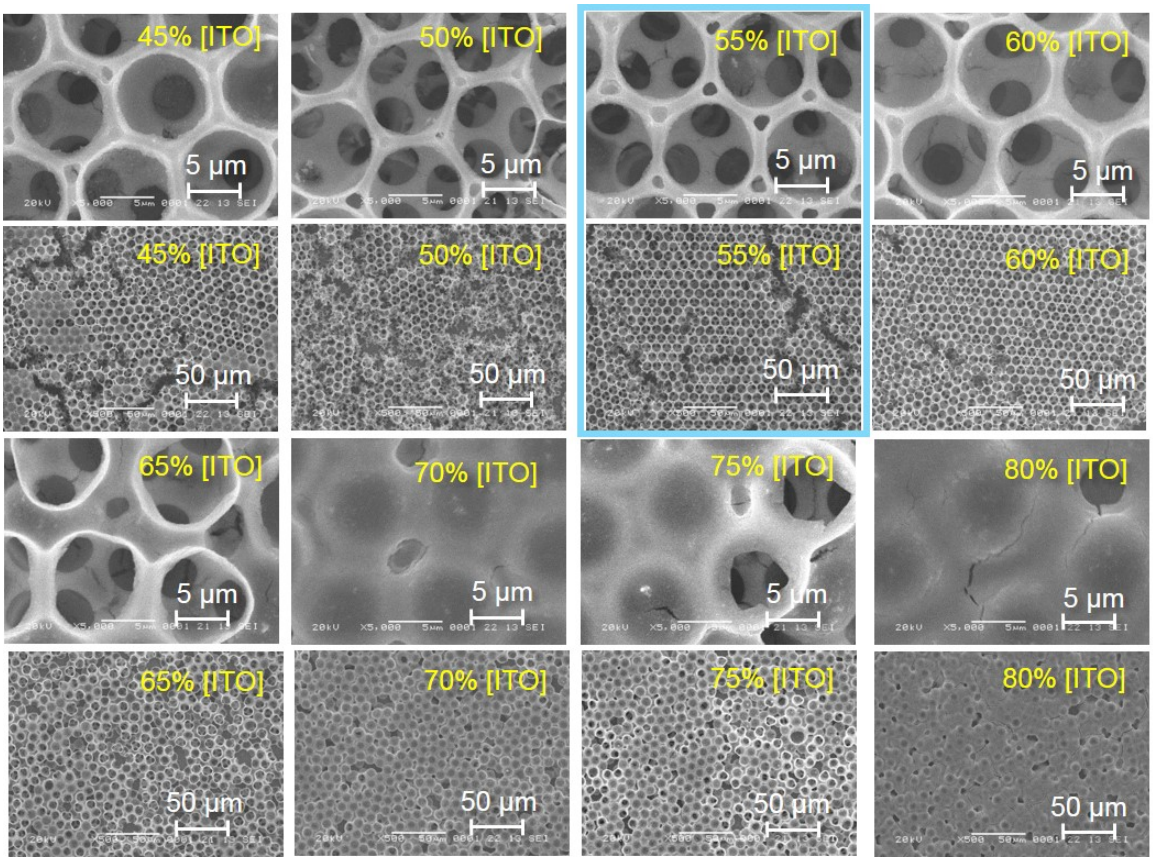

Figure A.8 **[ITO NP]:[PS bead] ratio screening of the 10 μm pore diameter IO-ITO electrode.** SEM top view images of films (20 μm thickness) fabricated via the infiltration method using varying ITO NP to PS bead ratio (w/w): from 0.8:1 (top left), 1.1:1, 1.4:1, 1.7:1, 2.0:1, 2.3:1, 2.6:1 to 2.9:1 (bottom right). 45% ITO NPs corresponds to 0.8:1 (w/w) ratio. Conditions: MeOH as a dispersion medium for ITO NPs, deposition temperature (RT/20°C). PS bead assembly conditions: sintering temperature (90°) and time (5 min). The selected conditions and best electrode morphology are highlighted with a light blue rectangle.

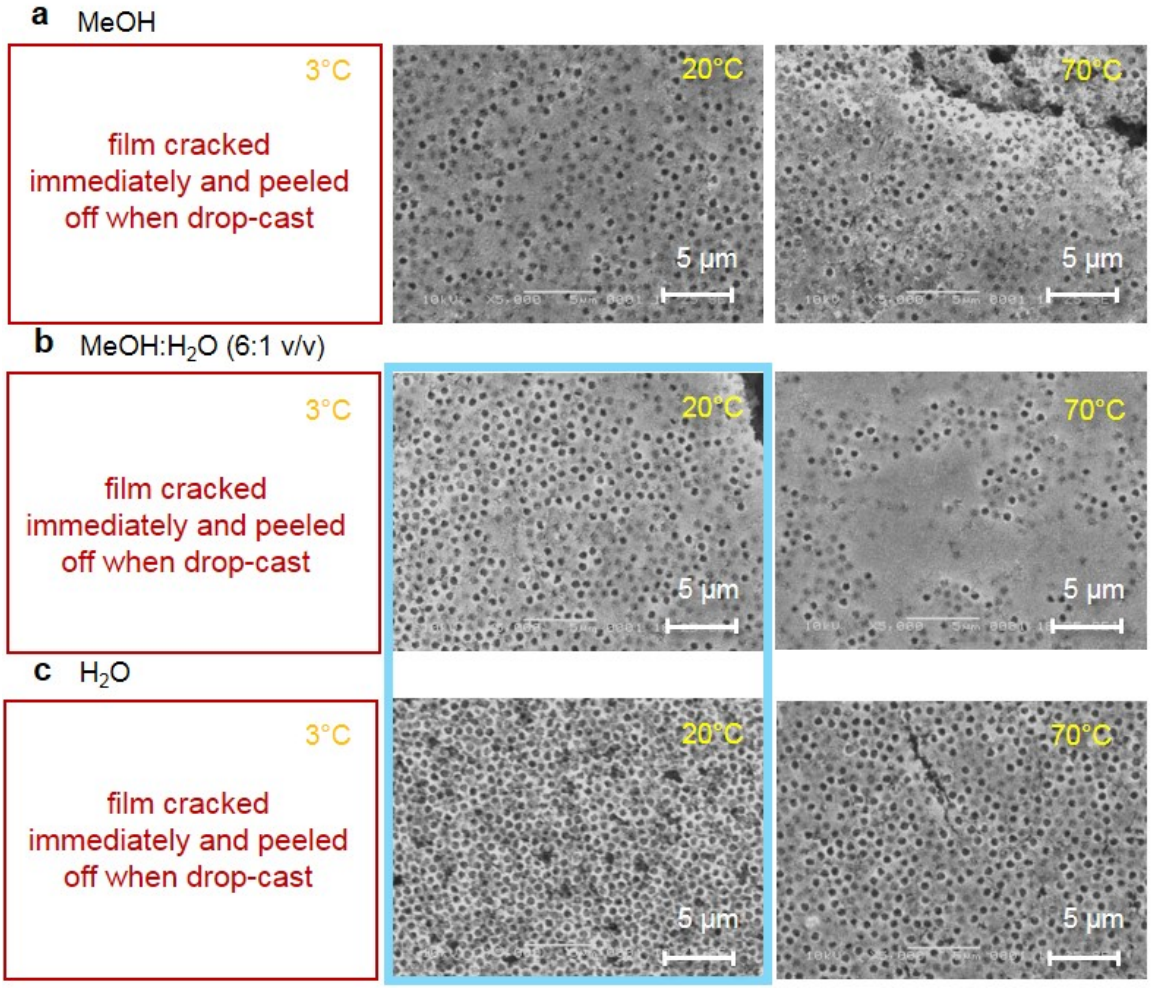

Figure A.9 **Solvent and deposition temperature screening of the 0.75 μm pore diameter IO-TiO_2 electrode.** SEM top view images of films (10 μm thickness) fabricated via the co-assembly method using **a**, MeOH as a dispersion medium for TiO_2 NPs, **b**, MeOH/H_2O mixture (6:1 v/v) and **c**, H_2O. Deposition temperatures: 3°, 20° (RT), 40° and 70°. [TiO_2 NP]:[PS bead] ratio used = 1.25:1 (w/w). The selected conditions and best electrode morphology are highlighted with a light blue rectangle.

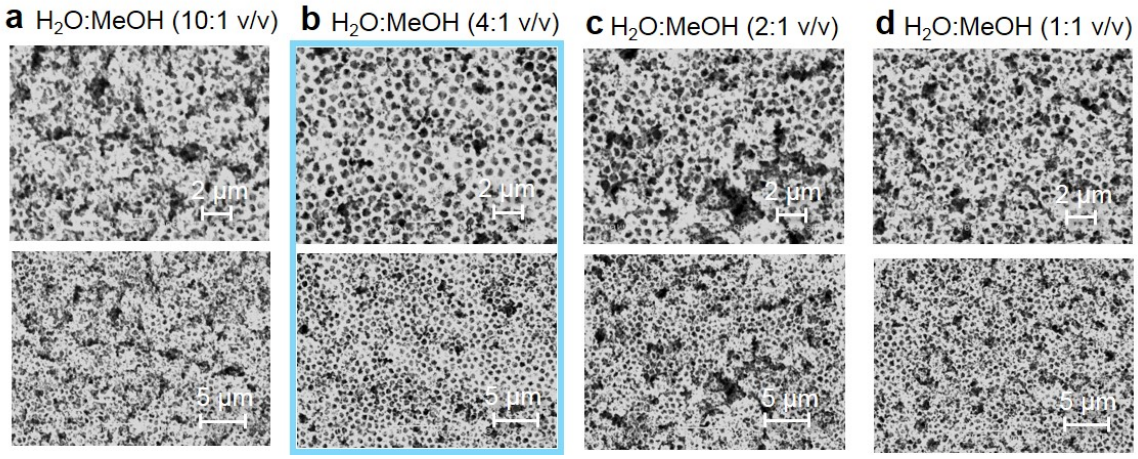

Figure A.10 **MeOH/H_2O ratio and deposition temperature screening of the 0.75 μm pore diameter IO-TiO_2 electrode.** SEM top view images of films (10 μm thickness) fabricated via the co-assembly method using **a**, H_2O/MeOH mixture (10:1 v/v) as a dispersion medium for TiO_2 NPs, **b**, H_2O/MeOH mixture (4:1 v/v), **c**, H_2O/MeOH mixture (2:1 v/v) and **d**, H_2O/MeOH mixture (1:1 v/v). Deposition temperature: 20° (RT). [TiO_2 NP]:[PS bead] ratio used = 1.25:1 (w/w). The selected conditions and best electrode morphology are highlighted with a light blue rectangle.

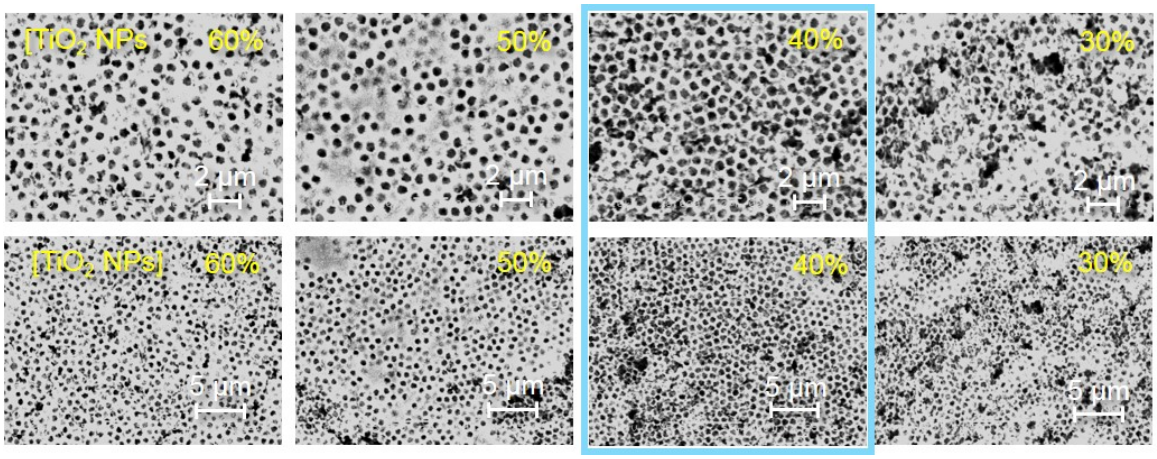

Figure A.11 **[TiO_2 NP]:[PS bead] ratio screening of the 0.75 μm pore diameter IO-TiO_2 electrode.** SEM top view images of films (10 μm thickness) fabricated via the co-assembly method using varying TiO_2 NP to PS bead ratio (w/w): from 1.25:1 (left), 1.00:1, 0.75:1 to 0.50:1 (right). 60% TiO_2 NPs corresponds to 1.25:1 (w/w) ratio. Conditions: H_2O/MeOH mixture (4:1 v/v) as a dispersion medium for TiO_2 NPs, deposition temperature (RT/20°C). The selected conditions and best electrode morphology are highlighted with a light blue rectangle.

Appendix B

Appendix to Chapter 3

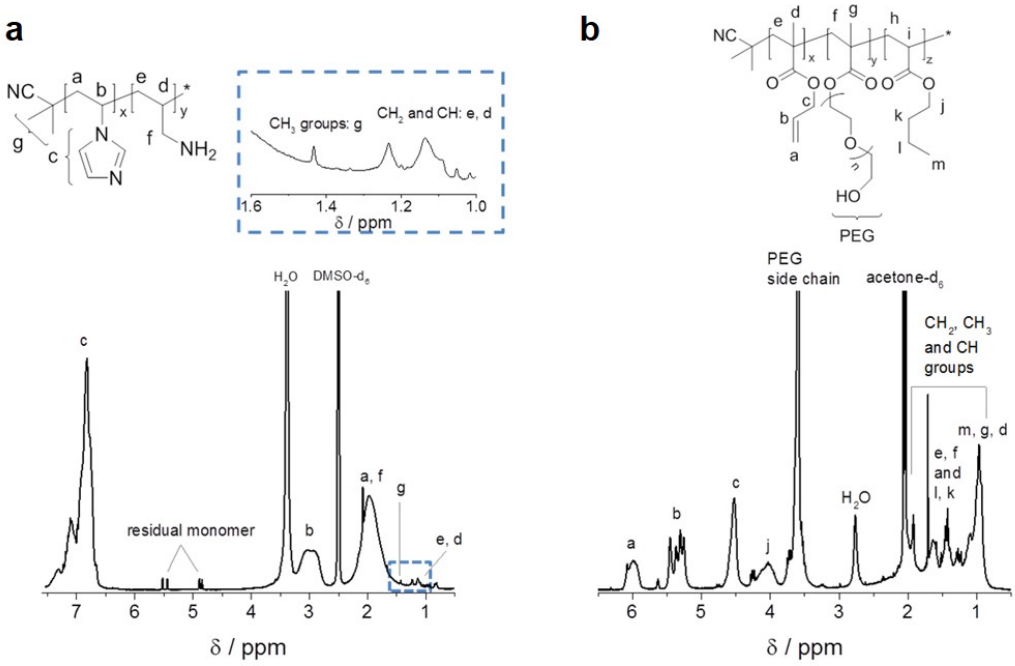

Figure B.1 **Redox polymer backbone ^{1}H NMR characterisation.** ^{1}H NMR spectra and molecular structures of the polymer backbones of **a**, P_{Os} and **b**, P_{Phen} in DMSO-d_6 and acetone-d_6, respectively, measured with a proton resonance frequency of 200.13 MHz; the residual solvent peak was used as internal standard. Inset in **a**, shows a magnification of the region between 1 to 1.6 ppm; the integral ratios c/g (150), b/g (38.5) and a/g (94.5) were used to estimate the molecular weight of the polymer backbone of P_{Os} (neglecting the allyl amine content y). Data recorded by Dr. Adrian Ruff. The figure adapted from Sokol et. al., *Energy Environ. Sci.*, 2016, **9**, 3698−3709.

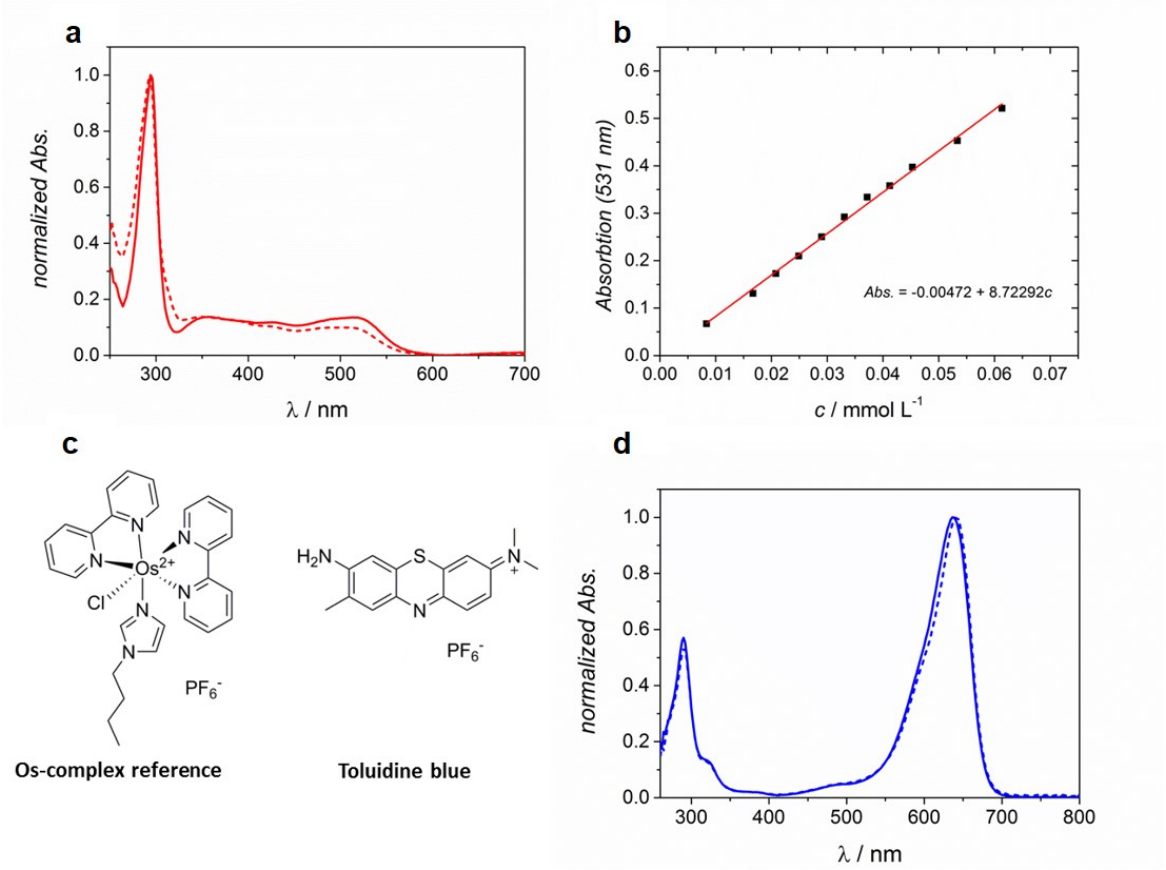

Figure B.2 **Redox polymer UV-Vis spectroscopy characterisation.** Normalised UV-vis spectra of **a**, P_{Os} (solid line) and the freely diffusing Os complex reference (dashed line) in MES buffer (20 mM, pH 6.5); **b**, representative plot of the absorption at 531 nm of the freely diffusing Os complex reference in DMSO as a function of concentration for the calculation of the Os complex loading within P_{Os} (note, the absorption measurements of P_{Os} for calculating the Os-complex content were also conducted in DMSO); **c**, molecular structures of the freely diffusing reference compounds; **d**, normalised UV-vis spectra of P_{Phen} (solid line) and the hexafluorophosphate salt of toluidine blue in DMSO; the PF_6^- salt of toluidine blue was prepared by a metathesis reaction with toluidine blue chloride and NH_4PF_6 in water to enhance the solubility in DMSO and the purity of the dye (note that the commercial available chloride salt has only a 80% dye content); DMSO stock solutions of the freely diffusing compounds were used for the measurements. Data recorded by Dr. Adrian Ruff. The figure adapted from Sokol et. al., *Energy Environ. Sci.*, 2016, **9**, 3698−3709.

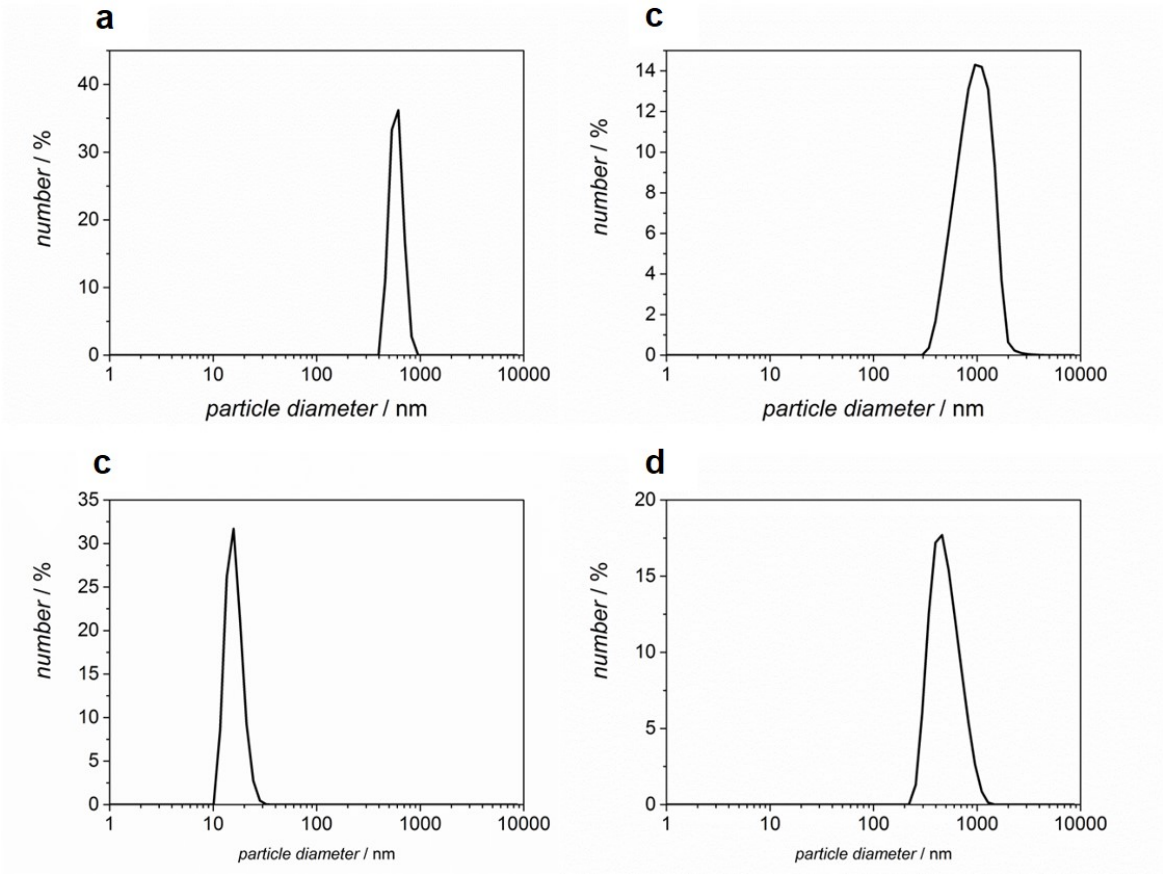

Figure B.3 **Redox polymer DLS characterisation.** Estimation of the hydrodynamic diameter of P_{Os} and P_{Phen} suspended in MES solution (20 mM, pH 6.5) by DLS. Particle size distribution (by number) of **a**, P_{Os} and **b**, P_{Phen}, respectively. Particle size distribution (by number) of filtered (200 nm PES-membrane filters) solutions of **c**, P_{Os} and **d**, P_{Phen}, respectively; P_{Phen} seems to form loosely bound agglomerates which can be dissociated when passing the solution through the membrane. After filtration the size of the agglomerates is still higher than the pore size of the used filters indicating fast re-agglomeration. Data recorded by Dr. Adrian Ruff. The figure adapted from Sokol et. al., *Energy Environ. Sci.*, 2016, **9**, 3698−3709.

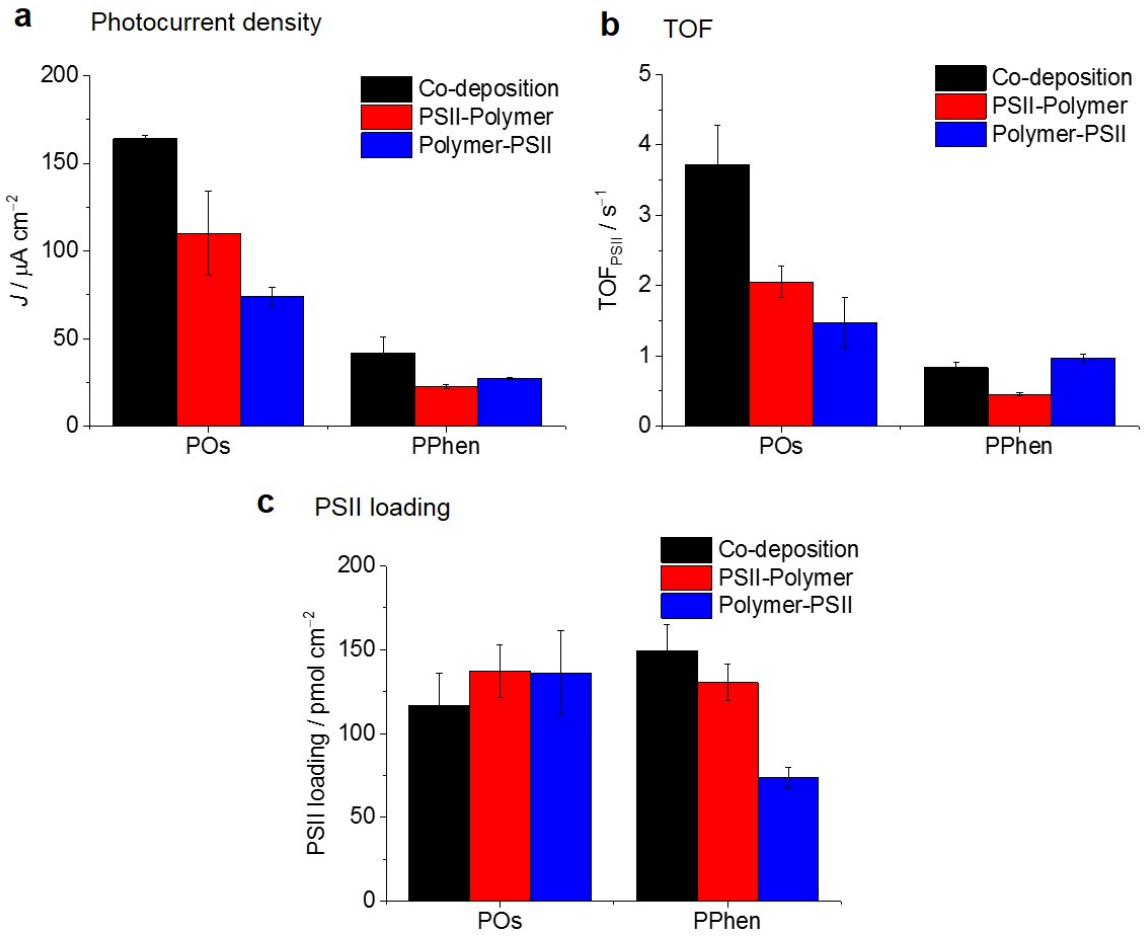

Figure B.4 **Polymer−PSII deposition screening.** The co-deposition method (1-step deposition of polymer−PSII mixture/blend) and 2-step deposition methods (polymer deposition followed by PSII and PSII deposition followed by polymer) for both, IO-ITO|P_{Os}−PSII and IO-ITO|P_{Phen}−PSII electrodes. Conditions: 1 μL P_{Os} (50 mg mL^{-1}), 1 μL P_{Phen} (10 mg mL^{-1}) and 1 μL PSII (2.6 mg mL^{-1} Chl *a*); 0.75 μm macropore IO-ITO electrode, 15 min incubation time. **a**, Photocurrent density, **b**, turnover frequency (TOF) and **c**, PSII loading determination of IO-ITO|P_{Os}−PSII and IO-ITO|P_{Phen}−PSII electrodes.

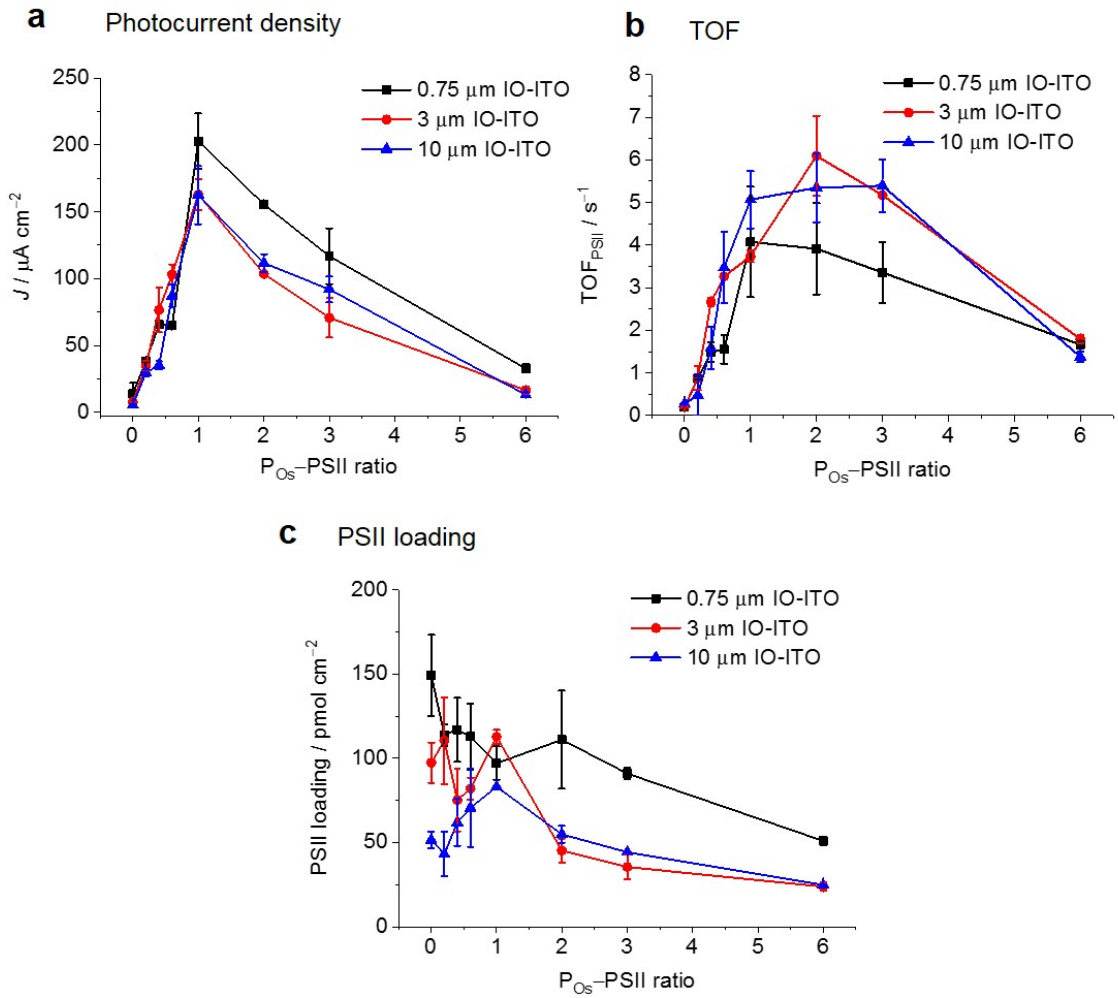

Figure B.5 **P_{Os}−PSII ratio and IO-ITO electrode macropore screening.** The IO-ITO|P_{Os}−PSII was assembled using 0.75 μm, 3 μm and 10 μm macropore IO-ITO electrodes via the co-deposition method (1-step deposition of polymer−PSII blend, 15 min incubation time). The polymer−PSII (v/v) ratio was varied from 0:1, 0.2:1, 0.4:1, 0.6:1, 1:1, 2:1, 3:1 and 6:1, where 1:1 was defined as 1 μL P_{Os} (10 mg mL^{-1}) to 1 μL PSII (2.6 mg mL^{-1} Chl *a*). PSII concentration was kept constant and the redox polymer concentration was varied (from 0, 2, 4, 6, 10, 20, 30 to 60 mg mL^{-1}). **a**, Photocurrent density, **b**, turnover frequency (TOF) and **c**, PSII loading determination of IO-ITO|P_{Os}−PSII electrode.

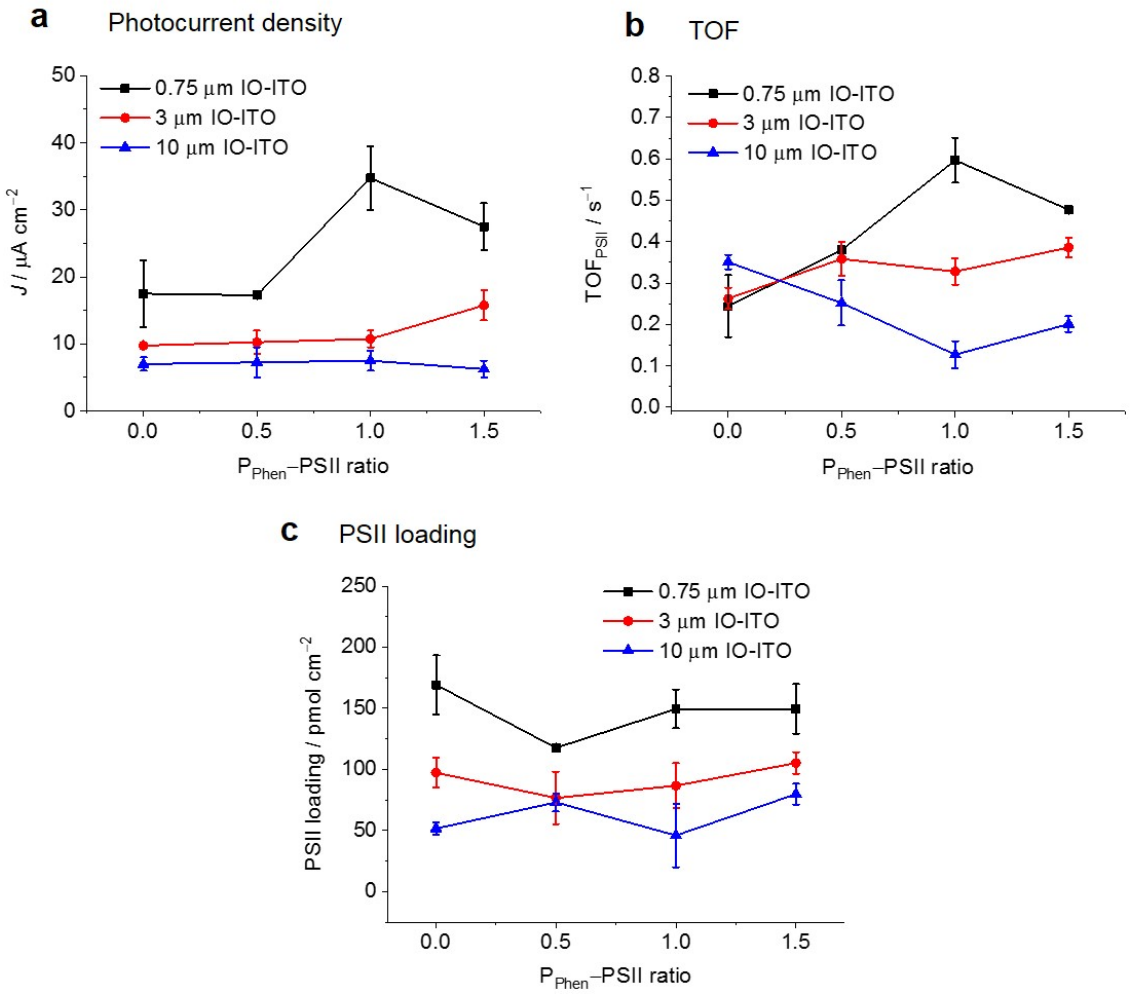

Figure B.6 **P_{Phen}−PSII ratio and IO-ITO electrode macropore screening.** The IO-ITO|P_{Phen}−PSII was assembled using 0.75 μm, 3 μm and 10 μm macropore IO-ITO electrodes via the co-deposition method (1-step deposition of polymer−PSII blend, 15 min incubation time). The polymer−PSII (v/v) ratio was varied from 0:1, 0.5:1, 1:1 and 1.5:1, where 1:1 was defined as 1 μL P_{Phen} (10 mg mL^{-1}) to 1 μL PSII (2.6 mg mL^{-1} Chl *a*). PSII concentration was kept constant and the redox polymer concentration was varied (from 0, 5, 10 to 15 mg mL^{-1}). **a**, Photocurrent density, **b**, turnover frequency (TOF) and **c**, PSII loading determination of IO-ITO|P_{Phen}−PSII electrode.

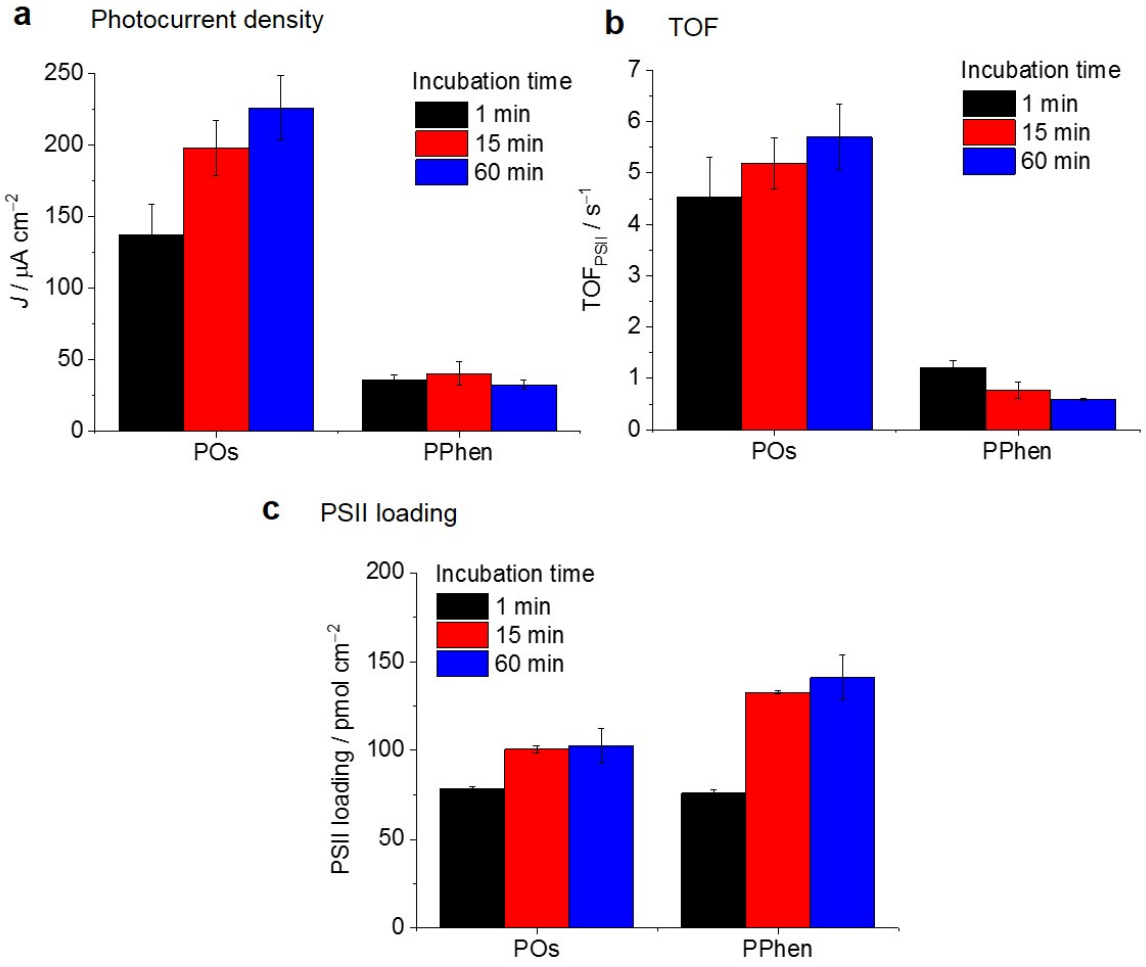

Figure B.7 **Polymer−PSII incubation time screening.** The IO-ITO|polymer−PSII electrodes were assembled using 0.75 μm macropore IO-ITO electrodes via the co-deposition method (1-step deposition of polymer−PSII blend). The polymer−PSII blend incubation (drying) time in the dark was varied from 1 min, 5 min to 60 min. Conditions: 1 μL P_{Os} (10 mg mL^{-1}), 1 μL P_{Phen} (10 mg mL^{-1}) and 1 μL PSII (2.6 mg mL^{-1} Chl *a*). **a**, Photocurrent density, **b**, turnover frequency (TOF) and **c**, PSII loading determination of IO-ITO|P_{Os}−PSII and IO-ITO|P_{Phen}−PSII electrodes.

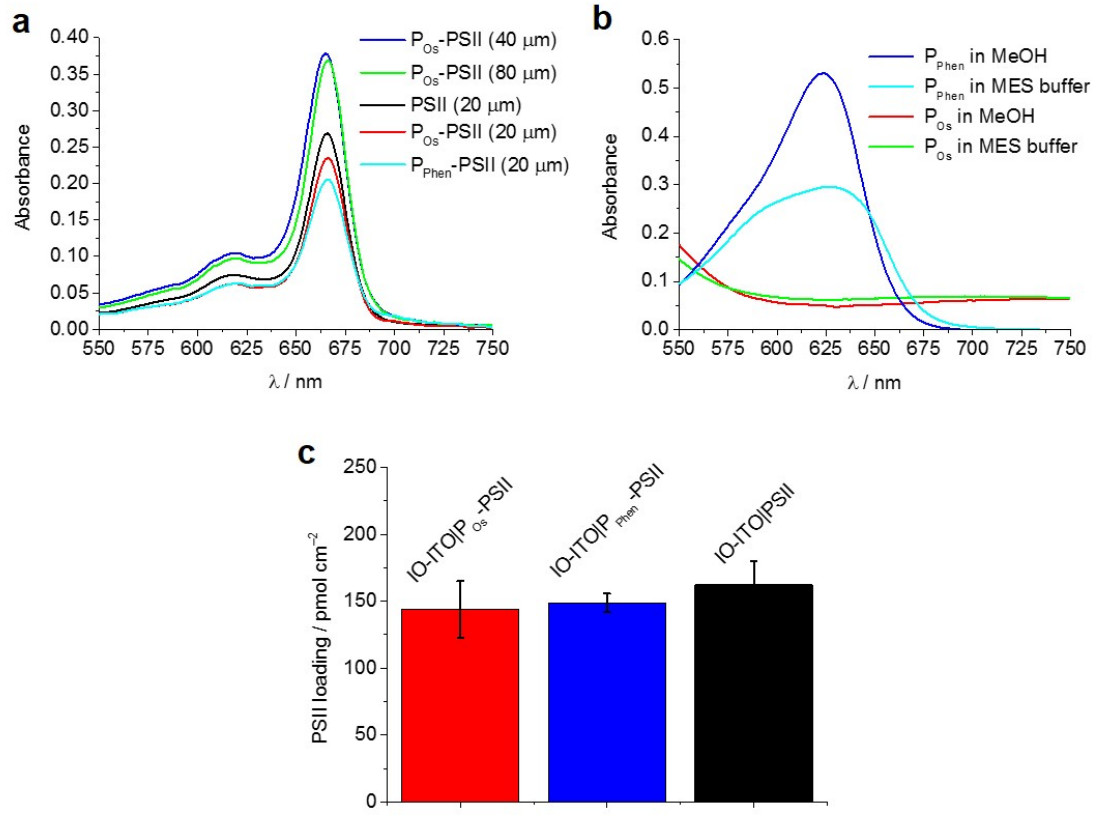

Figure B.8 **Quantification of PSII and redox polymer loading.** UV-vis spectra (λ = 550 - 750 nm) of **a**, Chl *a* from PSII entrapped on the modified IO-ITO|polymer−PSII photoanodes and extracted by MeOH. Briefly, following the chronoamperometry experiments, polymer−PSII was scratched off the glass substrate, washed with MeOH (500 μL) into a vial and centrifuged. The UV-vis spectrum of the supernatant was then recorded and the band with an absorption maximum of λ_{max} = 665 nm assigned to Chl *a* was used to calculate the amount of PSII monomers assuming 35 Chl *a* molecules per PSII monomer. UV-vis spectra of **b**, polymer solutions (0.02 mg mL^{-1}) in both MES electrolyte solution and MeOH, show negligible absorption at the irradiation wavelength used in PF-PEC (λ = 685 nm). **c**, A bar diagram showing the PSII loading on 20 μm thick modified electrodes measured after PF-PEC experiments: 162 $\pm$ 17 pmol cm^{-2} (IO-ITO|PSII), 144 $\pm$ 21 pmol cm^{-2} (IO-ITO|P$_{Os}$−PSII) and 149 $\pm$ 7 pmol cm^{-2} (IO-ITO|P$_{Phen}$−PSII). The figure adapted from Sokol et. al., *Energy Environ. Sci.*, 2016, **9**, 3698−3709.

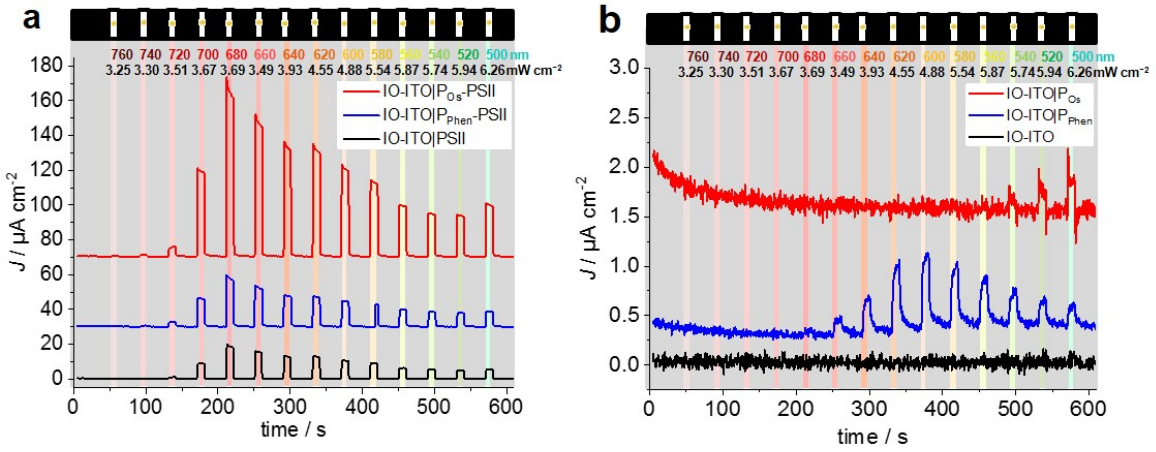

Figure B.9 **Photocurrent action spectra of IO-ITO|polymer−PSII photoanodes. a**, Action spectra showing the photocurrent density vs. irradiation wavelength of the IO-ITO|PSII (black), IO-ITO|P$_{Os}$−PSII (red) and IO-ITO|P$_{Os}$−PSII (blue) photoelectrodes (20 μm thickness) recorded with monochromatic light (λ = 420 to 760 nm) measured in 20 nm steps (E_e = 3.25 to 6.26 mW cm^{-2}). The error bars correspond to the standard deviation (N = 3). **b**, Control experiments with bare (PSII-free) IO-ITO (black), IO-ITO|P$_{Os}$ (red) and IO-ITO|P$_{Phen}$ (blue) electrodes showing no significant photocurrent density contribution. Short irradiation times (chopped 30 s dark and 10 s light irradiation time) are used in all experiments to prevent excessive PSII photodegradation over time. Conditions: E_{app} = 0.5 V vs. SHE, MES electrolyte solution (pH = 6.5, T = 25 °C). The figure adapted from Sokol et. al., *Energy Environ. Sci.*, 2016, **9**, 3698−3709.

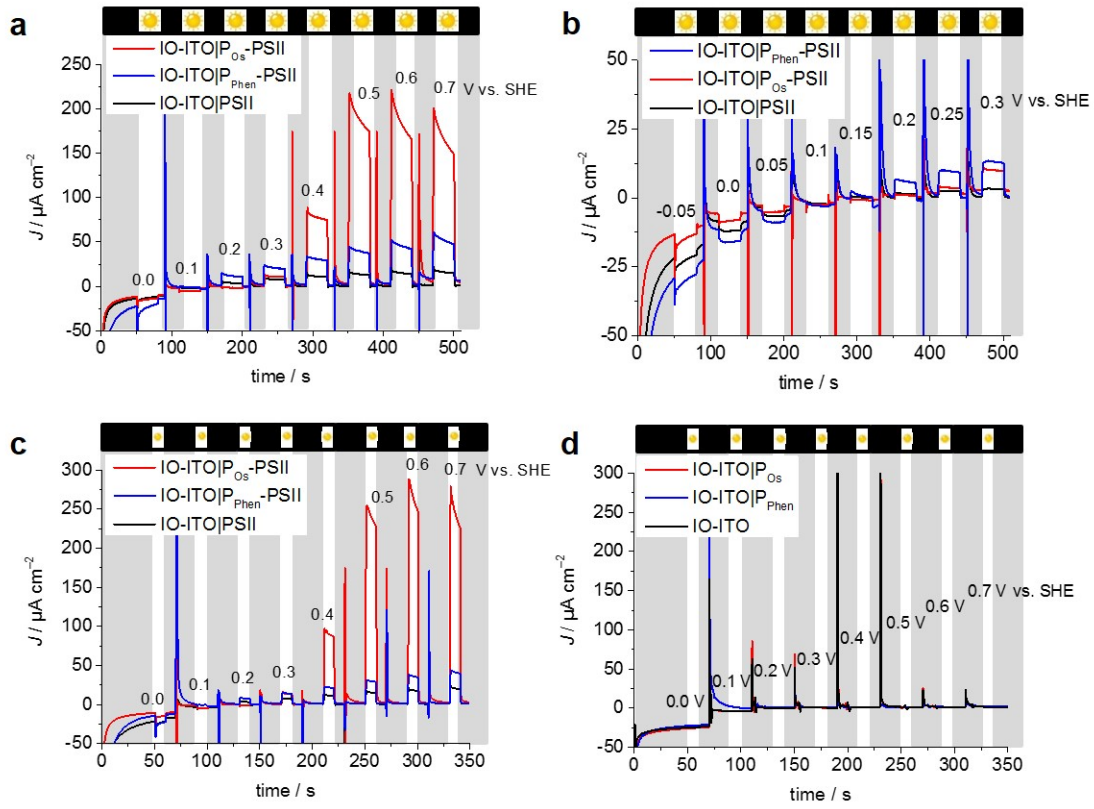

Figure B.10 **PF-PEC of IO-ITO|polymer−PSII photoanode and controls.** Stepped potential chronoamperometry for 20 μm thick IO-ITO|polymer−PSII and IO-ITO|PSII photoanodes (**a**, **b** and **c**) and **d**, PSII-free electrodes. Larger applied potential E_{app} step size (0.1 V) and range (0.0 - 0.7 V vs. SHE) of chronoamperometry (chopped 30 s dark and 30 s light irradiation times) in **a**, show the limiting photocurrent density for each system while in **b**, the onset potential for each system is emphasised (0.05 V steps in E_{app} range 0.0 - 0.5 V vs. SHE). Shorter irradiation times (chopped 30 s dark and 10 s light irradiation times) are used in **c**, and **d**, to prevent excessive PSII photodegradation over time. The PSII loading on each modified electrode was comparable: 162 $\pm$ 17 pmol cm^{-2} (IO-ITO|PSII), 144 $\pm$ 21 pmol cm^2 (IO-ITO|P$_{Os}$−PSII) and 149 $\pm$ 7 pmol cm^{-2} (IO-ITO|P$_{Phen}$−PSII). The redox-active centres loading was 25 $\pm$ 4 nmol cm^{-2} (P$_{Os}$) and 17 $\pm$ 4 nmol cm^{-2} (P$_{Phen}$). Conditions: pH = 6.5, T = 25 °C. The figure adapted from Sokol et. al., *Energy Environ. Sci.*, 2016, **9**, 3698−3709.

Appendix C

Appendix to Chapter 4

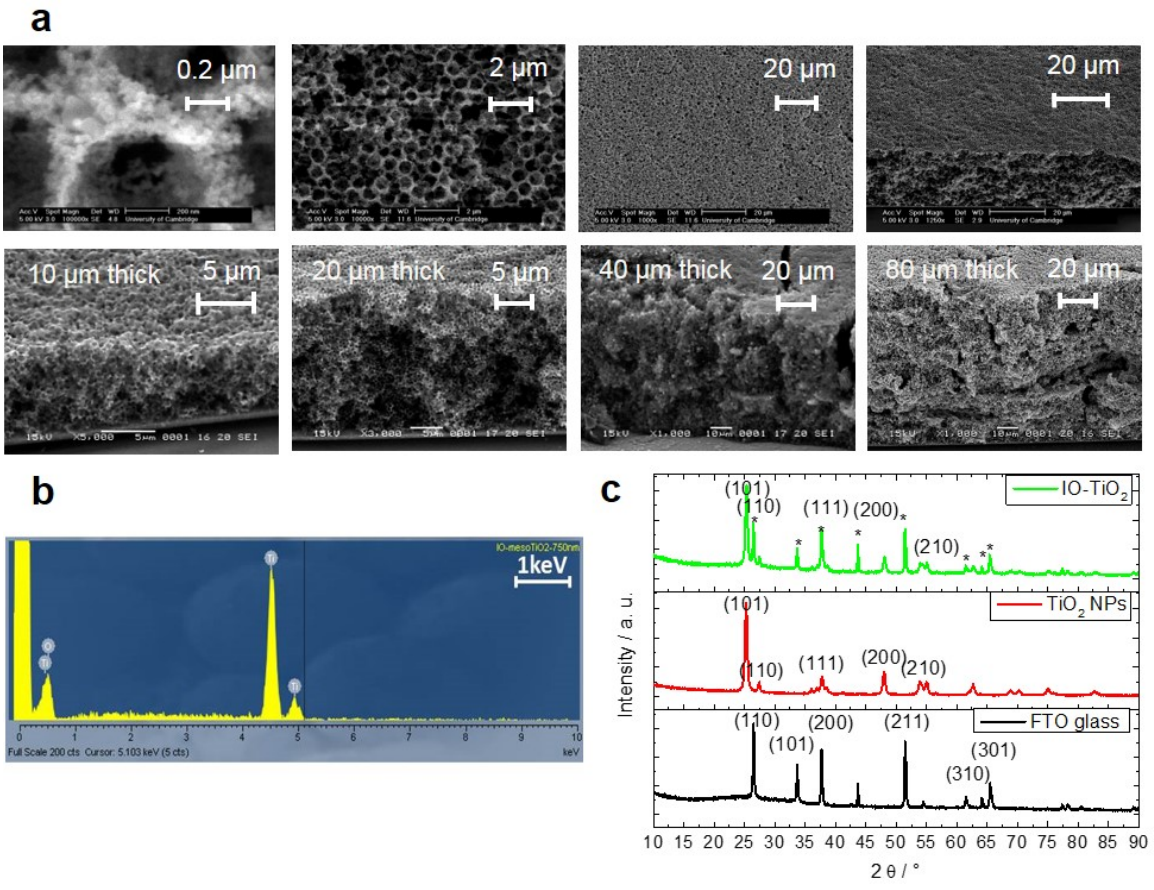

Figure C.1 **IO-TiO_2 electrode characterisation. a**, SEM images of the IO-TiO_2 electrode with 10, 20, 40 and 80 μm film thickness measured at 60° tilt angle. **b**, Energy-dispersive X-ray (EDX) spectroscopy and **c**, powder X-ray diffraction (PXRD) of the IO-TiO_2. The figure adapted from Sokol et. al., *Nat. Energy*, 2018, **3**, 944-951.

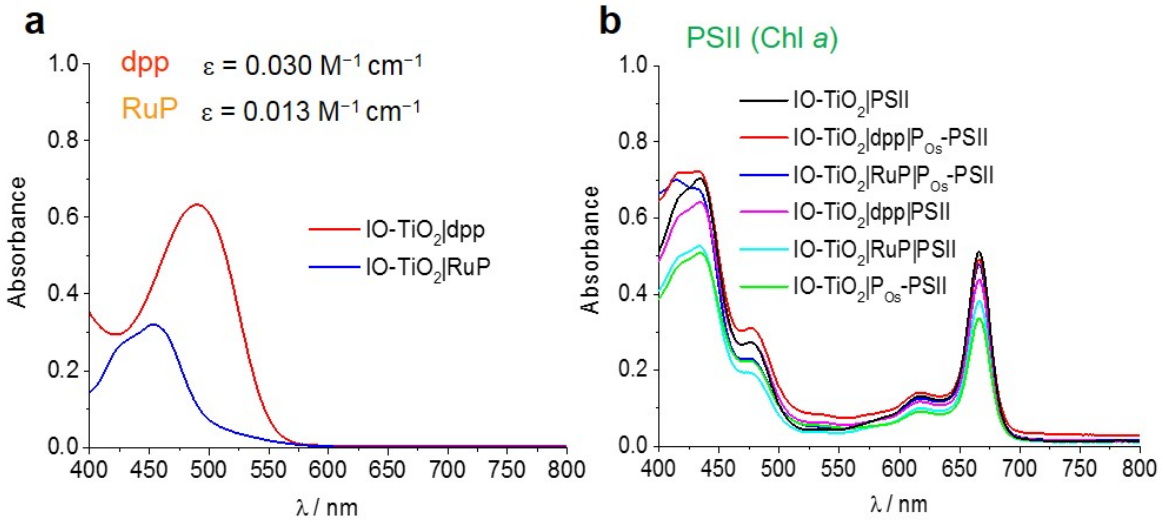

Figure C.2 **Quantification of dpp, RuP and PSII loading. a**, Transmission UV-Vis absorption spectra of dpp and RuP in solution following desorption from the IO-TiO_2 electrodes with tetrabutylammonium hydroxide (TBAOH) (0.1 M) in MeOH (500 μL). **b**, Spectra of Chl *a* from PSII quantified after scratching off PSII-modified IO-TiO_2 from the substrate and washing it with MeOH (500 μL). UV-Vis cuvette path length: 1 cm. The figure adapted from Sokol et. al., *Nat. Energy*, 2018, **3**, 944-951.

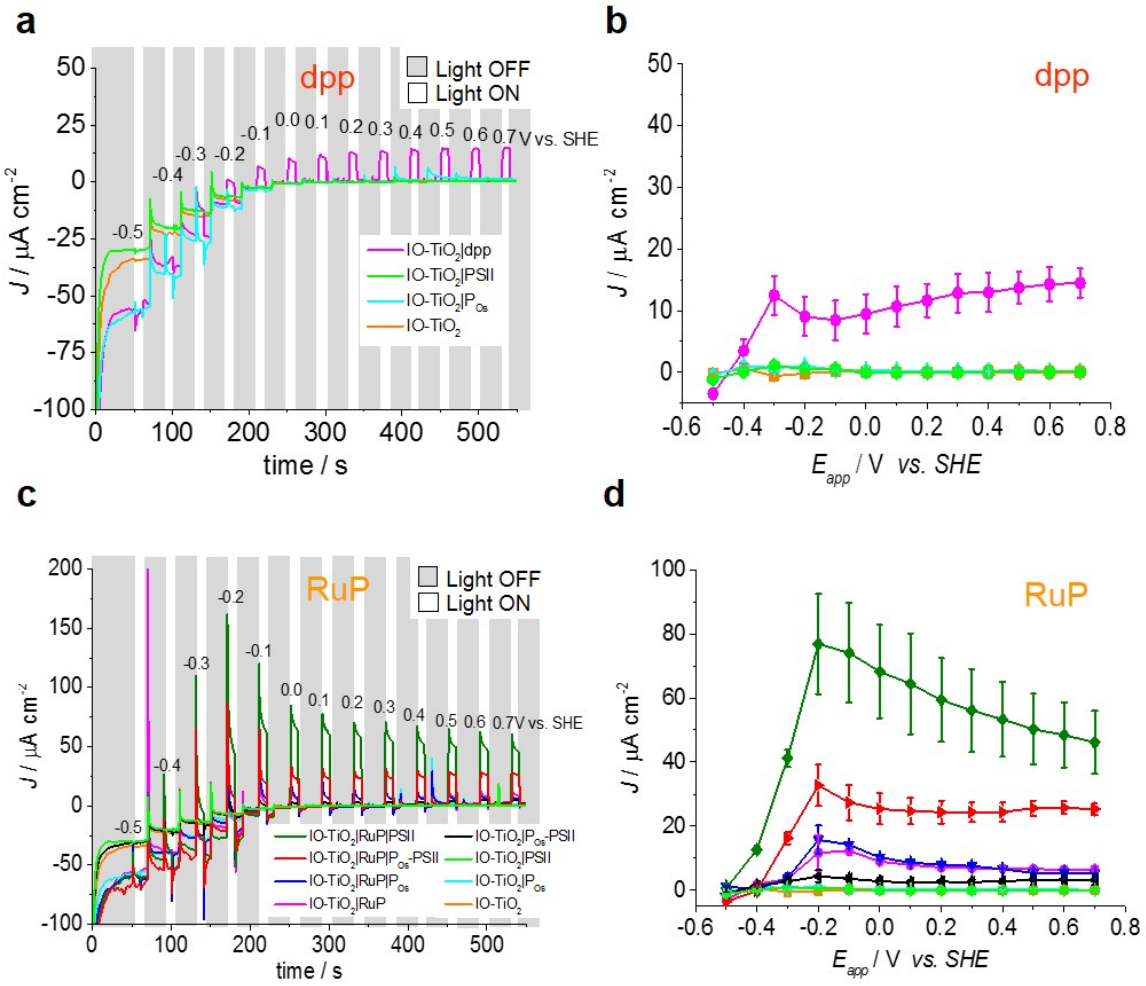

Figure C.3 **PF-PEC of tandem PSII−dye photoanode.** **a**, Stepped-potential (ΔE_{app} = 0.1 V) chronoamperometry of IO-TiO_2|dpp and the control photoanodes. The chronoamperometry (chopped 30 s dark and 10 s light irradiation times) show the onset potentials (E_{onset}) and limiting photocurrent density for each system. Short irradiation times are used to prevent excessive PSII photodegradation over time. **b**, Photocurrent density as a function of E_{app} for the photoanodes, determined by stepped-potential chronoamperometry in **a**. **c**, Stepped-potential chronoamperometry and **d**, the photocurrent density as a function of E_{app} for the RuP-sensitised photoanodes determined in **c**. Conditions: PSII electrolyte solution, pH = 6.5, T = 25 °C. A three-electrode configuration was employed with a Ag/AgCl (3 M KCl) reference and Pt wire counter electrode, respectively. The error bars correspond to the standard deviation (N = 3). The lower photocurrent observed for IO-TiO_2|RuP|P_{Os}−PSII compared to IO-TiO_2|RuP|PSII, indicates deleterious interactions between RuP and P_{Os} that affect electrode performance, possibly due to P_{Os} displacing RuP form the surface, displacement of bipyridine ligands on RuP by imidazole side groups on P_{Os}, or repulsion between the Ru^{2+} and $Os^{3+/2+}$ centres. In contrast to dpp, RuP-containing systems could not benefit from the gain in wiring efficiency enabled by P_{Os}. The figure adapted from Sokol et. al., *Nat. Energy*, 2018, **3**, 944-951.

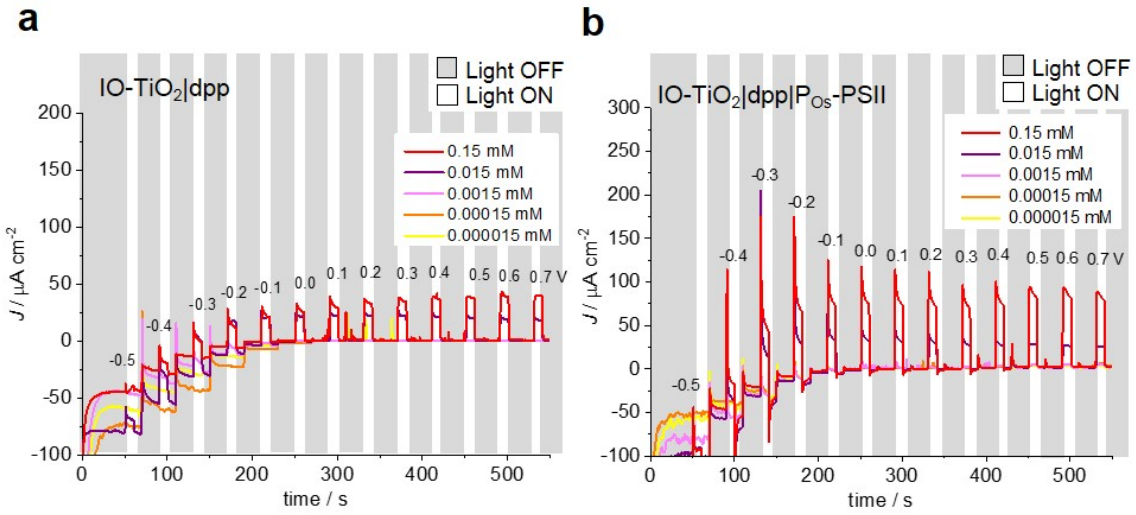

Figure C.4 **Photocurrent dependence on dpp dye loading.** **a**, Stepped-potential (ΔE_{app} = 0.1 V) chronoamperometry of 20 μm thick IO-TiO_2|dpp and **b**, IO-TiO_2|dpp|P_{Os}−PSII photoelectrodes was recorded (chopped 30 s dark and 10 s light irradiation times). The dpp loading was varied by changing the concentration of the dying solution in THF. The optimal dying solution concentration was found to be 0.15 mM. Conditions: E_{app} = 0.5 V vs. SHE, electrolyte solution pH = 6.5, T = 25 °C. The figure adapted from Sokol et. al., *Nat. Energy*, 2018, **3**, 944-951.

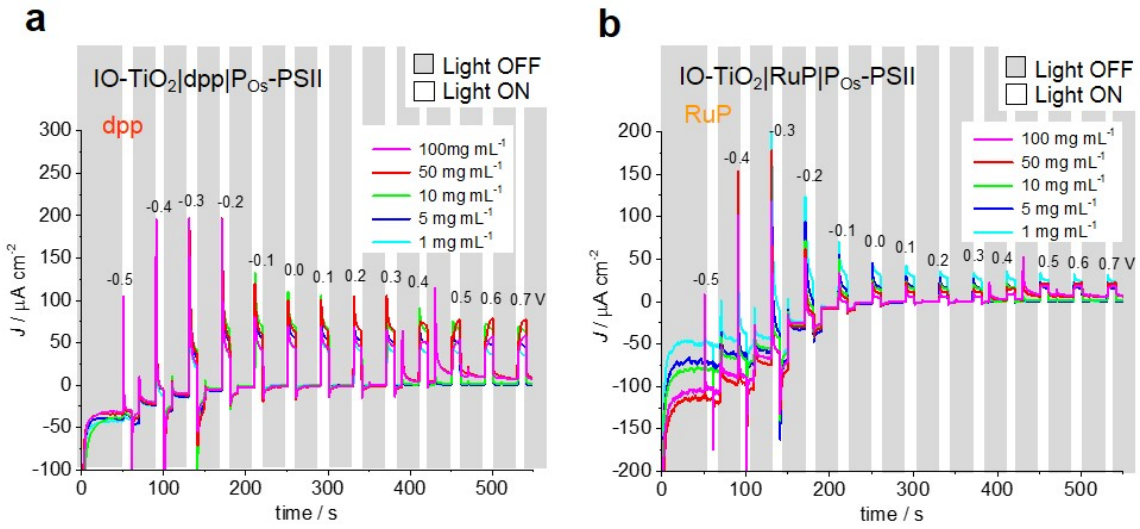

Figure C.5 **Photocurrent dependence on P_{Os} polymer concentration. a**, Stepped-potential (ΔE_{app} = 0.1 V) chronoamperometry of 20 μm thick IO-TiO_2|dpp|P_{Os}−PSII and **b**, IO-TiO_2|RuP|P_{Os}−PSII photoelectrodes was recorded (chopped 30 s dark and 10 s light irradiation times). The P_{Os} to PSII ratio was varied by changing the concentration of the P_{Os} solution in H_2O (1-100 mg mL^{-1}). The optimal P_{Os} concentration was found to be 10 mg mL^{-1} (deposited volume: 1 μL). Conditions: E_{app} = 0.5 V vs. SHE, electrolyte solution pH = 6.5, T = 25 °C. The figure adapted from Sokol et. al., *Nat. Energy*, 2018, **3**, 944-951.

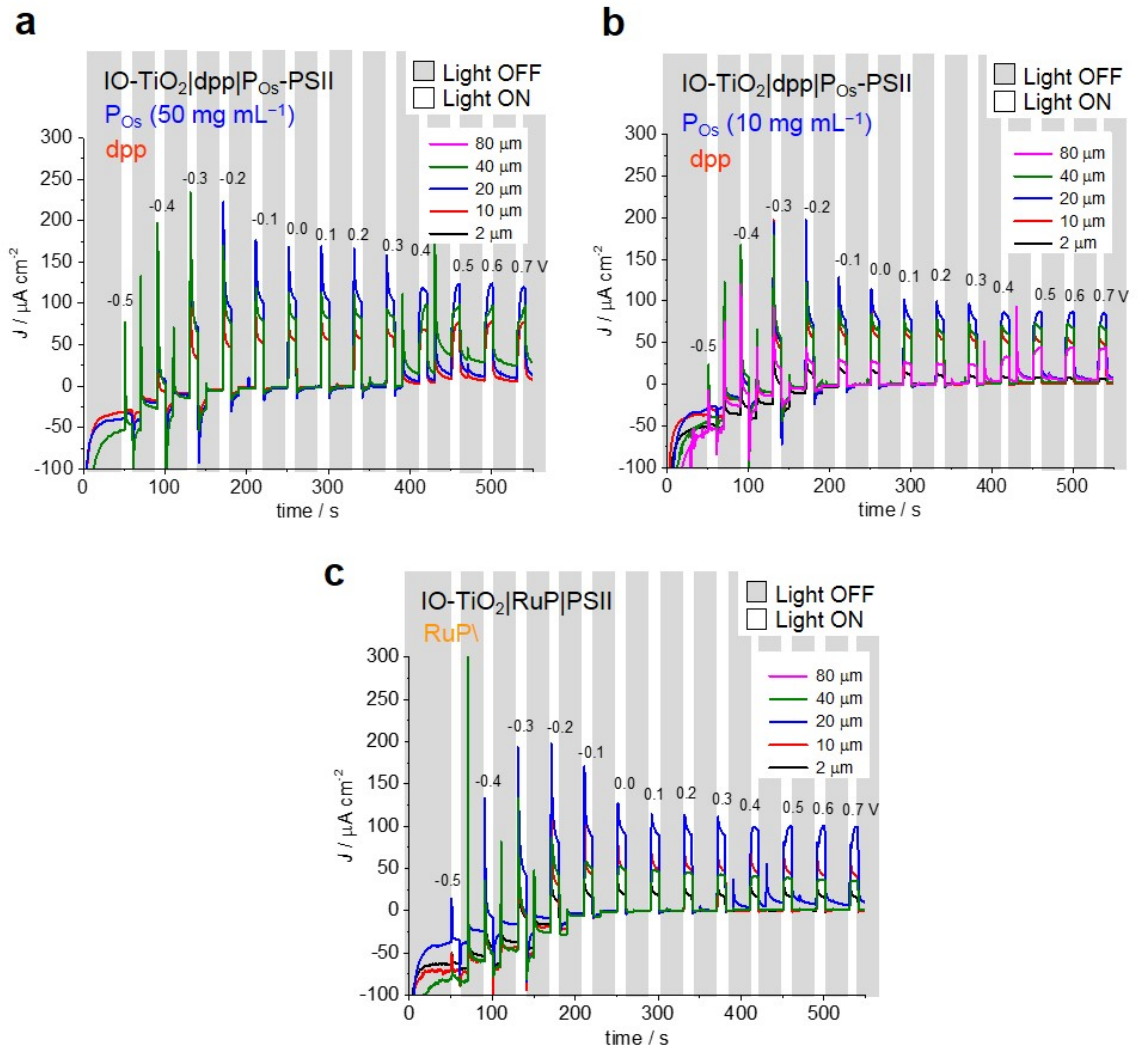

Figure C.6 **Photocurrent dependence on IO-TiO_2 electrode thickness.** **a**, Stepped-potential (ΔE_{app} = 0.1 V) chronoamperometry of 2-80 μm thick IO-TiO_2|dpp|P_{Os}−PSII (P_{Os} = 50 mg mL^{-1}), **b**, IO-TiO_2|dpp|P_{Os}−PSII (P_{Os} = 10 mg mL^{-1}) and **c**, IO-TiO_2|RuP|PSII photoelectrodes was recorded (chopped 30 s dark and 10 s light irradiation times). The optimal thickness was found to be 20 μm. Conditions: E_{app} = 0.5 V vs. SHE, electrolyte solution pH = 6.5, T = 25 °C. The figure adapted from Sokol et. al., *Nat. Energy*, 2018, **3**, 944-951.

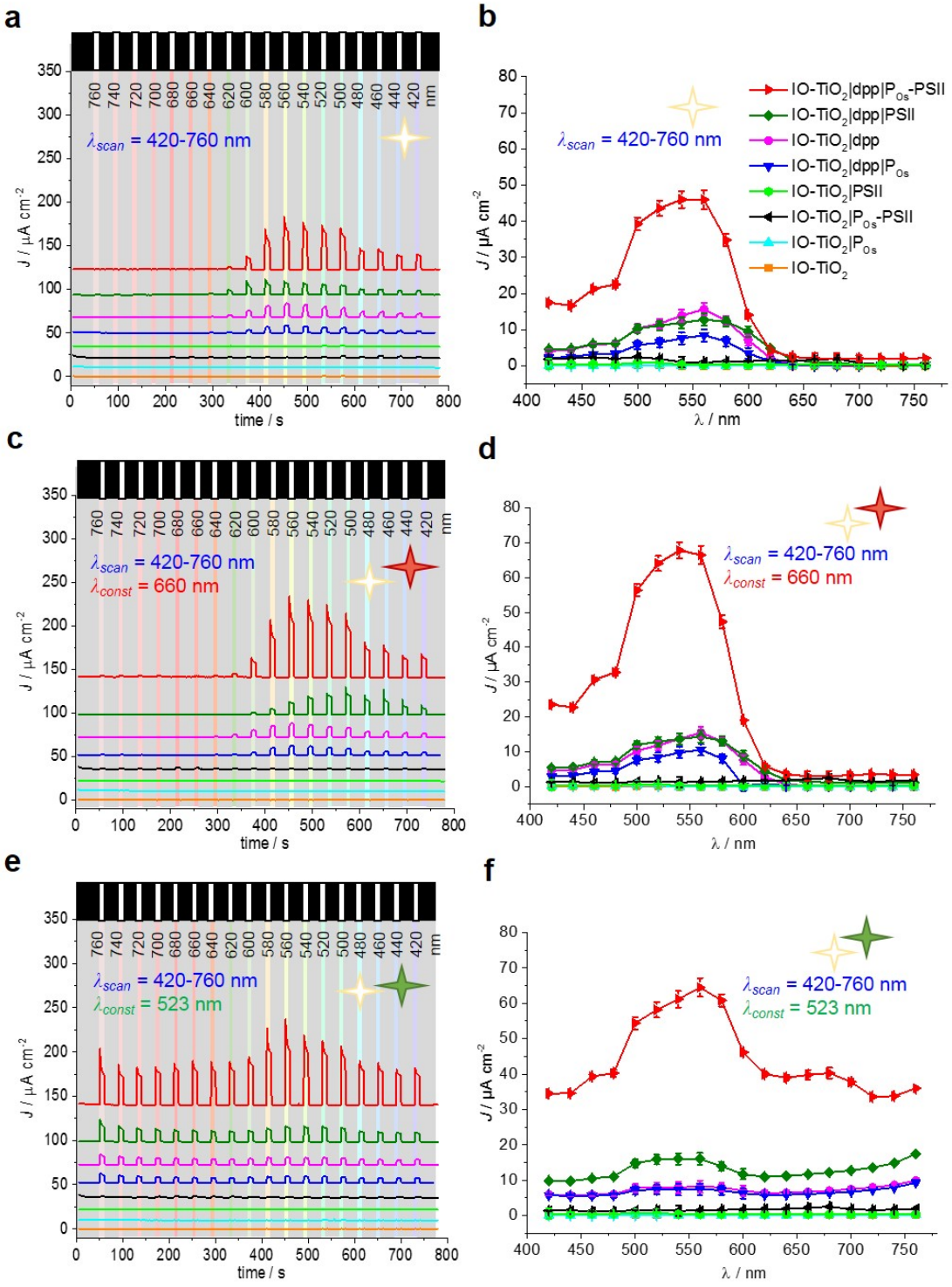

Figure C.7 **Photocurrent action spectra of IO-TiO_2|dpp|P_{Os}−PSII. a**, *J* dependence on the irradiation λ of IO-TiO_2|dpp|P_{Os}−PSII photoelectrodes recorded with monochromatic light (λ_{scan} = 420 to 760 nm measured in 20 nm steps; E_e = 3.3 - 6.3 mW cm^{-2}). **b**, *J* dependence on the λ of IO-TiO_2|dpp|P_{Os}−PSII photoelectrodes recorded with the monochromatic light determined in **a**. **c**, Dual-wavelength action spectra of the IO-TiO_2|dpp|P_{Os}−PSII photoelectrodes recorded with a second simultaneous irradiation of λ_{const} = 660 nm (4 mW cm^{-2}) and **d**, *J* as a function of the λ determined in **c**. **e**, Dual-wavelength action spectra of the IO-TiO_2|dpp|P_{Os}−PSII photoelectrodes recorded with a second simultaneous irradiation of λ_{const} = 523 nm (4 mW cm^{-2}) and **f**, *J* as a function of the λ determined in **e**. Conditions: E_{app} = 0.5 V vs. SHE, electrolyte solution pH = 6.5, T = 25 °C. The figure adapted from Sokol et. al., *Nat. Energy*, 2018, **3**, 944-951.

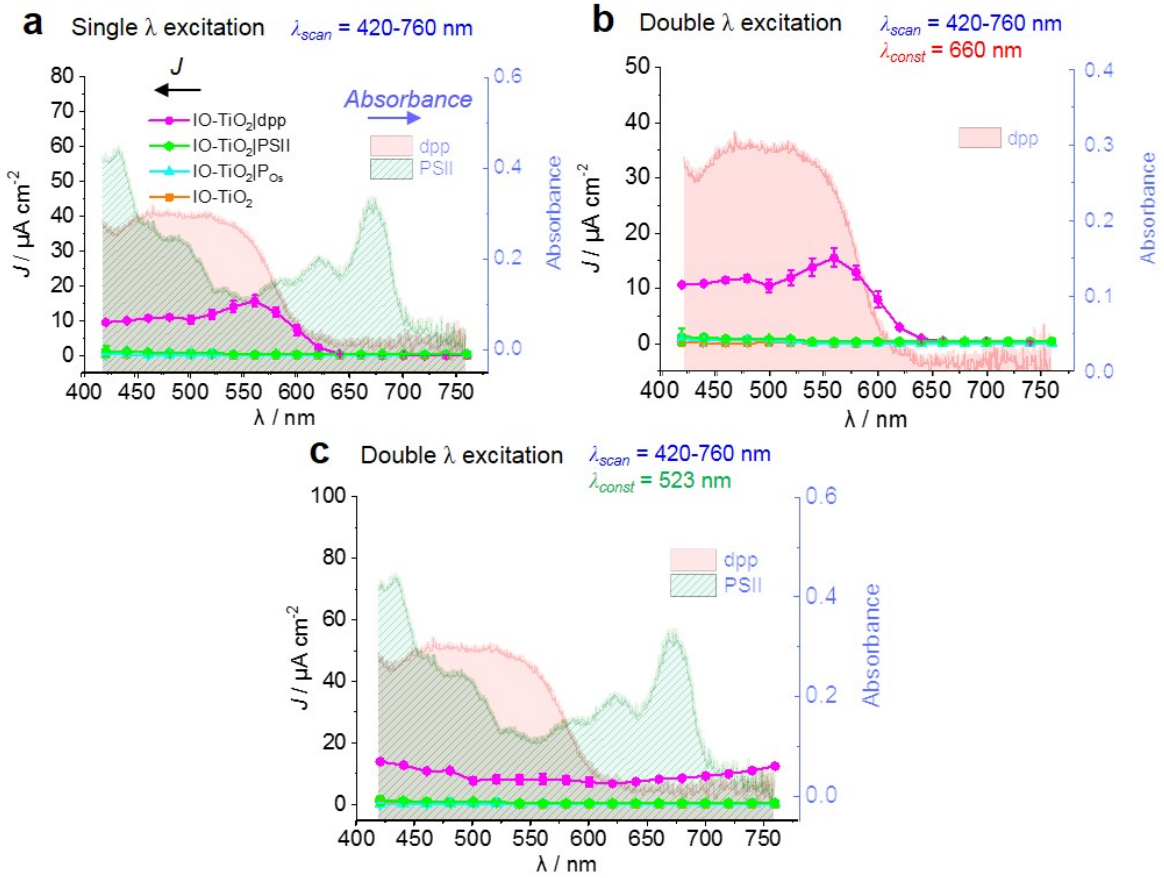

Figure C.8 **Photocurrent action spectra of IO-TiO_2|dpp|P_{Os}−PSII corrected and normalised to equal photon flux. a**, Photocurrent density vs. irradiation wavelength of the IO-TiO_2|dpp and control photoelectrodes recorded with monochromatic light (λ_{scan}) measured in 20 nm steps (E_e = 6 mW cm^{-2}). **b**, Dual-wavelength action spectra of the IO-TiO_2|dpp and control photoelectrodes recorded with a second simultaneous irradiation of λ_{const} = 660 nm (4 mW cm^{-2}) and **c**, 523 nm (4 mW cm^{-2}). The action spectra were corrected to equal photon flux at 500 nm (0.26 mmol m^{-2} s^{-1}) at each wavelength and normalised. The error bars correspond to the standard deviation (N = 3). The right y-axis refers to the UV-vis spectra of background-corrected dpp and PSII immobilised on the IO-TiO_2 electrodes (shaded in red and green in the background). Conditions: E_{app} = 0.5 V vs. SHE, PSII electrolyte solution pH = 6.5, T = 25 °C. The figure adapted from Sokol et. al., *Nat. Energy*, 2018, **3**, 944-951.

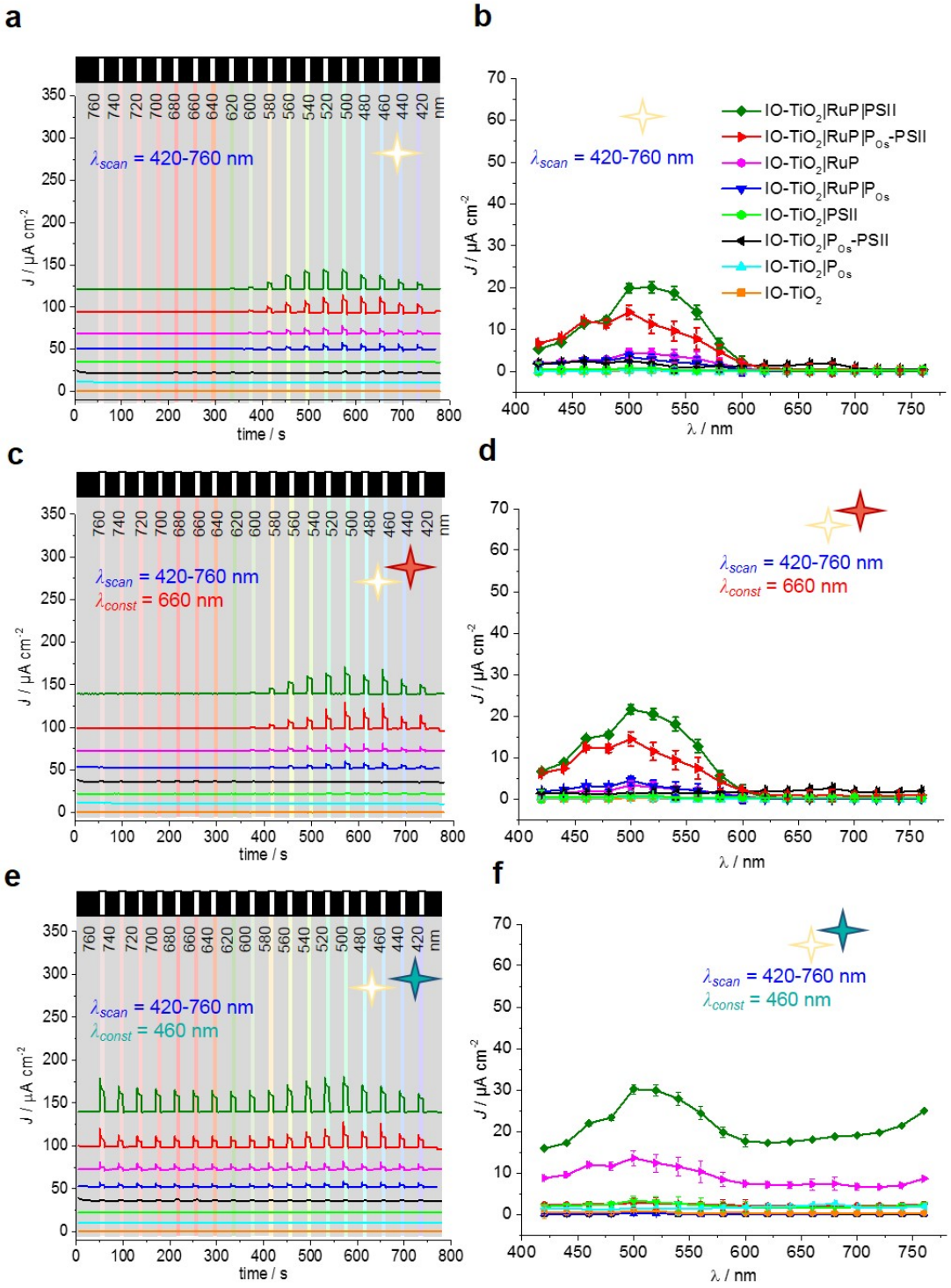

Figure C.9 **Photocurrent action spectra of IO-TiO_2|RuP|P_{Os}−PSII. a**, J dependence on the irradiation λ of IO-TiO_2|RuP|P_{Os}−PSII photoelectrodes recorded with monochromatic light (λ_{scan} = 420 to 760 nm measured in 20 nm steps; E_e = 3.3 - 6.3 mW cm^{-2}). **b**, J dependence on the λ of IO-TiO_2|RuP|P_{Os}−PSII photoelectrodes recorded with the monochromatic light determined in **a**. **c**, Dual-wavelength action spectra of the IO-TiO_2|RuP|P_{Os}−PSII photoelectrodes recorded with a second simultaneous irradiation of λ_{const} = 660 nm (4 mW cm^{-2}) and **d**, J as a function of the λ determined in **c**. **e**, Dual-wavelength action spectra of the IO-TiO_2|RuP|P_{Os}−PSII photoelectrodes recorded with a second simultaneous irradiation of λ_{const} = 460 nm (4 mW cm^{-2}) and **f**, J as a function of the λ determined in **e**. Conditions: E_{app} = 0.5 V vs. SHE, electrolyte solution pH = 6.5, T = 25 °C. The figure adapted from Sokol et. al., *Nat. Energy*, 2018, **3**, 944-951.

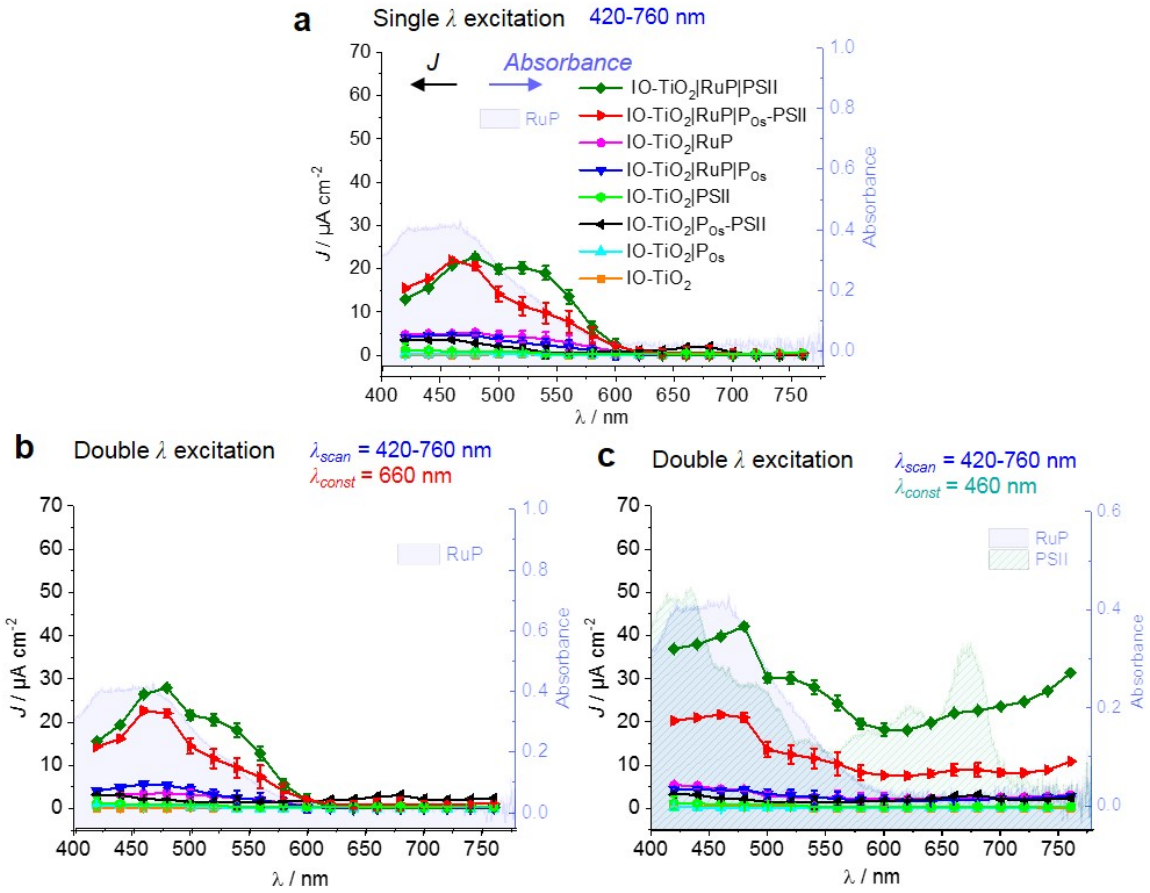

Figure C.10 **Photocurrent action spectra of IO-TiO_2|RuP|P_{Os}−PSII corrected and normalised to equal photon flux.** **a**, Photocurrent density vs. irradiation wavelength of the IO-TiO_2|RuP|P_{Os}−PSII and control photoelectrodes recorded with monochromatic light (λ_{scan}) measured in 20 nm steps (E_e = 6 mW cm^{-2}). **b**, Dual-wavelength action spectra of the IO-TiO_2|RuP|P_{Os}−PSII photoelectrodes recorded with a second simultaneous irradiation of λ_{const} = 660 nm (4 mW cm^{-2}) and **c**, λ_{const} = 460 nm (4 mW cm^{-2}). The action spectra were corrected to equal photon flux at 500 nm (0.26 mmol m^{-2} s^{-1}) at each wavelength and normalised. The error bars correspond to the standard deviation (N = 3). The second axis (right) refers to the UV-vis spectra of background-corrected RuP and PSII immobilised on the IO-TiO_2 electrodes overlaid behind. Conditions: E_{app} = 0.5 V vs. SHE, PSII electrolyte solution pH = 6.5, T = 25 °C. The figure adapted from Sokol et. al., *Nat. Energy*, 2018, **3**, 944-951.

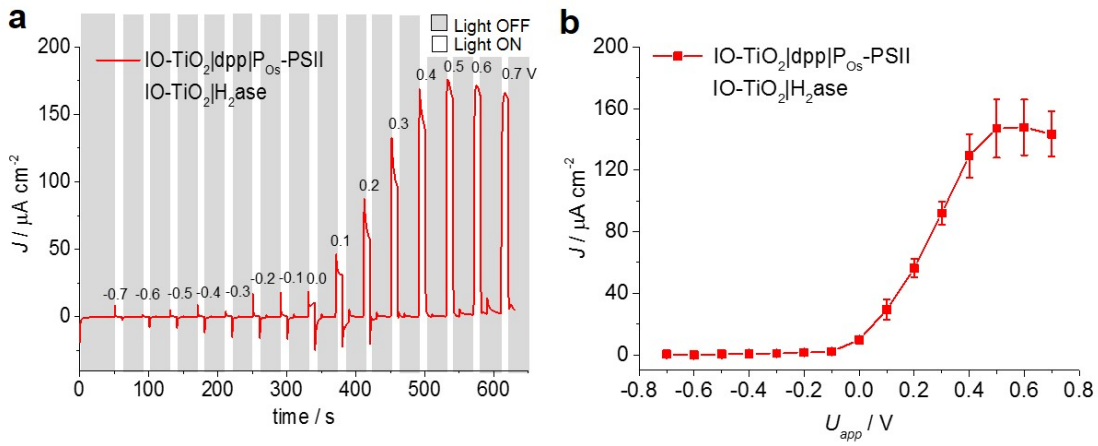

Figure C.11 **PF-PEC of tandem bias-free two-electrode system with an IO-TiO_2|H_2ase cathode. a**, Stepped-voltage (ΔU_{app} = 0.1 V) chronoamperometry (U_{app} = −0.7 to 0.7 V) of the IO-TiO_2|dpp|P_{Os}−PSII photoanode wired to IO-TiO_2|H_2ase cathode **b**, Photocurrent density as a function of U_{app} of the two-electrode system, based on the stepped-voltage chronoamperometry determined in **a**. Conditions: PSII electrolyte solution, pH = 6.5, T = 25 °C, continuous stirring, N_2 atmosphere. Light illumination (1 sun; 1.5 AM filter; E_e = 100 mW cm^{-2}; $\lambda > 420$ nm). The error bars correspond to the standard deviation (N = 3). The figure adapted from Sokol et. al., *Nat. Energy*, 2018, **3**, 944-951.

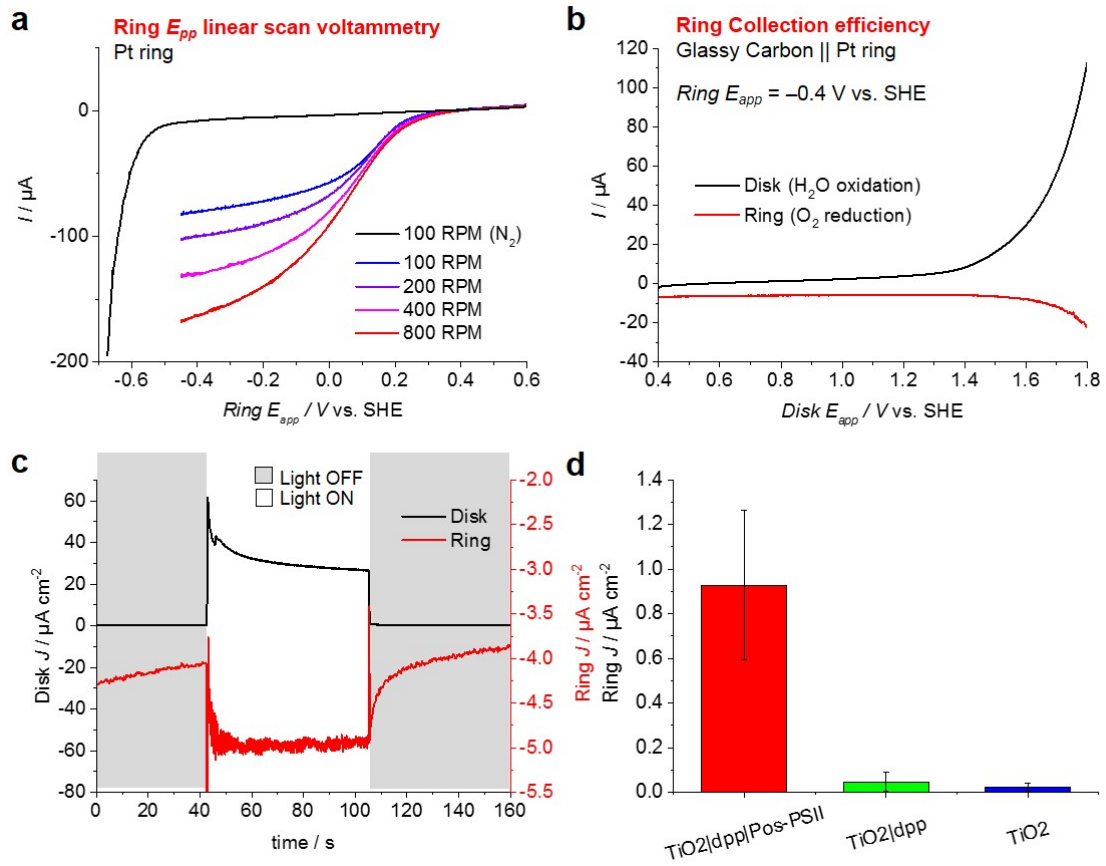

Figure C.12 **PSII photoactivity and O_2 detection with rotating ring-disk electrode (RRDE). a**, Linear scan voltammetry showing a cathodic (O_2 reduction) ring current in an air-saturated electrolyte solution at different electrode rotation rates. **b**, Linear scan voltammetry showing the estimation of the RRDE collection efficiency for O_2 reduction (20%). E_{app} (ring) = −0.4 V vs. SHE. Rotation rate: 400 r.p.m. **c**, Chronoamperometry showing the O_2 reduction by PSII in the RRDE setup. Black trace: disk current (PSII photocurrent), red trace: ring current (O_2 reduction). E_{app} (disk) = 0.5 V and E_{app} (ring) = −0.4 V vs. SHE. Rotation rate: 400 r.p.m. **d**, The ring currents for the mesoporous TiO_2|dpp|P_{Os}−PSII, mesoporous TiO_2|dpp and mesoporous TiO_2, determined by chronoamperometry in **c**. Conditions: PSII electrolyte solution, pH = 6.5, T = 25 °C, stirring. Light illumination (8 mW cm^{-2} white LED illumination). The error bars correspond to the standard deviation (N = 3). Data recorded by Dr. Nikolay Kornienko. The figure adapted from Sokol et. al., *Nat. Energy*, 2018, **3**, 944-951.

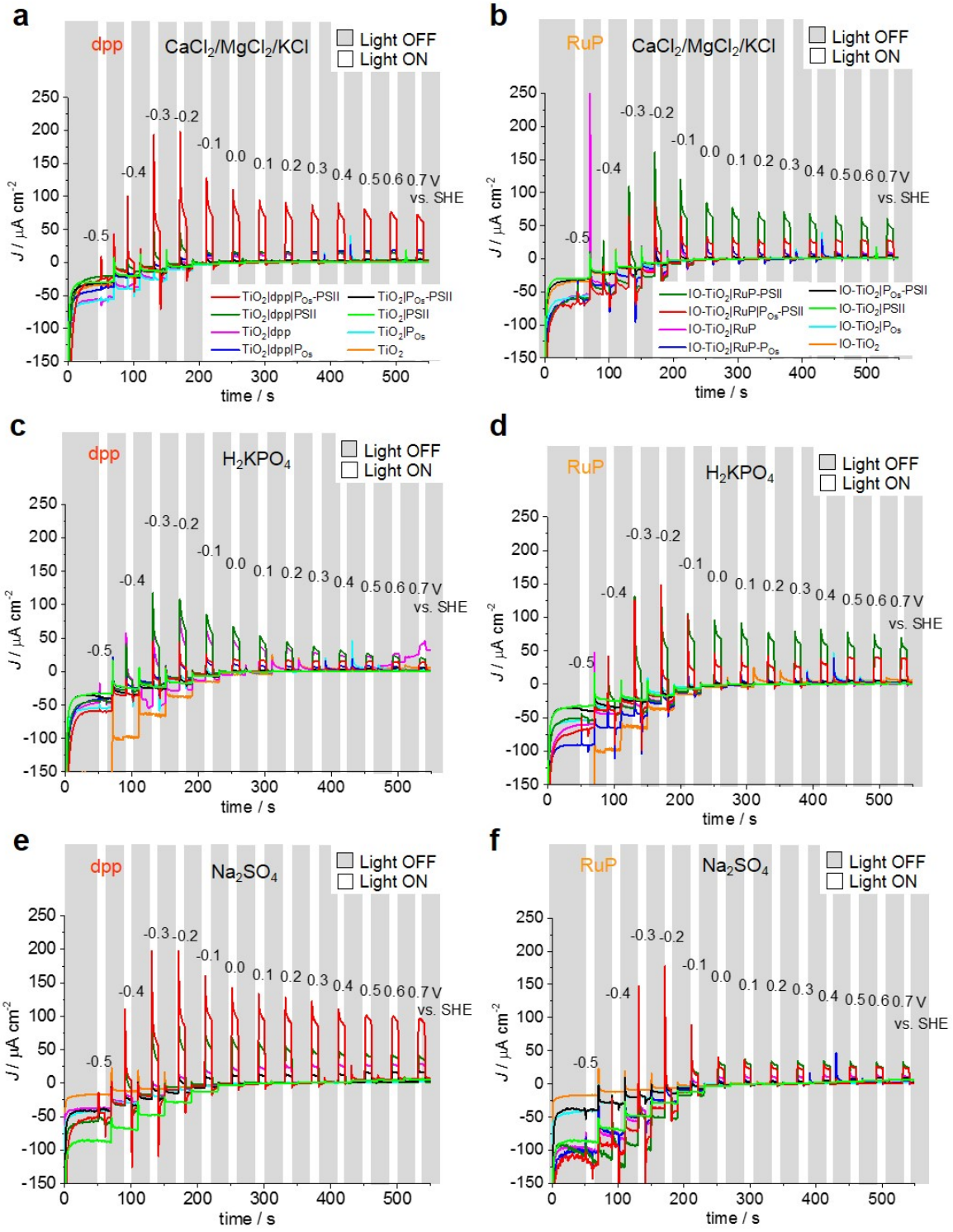

Figure C.13 **Photocurrent dependence of IO-TiO_2|dye|P_{Os}−PSII photoanode on electrolyte choice.** Stepped-potential (ΔE_{app} = 0.1 V) chronoamperometry (chopped 30 s dark and 10 s light irradiation times) of IO-TiO_2|dpp|P_{Os}−PSII and IO-TiO_2|RuP|P_{Os}−PSII photoanodes recorded in an aqueous 85 mM $CaCl_2$/$MgCl_2$/KCl electrolyte (**a** and **b**, respectively), an aqueous 100 mM H_2KPO_4 buffer electrolyte (**c** and **d**, respectively), and an aqueous 100 mM Na_2SO_4 electrolyte (**e** and **f**, respectively). Conditions: pH = 6.5, T = 25 °C. A three-electrode configuration was employed with a Ag/AgCl (3 M KCl) reference and Pt wire counter electrode, respectively.

Appendix D

Appendix to Chapter 5

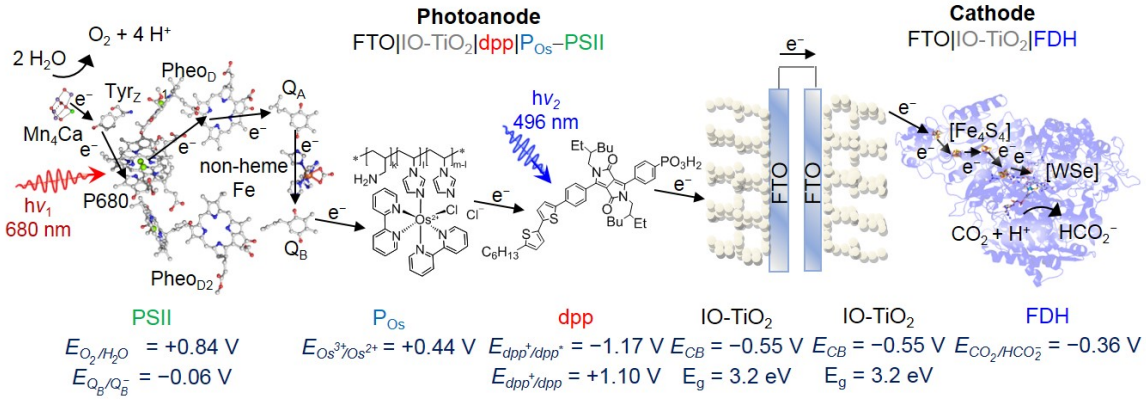

Figure D.1 **Elentron-transfer pathway of the PSII−FDH system.** Schematic representation of the dye-sensitised IO-TiO_2|dpp|P_{Os}−PSII photoanode wired to IO-TiO_2|FDH cathode (species size not drawn to scale). Abbreviations: Mn_4Ca, oxygen-evolving complex (OEC); Tyr_Z, tyrosine; P680, pigment/primary electron donor; $Pheo_{D1}$/$Pheo_{D2}$, pheophytin; Q_A/Q_B, plastoquinones; [Fe_4S_4], iron-sulphur clusters; [WSe], FDH active site; all potentials reported vs. SHE at pH 6.5. Scheme adopted from Sokol et. al., *Nat. Energy*, 2018, **3**, 944-951. The figure published in Sokol et. al., *J. Am. Chem. Soc.*, 2018, **140**, 16418–16422.

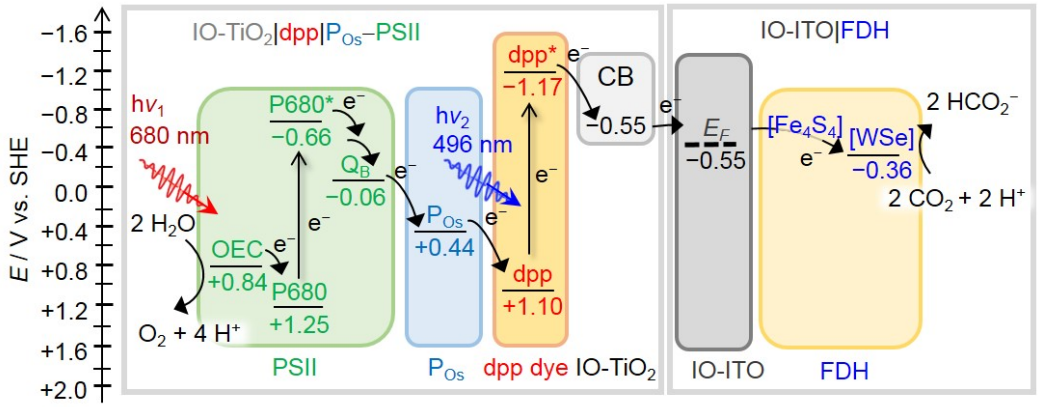

Figure D.2 **Energy level diagram of the IO-TiO_2|dpp|P_{Os}−PSII wired to IO-ITO|FDH.** Energy level diagram showing the electron-transfer pathway between PSII, the redox polymer (P_{Os}), the dye (dpp), the Fermi level energy (E_F) of IO-ITO electrodes, four [Fe_4S_4] clusters and the [WSe]-active site in FDH. All potentials are reported vs. SHE at pH 6.5. Abbreviations: Mn_4Ca, oxygen-evolving complex (OEC); P680, pigment/primary electron donor; Q_B, plastoquinone B; [Fe_4S_4], iron-sulfur clusters; [WSe], FDH active site.

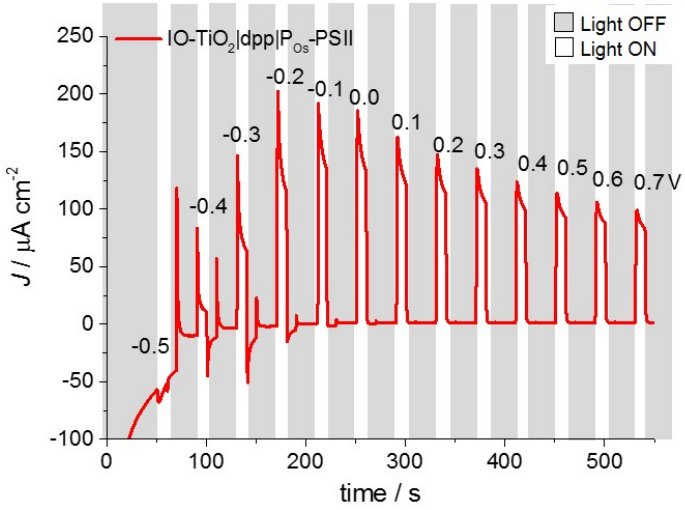

Figure D.3 **Three-electrode characterisation of the IO-TiO_2|dpp|P_{Os}−PSII photoanode.** Stepped-potential chronoamperometry (0.1 V potential steps with 30 s dark and 10 s light cycles) for the determination of onset potential (E_{onset}) and limiting photocurrent for IO-TiO_2|dpp|P_{Os}−PSII photoanode. E_{app} values (shown on top of the lines) are reported vs. SHE. Short irradiation times were used to minimise PSII photodegradation. Conditions: CO_2/$NaHCO_3$ (100 mM), KCl (50 mM), one atmosphere CO_2, pH = 6.5, T = 25 °C, continuous stirring. Simulated solar light source: AM 1.5G filter; E_e = 100 mW cm^{-2}; $\lambda >$ 420 nm. A three-electrode configuration employed a Ag/AgCl (saturated KCl) reference and Pt mesh counter electrode, respectively. The figure adapted from Sokol et. al., *J. Am. Chem. Soc.*, 2018, **140**, 16418–16422.

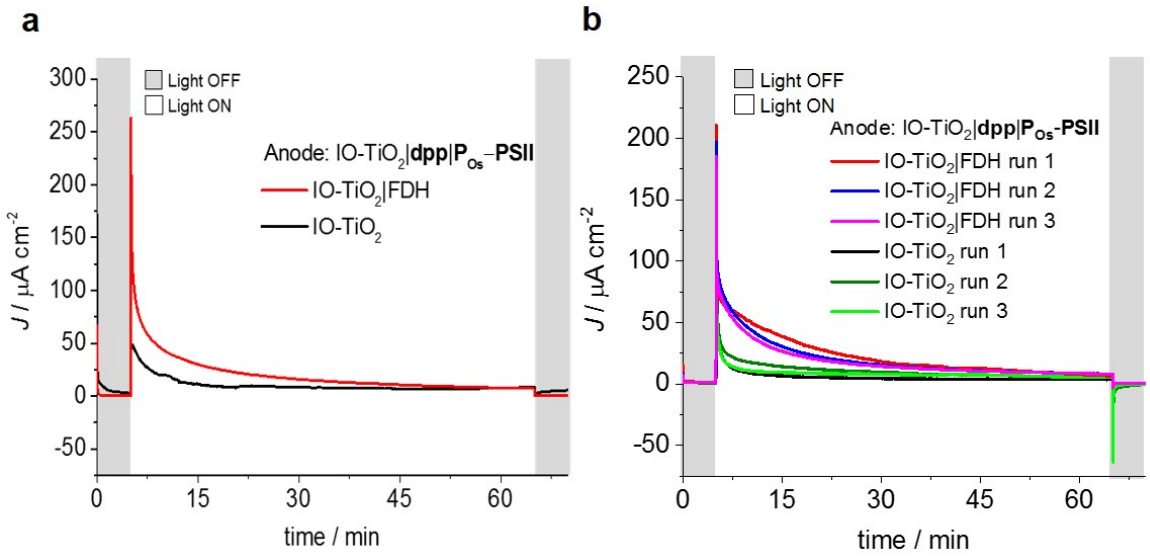

Figure D.4 **Two-electrode CPE of the IO-TiO_2|dpp|P_{Os}−PSII wired to IO-TiO_2|FDH. a**, CPE at U_{app} = 0.6 V of the two-electrode tandem system: IO-TiO_2|FDH (or enzyme-free IO-TiO_2) cathode wired to the IO-TiO_2|dpp|P_{Os}−PSII photoanode. Formate (n[HCO_2^-] = 0.209 μmol cm^{-2}, η_F = 95%) produced at the IO-TiO_2|FDH cathode (red trace) after continuous 1 h illumination was quantified by IC analysis. The control experiment in absence of FDH (black trace) is also shown (no formate detected). **b** CPE at U_{app} = 0.3 V of the two-electrode tandem system. Photocurrent density as a function of time plotted for three independent replicates (red, blue and magenta traces), indicating the reproducibility of the system. Formate (n[HCO_2^-] = 0.185 $\pm$ 0.017 μmol cm^{-2}, η_F = 70 $\pm$ 9%; N = 3) produced at the cathode after continuous 1 h illumination was quantified by IC analysis. The series of control experiments in absence of FDH (black, green and light green traces) are also shown. Conditions: CO_2/$NaHCO_3$ (100 mM), KCl (50 mM), one atmosphere CO_2, pH = 6.5, T = 25 °C, continuous stirring. Simulated solar light source: AM 1.5G filter; E_e = 100 mW cm^{-2}; λ > 420 nm. The figure adapted from Sokol et. al., *J. Am. Chem. Soc.*, 2018, **140**, 16418–16422.

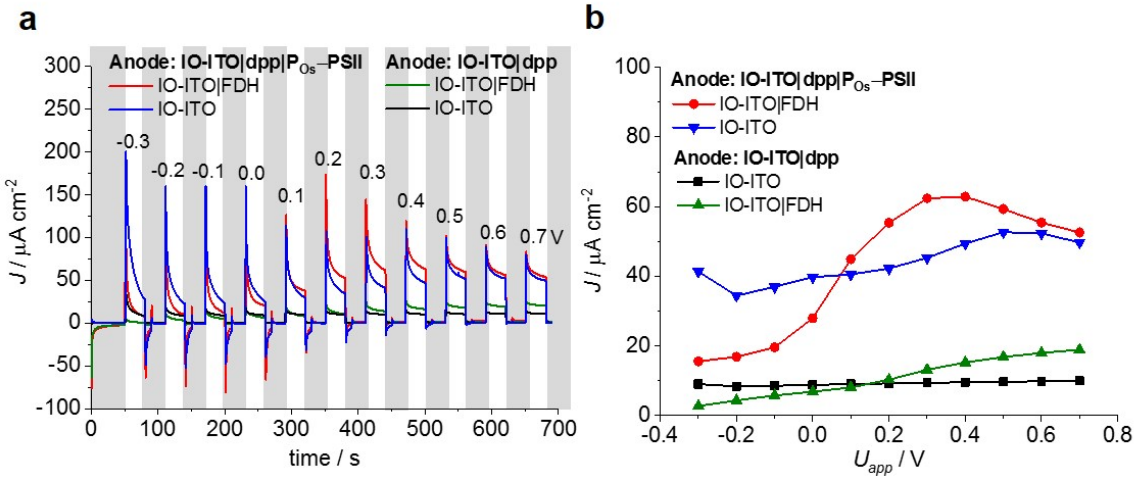

Figure D.5 **Characterisation of two-electrode PEC cell consisting of IO-TiO$_2$|dpp|P$_{Os}$–PSII wired to IO-ITO|FDH. a**, Representative stepped-voltage chronoamperometry (0.1 V voltage steps with 30 s dark and 30 s light cycles) of the fully assembled IO-TiO$_2$|dpp|P$_{Os}$–PSII || IO-ITO|FDH PEC cell (red trace). Control experiments in absence of PSII (green and black trace) and without FDH (blue and black trace) are also shown. Applied voltage (U_{app}) values are shown on top of the traces. **b**, Photocurrent density as a function of U_{app} based on chronoamperometry measurements determined in **a**. Steady-state J values were taken at the end of illumination and baseline-corrected for background dark current. Conditions: CO_2/$NaHCO_3$ (100 mM), KCl (50 mM), one atmosphere CO_2, pH = 6.5, T = 25 °C, continuous stirring. Simulated solar light source: AM 1.5G filter; E_e = 100 mW cm^{-2}; $\lambda > 420$ nm.